

THE RADIATION TOLERANCE AND DEVELOPMENT OF ROBOTIC PLATFORMS FOR NUCLEAR DECOMMISSIONING

A THESIS SUBMITTED TO THE UNIVERSITY OF MANCHESTER
FOR THE DEGREE OF DOCTOR OF PHILOSOPHY
IN THE FACULTY OF SCIENCE AND ENGINEERING

2017

Matthew J Nancekievill
School of Electrical and Electronic Engineering

Contents

Abstract	21
Declaration	22
Copyright Statement	23
Acknowledgements	24
List of Publications	25
1 Introduction	27
1.1 Current State of Nuclear Decommissioning	27
1.1.1 Radiation Tolerance of COTS Components	28
1.1.2 Development of Novel Robotic Platforms	28
1.2 Research outcomes	29
1.2.1 Knowledge transfer with Hitachi-GE, Japan through a 3-month internship	30
1.3 Thesis structure	30
2 Review of the Radiation Tolerance of Common Electronic Components	31
2.1 Fundamental Radiation Principles	32
2.1.1 Generalised radiation effects on electronic components	32
2.1.2 Expected Total Ionizing Dose (TID) and Dose-rate	33
2.2 Rad. Tolerance of Dielectrics and Conductors	34
2.2.1 Dielectrics	35
2.2.2 Conductors	36

2.3	Radiation Tolerance of Passive Components	38
2.3.1	Resistors	38
2.3.2	Inductors	39
2.3.3	Capacitors	39
2.4	Radiation Tolerance of Active Components	42
2.4.1	Semiconductors	42
2.4.2	Metal-Oxide-Semiconductor Field Effect Transistors	43
2.4.3	Bipolar Junction Transistors (BJTs)	45
2.5	Single-Event Effects (SEE)	47
2.5.1	Latch-up	47
2.6	Dose-rate effects	49
2.6.1	Enhanced Low Dose-Rate Sensitivity (ELDRS)	49
2.6.2	Elevated Temperature Irradiations (ETIs)	51
2.7	Annealing	51
2.8	Suggested Components for Experimentation	52
2.8.1	Linear Voltage Regulators	53
2.8.2	Inertial Measurement Units (IMUs)	53
2.9	Summary	54
3	Radiation Tolerance of Inertial Measurement Units	56
3.1	Radiation Tolerance of IMUs	57
3.1.1	Accelerometer Structure	57
3.1.2	Gyroscope Structure	60
3.2	Radiation tolerance of IMUs	62
3.2.1	Capacitive radiation tolerance	62
3.2.2	Piezoresistive radiation tolerance	63
3.2.3	Piezoelectric radiation tolerance	63
3.3	Analogue and Digital output MEMS	64
3.4	Summary of Chosen Parts	66
3.5	Experimental Setup	67
3.5.1	Experimental Facilities	67
3.5.2	Experimental Procedure	68

3.6	Digital IMU Results	69
3.6.1	LSM9DS0	70
3.6.2	MPU-6050	74
3.6.3	SEN-10121	75
3.7	Analogue IMU Results	77
3.7.1	ADXL335	78
3.7.2	ENC-03R	79
3.8	Results Analysis and Mitigation Techniques	80
3.9	Summary	81
4	Radiation Tolerance of Power Regulation Components	82
4.1	Introduction	82
4.2	Experimental Setup	83
4.2.1	Experimental Facilities	83
4.2.2	Experimental Procedure	83
4.3	Initial Results	86
4.3.1	Device Descriptions	86
4.3.2	Voltage References	86
4.3.3	Variable Load Experiments	87
4.3.4	Annealing	89
4.3.5	Voltage Regulator	90
4.3.6	No Load Experiments	92
4.3.7	Annealing	93
4.3.8	Analysis of Results	93
4.4	Further Experimentation on COTS Linear Voltage Regulators	95
4.4.1	Device Descriptions	95
4.4.2	Variable load experiments	96
4.4.3	No Load experiments	99
4.4.4	Anneal of voltage regulators	99
4.4.5	Analysis of Results	100
4.5	Discrete Voltage Regulator	102
4.5.1	Device Descriptions	102

4.6	Discrete regulator Results	104
4.6.1	Variable load experiments Alterations	104
4.6.2	No load experiments	106
4.6.3	Analysis of Results	109
4.7	Temperature Controlled Experiments	110
4.7.1	Fairchild KA7805	110
4.7.2	Discrete regulators	111
4.8	Interrupted Irradiation Thermal Anneal	113
4.8.1	Results Analysis	115
4.9	Conclusions	116
4.10	Initial results on COTS microcontroller radiation tolerance	118
4.10.1	Microcontroller testing	118
4.10.2	Microcontroller Results analysis and conclusions	119
5	Current Underground Robotic Platforms and Environment	121
5.1	Environment of Sellafield	122
5.1.1	Soil Composition	122
5.1.2	Radioactive leak pathways	124
5.1.3	Radionuclide Information	127
5.1.4	Dose-rates	128
5.2	Underground Burrower Requirements	129
5.3	Current Robotic Technology	130
5.3.1	Regolith Advanced Surface Systems Operations Robot	130
5.3.2	An Agile Burrowing Robot for Underground Chemical Source Location	131
5.3.3	Autonomous Burrowing Robot for Lunar Subsurface Exploration	132
5.3.4	DigBot	133
5.3.5	The Mars Underground Mole	133
5.3.6	Puncturing Mud Robot	135
5.3.7	Further Techniques Considered	135
5.3.8	Summary of Current Robotic Platforms	137
5.4	Summary and Evaluation of Current Research	138

6 Development of Underground Burrower	140
6.1 Contra-rotor screw mechanism development	140
6.1.1 Contra-rotor testing	145
6.2 Hammer mechanism development	146
6.2.1 Hammering mechanism structure	146
6.2.2 Force calculations	147
6.3 Initial hammering mechanism prototype	149
6.3.1 Initial Test Results	149
6.4 Developed Prototype	150
6.4.1 Optimisation of spring combinations	153
6.4.2 Resultant burrowing penetration results	154
6.4.3 Eccentric motor	155
6.5 Analysis of device development	157
6.6 Summary	158
7 A Review of Current Submersible Robotic Platforms	160
7.1 Environment	161
7.1.1 Sellafield Environment	161
7.1.2 Fukushima Environment	162
7.2 Submersible ROV Requirements	166
7.3 State-of-the-art Research	167
7.3.1 Ellipsoidal Vehicle for Inspection and Exploration (EVIE) . . .	168
7.3.2 The Eyeball ROV	168
7.3.3 EU-funded CoCoRo project	169
7.3.4 Swimming Robot	170
7.3.5 Deep Trekker (DTG2)	171
7.3.6 Video Ray	172
7.3.7 AC-ROV	173
7.3.8 OpenROV	174
7.3.9 Forth AVEXIS	175
7.3.10 AVEXIS	175
7.3.11 Evaluation of current Technology	177

7.4	Sensor Instrumentation	178
7.5	Summary and Evaluation of Current Research	179
8	Development of a Submersible ROV	180
8.1	Development and Integration of New Designs	181
8.1.1	Waterproofing and assembly	181
8.1.2	Communication Protocol	183
8.1.3	Electronic Design	186
8.1.4	Control Interface	187
8.2	Radiation Sensor Integration	188
8.2.1	CeBr ₃ detector implementation	189
8.2.2	Sonar implementation	193
8.3	Technical Demonstration NMRI, Japan	198
8.4	Software Development	201
8.4.1	Positioning system	201
8.4.2	3D point cloud construction	202
8.5	Summary	204
9	Conclusions and Future Work	205
9.1	Research Outcomes	205
9.2	Suggested Future Work	208
9.2.1	Radiation tolerance of COTS components	208
9.2.2	Robotic platforms	209
9.3	Summary	210
References		211
A Radiation Unit Comparison		228
B Further IMU data		230
B.1	Additional LSM9DS0 IMU test sample results	230
B.2	Additional MPU-6050 IMU test sample results	241
B.3	Additional SEN-10121 IMU test sample results	245
B.4	Additional ADXL335 IMU test sample results	248

C Supplementary Power Regulation Tests Information	253
C.1 Schematics	253

Word count 43543

List of Tables

2.1	Summary of radiation effects dependent on incident radiation type [7]	33
2.2	Example segment of European preferred parts list [67].	53
3.1	Main failure modes of MEMS dependent on actuation principle [72]	64
3.2	IMUs chosen for radiation tolerance testing	67
4.1	Devices Chosen for Experimentation.	86
4.2	The average output voltage of the Fairchild LM336Z5 voltage reference at intervals up to a TID of 5 kGy(Si)	87
4.3	The average output voltage of the Texas Instruments LM336Z5 voltage reference at intervals up to a TID of 5 kGy(Si)	88
4.4	The average output voltage of the Texas Instruments LM4040DIZ5 voltage reference at intervals up to a TID of 5 kGy(Si)	89
4.5	Output voltage of references monitored for 3 weeks post-irradiation.	89
4.6	Output voltage of KA7805 regulator monitored for 3 weeks post-irradiation.	93
4.7	Change in output voltage of COTS Voltage Regulators After a TID of 5 kGy(Si).	98
4.8	Change in output voltage of COTS Voltage Regulators After a TID of 3 kGy(Si)	99
4.9	Output voltage of MC7805 and L4941BV regulators monitored for 3 weeks post-irradiation.	99
4.10	Change in Output Voltage of Discrete Voltage Regulators After a TID of 5 kGy(Si).	108
5.1	Subdivision of the Quaternary Drift in the Sellafield Buried Channel [103]	124

5.2	Summary of radiation dose-rates and total doses of a representative nuclear environment [107].	129
5.3	MUM specifications [118].	134
5.4	Summary of the main specifications of literature research projects. . . .	138
6.1	Summary of spring optimisation	154
7.1	Summary of the main specifications of discussed submersible ROVs. . .	177
8.1	Summary of IMAGENEX 831L specifications.	194
A.1	Summary of derived SI units for radiation	228
A.2	Summary of conversion from SI units to widely used units in literature .	229

List of Figures

2.1	Fundamental configuration of conduction bands and valence bands for a) a conductor b) a semiconductor and c) a dielectric [21].	35
2.2	Approximate radiation tolerance of inorganic materials [23].	36
2.3	Approximate radiation tolerance of organic dielectrics [23].	37
2.4	Resistance change of carbon film and metal film resistors v.s. hours under radiation, dose rate of $5.9\text{kGy(Si).hr}^{-1}$ [30].	38
2.5	Typical structure of a capacitor [33].	40
2.6	Capacitance of one batch of samples before and after irradiation [36]. .	40
2.7	The capacitance and voltage of SiO_2 MOS capacitors at different TIDs [38].	41
2.8	The annealing progress of a MOS capacitor over 3 weeks [38].	41
2.9	Relative radiation sensitivity of capacitors [35].	42
2.10	Charge trapping in the Si/SiO_2 interface layer in a NMOS transistor [10].	43
2.11	Trapped charges in PMOS transistor and drain current/gate voltage curves representing threshold shift [7].	44
2.12	Trapped charges in NMOS transistor with drain current/gate voltage curves representing threshold shift [7].	44
2.13	Simplified physical model of a BJT [42].	45
2.14	Typical current gain characteristics for various levels of TID. β_{pk} is the peak pre-radiation current gain and V_{BE} is the base-emitter junction bias [45].	46
2.15	Normalised current gain for each PNP BJT vs emitter base voltage. Total dose 5 kGy(Si) (500 krad(Si)) [46].	47
2.16	Cross section of CMOS circuit depicting latch-up mechanism from in- cident cosmic ray [24].	48
2.17	Cross section of basic CMOS inverter with Latch-up circuit model [49].	48

2.18	Simplified illustration of ELDRS effect [52].	50
2.19	Sensitivity to gamma radiation of example electronic components, adapted from [9]. Black represents mild-to-moderate damage, grey represents moderate-to-severe and white represents severe permanent damage. . .	55
3.1	Fundamental structure of an accelerometer [74].	58
3.2	Structure of a capacitive accelerometer [75].	59
3.3	Possible arrangements of a piezoelectric accelerometer: A) Compression coupling, B) Flexural coupling, and C) Shear coupling [74].	59
3.4	Outline of the mechanical structure of a piezoresistive accelerometer [76].	60
3.5	Outline of a vibrating gyroscope mechanism showing a mass suspended by four springs with the mass oscillating into different positions dependent on rotation speed and direction [74].	61
3.6	a) Cylindrically shaped piezoelectric ceramic vibrating gyro. b) Alternating voltage applied to electrodes, which flexes the cylinder along an axis. C) Axial view of gyro cylinder, where Coriolis force flexes it along perpendicular axis [74].	61
3.7	Block diagram of the analogue output accelerometer ADXL335 indicative of many analogue accelerometers and gyroscopes [90].	65
3.8	Block diagram of the digital accelerometer ADXL345 indicative of all digital accelerometers and gyroscopes [91].	66
3.9	Decay scheme of ^{60}Co gamma source.	68
3.10	The ^{60}Co gamma irradiator.	68
3.11	Photo of compound angle mount and experimental set-up of ADXL335 IMU radiation tolerance tests placed within the Co-60 irradiator. . . .	69
3.12	Experimental procedure block diagram representing the data flow. . . .	69
3.13	Degradation of x, y and z-axis of the LSM9DS0 accelerometer.	70
3.14	Degradation of x, y and z-axis of the LSM9DS0 gyroscope.	72
3.15	Degradation of x, y and z-axis of the LSM9DS0 magnetometer	73
3.16	Degradation of x, y and z-axis of the MPU-6050 gyroscope.	74
3.17	Degradation of x, y and z-axis of the MPU-6050 accelerometer. . . .	75
3.18	Degradation of the x, y and z-axis of the ADXL345 accelerometer as part of the SEN-10121 IMU.	76

3.19	Degradation of the x, y and z-axis of the ITG-3200 gyroscope on-board the SEN-10121 IMU up to a TID of 1 kGy(Si)	77
3.20	Degradation of the x, y and z axis of the ADXL335 accelerometer.	78
3.21	Degradation of solitary axis of the ENC-03R gyroscope.	79
4.1	Block diagram of an example voltage regulator (Fairchild KA7805 [94]) test sample connected to a load switching circuit.	84
4.2	Photograph of example switching circuit.	84
4.3	Outline of Experimental circuit. The dashed line represents the irradiator boundary.	85
4.4	Voltage reference test circuit photograph.	87
4.5	Outline of voltage regulator circuit before and after irradiation.	91
4.6	Degradation of the Fairchild KA7805 voltage regulator during an irradiation with a TID of 5 kGy(Si). Showing change in output voltage with an increasing dose.	91
4.7	Degradation of a grounded Fairchild KA7805 COTS voltage regulator before and after irradiation with a TID of 10 kGy(Si).	92
4.8	Change in output voltage of the ON Semiconductor MC7805 voltage regulator during irradiation with a TID of 5 kGy(Si).	97
4.9	Degradation of the ST Microelectronics L4941BV voltage regulator during irradiation with a TID of 5 kGy(Si).	98
4.10	Degradation of eight separate Fairchild KA7805 COTS voltage regulators during an irradiation with TID of 5 kGy(Si). Only the 700 mA load is shown.	100
4.11	Schematic of discrete voltage regulator designed for decreased device degradation. Transistors are PNP BJTs as opposed to common NPN types.	102
4.12	Degradation of TIP2955 discrete voltage regulator during an irradiation with a TID of 10 kGy(Si) and 5 minute no load interruptions at 4 kGy(Si) and 8 kGy(Si).	105
4.13	Degradation of TIP36C discrete voltage regulator during an irradiation with a TID of 5 kGy(Si).	106

4.14 Degradation of BD250C discrete voltage regulator during an irradiation with a TID of 5 kGy(Si)	107
4.15 Degradation of a no load TIP2955 discrete voltage regulator before and after an irradiation with a TID of 5 kGy(Si). Only the 2 A load is shown as all other currents show lesser or minimal degradation.	108
4.16 Degradation of COTS voltage regulator KA7805 at temperatures of 50°C, 65°C and 80°C.	111
4.17 Degradation of TIP2955 discrete voltage regulator during an irradiation with a TID of 5 kGy(Si) at temperatures of 50°C, 65°C and 80°C.	112
4.18 Degradation of TIP36C discrete voltage regulator during an irradiation with a TID of 5 kGy(Si) at temperatures of 50°C, 65°C and 80°C.	112
4.19 Degradation of BD250C discrete voltage regulator during an irradiation with a TID of 5 kGy(Si) at temperatures of 50°C and 80°C.	113
4.20 Interrupted irradiation with thermal anneal for the TIP2955 discrete voltage regulator.	114
4.21 Interrupted irradiation with thermal anneal for the TIP36C discrete voltage regulator.	114
4.22 Interrupted irradiation with thermal anneal for the BD250C discrete voltage regulator.	115
4.23 The memory of the Microchip PIC18F4520 before (on the left) and after (on the right) irradiation with a TID 1.2 kGy(Si).	119
 5.1 Overview of the superficial deposits on top of the bedrock at the Sellafield site	123
5.2 Contour map of the Sherwood Sandstone Rockhead Surface (mAOD) [104].	125
5.3 Overview of potential leaks and groundwater movement [102].	126
5.4 List of radionuclides found beneath the Sellafield site and their predicted travel velocities [101].	127
5.5 NASA's RASSOR robot used for lunar excavation and geological sampling [111].	130
5.6 An Agile Burrowing Robot for Underground Chemical Source Location [112]	131

5.7	Device used to deploy sensor node as close to chemical source as possible [113].	132
5.8	Screw mechanisms prototyped to find optimum solution [115].	132
5.9	DigBot prototype demonstrating contra-rotor screw [116]	133
5.10	Mars Underground Mole hammering mechanism.	134
5.11	Turning device of puncturing mud robot [119].	135
5.12	Side-by-side comparison of mole morphology and robot design [120]. . .	136
5.13	Deployment of a feather vane [121].	136
5.14	Bivalve configuration for anchoring a device [122].	137
6.1	a) Front half of contra-rotor screw, b) back half of contra-rotor screw with in-built planetary gearbox.	142
6.2	Technical drawing of the front half of a contra-rotor screw.	142
6.3	Technical drawing of the back half of a contra-rotor screw.	143
6.4	a) Side view of the initial contra-rotor prototype, b) rear-view showing the planetary gearbox used to rotate the halves in different directions. .	143
6.5	Direction of soil expulsion of a conical shaped screw during sub-surface locomotion [128].	144
6.6	CAD models of example contra-rotor mechanism prototypes.	145
6.7	Example of cam system used	146
6.8	Simplified model of internal hammering mass attached to spring	147
6.9	Model of an inclined plane, representative of a cam.	147
6.10	a) Outline of internal hammering mechanism, b) removable nose cone that can be replaced with different end effectors.	149
6.11	Average of ten attempts of the device to penetrate to a depth of 250 mm.	150
6.12	Motor now encased in a brass housing acting as suppressor mass. . . .	150
6.13	Housing for the motor, cam and axle rotator in the developed hammering prototype	151
6.14	Technical drawing of cam manufactured for developed prototype	151
6.15	Technical drawing of axle rotator mounted above the cam.	152
6.16	Technical drawing of the hammer mass developed for the hammering prototype.	152
6.17	Overview of the test set-up for the hammering mechanism device. . . .	154

6.18	Outline of the average time taken for the device to reach a depth of 25 cm.	155
6.19	Outline of eccentric motor size and mounting structure. The two threaded holes mounted the motors to the outer casing.	156
6.20	Sensing unit application suggestion.	158
7.1	The current state of one of Sellafield's storage ponds [135]	162
7.2	CAD overview of PCV, pedestal, grating and predicted fuel debris location [136].	163
7.3	Shape changing robot developed and deployed by Hitachi [137].	163
7.4	One of the shape-changing robots stuck in grating gap.	164
7.5	Visual inspection of grating surrounding the pressure containment vessel [138].	164
7.6	Collapsed grating within the Fukushima Power Plant [138].	164
7.7	Footage of Hitachi's "swimming robot" deployed in Fukushima Daiichi Torus room [136].	165
7.8	Fallen debris within the flooded suppression chamber [138].	166
7.9	a) Outline of developed "little sunfish" and b), photo taken by the ROV from inside the PCV [140,141].	167
7.10	Dimensions of the EVIE robotic platform project [142].	168
7.11	Overview of spherical robot with camera fixed on the exterior surface of the robot [143].	169
7.12	a) Overview if Lily robot design [147] and b), overview of Jeff robot design [146].	170
7.13	Hitachi's submersible robot for surveying of leakage points from PCV [136]	171
7.14	Deep Trekker (DTG2) starter pack [148].	172
7.15	VideoRay voyager submersible [150].	172
7.16	AC-CESS AC-ROV submersible ROV [151].	173
7.17	OpenROV v2.8 kit [152].	174
7.18	FORTH AVEXIS [153].	175
7.19	The University of Manchester's original concept AVEXIS [154].	176
7.20	The University of Manchester's AVEXIS [4].	176
8.1	End-caps made from PVC with two o-rings for waterproofing.	182

8.2	Dimensions of AVEXIS ROV	182
8.3	Outline of cable penetrators manufactured for watertight seal around entry cables.	183
8.4	The outer white tether was the initial design. A twisted pair of 20 AWG can be seen in the centre for comparison.	184
8.5	A local network is created from a surface laptop and multiple devices can attach to the same network through multiple powerline adaptors [158].	185
8.6	Overview of the communication from a surface based computer to the submersible.	185
8.7	Initial two-wire tether prototype.	186
8.8	A comparison of new and old boards showing the modifications in terms of size and robustness.	186
8.9	Block diagram of the ROV's PCB.	187
8.10	Screenshot of the camera feed as seen in a web browser.	188
8.11	Overview of the CeBr ₃ gamma detector.	189
8.12	CeBr ₃ detector and bespoke water-tight container.	190
8.13	Exposure of the CeBr ₃ gamma detector integrated within the ROV to a Cs ¹³⁷ source on a lab bench-top.	191
8.14	Initial measurement of radioactive counts exposed on a lab benchtop whilst integrated within the ROV for 10 minutes.	191
8.15	Exposure of the CeBr ₃ gamma detector integrated within the ROV to a Cs ¹³⁷ source whilst submerged.	192
8.16	Counts observed with the ROV submerged but as close as possible to the source for 10 minutes.	192
8.17	Counts observed with the ROV 50 cm from the tank edge and radioactive source for 10 minutes.	193
8.18	IMAGENEX 831L pipe profiling sonar [162].	194
8.19	Initial sonar communication testing.	195
8.20	Sonar integrated with the AVEXIS.	196
8.21	Screenshot of sonar output from Forth test. The two shapes represent a hose on the bottom of the tank.	197
8.22	NMRI water tank, dimensions 8 m x 50 m x 6 m (w x l x d).	198

8.23	Simulated debris placed at the bottom of the tank.	199
8.24	AVEXIS deployed within NMRI tank.	199
8.25	Sonar output over simulated debris.	199
8.26	Screenshot of on-board camera taking a picture of a pole placed approximately 2 m away in poor lighting.	200
8.27	Screenshot of prototype vision positioning system showing a mock AVEXIS and tank.	202
8.28	a) Side-on view of 3D reconstruction from water tank and b) isometric view with colour removed and annotation added to highlight the 3D image.	203
B.1	Further test sample of LSM9DS0 showing accelerometer degradation . . .	230
B.2	Further test sample of LSM9DS0 showing gyroscope degradation . . .	231
B.3	Further test sample of LSM9DS0 showing magnetometer degradation .	231
B.4	Further test sample of LSM9DS0 showing accelerometer degradation . .	232
B.5	Further test sample of LSM9DS0 showing gyroscope degradation . . .	232
B.6	Further test sample of LSM9DS0 showing magnetometer degradation .	233
B.7	Further test sample of LSM9DS0 showing accelerometer degradation . .	233
B.8	Further test sample of LSM9DS0 showing gyroscope degradation . . .	234
B.9	Further test sample of LSM9DS0 showing magnetometer degradation .	234
B.10	Further test sample of LSM9DS0 showing accelerometer degradation . .	235
B.11	Further test sample of LSM9DS0 showing gyroscope degradation . . .	235
B.12	Further test sample of LSM9DS0 showing magnetometer degradation .	236
B.13	Further test sample of LSM9DS0 showing accelerometer degradation . .	236
B.14	Further test sample of LSM9DS0 showing gyroscope degradation . . .	237
B.15	Further test sample of LSM9DS0 showing magnetometer degradation .	237
B.16	Further test sample of LSM9DS0 showing accelerometer degradation . .	238
B.17	Further test sample of LSM9DS0 showing gyroscope degradation . . .	238
B.18	Further test sample of LSM9DS0 showing magnetometer degradation .	239
B.19	Further test sample of LSM9DS0 showing accelerometer degradation . .	239
B.20	Further test sample of LSM9DS0 showing gyroscope degradation . . .	240
B.21	Further test sample of LSM9DS0 showing magnetometer degradation .	240
B.22	Further test sample of MPU-6050 showing accelerometer degradation .	241

B.23 Further test sample of MPU-6050 showing gyroscope degradation	241
B.24 Further test sample of MPU-6050 showing accelerometer degradation . .	242
B.25 Further test sample of MPU-6050 showing gyroscope degradation	242
B.26 Further test sample of MPU-6050 showing accelerometer degradation . .	243
B.27 Further test sample of MPU-6050 showing gyroscope degradation	243
B.28 Further test sample of MPU-6050 showing accelerometer degradation . .	244
B.29 Further test sample of MPU-6050 showing gyroscope degradation	244
B.30 Further test sample of SEN-10121 showing accelerometer degradation . .	245
B.31 Further test sample of SEN-10121 showing gyroscope degradation	246
B.32 Further test sample of SEN-10121 showing accelerometer degradation . .	246
B.33 Further test sample of SEN-10121 showing gyroscope degradation	247
B.34 Further test sample of ADXL335 accelerometer showing degradation with an increasing dose	248
B.35 Further test sample of ADXL335 accelerometer showing degradation with an increasing dose	248
B.36 Further test sample of ADXL335 accelerometer showing degradation with an increasing dose	249
B.37 Further test sample of ADXL335 accelerometer showing degradation with an increasing dose	249
B.38 Further test sample of ADXL335 accelerometer showing degradation with an increasing dose	250
B.39 Further test sample of ADXL335 accelerometer showing degradation with an increasing dose	250
B.40 Further test sample of ADXL335 accelerometer showing degradation with an increasing dose	251
B.41 Further test sample of ADXL335 accelerometer showing degradation with an increasing dose	251
B.42 Further test sample of ADXL335 accelerometer showing degradation with an increasing dose	252
C.1 Schematic of the switching circuit used during irradiation tests	253
C.2 Schematic of the relay drivers used to control the switching circuit used during irradiation tests	254

C.3 Schematic of the voltage reference test sample circuit used during irradiation tests	254
C.4 Schematic of the voltage regulator test sample circuit used during irradiation tests	255

The University of Manchester

Matthew J Nancekievill

Doctor of Philosophy

The Radiation Tolerance and Development of Robotic Platforms for Nuclear Decommissioning

December 20, 2017

There is an increasing desire to deploy low-cost robotic systems in nuclear decommissioning environments. These environments include long-standing nuclear fuel storage ponds such as those at the Sellafield site in Cumbria, UK as well as areas affected by expulsion of radioactive material from sites such as the Fukushima accident in Japan 2011.

An area of concern for the successful deployment of robotic platforms in a radioactive field is their radiation tolerance. It is necessary to understand how the low-cost components used within robotic platforms react to radiation exposure in a nuclear decommissioning environment.

This thesis discusses the radiation tolerance of multiple commercial-off-the-shelf (COTS) components that are commonly used within a robotic platform up to an expected yearly total dose of 5 kGy(Si). It was found that COTS voltage regulators are susceptible to gamma exposure, however, development of a discrete voltage regulator showed an increased tolerance to radiation under certain load and temperature conditions. Inertial measurement units were also investigated and found to be susceptible to a total ionising dose <1 kGy(Si).

Applying experimental results gathered from the radiation tolerance of COTS components should allow the development of low-cost robotic platforms that are capable of characterising nuclear decommissioning environments increasing efficiency and safety.

Two robotic platforms were designed as part of this research study with the nuclear decommissioning environments prioritised for characterisation the internal state of submerged nuclear facilities and the surrounding geology of nuclear fuel storage ponds. Over-used facilities such as the Sellafield legacy ponds, and hurriedly contained radioactive leaks from the Fukushima accident have created environments that require characterisation. In both instances, the exact location of spent fuel is not fully understood, with the likelihood that leaks into the surrounding geology have formed and remain uncharacterised.

An underground burrower capable of characterising the radiological environment of the geology underneath and surrounding spent nuclear fuel storage ponds has been researched and prototyped. Experimentation has suggested the use of a hammering mechanism device may be capable of deployment with future work required to develop the device further.

A second robotic platform entitled AVEXIS was also developed to characterise the unknown physical and radiological submerged environment. Work undertaken included development of the robotic platform to increase robustness and allow the deployment of multiple sensing technologies. Technical demonstrations of the submersibles' abilities were conducted in Japan to confirm the capability of the platform to characterise the Fukushima Nuclear Power Plant.

Declaration

No portion of the work referred to in the thesis has been submitted in support of an application for another degree or qualification of this or any other university or other institute of learning.

Copyright Statement

- i. The author of this thesis (including any appendices and/or schedules to this thesis) owns certain copyright or related rights in it (the “Copyright”) and s/he has given The University of Manchester certain rights to use such Copyright, including for administrative purposes.
- ii. Copies of this thesis, either in full or in extracts and whether in hard or electronic copy, may be made **only** in accordance with the Copyright, Designs and Patents Act 1988 (as amended) and regulations issued under it or, where appropriate, in accordance with licensing agreements which the University has from time to time. This page must form part of any such copies made.
- iii. The ownership of certain Copyright, patents, designs, trade marks and other intellectual property (the “Intellectual Property”) and any reproductions of copyright works in the thesis, for example graphs and tables (“Reproductions”), which may be described in this thesis, may not be owned by the author and may be owned by third parties. Such Intellectual Property and Reproductions cannot and must not be made available for use without the prior written permission of the owner(s) of the relevant Intellectual Property and/or Reproductions.
- iv. Further information on the conditions under which disclosure, publication and commercialisation of this thesis, the Copyright and any Intellectual Property and/or Reproductions described in it may take place is available in the University IP Policy (see <http://documents.manchester.ac.uk/DocuInfo.aspx?DocID=2442>), in any relevant Thesis restriction declarations deposited in the University Library, The University Library’s regulations (see <http://www.manchester.ac.uk/library/about/regulations>) and in The University’s Policy on Presentation of Theses.

Acknowledgements

I would like to thank Professor Barry Lennox, Mr Peter R. Green and Dr. Simon Watson for their supervision and support throughout the course of this PhD. I am eternally grateful for their guidance and the lessons they taught me.

It would also be impossible to build anything without the help of the electronic and mechanical workshops. Special thanks to Paul Shaw, Chris Kirkham, Danny Vale, Harris Maudsley, John Bramwell and Glyn Ireland from mechanical, as well as Derrick Bradshaw and Gary McStravick from PCB fabrication.

List of Publications

M. Nancekievill, A.R. Jones, M.J. Joyce, B. Lennox, J. Katakura, K. Okumura, S. Kamada, M. Katoh and K. Nishimura, “Application of Submersible ROV using Noel Radiation Sensing Techniques to aid in the Decommissioning of Fukushima Daiichi,” *IEEE Trans. Nucl. Sci Submission Pending*

M. Nancekievill, S. Watson, P.R. Green, and B. Lennox, “A Radiation Tolerant Discrete Voltage Regulator Using Commercial-Off-The-Shelf Components for Nuclear Decommissioning Environments,” *IEEE Trans. Nucl. Sci Submission Pending.*

B. Lennox, F. Arvin, B. Bird, L. Brown, W. Cheah, A. Di Buono, J. Espinosa, K. Gornicki, A. Griffiths, K. Groves, A. Gupta, J. Jones, H. Martin, M. Nancekievill, X. Poteau, S. Tournier, S. Watson, and T. Wright, “Robotic Platforms for Remote Access and Sensing Applications for Nuclear Decommissioning,” in *WM Symposia*, 2018, Submitted.

M. Nancekievill, A. Jones, M.J. Joyce, B. Lennox, S. Watson, J. Katakura, K. Okumura, S. Kamada, M. Katoh, and K. Nishimura, “A Remote-operated System to Map Radiation Dose in the Fukushima Daiichi Primary Containment Vessel,” in *ANIMMA*, 2017, Accepted

M. Nancekievill, S. Watson, P.R. Green, and B. Lennox, “Radiation tolerance of commercial-off-the-shelf components deployed in an underground nuclear decommissioning embedded system,” *IEEE Radiation Effects Data Workshp*, 2017.

L. Leay, W. Bower, G. Horne, P. Wady, A. Baidak, M. Pottinger, M. Nancekievill, A.

Smith, S. Watson, P. Green, B. Lennox, J. LaVerne, and S. Pimblott, “Development of irradiation capabilities to address the challenges of the nuclear industry,” *Nuclear Instruments and Methods in Physics Research B*, vol. 343, pp. 62-69, Nov 2015

Chapter 1

Introduction

1.1 Current State of Nuclear Decommissioning

With the increased use of robotics in many industries, there is a desire to deploy robotic platforms in radioactive environments in the nuclear decommissioning industry [1]. Areas highlighted for concern include the radioactive contamination of geology surrounding nuclear storage ponds and the decommissioning of nuclear sites including the Fukushima accident.

The Nuclear Decommissioning Authority (NDA) estimate the cost of nuclear clean-up in the UK to be in excess of £100bn over the next 120 years [2]. There is a requirement for low-cost robotic platforms, with the ability to reduce risk, as an alternative to current manual processes such as cutting, surveying and disposal. These processes are currently undertaken in cumbersome protective suits. The Fukushima accident of 2011 has also illustrated the need for robotic systems capable of surviving high radiation fields [3].

Very little work has been undertaken to characterise the radiation tolerance of low-cost robotic platforms that could be deployed in a nuclear decommissioning environment for sustained periods of time. The use of low-cost, commercial-off-the-shelf (COTS) embedded systems could help provide enhanced knowledge from inside radioactive environments where it is unsafe for human workers.

Due to the need for radiation tolerant robotic platforms, this study included work in two distinct areas. Firstly, the radiation tolerance of low-cost, COTS components, and secondly, the development of bespoke robotic platforms for a nuclear decommissioning

environment.

1.1.1 Radiation Tolerance of COTS Components

A thorough review of the state-of-the-art literature was conducted to direct research into the most susceptible low-cost COTS components.

This led to the testing of multiple COTS components typical of low-cost robotic platforms to determine their radiation tolerance and degradation modes. The results of these experiments will be discussed and analysed with future work suggested based on the outcomes.

1.1.2 Development of Novel Robotic Platforms

Two separate robotic platforms have been developed as part of this research project. Initially, a novel underground burrower was developed before work was undertaken on re-designing the University of Manchester's research project concerning the development of a submersible ROV called AVEXIS.

Underground burrower

Current technology to monitor the geology surrounding nuclear storage ponds is limited. A new device capable of burrowing beneath the Sellafield legacy ponds to characterise radiation leaks from beneath the storage facility was considered desirable [1]. This section of the research project, presents related work in the current state-of-the-art before developing these ideas to prototype a device capable of burrowing in a range of soils.

Submersible ROV

The University of Manchester has developed a submersible ROV, the Aqua Vehicle Explorer for In-Situ Sensing (AVEXIS) [4]. It was designed to characterise the Sellafield legacy ponds, identifying unknown locations of devices and fuel in the ponds.

It was suggested that the AVEXIS could be adapted to work within the Fukushima Daiichi power plant where the pressure containment vessel (PCV) has been flooded to keep the reactors cool. The location of the spent nuclear fuel remains unknown and a

device capable of characterising the location and activity of radioactive matter would aid in the efficiency and speed of decommissioning efforts.

Work undertaken to integrate a novel gamma detector and sonar to characterise the physical layout of the internals is described in this work with the results of technical demonstrations of the capabilities at test facilities in Japan presented.

1.2 Research outcomes

This section outlines the contribution to knowledge achieved within this research project before Chapter 9 analyses the success of these outcomes.

- **Experimental validation of the degradation modes COTS inertial measurement units (IMUs) experience when exposed to γ -radiation:** Experiments were undertaken that explored and analysed the degradation modes of multiple low-cost IMUs. The characterisation of low-cost IMUs has not been described in the currently available literature.
- **Analysis of the observed degradation modes of COTS power regulation components:** Multiple power regulation COTS components were exposed to γ -radiation with the results outlining which devices are most susceptible to failure. Little work had been conducted on the radiation tolerance of low-cost COTS power regulation components.
- **Investigation into the radiation tolerance of a bespoke discrete voltage regulator:** Verification of a more radiation tolerant and consistent degradation mode, of a low-cost, power regulation system, was achieved via development of a discrete linear voltage regulator. There were no known examples of this technique applied to low-cost systems in the current literature.
- **Analysis of appropriate underground burrowing techniques:** Development of an underground burrower prototype suggested the use of a hammering mechanism device should be prioritised for development. This study outlines progress made and verifies the applicability of the chosen mechanism.
- **Development of an ROV capable of characterising submerged nuclear decommissioning environments:** The development of a device capable of monitoring existing storage ponds and adaptable to nuclear accidents such as

Fukushima has been completed with technical demonstrations of the ROV's capabilities completed in Japan.

1.2.1 Knowledge transfer with Hitachi-GE, Japan through a 3-month internship

A 3-month internship with Hitachi-GE was completed during the PhD but is not discussed in this thesis due to IP issues. An application to a competitive scheme offered across multiple universities was accepted after interview to enable work to be undertaken with Hitachi-GE based in Hitachi City, Ibaraki prefecture, Japan.

Work was conducted within the department of the company tasked with decommissioning of Unit 1 at the Fukushima site (Fukushima Daiichi). An example of work completed included development of a device to be added to the shape changing robot [5] developed by Hitachi to characterise the grating surrounding the PCV. This was recently deployed into Fukushima.

1.3 Thesis structure

This thesis is not presented chronologically as much of the work was conducted concurrently. Therefore, the thesis is outlined as follows; Chapters 2 to 4 focus on the radiation tolerance of COTS electronic components and the development of possible solutions. Chapter 2 reviews the current state of the art literature before experimental results from radiation tolerance testing of IMUs and power regulation components is then presented and analysed in Chapters 3 and 4.

Chapters 5 to 8 of this thesis are focussed on the development of robotic platforms to be deployed in nuclear decommissioning environments. Chapters 5 and 7 present a review of the current state-of-the-art underground burrowers and submersibles respectively, before Chapter 6 discusses work undertaken to develop an underground burrower. Chapter 8 outlines the work completed in developing the capabilities of the AVEXIS with results from technical demonstrations discussed. Chapter 9 concludes this thesis with future work and a summary of the outcomes achieved throughout this study

Chapter 2

Review of the Radiation Tolerance of Common Electronic Components

A review of the state-of-the-art research conducted on the radiation tolerance of low-cost commercial-off-the-shelf (COTS) electronic components is presented in this chapter. Components chosen for review represent typical devices deployed within a low-cost robotic platform.

The effects of radiation on an atomic level are briefly summarised and then developed into the radiation effects on generalised component sub-sets such as resistors, transistors and linear integrated circuits (ICs) fabricated from silicon semiconductor technologies. Silicon based devices were chosen due to their wide use in components and low-cost.

A summary of the expected dose-rates and total-ionising doses (TIDs) in a nuclear decommissioning environment will be outlined as this research is being conducted to aid in the design of robotic platforms for nuclear decommissioning. An explanation of how these values may influence changes in current experimental procedures for radiation tolerance of electronic components is also discussed.

Gaps in the literature are highlighted to form the basis of experiments to determine the radiation tolerance of typical sub-systems of a low-cost robotic platform. The results are then discussed in Chapters 3 and 4

It is intended that through targeted experimentation on the radiation tolerance of electronic components outside the scope of the state-of-the-art literature, there is potential for a set of guidelines to be created to aid in the design of any embedded

system for a nuclear decommissioning environment.

This initially requires a fundamental understanding of the underlying principles for radiation degradation.

2.1 Fundamental Radiation Principles

There are three main types of radiation; alpha (α), beta(β) and gamma (γ) [6]. For the purpose of this work, γ -radiation was chosen for all component testing.

Any robotic platform developed for this research project will be manufactured with a metallic hull or body. Both α and β radiation can be shielded against with a thin metallic case. Therefore, α and β radiation were considered a low-priority for experimentation.

2.1.1 Generalised radiation effects on electronic components

There are two fundamental types of radiation effects that can be observed in electronic components during irradiation. These are [7];

1. Physical effects/atomic displacement, for example, nucleus displacement that creates knock-on effects as well as scattering of the incident beam, resulting in a secondary emission of radiation.
2. Ionization effects.

Atomic displacement causes defects and impurities within the material of an electronic component that affect its properties [8]. This is the process of breaking bonds and the formation of new atomic bonds within the component core material.

Ionization effects manifest as electrical paths that cross isolated boundaries. The promotion of electrons forms an unwanted charge, leading to increased leakage currents whilst exposed to radiation [9]. Over time, devices or device junctions degrade with the increased leakage current [10].

Table 2.1 highlights which effect is more prevalent in a device dependent on the type of radiation and its energy level. Silicon and silicon dioxide (SiO_2) are shown as they are the major constituent parts in many active COTS components.

It shows that α and β -radiation primarily cause displacement damage whereas

Table 2.1: Summary of radiation effects dependent on incident radiation type [7].

Radiation Type	Energy Range	Main Type of Interaction	Primary effects in Si and SiO ₂	Secondary effects in Si and SiO ₂
γ	Low energy	Photoelectric effect	Ionising phenomena	Displacement damage
	Medium energy	Compton effect		
	High energy	Pair production		
α/β	Low energy	Capture and nuclear reaction	Displacement damage	Ionising phenomena
	High energy	Elastic scattering		

γ -radiation principally causes ionization effects. Although these are the primary interactions, it is possible that γ -radiation can cause atomic displacement and α and β -radiation can cause ionisation effects.

The effects of radiation, on an atomic level, dictate how materials react to exposure. Analysis of the effect of radiation on component packaging materials is discussed in Section 2.2.1 with effects on materials that make up the working part of the component discussed from Section 2.3 onwards. Each component comprises of a different set of materials with a different atomic structure, which react differently to radiation exposure. It is important to understand these different reactions for common components in embedded systems.

2.1.2 Expected Total Ionizing Dose (TID) and Dose-rate

As well as understanding the effects of radiation on an atomic level, we must determine the total level of radiation exposure expected in a nuclear decommissioning environment. This would allow targeted experimentation of components for deployment in the required nuclear decommissioning environment.

Typical total ionizing doses (TIDs) found in a first generation Magnox storage pond can be as high as 0.5 MGy(Si) over a 10 year period [11]. This equates to a dose-rate of 1570 μ Gy(Si).s⁻¹. Similar dose-rates have been recorded around the Fukushima power plant with dose-rates of 4 to 6 Gy(Si).hr⁻¹ (approximately 1,000 to 1,600 μ Gy(Si).s⁻¹) observed by Hitachi's shape-changing robot used to characterise Unit 1's Primary Containment Vessel (PCV) [12].

If an embedded system was deployed in a nuclear decommissioning environment for approximately 4 hours a day, 5 days a week for one year, it would be exposed to an average dose-rate of $1.4 \text{ mGy(Si).s}^{-1}$. This means that the TID for the system would be approximately 5.2 kGy(Si) . This was considered the first aim for an operating lifetime expectancy of any developed robotic platform.

Currently deployed components in radioactive environments are split into three categories; commercial-off-the-shelf (COTS), radiation tolerant COTS (such as [13]) and bespoke or hardened by design application-specific integrated circuits (ASICs). Current academic research has focused on understanding the performance of these components when they are exposed to the low Total Ionising Doses (TIDs) experienced on space missions (approximately 100 Gy.yr^{-1}) and also the large TIDs experienced in the vacuum chamber of CERN [14–18]. Testing of these components follow the standard MIL-STD-883k regime [19].

TID levels for these experiments reached a maximum of 0.5 to 1 kGy(Si) for COTS components and greater than 3 kGy(Si) for radiation tolerant COTS components. ASICs are tested to their specific requirements and range up to MGy TIDs.

COTS components are rarely tested over 1 kGy, with radiation tolerant COTS components offering higher guaranteed TID tolerance but at a much greater expense. Radiation tolerant ASICs require long development cycles and are very expensive consisting of bespoke silicon structures created for specific components [20]. A low-cost embedded system cannot use the expensive radiation tolerant COTS components or bespoke ASICs, therefore understanding the limitations of COTS components at higher TIDs is required.

It is also important to note that other than high-cost bespoke ASICs, the TID tests conducted on many components is considerably lower than the TID found in a typical decommissioning environment [14–18].

2.2 Rad. Tolerance of Dielectrics and Conductors

This section outlines the radiation tolerance of dielectrics and conductors. This highlights any susceptible dielectric to avoid between capacitor plates as well as understanding the interaction of radiation with conductors used to couple components in a

circuit.

2.2.1 Dielectrics

The difference between a dielectric and a conductor can be explained by the state of their conduction and valence bands. Fig. 2.1 shows the different fundamental characteristics of each type of material. It can be seen that a dielectric has a large energy band gap and an empty conduction band.

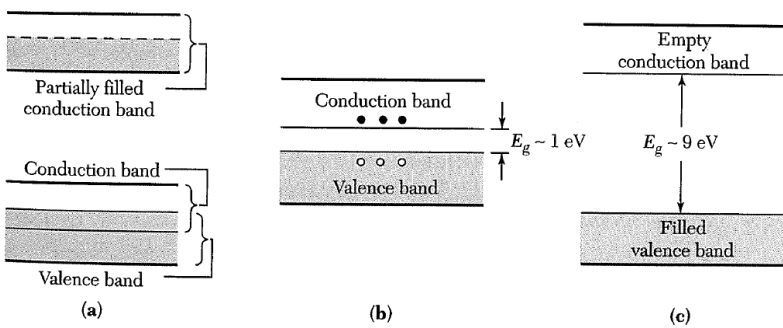


Figure 2.1: Fundamental configuration of conduction bands and valence bands for a) a conductor b) a semiconductor and c) a dielectric [21].

For electrical conductivity to occur, electrons must be excited from the valence band, into the conduction band [22]. The high energy level required to do this however, is more than room temperature thermal agitation or an electric field can provide [21].

Exposure of a dielectric to gamma radiation can cause excitation of an electron from the valence band to the conduction band as it is of a much higher energy than normal thermal agitation. Electrons promoted to the conduction band create electrical currents, breaking down the potential barrier, inducing leakage currents [9] and reducing resistance value [23].

Although temporary in many dielectrics [23, 24], this effect can be permanent. Excited electrons get trapped in lattice imperfections (due to atomic displacement or an inherently impure dielectric) resulting in permanent changes [25]. For example, PTFE wire insulation displays degradation at doses as low as 10 Gy(Si) with decreased flexibility and disintegration of material resulting in short-circuits between adjacent conductors.

Inorganic dielectrics are generally more radiation tolerant than organic [23]. Inorganic dielectrics are chemically unchanged after atomic displacement, whereas an

organic dielectric is chemically altered [23]. Any alteration chemically, can lead to physical changes in parameters such as tensile strength and thermal response.

Figs. 2.2 and 2.3 depict the difference in tolerance between some common organic and inorganic dielectrics.

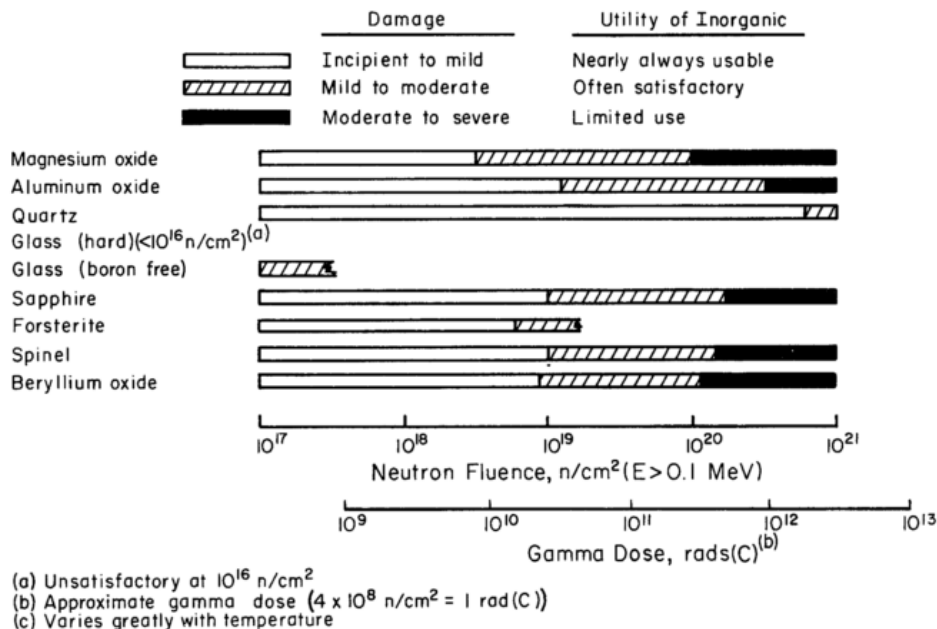


Figure 2.2: Approximate radiation tolerance of inorganic materials [23].

The graphs in Figures 2.2 and 2.3 suggest that most organic dielectrics fail at a total ionising dose (TID) less than 10⁸ Gy(Si), whereas inorganic dielectrics show no degradation up to 10¹⁰/10¹¹ Gy(Si). Care must be taken when choosing materials for deployment in a radiation environment, however, inorganic dielectrics should be preferred to organic alternatives due to their improved radiation tolerance. It should be noted, however, that organic dielectrics show no degradation up to the total dose expected in a nuclear decommissioning environment, and therefore, should also be suitable.

2.2.2 Conductors

As can be seen in Fig. 2.1, ionisation in conductors that promotes electrons from the valence band to the conduction band creates a larger current. It is possible that this increase in current may affect sensitive circuits with tight power source requirements [26]. However, the change in current is negligible and there is no permanent

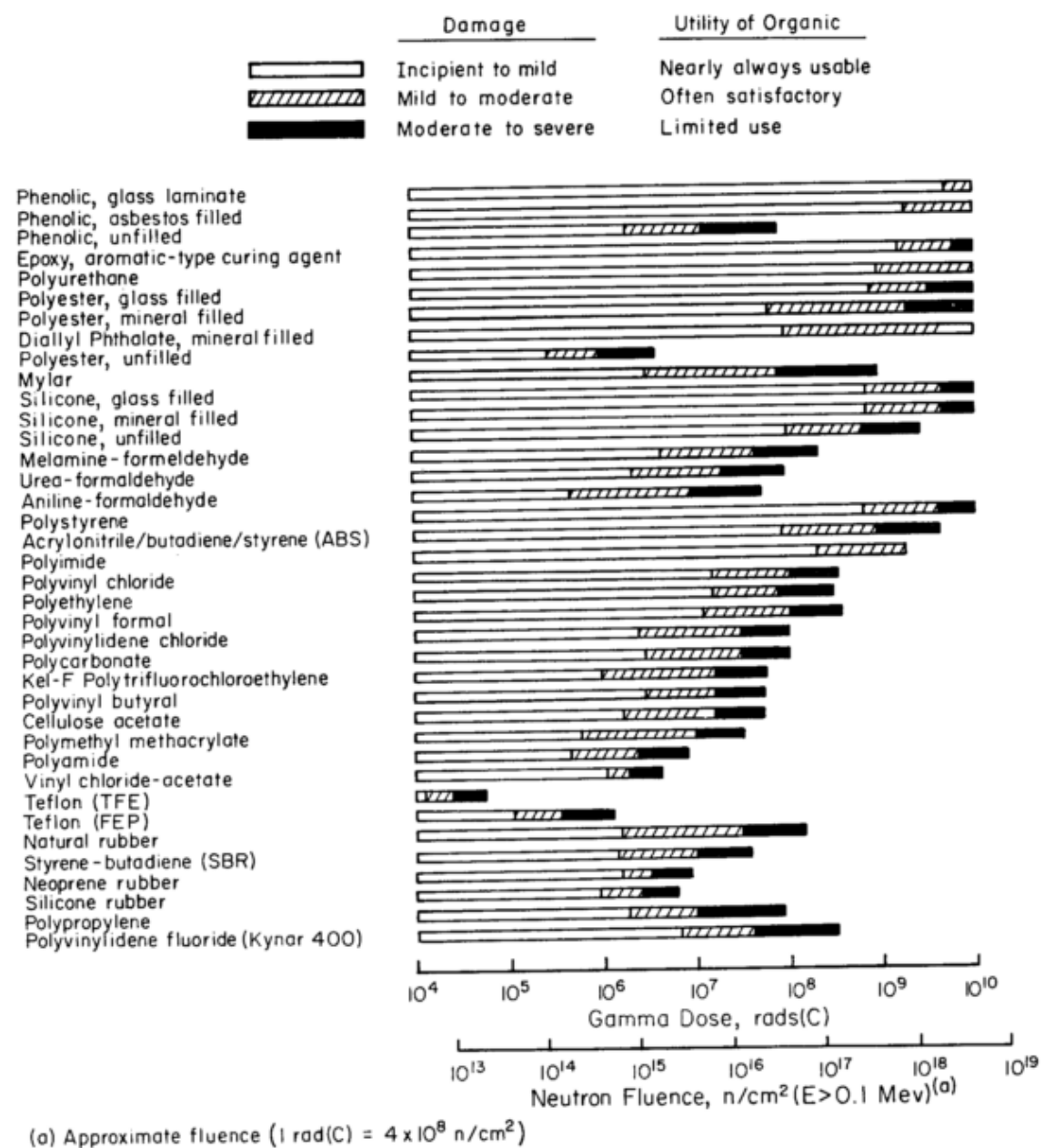


Figure 2.3: Approximate radiation tolerance of organic dielectrics [23].

damage in metallic bonding as the excited electrons quickly return to their normal energy level [25].

As an atom is displaced in a metal, a defect is created. An electron incident upon this point would be deflected and its path through the conductor lengthened. This reduces the speed of electrons through the conductor which causes a reduction in carrier mobility. A decrease in mobility equates to a reduced conductivity and increased resistivity [27].

The two radiation effects result in opposing changes in conductor characteristics.

However, the magnitudes of each effect are negligible and there has been no important example of a degradation of a metal by radiation in space” [28]. It is suggested, therefore, that they are safe to use in a robotic platform for nuclear decommissioning.

2.3 Radiation Tolerance of Passive Components

The review of the radiation tolerance of electronic components has been separated into two sections. Initially, the affects of radiation on passive components are discussed. Finally, the radiation tolerance of active components (those based on semiconductor technology) is reviewed. This section discusses the effect of radiation on passive components such as resistors, inductors and capacitors.

2.3.1 Resistors

Resistors come in many forms, for example; film, foil and wirewound composition [29]. Both atomic displacement and ionisation effects have a negligible effect on all types of resistors [24]. Research has validated that the effect of radiation on film resistors is minimal [30] and also can be considered negligible in diffused resistors fabricated through p-type diffusion into an n-type background [31].

Fig. 2.4 depicts the change in resistance for two resistors irradiated at a dose-rate of $5.9 \text{ kGy(Si).hr}^{-1}$. It can be seen that after 120 hrs (708 kGy(Si); approximately 150 times the yearly dose in a nuclear decommissioning storage pond) the magnitude of resistance deviated $<0.25\%$. This is within the manufacturer’s tolerances of the majority of COTS resistors and is therefore regarded as an allowable degradation of resistance.

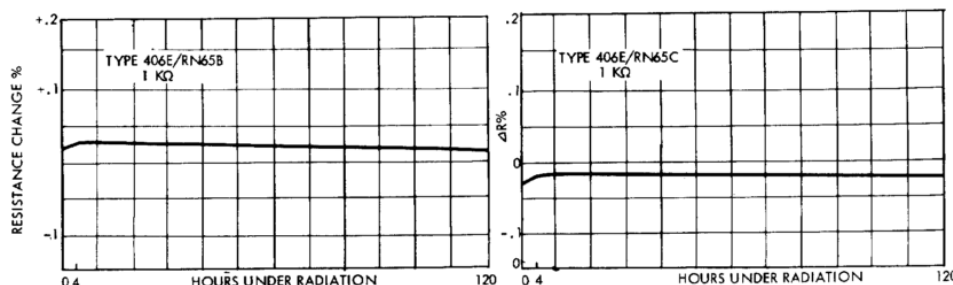


Figure 2.4: Resistance change of carbon film and metal film resistors v.s. hours under radiation, dose rate of $5.9 \text{ kGy(Si).hr}^{-1}$ [30].

There has been very little recent work on the radiation effects on resistors due to a large body of anecdotal evidence of resistor survival in orbiting satellites.

2.3.2 Inductors

Inductors have a very simple structure and are constructed primarily from a metal coil. This can be coiled around a ferromagnetic material. The use of mainly conductor materials mean they are naturally tolerant to radiation. Conduction in metals is not affected by gamma rays [24].

The main part of an inductor that could be susceptible to radiation is the ferromagnetic material that may form the core rather than air in an air-cored inductor. However, a study conducted on the effect of γ -radiation on ferromagnetic materials suggested there was no effect from a ^{60}Co -source up to a TID of 500 kGy(Si) [32]. This is much greater than our requirements.

2.3.3 Capacitors

All capacitors share a common construction. Two conductive plates separated by a dielectric. Dielectrics range from air to an aluminium oxide film to plastic.

Capacitors are manufactured with variations in distances between conductive plates, plate size and the permittivity of the dielectric between them. This alters its inherent capacitance. Fig. 2.5 highlights the structure for a typical aluminium electrolytic capacitor.

Electrolytic Capacitors

Radiation exposure creates atomic displacement in dielectrics, however, it is rare that such defects affect operation as it is not necessary for a dielectric to have crystalline perfection to be a “good dielectric”. Therefore, atomic displacements have negligible effects [34].

Energy received from gamma exposure can, however, be trapped as charge in the metallic oxide of the electrolytic anode [24]. This can increase the conductivity during operation and also increases the leakage current [35].

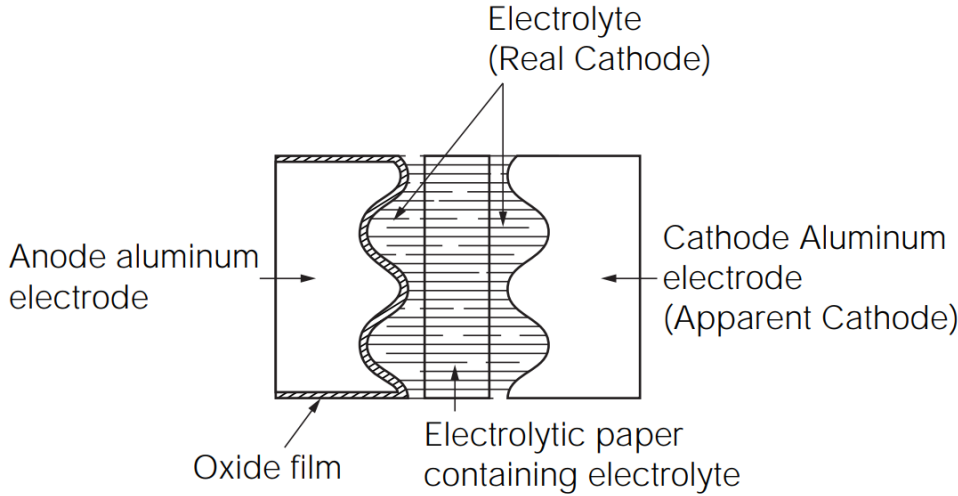


Figure 2.5: Typical structure of a capacitor [33].

Non-electrolytic Capacitors

Mica film capacitors that have an inorganic dielectric are not affected by gamma radiation [36]. Fig. 2.6 shows a small decrease in mica film capacitance after irradiation of approximately 2 pF. This is 0.63% of the total capacitance, which is a negligible change and is within the majority of capacitor tolerances.

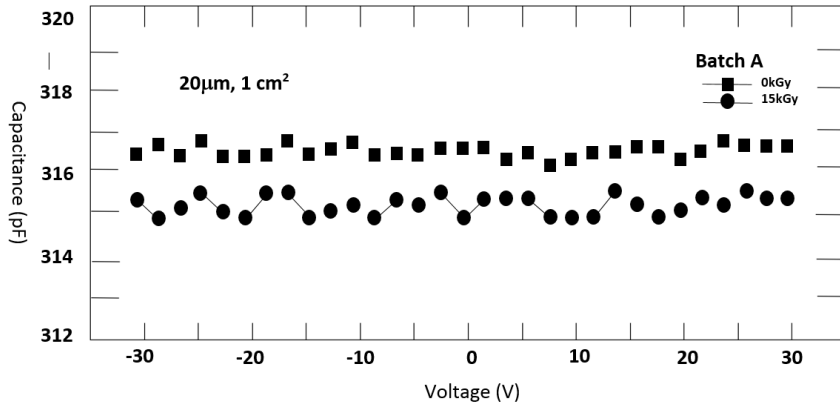


Figure 2.6: Capacitance of one batch of samples before and after irradiation [36].

Capacitors created within integrated circuits, such as an Al_2O_3 MOS device, show an increase of positive trapped charge with an increased dose of ^{60}Co γ -radiation up to 4 kGy when the increase saturated [37].

A series of tests on MOS capacitor wafer samples made from SiO_2 found that over 50 % of samples survived and operated to a TID of 10 kGy [38]. However, Fig. 2.7 outlines a capacitor-voltage profile, created by applying a voltage across the semiconductor within the device and measuring the capacitance as a function of voltage

bias, indicating increased defects at an increased dose-level resulting in a flattening of the capacitance curve with an increasing TID.

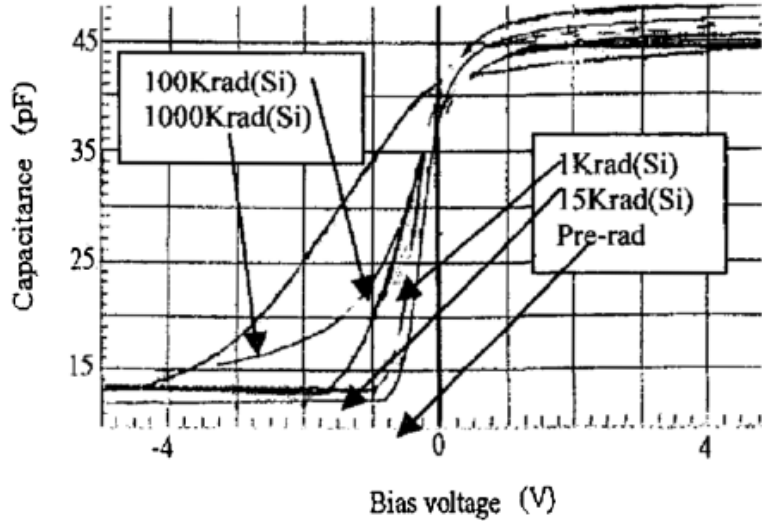


Figure 2.7: The capacitance and voltage of SiO_2 MOS capacitors at different TIDs [38].

It can be seen in Fig. 2.8 that the capacitance curve recovers toward its initial specification when left to recover for 3 weeks. This is called the annealing effect and will be discussed in section 2.7.

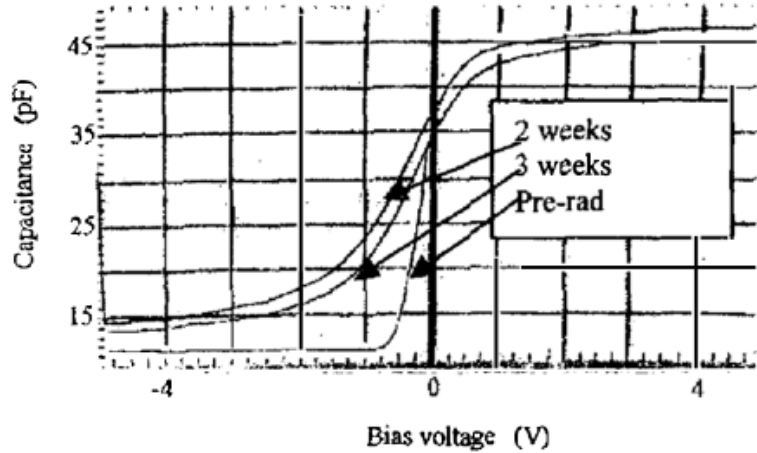


Figure 2.8: The annealing progress of a MOS capacitor over 3 weeks [38].

The primary parameter that determines a capacitor's radiation tolerance is the difference between organic and inorganic dielectrics. Organic devices fail at low TIDs and the inorganic mica film/ceramic based capacitors are much more tolerant as can be seen in Fig. 2.9.

With targeted component use, low-cost inorganic dielectric based capacitors could

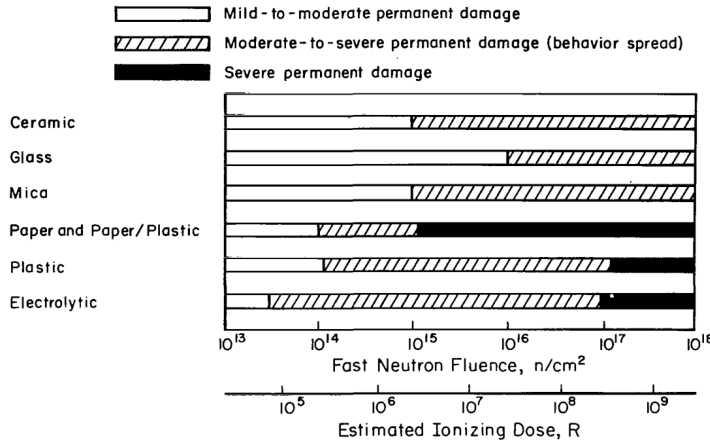


Figure 2.9: Relative radiation sensitivity of capacitors [35].

be used within robotic platforms showcasing negligible degradation to radiation exposure. Where the use of inorganic dielectrics is impossible due to capacitance values required, organic dielectrics should still survive more than required exposure in a nuclear decommissioning environment due to the relatively high radiation tolerance of organic dielectrics (>5 kGy(Si)).

2.4 Radiation Tolerance of Active Components

Having discussed the high natural tolerance (above our required 5 kGy yearly dose) of passive electronic components to radiation exposure, the effects of γ -radiation on active components must be addressed. The magnitude and range of effects witnessed in semiconductor materials complicates the choice and design of integrated circuits deployed in nuclear environments.

2.4.1 Semiconductors

Fig. 2.10 outlines the basic structure of a typical Metal-Oxide-Semiconductor Field-Effect-Transistor (MOSFET). A gate with an oxide insulating layer (in this instance silicon dioxide) on top of a semiconductor material (in this instance silicon).

Incident gamma radiation creates free electrons in the insulating layer. These electrons have enough energy to move within the insulated boundary and create electron-hole pairs, which enhances the conductivity temporarily [39]. These electron-hole pairs recombine and create a charge that may cause a transistor to switch on [7]. However,

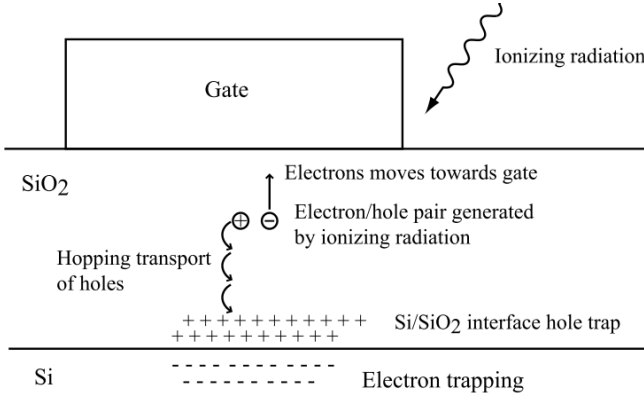


Figure 2.10: Charge trapping in the Si/SiO₂ interface layer in a NMOS transistor [10].

the primary damage caused by ionising radiation is the build-up of charge in the silicon dioxide layer (SiO₂).

Charge is trapped on the SiO₂ layer as electrons move more freely and rapidly than holes, diffusing or being attracted out of the oxide layer by the gate, leaving the holes [39]. This means that there is a shift in ratio of electrons to holes, creating a charge trapped in the SiO₂ layer. This can cause changes in threshold voltage [10], decrease of transconductance, increased leakage currents and a reduction of surface mobility [7].

With gamma-exposure effecting the fundamental materials used in active components, it is important to understand and research the radiation effects in multiple semiconductor based technologies.

2.4.2 Metal-Oxide-Semiconductor Field Effect Transistors

Figs. 2.11 & 2.12 show charge built up in the oxide layer of an npn and pnp Metal Oxide Semiconductor Field Effect Transistor (MOSFET). This affects the threshold voltage, which increases with an increased dose for a PMOS transistor, whereas an NMOS transistor's threshold voltage decreases for an increased dose [7].

The trapped positive charge in NMOS transistors induces a negative charge in the substrate and gate, this increases conductivity, therefore reducing the threshold voltage [24]. The same effect can be seen in PMOS transistors, however, a PMOS transistor requires a negative gate bias for operation, therefore increased conductivity is observed as an increased voltage threshold [24].

The electric field created in the silicon oxide due to trapped charge determines the

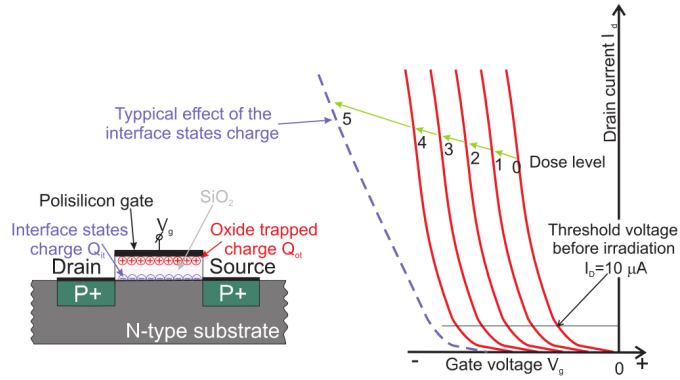


Figure 2.11: Trapped charges in PMOS transistor and drain current/gate voltage curves representing threshold shift [7].

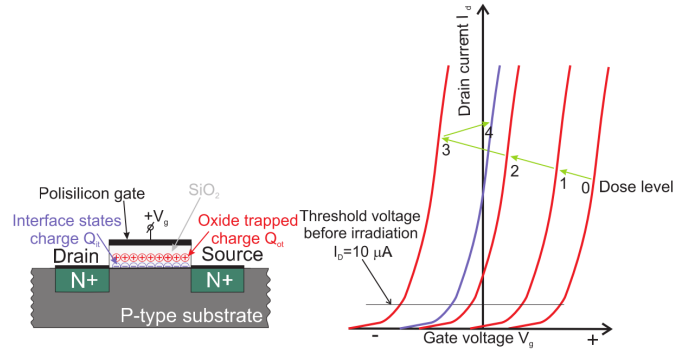


Figure 2.12: Trapped charges in NMOS transistor with drain current/gate voltage curves representing threshold shift [7].

magnitude of the shift in threshold voltage [7]. The gate bias voltage strongly affects this electric field as a negative bias voltage (seen in a PMOS transistor) attracts the positive trapped charge in the oxide layer, decreasing the distance between the charge sheet and gate terminal, whereas a positive voltage (as seen in an NMOS transistor) would repel this charge [40].

The electric field has a less observable effect when it is closer to the gate terminal, PMOS transistors are therefore considered more radiation tolerant than NMOS transistors [7].

In a real-world application however, complimentary metal-oxide-semiconductor (CMOS) technology is used. This is the process of pairing an NMOS transistor with a PMOS transistor and connecting their respective drains and gates together to reduce power consumption. As this technology is implemented in the majority of Integrated Circuits (ICs), it is unlikely that we could pick PMOS transistors over NMOS in our design for a robotic platform.

2.4.3 Bipolar Junction Transistors (BJTs)

Bipolar Junction Transistors (BJTs) are manufactured with old processing concepts but are still widely used in industry and form an important part of the electronic components used in typical embedded systems [41]. Two types of BJTs: NPN and PNP, are used for current amplification and switching. This makes them an important part of power regulation circuitry [41]. Fig. 2.13 outlines the basic model of a BJT.

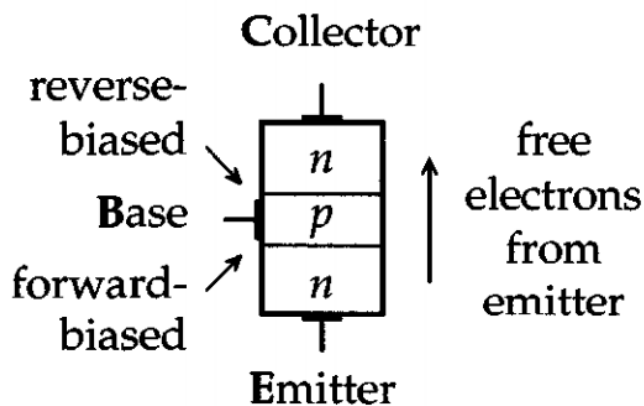


Figure 2.13: Simplified physical model of a BJT [42].

A BJT is made up of two junction diodes that are formed on a single semiconductor crystal. For an NPN transistor, a thin p-type base region separates n-type regions for the collector and emitter. This is reversed for a PNP BJT.

The degradation characteristics of bipolar technologies exposed to γ -radiation are widely understood: ionisation and displacement damage contributes to an increase in recombination of minority carriers [43] and this has the effect of reducing the minority carrier lifetime, which lowers the current gain of the device (β) [44].

An example of this current gain degradation at various dose levels between 0 and 5 kGy(Si) (500 krad(Si)) can be seen in Fig. 2.14.

The TID effects experienced by a bipolar structure are dependent on a number of factors including emitter bias, transistor geometry, polarity, emitter technology and dose-rate [43–45], which creates added complexity when attempting to analyse the susceptibility of components to the effects of radiation.

NPN and PNP BJTs both degrade in similar ways, however, PNP is not as susceptible to radiation damage because the positive trapped charge has less effect on

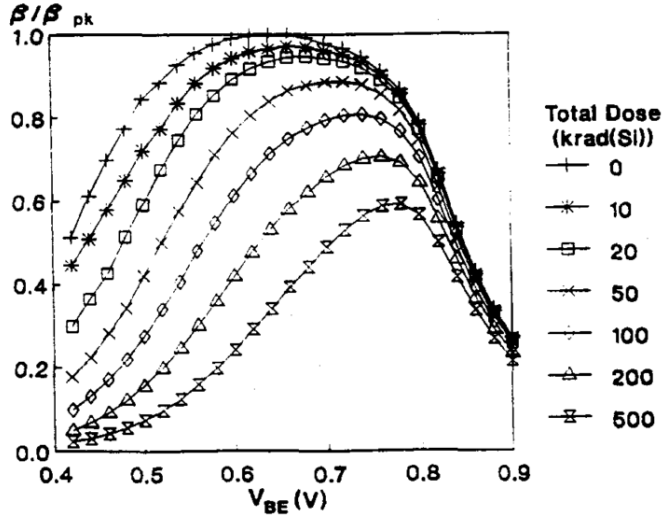


Figure 2.14: Typical current gain characteristics for various levels of TID. β_{pk} is the peak pre-radiation current gain and V_{BE} is the base-emitter junction bias [45].

the heavily doped p-type emitter and therefore causes very little depletion of the surface [45].

There are also differences within PNP technologies with vertical (VPNP), lateral (LPNP) and substrate (SPNP) devices degrading at different rates [46]. Lateral devices degrade more quickly than vertical or substrate devices since the current travels laterally along the surface between the p-type emitter and collector, increasing the effect of surface mechanisms, including hole depletion and recombination [46].

Fig. 2.15 shows a comparison of the current gain vs the emitter base voltage for VPPN, SPNP and LPNP transistors [46]. The total dose was 5 kGy(Si) (500 krad) and dose-rate was approximately $1.6 \text{ Gy(Si).s}^{-1}$ (160 rad(Si)).

The LPNP transistor exhibited the greatest gain degradation, whereas the VPPN exhibited the least gain degradation. The current gain degradation is also dependent on the transistor bias level with greater degradation at low bias levels [46].

Having analysed the state-of-the-art literature on the radiation effects witnessed within BJTs, it is suggested that VPPN transistors are primarily used if and when possible with a general trend of PNP use over NPN technology. This will be difficult as it is uncommon for manufacturers to publish the structure of BJTs within their digital ICs, but the suggestion is included for implementation when it is possible.

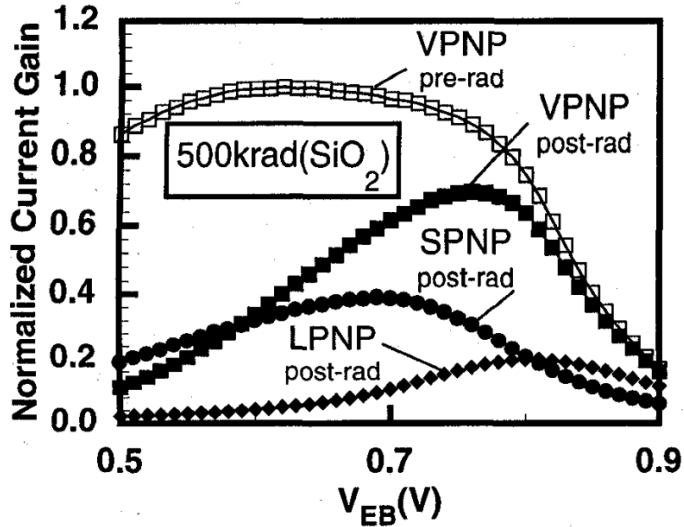


Figure 2.15: Normalised current gain for each PNP BJT vs emitter base voltage. Total dose 5 kGy(Si) (500 krad(Si)) [46].

2.5 Single-Event Effects (SEE)

Single-Event Effects (SEEs) are of great importance. They are created in transistor technologies due to the ionisation effect of incident gamma radiation [47]. There are many different examples of SEEs, including Single-event upset (SEU), single-event latch-up (SEL), single-event transients (SET), single-event gate rupture (SEGR) and more [24]. They also have differing degrees of criticality associated with them.

Some are destructive, for example SEL, and some are non-destructive or temporary e.g. SEU [48]. Effects observed are changes to the state of a latch (for example a memory value) and transients in voltage at internal circuit nodes [47], which can have a knock-on effect to the rest of a system. Voltage spikes can also cause permanent degradation of the transistor structure.

Fig. 2.16 shows that via the collision of a γ -ray a current pulse is induced in the junction. This is achieved by the particle creating a trail of electron-hole pairs along its path [39]. This charge deposition at a sensitive (off) node may exceed its threshold charge, changing the state of logic [24].

2.5.1 Latch-up

A change in transistor logic is not necessarily destructive. It is possible that a re-write of a memory cell will revert the transistor back to its required state [24]. In some

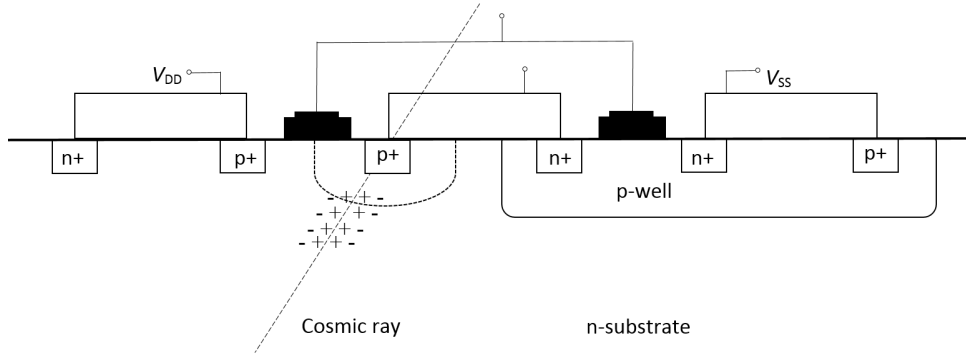


Figure 2.16: Cross section of CMOS circuit depicting latch-up mechanism from incident cosmic ray [24].

instances, especially with CMOS technology, a permanent latch-up can occur. This degrades transistor properties and can ultimately lead to the destruction of the device via thermal overload [10]. Fig. 2.17 shows a model of the latch-up circuit.

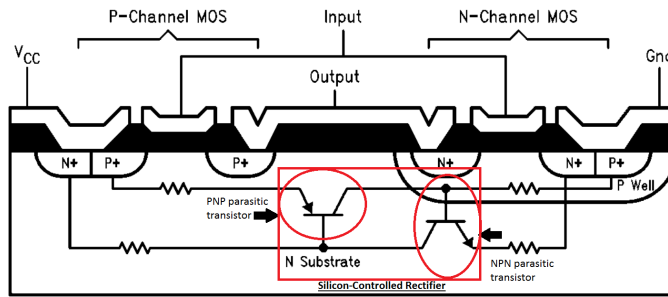


Figure 2.17: Cross section of basic CMOS inverter with Latch-up circuit model [49].

The circuit is constructed of two parasitic bipolar transistors. This structure is called a silicon-controlled rectifier (SCR) [10]. Under normal operating conditions the MOS source and drain junctions are reverse-biased. Current injected into the P-channel MOS emitter-base junction by incident radiation causes current to flow and forward biases it. This current flows into the p-well, which turns the N-channel MOS device on, which in turn, increases the base drive to the P-channel MOS [49].

With the SCR turned on there is no possibility of it being switched off without removing the voltage across it [10], therefore there will be a constant current flow through the device when in latch-up mode. If this is not limited the device will overload thermally [10].

It is also important to note that during operation of a robot in a nuclear decommissioning environment, it may not be possible to re-write the memory of a microcontroller, therefore, a SEE can drastically effect the operational capacity of the device.

This could possibly lead to loss of control, or worse, unexpected movements/behaviour due to corrupted memory.

The experimental testing of especially susceptible devices to SEE such as microcontrollers must be conducted prior to deployment to understand the TID achievable with the device, however, it was not a priority during this research project with other memory architectures not discussed because of this. A common example of a microcontroller was irradiated to determine if further testing would be required and the results are discussed in Chapter 4

2.6 Dose-rate effects

The effects observed in common components from incident radiation can be observed and predicted based on an understanding of the mechanisms on an atomic level. Variations in the magnitude of degradation are observed based on many factors. Dose-rate, total ionising dose (TID) and device temperature all effect the magnitude of degradation.

2.6.1 Enhanced Low Dose-Rate Sensitivity (ELDRS)

The enhanced low dose-rate sensitivity (ELDRS) effects seen in bipolar technology have long been observed and discussed [50]. It was soon concluded through experimentation that rather than an enhanced degradation at a low dose-rate, a reduced degradation at a high dose-rate was responsible for over estimation of component radiation tolerance [50].

Greater degradation is observed at lower dose-rates than at higher dose-rates with saturation of the degradation magnitude occurring between $0.01\text{-}0.05 \text{ mGy(Si).s}^{-1}$ [51]. Fig. 2.18 outlines the difference in degradation mechanisms for low dose-rate and high dose-rate environments.

At high dose-rate, ionizing radiation introduces a positive charge into the oxide layer. This is coupled with the creation of holes, defects and Hydrogen ions from the cracking of H_2 molecules from other radiation defects [53]. This induced positive charge creates an alternative energy level allowing recombination at an increased rate due to the smaller proportion of carrier concentrations near the surface. This reduces

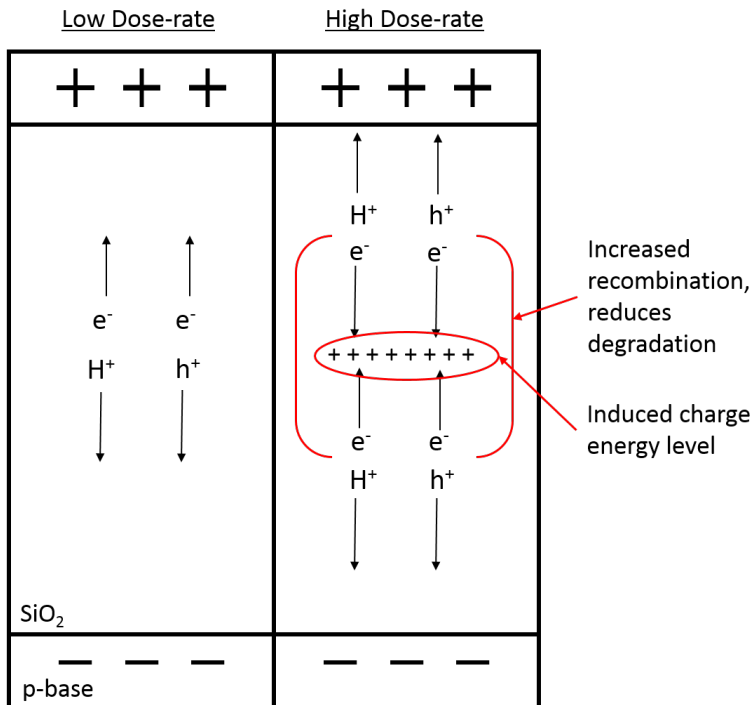


Figure 2.18: Simplified illustration of ELDRS effect [52].

the degradation of the device [52].

At a low-dose-rate, the same induced charge and multiple energy levels within the oxide layer is not witnessed, therefore, recombination of holes and positive charges occurs at a reduced rate, increasing degradation of the device. This is called the "True dose-rate effect" [52].

There are many examples of ELDRS effects in components [54, 55]. There have also been attempts to simulate the effect [56]. These simulations allow a basic understanding of the components likely to suffer from ELDRS effects and also a more accurate prediction of their total dose tolerance.

Calculations for the ELDRS dose tolerance from a high dose-rate test can only be considered a guideline. Specific testing for parts used within a completed device require experimental validation to determine their tolerance to radiation to a standard testing regime such as MIL-STD-883K [19]. It is difficult to replicate a low dose-rate environment due to time, facility access and cost restraints. Therefore, the increased time required to conduct a low dose-rate test is infeasible. For example, the dose-rate available in the Dalton Cumbrian Facility's irradiator [57] can be as large as $450 \text{ Sv} \cdot \text{min}^{-1}$ which can expose devices to an operational year's TID within 15 mins.

It is important to note, that the dose-rates observed in typical nuclear decommissioning environments for robotic platforms are approximately 100 times above the saturation limit [51]. Therefore, experimental results gathered in the literature, such as [58–60], outlining the ELDRS response do not indicate any increased degradation of a device in a nuclear decommissioning environment and it is possible a different low dose-rate set of tests, may or may not, need to be conducted for representation of the applicable environment or may not be required.

2.6.2 Elevated Temperature Irradiations (ETIs)

There have been many attempts to develop methods to decrease the total time of experiments investigating ELDRS effects. One suggestion is elevated temperature irradiations (ETIs) [61,62]. This is the process of applying an elevated temperature to the device during irradiation. This has been observed to cause an increase in device degradation. There have, however, been large discrepancies observed between ETIs and room temperature low dose-rate experiments [63].

The majority of the literature concludes that ETIs can be used to highlight ELDRS dependencies in devices, even if full characterisation of ELDRS effects remain uncertain [50,64]. Specific ELDRS tests could be conducted on components that have been highlighted as ELDRS dependent from ETI experimentation rather than completing such tests on entire component catalogues.

It is possible that in future iterations of this research, ETIs could be used to reduce irradiator time, with devices that show an increased degradation at higher temperatures highlighted for further tests rather than completing “blanket” low dose-rate tests.

2.7 Annealing

As well as understanding the difference in radiation degradation mechanisms and modes, it would be useful to understand possible specification recovery methods. Annealing refers to the improvement of device specifications post-irradiation. It is achieved by allowing natural recovery over time or by increasing the temperature of the system. This can be at a high temperature (approximately 400°C) or at room

temperature, although room temperature has limited success [24].

An example of annealing is when a charge, trapped in the oxide layer of a transistor, is not trapped there forever [10]. The charge may dissipate over time through recombination with electrons near the interface with silicon, or be removed by thermal annealing [65]. There is no specific temperature outlined as optimum for annealing as it depends on the mechanical properties of the component and time constraints. However, as an example, packaged bipolar junction transistors have been annealed back to specification within 12 mins when exposed to a temperature of 400°C in an atmosphere of N₂ [66]. The increase in temperature increases the rate of recombination and slowly removes the trapped charge.

2.8 Suggested Components for Experimentation

Current state-of-the-art research contributes to databases maintained by the European Space Components Information Exchange System (ESCIERS) and the European Space Components Coordination (ESCC). For example, ESA has published the European Preferred Parts List (EPPL) [67]. Through analysis of this information it is possible to gather an understanding as to the components not susceptible to radiation. Table 2.2 shows an example segment of the database compiled by ESA.

Through analysis of this information and anecdotal evidence from previous research conducted at the University of Manchester, multiple COTS components vital to the correct operation of an embedded system were chosen to be exposed to a representative TID of 5 kGy(Si). This is the expected yearly dose of a robotic platform in a nuclear decommissioning environment, as discussed in Section 2.1.2.

Literature describing state-of-the-art research concentrates on the response of individual components to radiation exposure. Comparatively little work has been completed on Integrated Circuits (ICs). It is possible to predict the degradation mode based on the degradation of each individual component, however, due to inherent assumptions made in simulations, it is possible that some effects are missed. It is therefore important to test COTS ICs to determine their suitability for a low-cost robotic platform.

Table 2.2: Example segment of European preferred parts list [67].

Part Type	Description	Detail	Spec.	Package	Manufacturer	Qualification Status
4001B	Quad 2 - Input NOR Gate	ESCC	9201/041	FP, DIL	STMicroelectronics	ESCC QPL
4002B	Dual 4-Input NOR Gate	ESCC	9201/042	FP, DIL	STMicroelectronics	ESCC QPL
4008B	4-Bit Full Adder	ESCC	9202/039	FP, DIL	STMicroelectronics	ESCC QPL
40103B	Pre-settable 8-bit Synchronous Down-Counter	ESCC	9204/036	FP, DIL	STMicroelectronics	ESCC QPL
40106B	HEX Schmitt Trigger	ESCC	9409/005	FP, DIL	STMicroelectronics	ESCC QPL
40107B	Dual 2-Input NAND Buffer/Driver	ESCC	9401/013	FP, DIL	STMicroelectronics	ESCC QPL

2.8.1 Linear Voltage Regulators

The literature highlights linear IC voltage regulators as being particularly susceptible to the effects of radiation [40, 56, 68]. Voltage regulators are a critical component used within embedded systems and their failure can cause the subsequent failure of multiple sub-systems due to the sensitivity of some device's required supply rail. Therefore, they are chosen in this study for radiation damage characterisation.

Multiple devices with similar specifications, but from different manufacturers, were chosen for experimentation. This was to determine if there were common failure modes across manufacturers or whether a variety of degradation modes were witnessed.

A small selection of voltage references were also chosen as they are often a constituent part of a voltage regulator and could indicate possible failure mechanisms.

2.8.2 Inertial Measurement Units (IMUs)

There are currently very few papers regarding the radiation tolerance of IMUs. Work has been done on the radiation tolerance of microelectromechanical systems which form the basis of IMUs but very few experiments on complete systems have been

completed. Examples of current research include [69–72].

Mechanical properties of silicon suggest a high radiation tolerance of the microelectromechanical (MEM) actuation system. The control and filtering electronics however, fail at much lower doses [72]. Therefore, MEMs that operate on electrostatic principles are sensitive to accumulation of charge caused by radiation exposure, whereas those based on electromagnetically or thermally actuated models are much more radiation tolerant.

An example of a commercial radiation tolerant IMU is [73], which advertises a radiation tolerance of 1 kGy. This is 5 times lower than the expected dose-rate of a nuclear decommissioning environment.

A selection of digital and analogue commercial IMUs were chosen for radiation tolerance experimentation with the aim of highlighting common failure modes and reaching a similar or greater radiation tolerance than currently advertised radiation tolerant IMUs.

2.9 Summary

Fig. 2.19 summarises the information presented in this chapter. It presents typical responses of a range of devices that have been exposed and tested for gamma radiation effects.

It shows that capacitors, resistors, magnetic materials and inorganic dielectrics can all survive doses of up to 10^8 Gy(Si) (10^{10} rad). This is equivalent to roughly 16,500 years of radiation a service robot would receive working at the Sellafield legacy ponds 24 hours a day. This would suggest that passive components and inorganic dielectrics can be used in any embedded system for deployment in a nuclear decommissioning environment.

Semiconductors show radiation damage from as little as 1 kGy(Si) (10 krad) and are therefore susceptible to damage within a nuclear decommissioning environment. Experimentation of COTS components to be deployed in such an environment concentrated on semiconductor based devices such as voltage regulators and IMUs.

Very little work has been undertaken to characterise low-cost embedded systems or their electronic components for deployment in a nuclear decommissioning environment

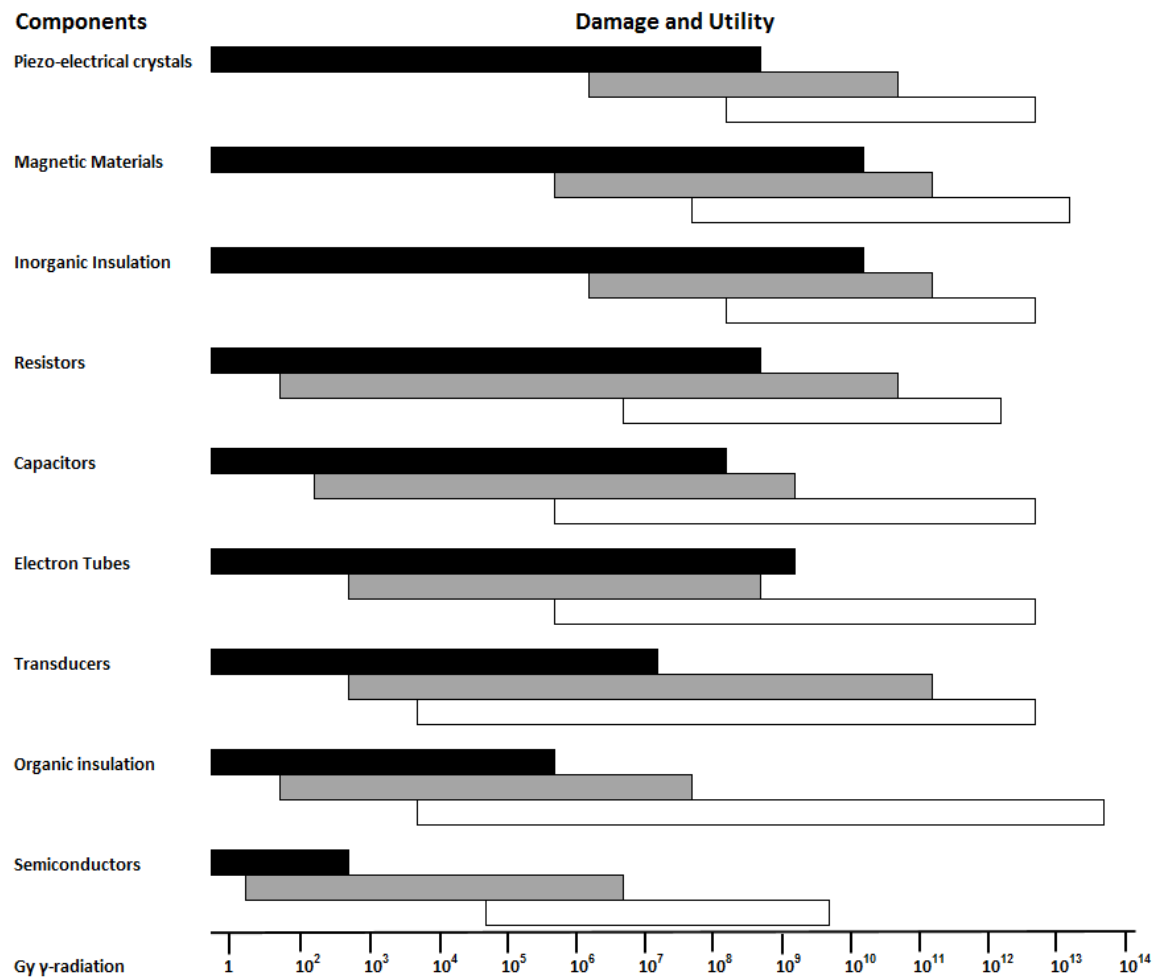


Figure 2.19: Sensitivity to gamma radiation of example electronic components, adapted from [9]. Black represents mild-to-moderate damage, grey represents moderate-to-severe and white represents severe permanent damage.

with most research concentrating on the relatively low TIDs of space orbits. It was hoped that the experiments discussed in Chapter 4 would aid in the understanding of the effects of radiation exposure on COTS components commonly used in robotic platforms.

Chapter 3

Radiation Tolerance of Inertial Measurement Units

After analysis of the current state-of-the-art literature, it was decided to test the radiation tolerance of a mission critical sub-system, the inertial measurement unit (IMU). IMUs normally contain both accelerometers and gyroscopes with 3-axes of each sub-system placed orthogonally to each other within one integrated circuit (IC) to represent the x, y and z-axes. Some examples of IMUs also contain magnetometers, but these were not prioritised for analysis in this study.

IMUs are an important part of a robotic platform as they output the force acted upon the device in each direction, which can be filtered to output the orientation of the system. This orientation data is included within a global positioning system to allow for accurate localisation, therefore, IMUs are very common on almost all robotic platforms, from low-cost hobby electronics to high-cost space orbit satellites.

Exact orientation data is critical within a nuclear environment as it decreases the error when localising the platform. Contamination of a robotic system with radioactive substances due to errors in the localising system increases the risk of contamination, which in turn could increase the spread of radioactive substances. This eventuality could endanger the safety of workers and increase the chance of contamination of the surrounding environment.

A positioning system with reduced errors also enables on-board sensors to localise measured radioactivity and debris accurately. This leads to more efficient nuclear decommissioning at a reduced risk to workers and the environment.

IMUs have various mechanical structures to measure the forces acting upon them, usually paired with a capacitive, piezoelectric or piezoresistve sensing element. Another variation within low-cost IMUs is whether they output digital or analogue data. Therefore, the characterisation and analysis of multiple COTS IMUs with varying mechanical structures and output data were chosen to be tested.

This chapter first outlines the structures of the common microelectromechanical systems (MEMSs) to create accelerometers and gyroscopes, before discussing the radiation tolerance of the devices. Experimental procedures to determine the radiation tolerance of multiple COTS IMUs of both analogue and digital types are discussed. It was hoped that a predictable pattern of degradation would be observed to suggest either a failure mechanism, or allow replacement of a device before failure.

3.1 Physical Structure of Accelerometer and Gyroscope MEMS

This section outlines the structure of common accelerometers and gyroscopes. The various MEMS used to measure forces acted upon it are analysed for their radiation tolerance and discussed.

3.1.1 Accelerometer Structure

Accelerometers are one subset of a family of “Inertial Linear Sensors”. This means that only a change in shape or size of an object is necessary to determine the magnitude of acceleration acted upon it [74]. An external force exerted upon an accelerometer can take many forms, such as slow changes in direction, vibrations and vigorous impacts. This force (F), as calculated by Newton’s second law, equals the product of acceleration (a) and mass (M) of the accelerometer.

To measure acceleration we require the mass of the measurement element (which is pre-determined) and also the force acted on the mass. A force sensor can be modelled as a spring of known characteristics. The magnitude of deformation of the spring is related to the magnitude of the force. Therefore, the basic structure of an accelerator takes the form as shown in Fig. 3.1.

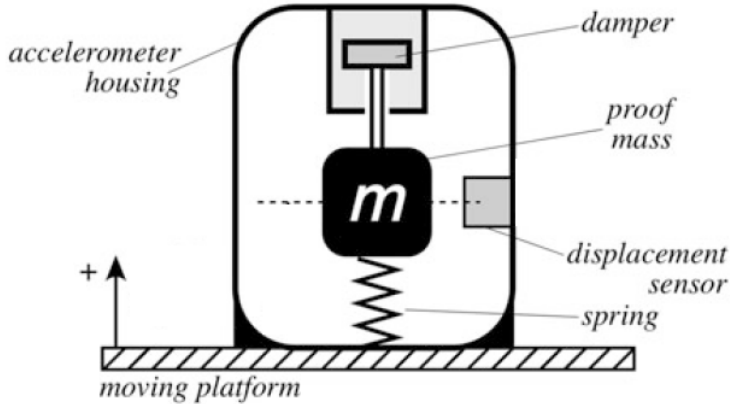


Figure 3.1: Fundamental structure of an accelerometer [74].

By knowing the spring constant and the magnitude of deformation we can work out the magnitude of the acceleration, however, there are many techniques to measure the deformation of the spring. The three primary ways of converting the initial mechanical movement to an electrical signal are via piezoelectric, piezoresistive and capacitive components [74].

Capacitive sensing element

The structure of a capacitive sensing element sees one of two capacitor plates securely fastened to the housing of the accelerometer, whilst the other is attached to the cantilevered mass. This forms a capacitor whose value depends on the distance between the plates (as long as the size of the plates and dielectric remain constant). A capacitive transducer has been shown to have high accuracy when miniaturized and are available at a low-cost [74]. An example of a capacitive accelerometer is shown in Fig. 3.2.

Piezoelectric sensing element

Another common sensing element of an accelerometer is a piezoelectric material. This directly converts mechanical deformation of a piezoelectric crystal into electric charge. There are many ways that a piezoelectric material can be mounted to form an accelerometer. Fig. 3.3 outlines some of the possible mounting variations of the crystal, mass and housing.

The compression coupling (a), measures output via a mass placed on a vibrating

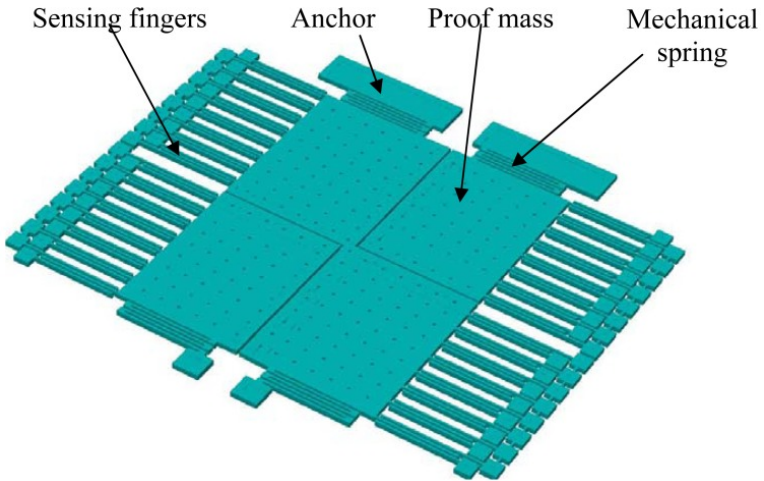


Figure 3.2: Structure of a capacitive accelerometer [75].

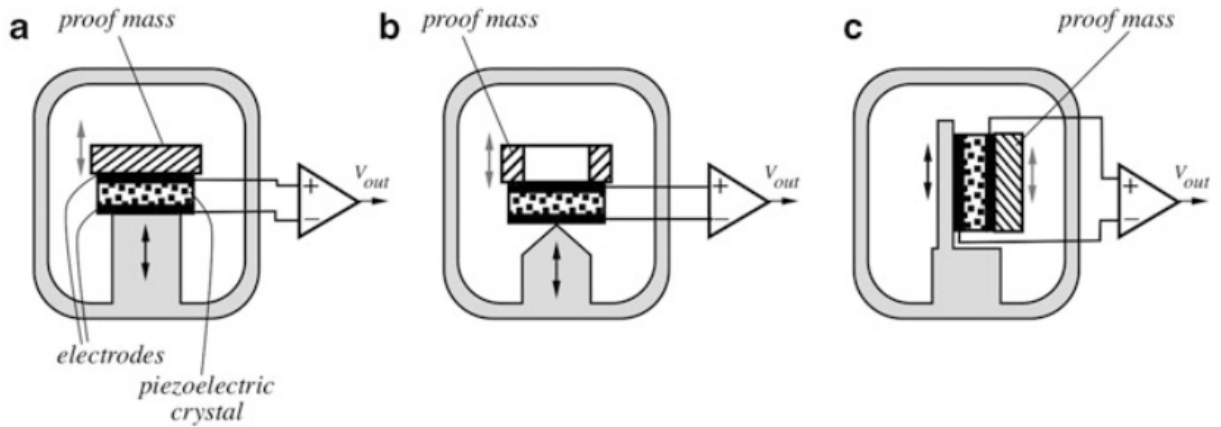


Figure 3.3: Possible arrangements of a piezoelectric accelerometer: A) Compression coupling, B) Flexural coupling, and C) Shear coupling [74].

base, whereas the flexural coupling (b) places a mass either side of a central support pin causing deformation on both sides of the pin, finally, the shear coupling arrangement (c), causes the piezoelectric material to tilt under a shear force.

Piezoresistive sensing element

A piezoresistive accelerometer works in the same way, but the sensing unit of deformation incorporates piezoresistive material that changes resistance when strain is acted upon it by a mass. Fig. 3.4 outlines the common structures of a piezoresistive accelerometer.

A mass is suspended between or by a beam, that flexes due to an external force on the accelerometer housing. The deflection of the beam is proportional to the force and

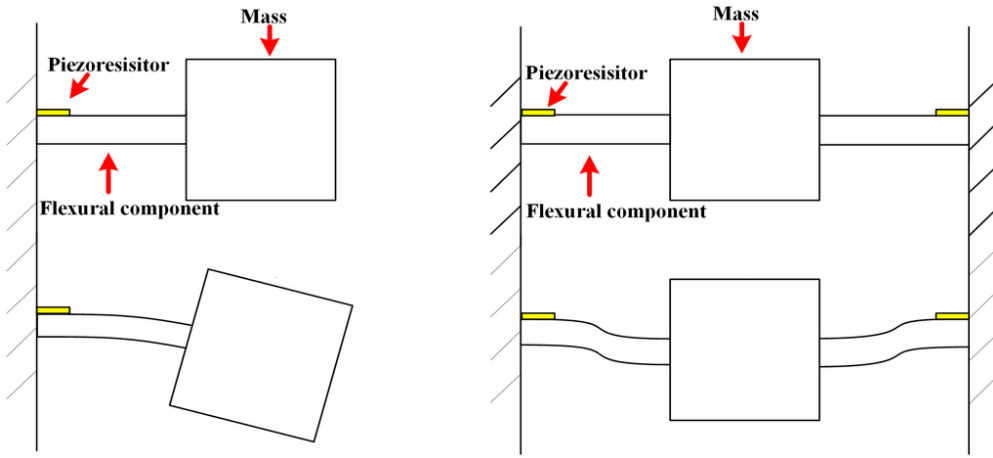


Figure 3.4: Outline of the mechanical structure of a piezoresistive accelerometer [76].

the resistance change of the piezoresistive material, which indicates the magnitude of force exerted onto the device.

All accelerometer variations see a mass deflected by an external force with a deformation created and measured to determine the magnitude of force. The main variation that is likely to be susceptible to radiation exposure is the technology of the deformation sensing unit. The radiation tolerance will be discussed in Section 3.2.

3.1.2 Gyroscope Structure

MEMS gyroscopes are made from a vibrating structure, and use the Coriolis force to determine angular velocity, which indicates the magnitude of rotational force. This works under the principle that an object that is held in the centre of a mount via springs subjected to a rotational force, will gain a tangential velocity. The further the object travels, the greater the velocity imparted on the object, and therefore, the greater the rotational force. An overview of the structure of a gyroscope in one axis can be seen in Fig. 3.5.

Vibrating gyroscopes are preferred over conventional mechanical rotating gyroscopes as they are low-cost and of a similar accuracy [74]. There are many ways to build a vibrating gyroscope, however, they can be divided into three primary groups [77]:

1. Simple oscillators (mass on a spring, beams)
2. Balanced oscillators (tuning forks)
3. Shell resonators (“Wine glass”, cylinder ring)

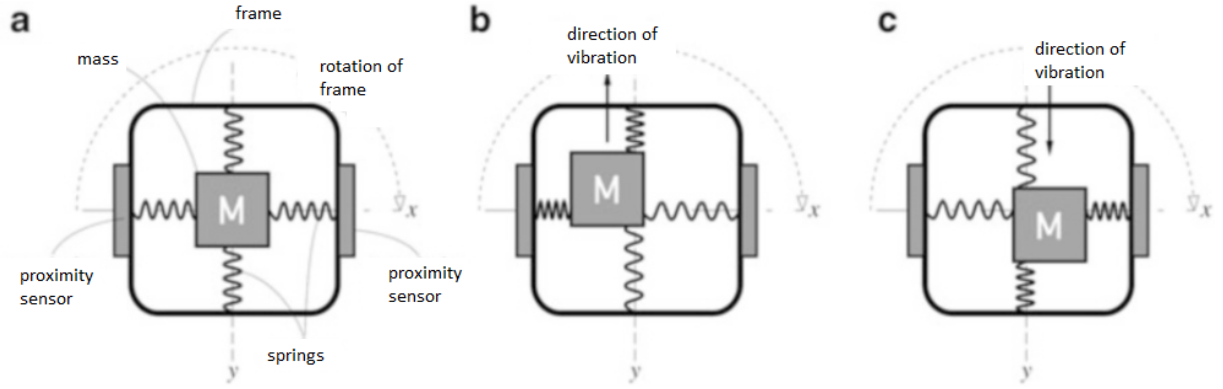


Figure 3.5: Outline of a vibrating gyroscope mechanism showing a mass suspended by four springs with the mass oscillating into different positions dependent on rotation speed and direction [74].

All of these techniques have been used to create a measurable alteration in vibration within a gyroscope. However, as discussed in Section 3.1.1, there are many ways to measure the displacement of the vibratory mass. Capacitive, piezoresistive and piezoelectric sensing elements are used in the same configuration as seen in Section 3.1.1 for accelerometers. The only change is mounting orientation.

An example design within a gyroscope using the piezoelectric effect can be seen in Fig. 3.6.

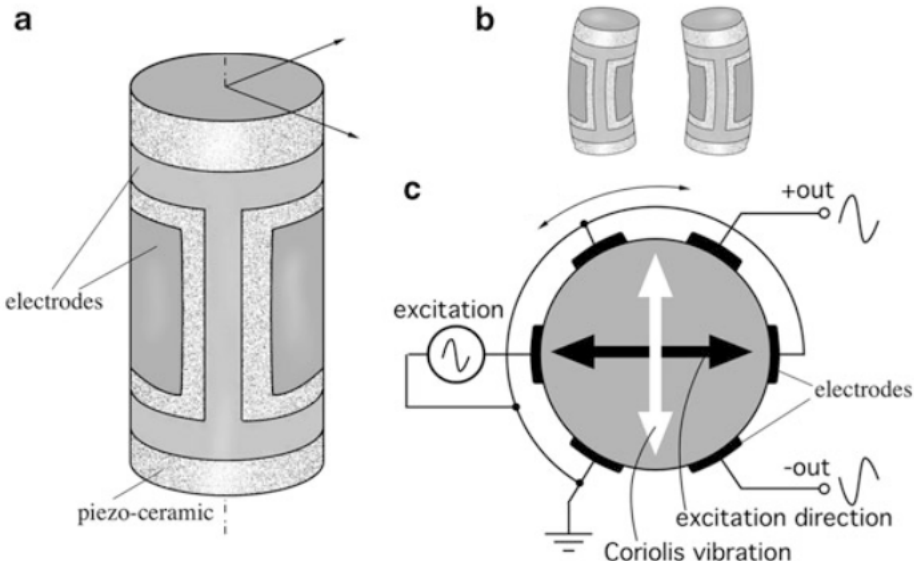


Figure 3.6: a) Cylindrically shaped piezoelectric ceramic vibrating gyro. b) Alternating voltage applied to electrodes, which flexes the cylinder along an axis. C) Axial view of gyro cylinder, where Coriolis force flexes it along perpendicular axis [74].

The cylinder is made of a piezoelectric ceramic with six different electrodes deposited on its exterior. The two driving electrodes force the cylinder to strain in the direction of the black arrow, whereas strain on the cylinder via the Coriolis effect, when the gyroscope is rotated, creates a strain in the white arrow direction. This creates a sinusoidal, out of phase, electric charge at the output electrodes. This charge is then processed and amplified, with the magnitude of this charge determining the direction and speed of rotation.

3.2 Radiation tolerance of IMUs

There is little research that has been conducted on COTS IMUs [78, 79]. Many IMUs currently used in satellites, orbiting the Earth, are bespoke or expensively tested radiation tolerant commercial devices, such as [73]. Therefore, MEMS have primarily been radiation tolerance tested with respect to a space orbit radiation field [80]. Radiation in space takes the form of energetic particles, either through particles trapped in Earth's magnetic fields, cosmic rays made from heavy ions or solar flares. Many of these particles can be halted through the use of thin metallic shielding, this coupled with the lower magnitude of radiation in a space orbit results in lower doses than a decommissioning environment.

Due to the increased usage of microelectromechanical systems (MEMS) in many applications, there has been research on how radiation effects general MEMS silicon structures [81–83], but very few have mentioned or concentrated on accelerometers or gyroscopes. The various degradation patterns witnessed in general MEMS structures allows some prediction of the effects of radiation on COTS IMUs [72].

3.2.1 Capacitive radiation tolerance

Changes in the calibration of accelerometers due to trapped charge in the dielectric has been seen at doses up to 1 kGy(Si) [84, 85]. The XMMAS40G accelerometer was tested and failed at a dose of only 40 Gy(Si) [84]. However, it was possible this was due to the output CMOS circuitry failing, rather than the active sensing unit. This highlights the difficulty in pin-pointing a specific cause of degradation within complicated MEMS.

Comb-drive poly-silicon devices, manufactured by Analog Devices, have been tested

for their TID tolerance [81, 82, 84]. A capacitive sensing element is used to measure the external force on the accelerometer, therefore, it is susceptible to static charge deposited in the dielectric [82]. Tests showed that the accelerometers (ADXL50 & ADXL150) showed degradation in the 500 Gy(Si) range. Whereas a similar device, where a poly-silicon film was placed over the dielectric, exhibited no degradation with radiation exposure up to a dose of 30 kGy(Si) [82]. It was believed this was caused by the electrical shielding of the active device from trapped charge due to the poly-silicon film.

3.2.2 Piezoresistive radiation tolerance

The radiation tolerance of piezoresistive pressure sensors and MEMS accelerometers have been measured [86, 87]. Two examples of the Endevco 7264B-500T saw a shift in outputted values up to a TID of 730 kGy(Si) with no catastrophic failure. The devices could also be recalibrated after irradiation. The Kulite XT-190-25A pressure transducers showed varying radiation tolerance with one failure at 70 kGy(Si), another at 250 kGy(Si) and four other devices still operational after 200 kGy(Si) [86, 88].

The degradation mechanism for the piezoresistive MEMS is caused by an increased resistance of the piezoresistive sensing element due to trapped hole charges. This charge in the surrounding oxide-layer of the piezoresistor induces a depletion region within the semiconductor, which increases the device resistance [86].

3.2.3 Piezoelectric radiation tolerance

Little work has been conducted on piezoelectric MEMS. An example study on the radiation tolerance of a piezoelectric mirror array was conducted [89]. This suggested that the device remained operational up to a dose of 10 kGy(Si), but exhibited radiation induced changes from as low as 200 Gy(Si).

Table 3.1 outlines the sensitivity of a MEMS device dependent on its measurement technique. It can be seen that devices reliant on electrostatic principles such as capacitive sensing elements are sensitive to dielectric charging from gamma exposure, whereas piezo materials are less susceptible to dielectric charging, and therefore, offer higher radiation tolerance.

Table 3.1: Main failure modes of MEMS dependent on actuation principle [72].

MEMS actuation type	Sensitivity to dielectric charging	Failure modes due to dielectric charging
Capacitive	High (Design dependent)	Stuck comb-drive, snapped-down parallel plates, change in calibration of parallel plate of comb-drive sensors and actuators
Piezo	Low	Calibration change (failures are due to Non Ionizing Energy loss, particle interaction/displacement)

Although there is very little research on the radiation tolerance of MEMS, the research that has been conducted suggests that all MEMS devices are capable of surviving space orbit for many years with piezo powered devices offering greatest resistance [72]. Therefore, further research hasn't been necessary for current use-case scenarios and the number of papers concerning the radiation tolerance of MEMS remains low. This means further research is required to determine the effect of radiation on low-cost IMUs to define their suitability for deployment in a nuclear decommissioning environment.

To develop a low-cost robotic platform, it is not possible to use piezo devices such as the Endevco 7264B-500T mentioned previously, as it costs in the region of £360. Most manufacturers now favour development of capacitive MEMS due to increased reliability, accuracy and low-cost for standard environments [74]. Therefore, capacitive MEMS were chosen for radiation tolerance testing.

It was hoped consistent failure modes could be found that would enable mitigation techniques to be applied. Software calibration, or prediction of TID failure threshold, might allow replacement of the device prior to failure.

3.3 Analogue and Digital output MEMS

There are multiple interface options when considering which accelerometer or gyroscope to use. These can broadly be split into two groups, analogue output and digital output. Analogue IMUs output an analogue voltage that can be read by a microcontroller via its in-built analogue to digital converter (ADC). This is very easy to interface with many microcontrollers, but one analogue input for each axis is required, which means that the number of axes is limited to the number of ADC's available.

Some analogue sensors incorporate amplifiers within the device, to output a magnified and filtered signal from the sensing element, whereas other designs require amplification circuitry to be designed by the end-user and placed in their circuit. A block diagram of an example analogue output accelerometer can be seen in Fig. 3.7.

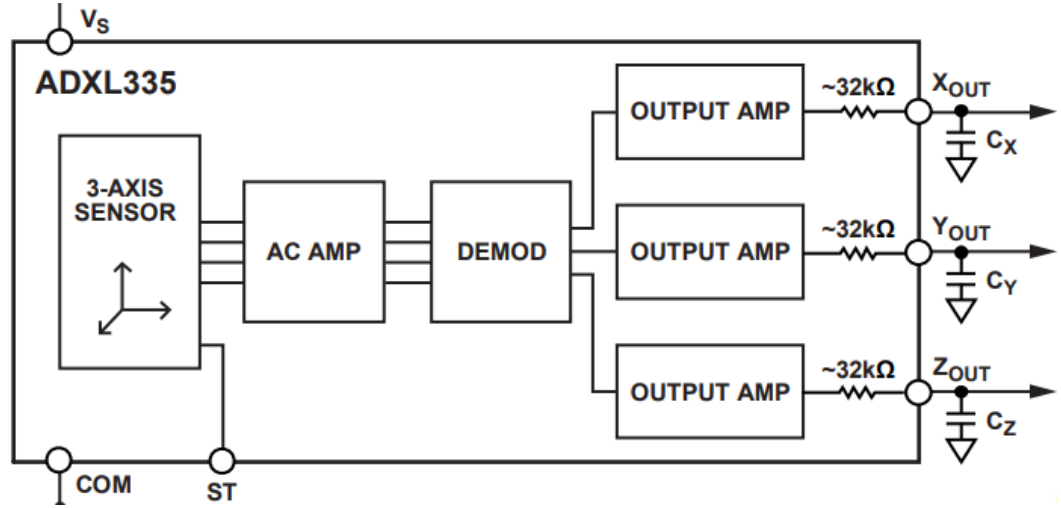


Figure 3.7: Block diagram of the analogue output accelerometer ADXL335 indicative of many analogue accelerometers and gyroscopes [90].

In comparison to the Analogue accelerometers, digital IMUs require both analogue filters and a greater amount of digital filtering of the output values and therefore have more circuitry. Digital IMUs normally interface with a microcontroller via either Serial Peripheral Interface (SPI) or Inter-Integrated Circuit (I^2C) serial communications requiring further I/O circuitry to be added to the device. A block diagram of the typical structure of a digital accelerometer can be seen in Fig. 3.8.

Digital IMUs are more common than analogue IMUs. They have more in-built features for controllability and have therefore become industry standard for many applications. Due to the output filtering of the basic analogue voltage to an electrical signal and the subsequent formatting to a digital communication system, there are many constituent parts that are susceptible to radiation damage.

To determine if one type of output is more or less radiation tolerant than the other, IMUs with different outputs were chosen. The difference in radiation sensitivity of each device would be analysed to determine a preferred version.

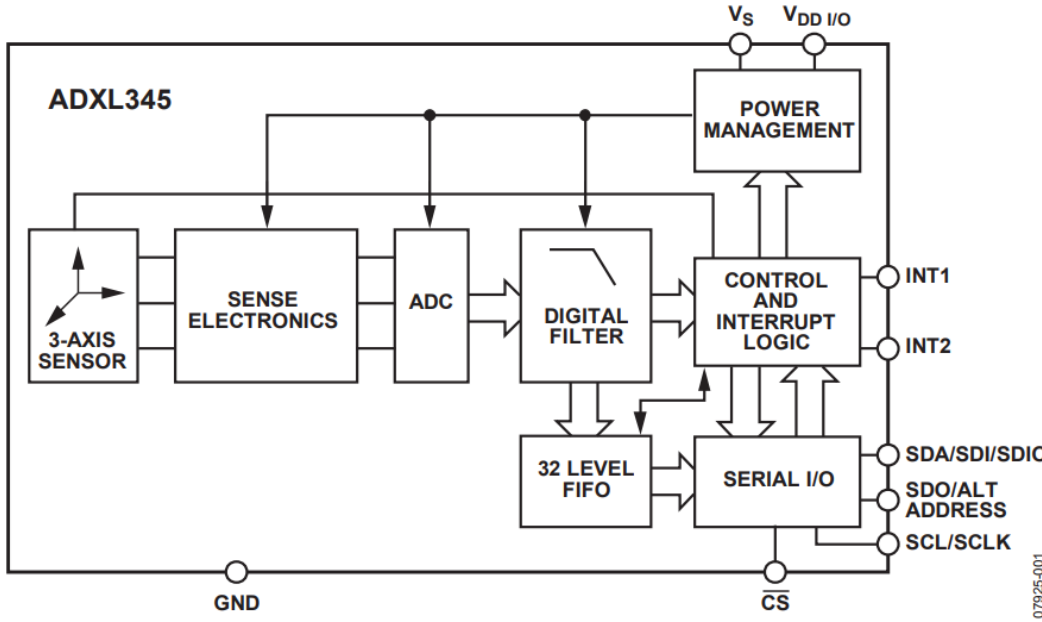


Figure 3.8: Block diagram of the digital accelerometer ADXL345 indicative of all digital accelerometers and gyroscopes [91].

3.4 Summary of Chosen Parts

There are many different types of IMUs in the form of complete ICs or individual accelerometers, gyroscopes and magnetometers. Some more recent versions also include barometers.

With many different technologies incorporated into one package it is important to monitor the effects of radiation on IMUs typical of a low-cost robotic platform with varying manufacturers.

Table 3.2 summarises the IMUs chosen for experimental analysis in this work. They were chosen for their similarities to each other, to determine consistent degradation modes or mechanisms, as well as their low-cost and common use in robotic platforms. Low-cost IMUs were chosen to enable the constituent parts of the robotic platform to remain below £200. This price could increase if the benefits of an increased tolerance device outweighed the cost of replacement of a low-cost device.

It should be noted that all IMUs are of the capacitive sensing element type. This is due to the high-cost and rarity of piezoresistive and piezoelectric IMUs and the need to characterise those devices for a nuclear decommissioning environment. With very few papers, prediction of radiation tolerance is difficult. It also allows comparisons between manufacturers, irrespective of sensing element.

Table 3.2: IMUs chosen for radiation tolerance testing

IMU	Specifications			
	Interface	Gyro	Accelerometer	Magnetometer
MPU6050	I ² C	Yes	Yes	N/A
LSM9DS0	SPI/I ² C	Yes	Yes	Yes
SEN-10121	I ² C	Yes	Yes	N/A
ADXL335	Analogue Voltage	N/A	Yes	N/A
ENC-03R	Analogue Voltage	Yes	N/A	N/A

The SEN-10121 was an IMU made from two individual chips, the ITG3200 gyroscope and the ADXL345 accelerometer. It was hoped that separating the two chips may highlight the difference in effects for gyroscopes in comparison to accelerometers when separated in comparison to the “one-chip” design of the LSM9Ds0 and MPU-6050 IMUs.

The ADXL335 and ENC-03R are very simple examples of analogue motion sensors. The ENC-03R contains only one axis, which means for a real-life application, three of the chips would be placed orthogonally to each other to gather sensor information for each axis.

3.5 Experimental Setup

This sections describes the experimental facilities used to determine the radiation tolerance of COTS IMUs and the experimental procedures used during γ -exposure of the devices.

3.5.1 Experimental Facilities

Testing was undertaken using the ^{60}Co irradiator at the Dalton Cumbrian Facility, owned by the University of Manchester [57], as seen in Fig.3.10. With the decay scheme seen in Fig. 3.9.

The dose-rate used was $52 \text{ Gy(Si).min}^{-1}$ after an initial test at $90 \text{ Gy(Si).min}^{-1}$ suggested a rapid degradation. Due to time constraints accessing the irradiator, using the MIL-STD-883K [92] testing regime and the number of samples, $90 \text{ Gy(Si).min}^{-1}$ was chosen initially. As the devices degraded quicker than expected, the dose-rate was

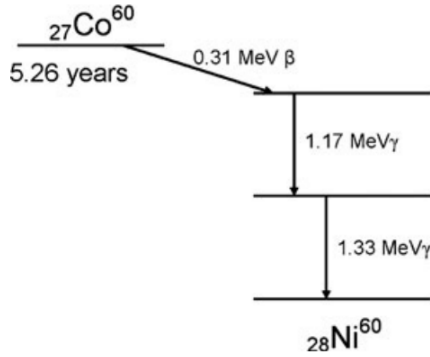


Figure 3.9: Decay scheme of ^{60}Co gamma source.



Figure 3.10: The ^{60}Co gamma irradiator.

reduced. A reduced dose-rate allowed greater accuracy in pin-pointing degradation at low TIDs. An ionization chamber was used to verify the dose-rate.

3.5.2 Experimental Procedure

A mount was made to hold each IMU stationary at a compound angle so no axis should be at its maximum or minimum output whilst irradiation took place as can be seen in Fig. 3.11. This was to enable observation of possible changes in sensing element movement that may be masked if the sensing element is at its maximum or minimum position.

Wires were passed into the chamber to power the IMU and to read the IMU output values during irradiation. If no degradation occurred a flat continuous line would be observed for each axis. Any other data points would suggest degradation. Fig. 3.12 outlines the experimental set-up.

As this experiment was designed to test the output of each IMU during exposure



Figure 3.11: Photo of compound angle mount and experimental set-up of ADXL335 IMU radiation tolerance tests placed within the Co-60 irradiator.

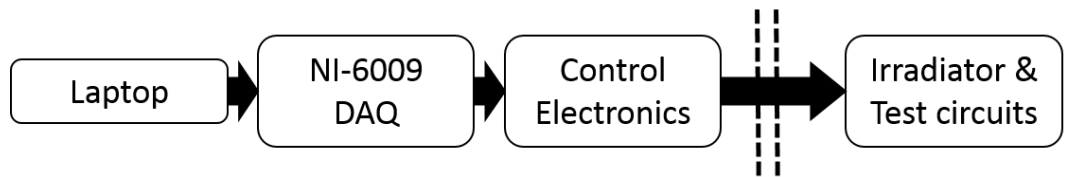


Figure 3.12: Experimental procedure block diagram representing the data flow.

to gamma irradiation raw values were gathered from each device, with the change in pre-irradiation values plotted against an increasing dose. Under certain operating circumstances, software calibration would take place to determine initial orientation, but this was not necessary for this study due to testing of the individual outputted signals.

3.6 Digital IMU Results

This section presents data gathered whilst irradiating the digital LSM9DS0, MPU-6050 and SEN-10121 IMUs. The results are graphically displayed before they are analysed and discussed. Eight samples of the LSM9DS0 were irradiated, five samples of the MPU-6050 and three samples of the SEN-10121.

3.6.1 LSM9DS0

Figs. 3.13-3.15 show the raw value output of the x, y and z-axis for the accelerometer, gyroscope and magnetometer parts of one LSM9DS0 IMU against an increasing TID.

Fig. 3.13 outlines the degradation of the accelerometer output of the LSM9DS0 IMU. It can be seen that there is a gradual decrease in Accel X and Accel Y output with intermittent spikes in outputted values. However, the same is not true for Accel Z which does not increase or decrease but only exhibits sudden spikes in values intermittently through time.

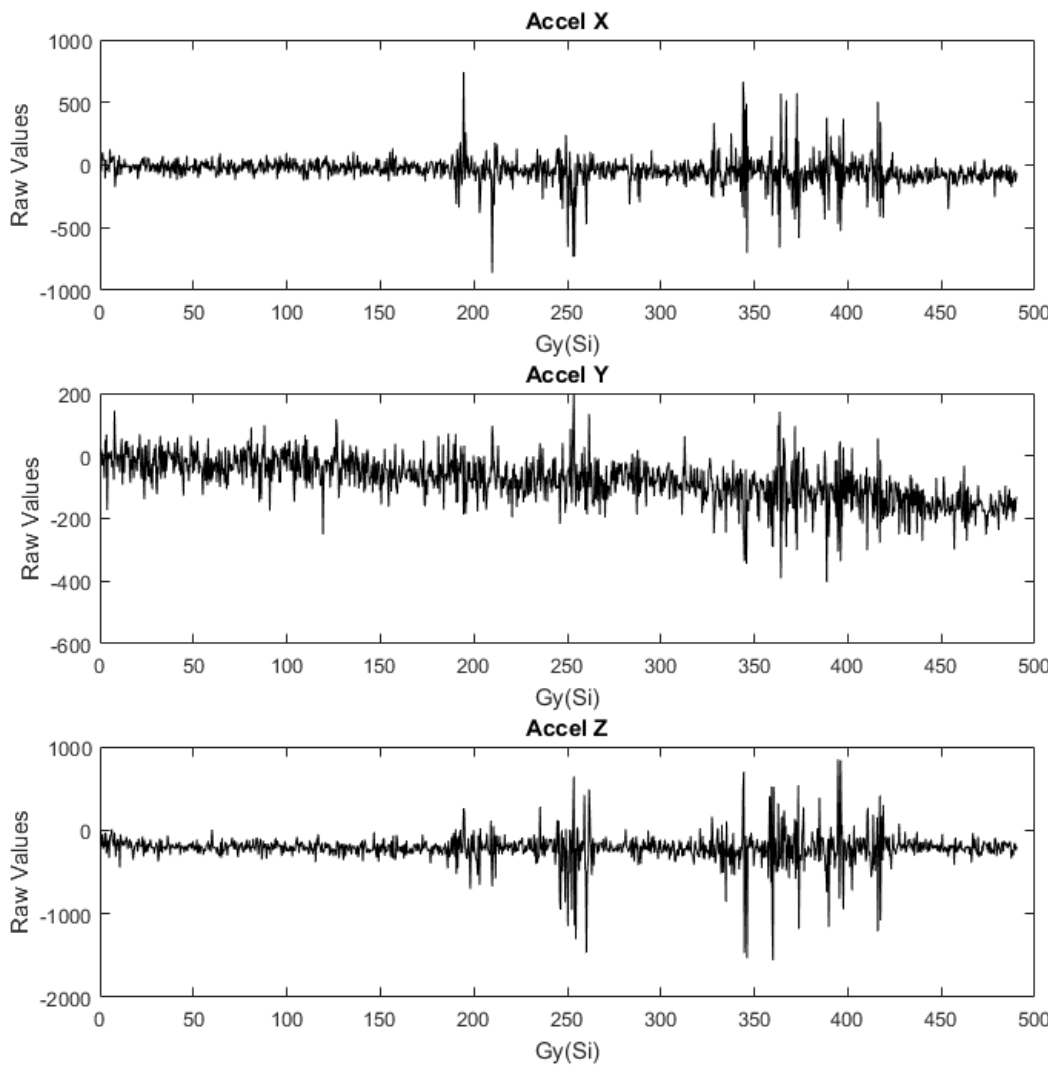


Figure 3.13: Degradation of x, y and z-axis of the LSM9DS0 accelerator.

The largest spikes in output values have a magnitude up to 900, this would suggest a multiple bit failure of the analogue to digital electronics as the maximum spike of a one bit failure would be 256. After a spike in output, the outputted value returns

close to the original value, however, there are small spikes in output in the range of 32 to 128, which is outside the normal range of values outputted by a stationary IMU of approximately ± 10 . This suggests that single-bits of the analogue to digital electronics are failing.

Fig. 3.14 outlines a consistent decrease in output of Gyro X and Gyro Y but at varying rates as the difference in starting value and finishing value for Gyro X is approximately 900 and for Gyro Y 250. Gyro Z exhibits an increasing output for an increasing gamma dose, with an increase of 400 in its raw output value witnessed.

This gradual decrease or increase in output is likely caused by a build up of charge on, or near, the sensing element, causing distortion of the system. The spikes seen in each axis have a magnitude of approximately 250, which suggests failure of single bits in the analogue to digital electronics.

The LSM9DS0 is the sole IMU with an in-built magnetometer, therefore, the results gathered are displayed as an indication of the effects of radiation exposure on magnetometers.

Fig. 3.15 shows the change in raw value output during irradiation. The Mag X exhibits a decrease in output value, whereas the Mag Y outputs show an increase in output value. The z-axis exhibits a small increase in raw output values (less than 100), but with spikes of data both negative and positive shown during irradiation.

It is difficult to de-couple the effect of radiation exposure to the magnetometer from the un-calibrated environment of the enclosed metal test chamber of the irradiator, which would naturally cause changes in magnetometer output. However, the spikes witnessed on the Z-axis suggested that the radiation causes failures of single-bits in the analogue to digital electronics.

Most of the LSM9DS0 devices exhibited an increase or decrease in raw output values or spikes of erroneous data. However, there are also inconsistencies between each IMU of the same manufacturer. Appendix B includes test results from other LSM9DS0 samples, which highlights the range of degradation modes.

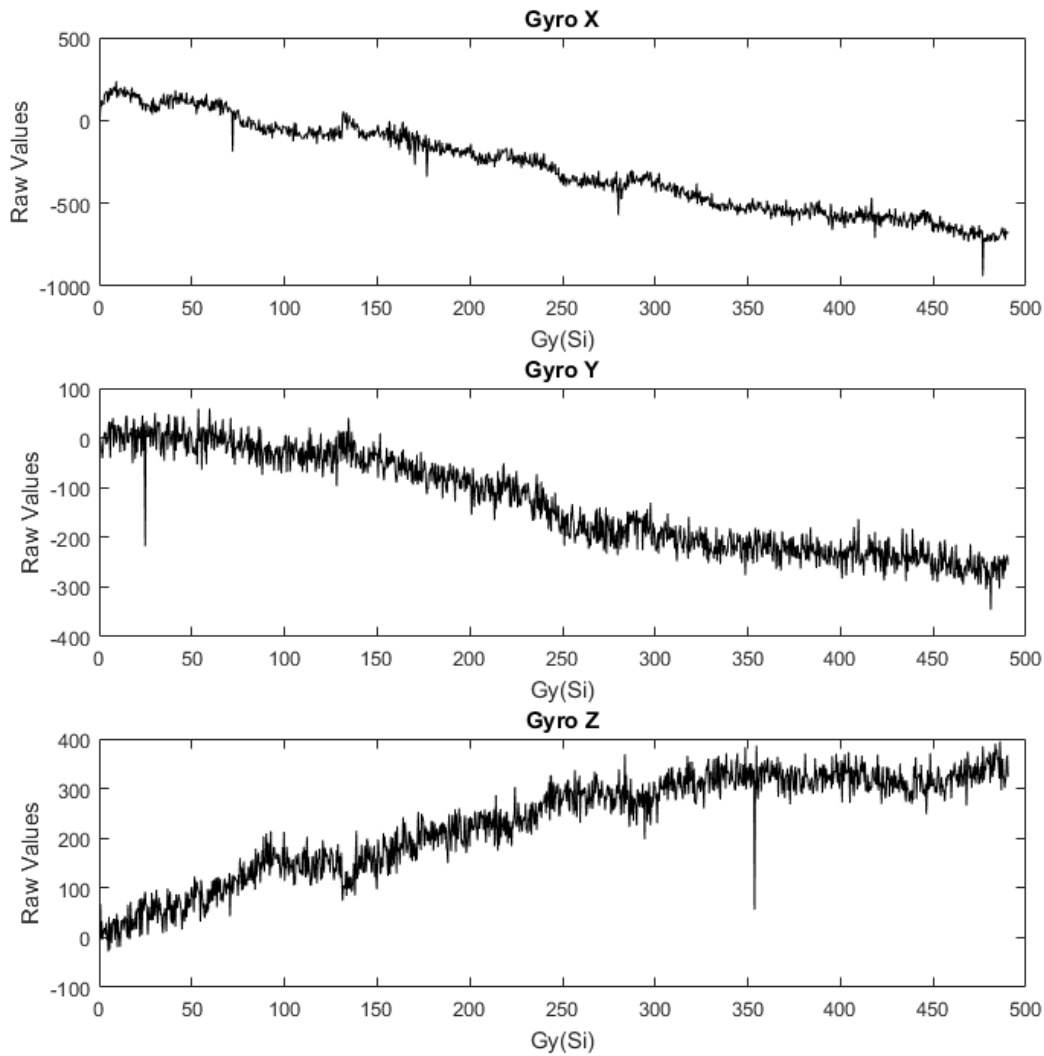


Figure 3.14: Degradation of x, y and z-axis of the LSM9DS0 gyroscope.

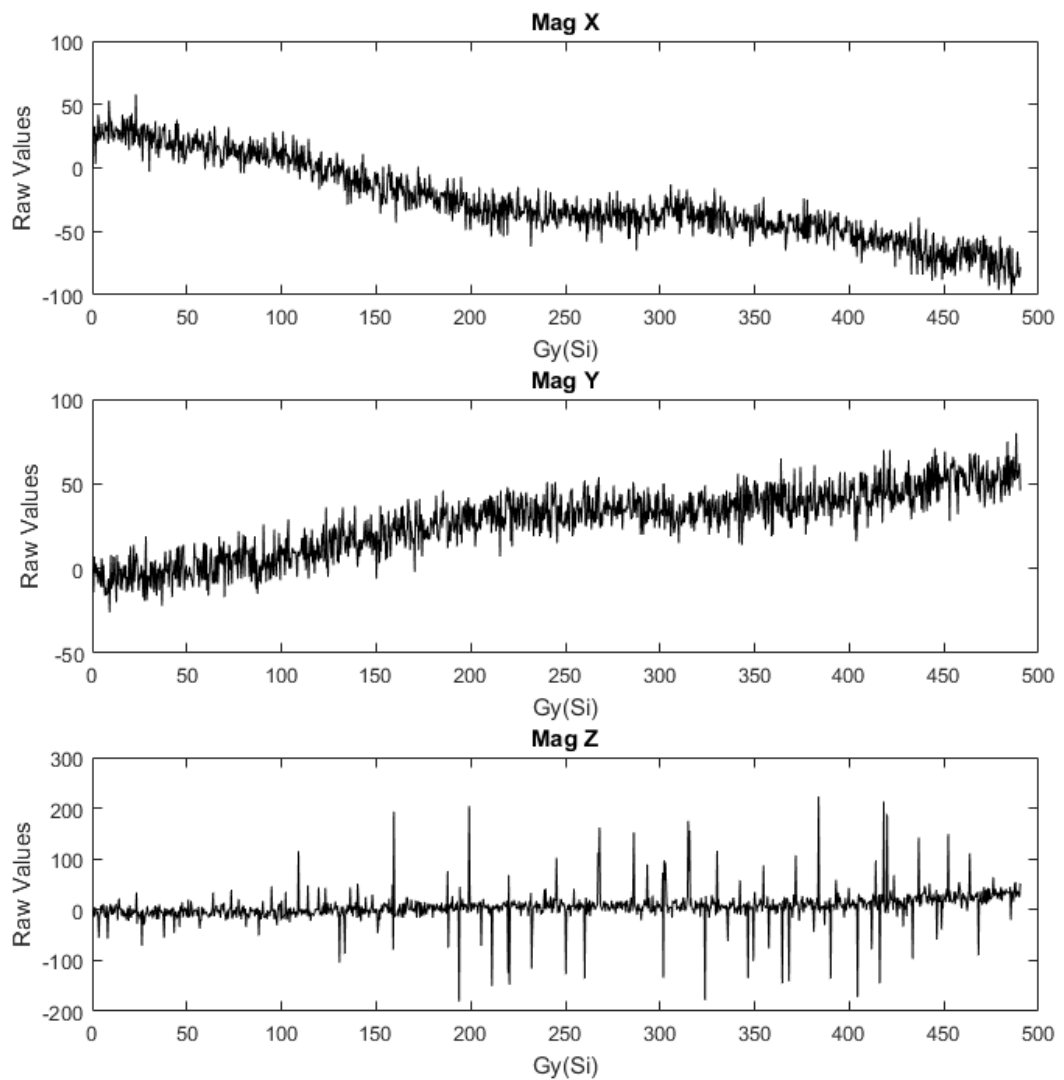


Figure 3.15: Degradation of x, y and z-axis of the LSM9DS0 magnetometer

3.6.2 MPU-6050

Fig. 3.16 shows the sudden degradation of all three gyroscope axis outputs after a TID of 800 Gy(Si). Appendix B shows that this degradation mode is similar for most MPU-6050 IMUs, however, there is one sample with a failure at a TID of 450 Gy(Si). Changes in output values from 5000 to 20,000 suggest a complete failure of the device, with little indication to the failure mechanism.

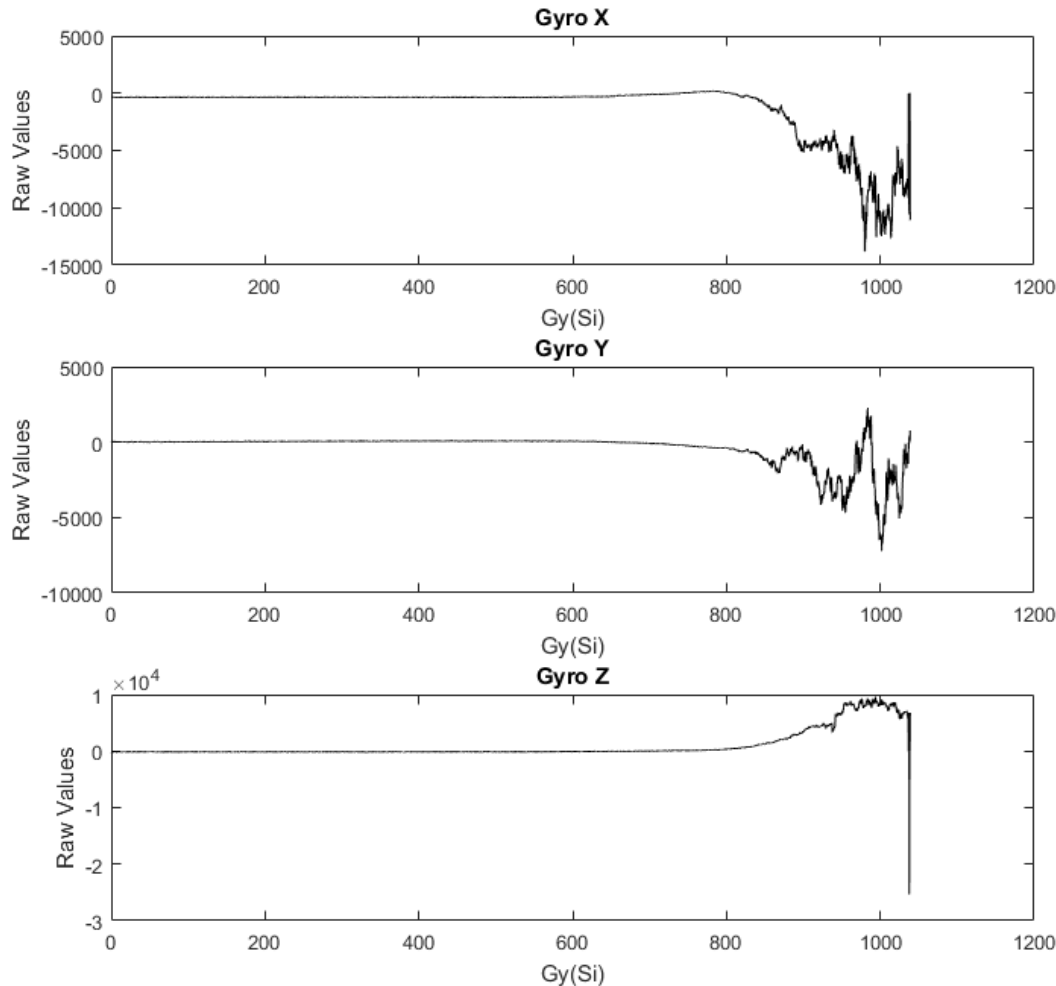


Figure 3.16: Degradation of x, y and z-axis of the MPU-6050 gyroscope.

Fig. 3.17 outlines a similar sudden degradation of the accelerometer as witnessed for the gyroscope from approximately 800 Gy(Si) onwards. As both parts of the device failed simultaneously, this could suggest a failure of the dielectric surrounding the sensing elements. Degradation of output circuitry would likely cause either the accelerometer or gyroscope to fail before the other with differences between axes.

Both the gyroscope and accelerometer show minimal degradation before 800 Gy(Si) and complete failure after this point. This suggests that the failure rate is predictable

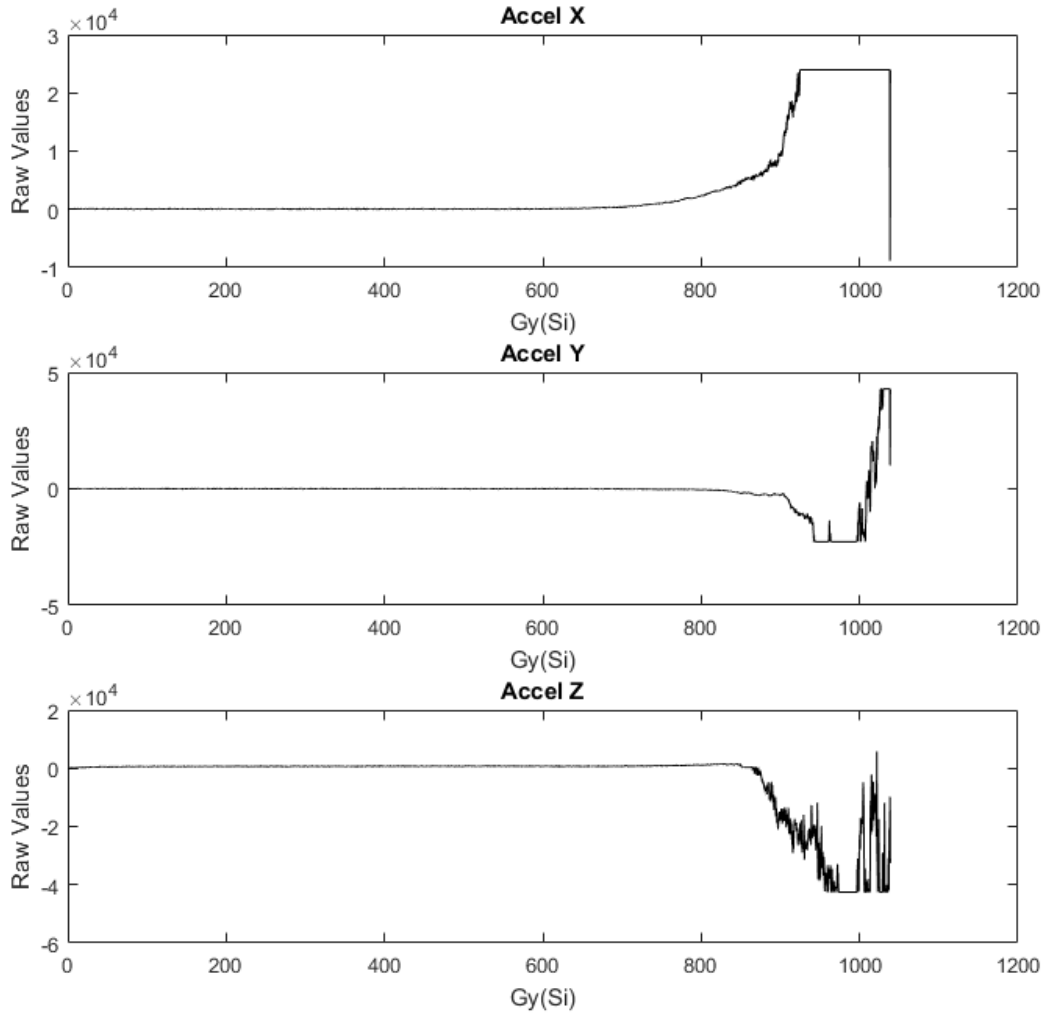


Figure 3.17: Degradation of x, y and z-axis of the MPU-6050 accelerometer.

with respect to TID. If the TID that the robotic platform is exposed to can be recorded, this IMU may be replaceable before it reaches that point, therefore not resulting in loss of device or down-time in operation of the robot.

3.6.3 SEN-10121

The SEN-10121 is made up of separate accelerometer and gyroscope ICs. The accelerometer used was the ADXL345 and the gyroscope used was the ITG-3200. By using a digital IMU with separate accelerometer and gyroscope chips, it was hoped to determine if there are different degradation modes for a combined chip over separated chips.

Fig. 3.18 shows the output of the ADXL345 accelerometer within the SEN-10121 IMU. Different failure modes can be seen. Accel X and Accel Y show small decreases

in output values before failure at approximately 880 Gy(Si) with random output witnessed from this point. Accel Z outputs decreasing values with steps at approximately 300 Gy(Si), 600 Gy(Si) and 900 Gy(Si).

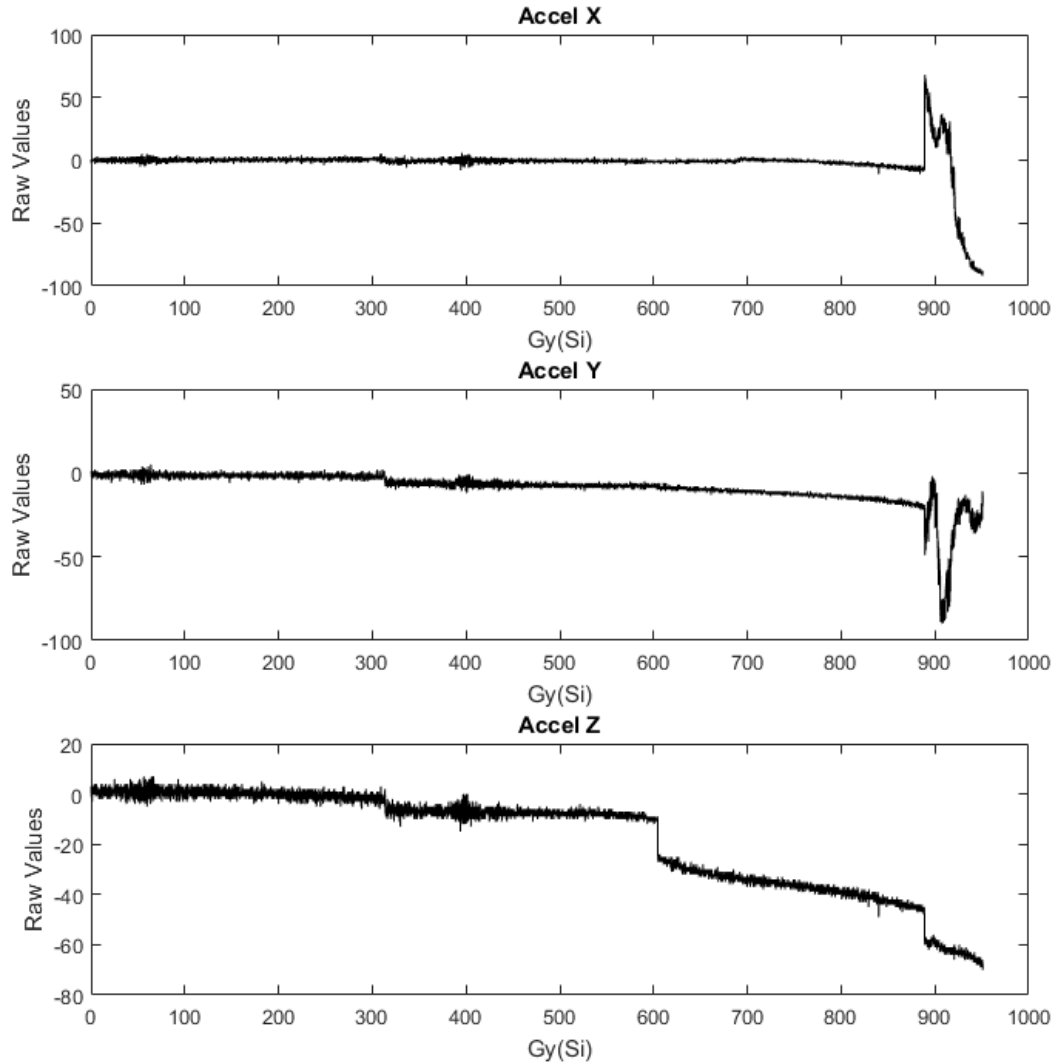


Figure 3.18: Degradation of the x, y and z-axis of the ADXL345 accelerometer as part of the SEN-10121 IMU.

Step changes of approximately 8 and 16 for Accel Z suggest failure of single-bits in the analogue to digital electronic circuitry. This can also be seen at approximately 300 Gy(Si) for Accel Y. The output appears to step over values suggesting the possibility that the IMU can no longer output certain values, however, further testing of this device would be required to determine if this is the case.

Fig. 3.19 outlines the response of the ITG-3200 gyroscope to gamma radiation exposure. Step changes in values can again be seen in the output of each axis, however, the magnitude of the step changes is very large. This could be due to a multiple bit

failure in the analogue to digital circuitry of the IMU suggesting multiple transistors were thermally overloaded or latched up.

Appendix B shows the same failure modes of the other two SEN-10121 IMUs but at varying magnitudes. This makes failure prediction difficult, and therefore suggests this device is unsuitable for use in a nuclear decommissioning environment.

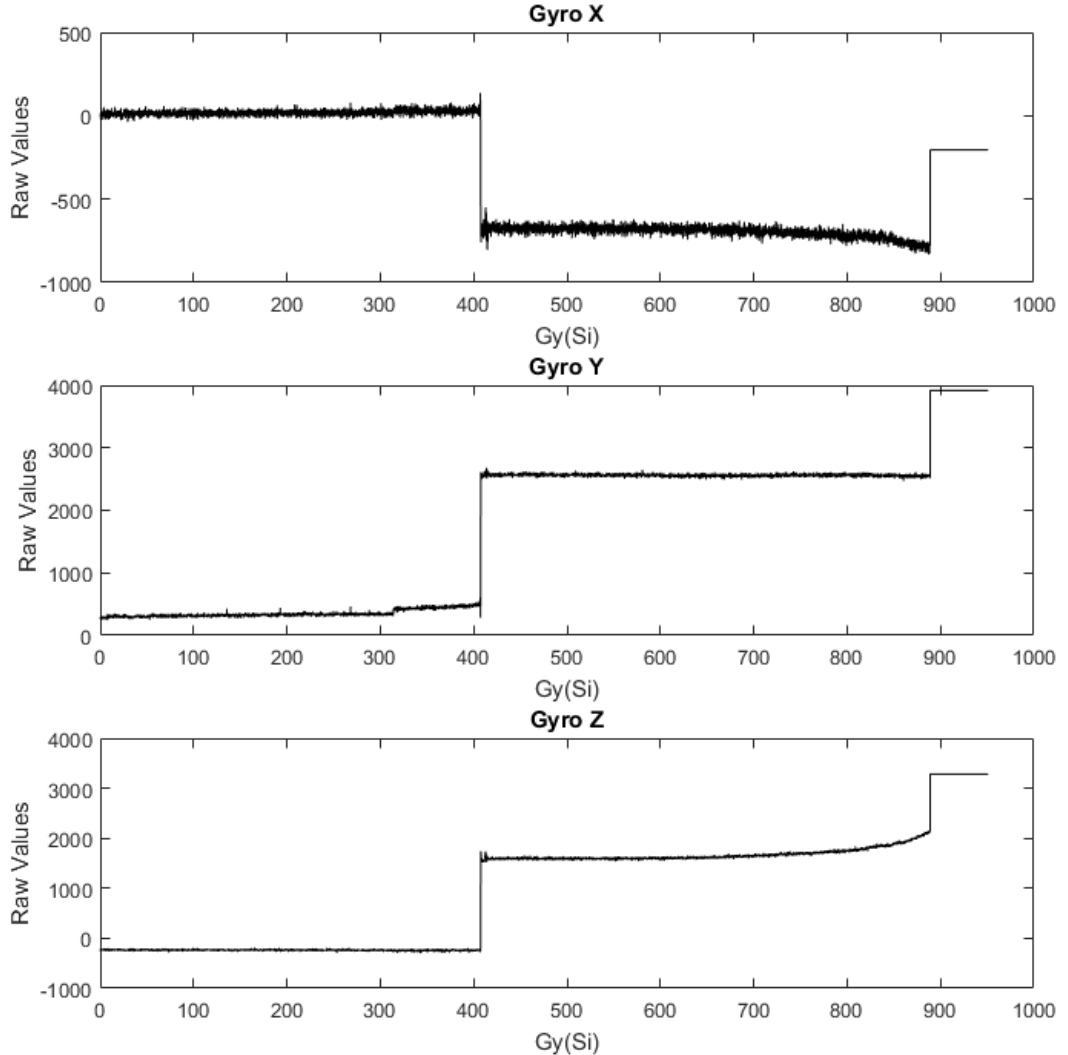


Figure 3.19: Degradation of the x, y and z-axis of the ITG-3200 gyroscope on-board the SEN-10121 IMU up to a TID of 1 kGy(Si).

3.7 Analogue IMU Results

Having analysed the radiation tolerance of 3 separate digital IMUs, examples of analogue gyroscopes and accelerometers were chosen for comparative experimental work. Ten examples of ENC-03R gyroscopes and ADXL335 accelerometers were tested.

3.7.1 ADXL335

Fig. 3.20 outlines the degradation of the output raw values for one ADXL335 accelerometer. It can be seen that all axes show degradation from 700 Gy(Si) onwards with the largest change seen in the z-axis.

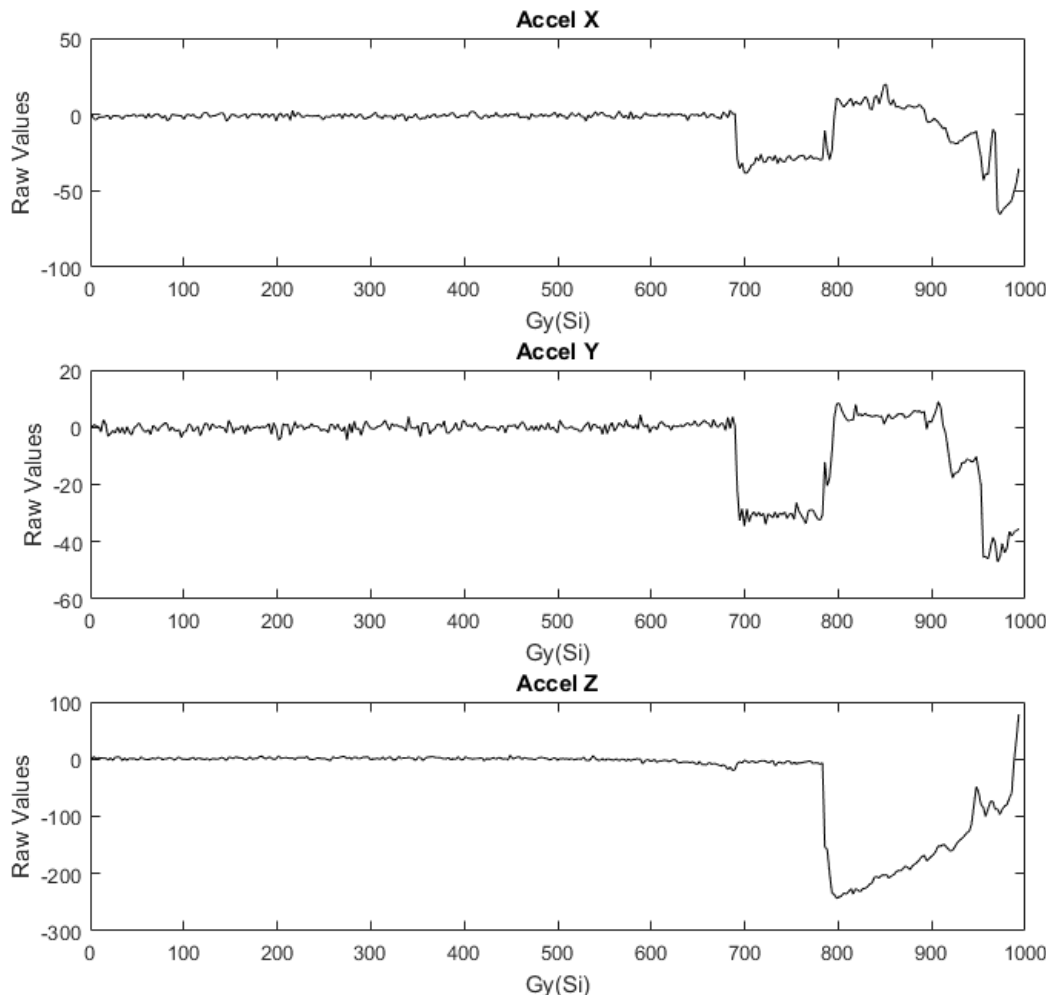


Figure 3.20: Degradation of the x, y and z axis of the ADXL335 accelerometer.

Accel X and Accel Y exhibit an initial step change of approximately 30, with Accel Z exhibiting a step of approximately 250. This suggests single bit failures are responsible for degradation of each axis. Past this point, a further step change can be witnessed for the Accel X and Accel Y figures before all axes exhibit random output behaviour.

As no change in outputted values occur before 700 Gy(Si), this suggests that the accelerometer could be used before this threshold is reached with all tested ADXL335 accelerometers showing degradation after 700 Gy(Si). Past this point, there is very

little predictability in the degradation pattern. Graphs of all other tested ADXL335 accelerometers can be seen in Appendix B

3.7.2 ENC-03R

The ENC-03R gyroscope features only one axis. In a real world application, three would be deployed at 90 degrees to each other to form an x, y and z axis configuration. However, for the purposes of understanding the radiation tolerance of the device, one axis was considered sufficient.

Fig. 3.21 shows the output of one ENC-03R gyroscope up to a TID of 1 kGy(Si). Negligible degradation was seen over the duration of the irradiation. This is repeated for each of the 10 gyroscopes tested with all devices showing no failure or drift during irradiation. This suggests that this gyroscope was tolerant to a TID radiation dose of 1 kGy(Si).

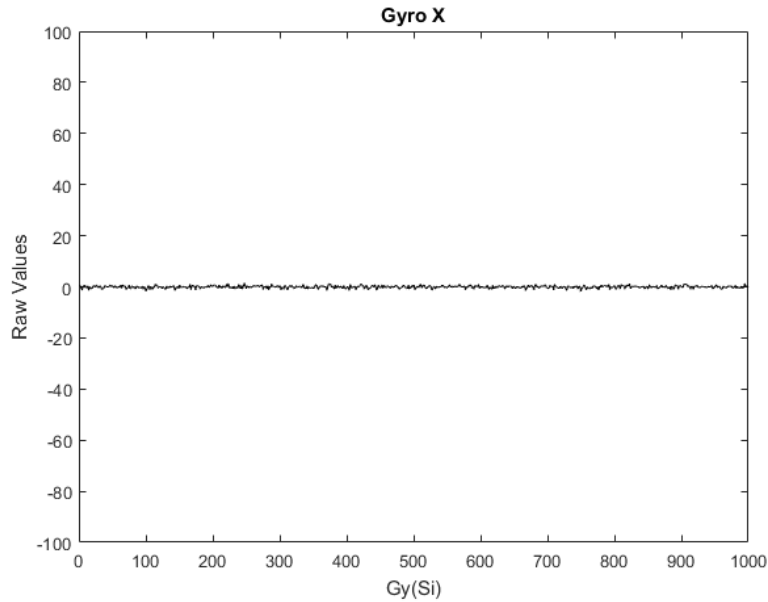


Figure 3.21: Degradation of solitary axis of the ENC-03R gyroscope.

As it was irradiated last and all other IMU devices showed degradation at a TID below 1 kGy(Si), the ENC-03R gyroscope was not irradiated to a greater dose. Therefore, a limit of TID tolerance was not found.

3.8 Results Analysis and Mitigation Techniques

The experimental results show that all except the ENC-03R gyroscope fail before a TID of 1 kGy(Si). Therefore, IMUs are found to be susceptible to gamma exposure. Great care will be required during deployment of IMUs on a robotic platform to be used in a nuclear decommissioning environment.

The change in raw output values of the LSM9DS0 was observed as a slow increase or decrease in raw value output. This suggests a charge deposited on the silicon, slowly causing an increased deflection of the in-built mass or increased charge in the dielectric between the capacitor plates. There were also spikes in output voltage suggesting failure of transistors in the analogue to digital circuitry.

The varying degradation modes exhibited by the MPU-6050, SEN-10121 and ADXL335 suggest that the susceptible part within these IMUs was the digital filtering and communications electronics on the output of the sensor. In many cases, spikes in outputted values represented a change of transistor state logic with magnitudes in the region of 32 to 254 suggesting single-bit failures. However, there were also large spikes and random behaviour exhibited by each of these devices suggesting further failure of the digital electronics.

Further analysis of the silicon layout would be required to confirm the change in output was attributed to a build up of charge in the silicon surrounding the physical MEMS or digital filtering circuit, however, access to this information was not possible during analysis.

Based on the experimental results, the ENC-03R would be recommended as the most radiation tolerant gyroscope, whereas the ADXL335 and MPU-6050 exhibit the greatest consistency of output for an accelerometer before a predictable threshold of sudden degradation. They are therefore the favoured options within the chosen IMUS to be deployed in a nuclear decommissioning robotic platform as long as mitigation techniques are put in place to replace the devices prior to degradation, with software algorithms implemented to filter the expected spikes in value caused by transistor latch-up. However, it is suggested that alternatives be found that exhibit a similar radiation tolerance to the ENC-03R.

Multiple techniques could be employed to mitigate against some of the degradation.

Primarily, the IMU could be designed as a detachable unit, easy to replace in case of degradation within a safety factor to avoid reaching an unexpected early failure. This technique enables the almost continual deployment of the robotic platform with very little added cost or time, with each IMU less than £10 to replace.

Shielding could be placed around the device, through introduction of a layer of lead or similarly dense material, reducing the total dose received by the IMU. However, this will increase the complexity of the robotic platform as shielding must be dense to block gamma rays, which increases the weight of the device, increasing the power required by each actuator. A mission analysis of benefits versus disadvantages caused by the extra shielding must be conducted for each deployment.

3.9 Summary

The analysis of multiple COTS IMUs similar to many on the market that could be deployed within a nuclear decommissioning embedded system has highlighted the variable responses of an important part of a robotic platform to gamma radiation exposure. Large variations in the response to gamma exposure has been seen. Therefore, further analysis of the degradation modes are suggested and it is recommended that any IMU deployed in an embedded system is tested for its radiation tolerance prior to deployment if possible.

The failures of the IMUs all occurred at a TID less than 1 kGy(Si) (except for the ENC-03R gyroscope). This is 5 times lower than the expected dose in a nuclear decommissioning environment and therefore mitigation techniques must be considered.

These results suggest a slight increase in tolerance seen for analogue solutions with predictable failure thresholds seen for the ADXL335 and MPU-6050. The variety of degradation modes suggest that reliable predictions are unreliable and further experimentation is required.

Chapter 4

Radiation Tolerance of Power Regulation Components

4.1 Introduction

Power supply regulation components are of utmost importance in low-cost robotic platforms. Failure of these components leads to failures of subsequent components reliant on their operation. Previous projects found voltage regulators to fail during γ exposure, and therefore, they require further experimental verification of the degradation modes. As voltage references are often used within voltage regulator design, it was thought that analysis of the radiation tolerance of multiple voltage references may indicate possible failure modes for linear voltage regulators.

Multiple examples of linear voltage regulators were also exposed to γ -radiation to determine if the degradation modes of each sample were consistent or if variation in degradation occurred. The results of these experiments led to the development of a discrete voltage regulator solution to determine if greater radiation tolerance could be created via component selection.

Microcontrollers are another example of a component whose failure effects multiple sub-systems reliant on it for correct operation. Therefore, an example microcontroller flash memory was tested for its radiation tolerance as an initial study to determine if further work was required on the understanding of its degradation mode.

It was hoped that experimental results would lead to a compendium or set of design rules for COTS components suitable for low-cost robotic solutions deployed within a

nuclear decommissioning environment.

This chapter first outlines the experimental facilities and procedures used to determine the radiation tolerance of these components. The results are then discussed with a new discrete voltage regulator design suggested and analysed in comparison to COTS voltage regulators.

4.2 Experimental Setup

This section describes the experimental procedures and the facilities used to assess the response of COTS voltage references, microcontrollers and voltage regulator components to γ -exposure.

4.2.1 Experimental Facilities

Testing was undertaken using the same ^{60}Co irradiator as described in Chapter 3. A dose-rate of $2.3 \text{ Gy(Si).s}^{-1}$ was used, which is within the range outlined by MIL-STD 883 for qualifying electronic systems (0.5 to 3 Gy(Si).s^{-1} [93]). This dose-rate was chosen to enable all devices to be irradiated during the time constraints of access to the irradiator, whilst remaining within the industry standard for testing electronic components. An ionization chamber was used to verify the dose-rate.

4.2.2 Experimental Procedure

A switching circuit, tolerant to radiation, was constructed using mechanical relays and resistors to alter the load on each voltage reference or regulator tested. Different value resistors could be chosen dependent on the required load for the tested devices. A block diagram of this circuit can be seen in Fig. 4.1.

Plug-in connectors allowed quick and easy replacement of the required test devices onto the radiation tolerant switching circuit. A ribbon cable was used to connect the circuits inside the irradiator to a control circuit outside the irradiator attached to a National Instruments (NI) USB-6009 data acquisition unit [95]. This was connected to a laptop running LabVIEW software. Fig. 4.2 shows a photograph of an assembled switching circuit.

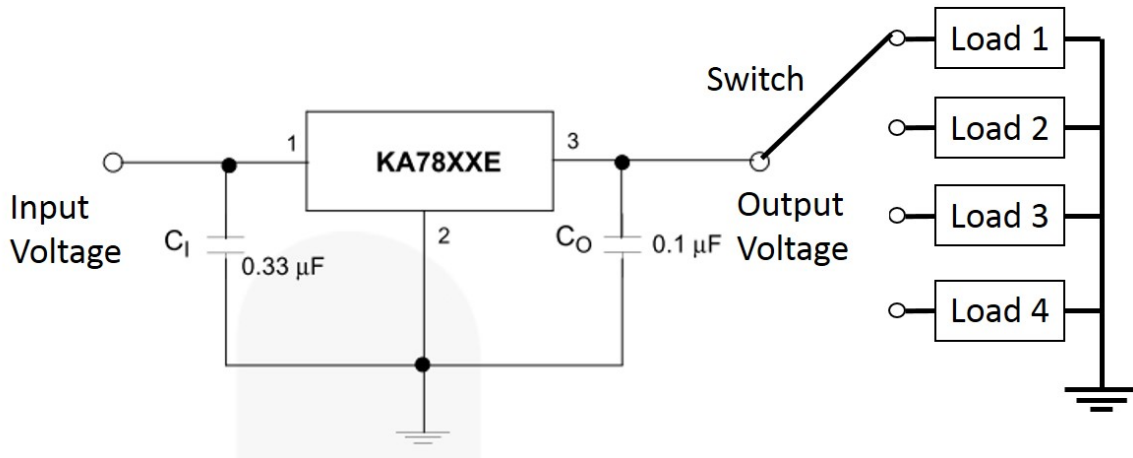


Figure 4.1: Block diagram of an example voltage regulator (Fairchild KA7805 [94]) test sample connected to a load switching circuit.



Figure 4.2: Photograph of example switching circuit.

This allowed the measurement of the test devices' output voltages during irradiation whilst controlling the load current to determine the effects of varying bias. Samples of the output voltage were taken at a frequency of 10 Hz.

A complete experimental circuit block diagram is shown in Fig. 4.3. An example test circuit is shown connected to the switching circuit inside the irradiator. The dashed line represents the irradiator boundary.

Load Variation Experiments

Circuits containing the voltage references and voltage regulators were connected to the switching circuit described in Section 4.2.2 and placed inside the irradiator. Four resistors (Load1–Load4 in Fig. 4.1) were chosen to alter the load during irradiation to determine if the magnitude of current effected degradation modes.

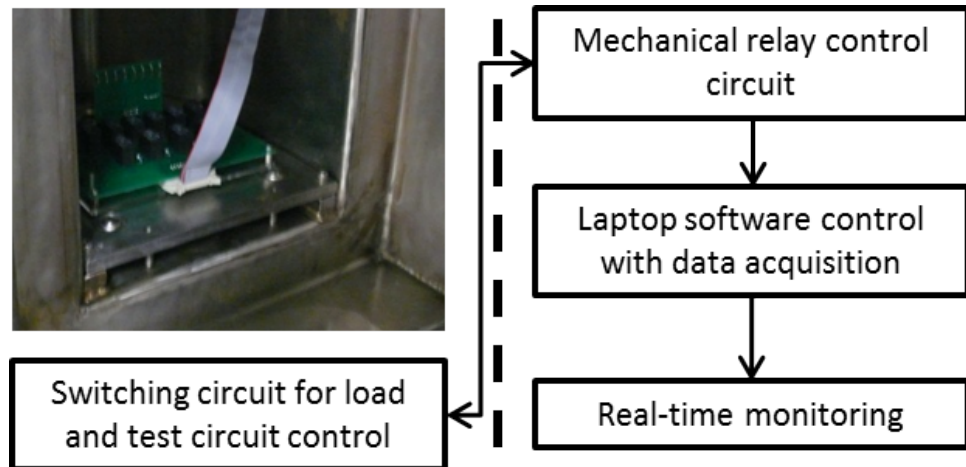


Figure 4.3: Outline of Experimental circuit. The dashed line represents the irradiator boundary.

During irradiation, the first load was applied to the test circuit. This load was applied across individual test samples on the test circuit, which were switched every two seconds. The output voltage of the test sample was measured with a sampling frequency of 10 Hz. Once every load had been applied, the loading cycle was restarted from the first load. This allowed all test circuits to have a varying current flow during irradiation at four different load currents. A constant input voltage of +14 V was chosen to be representative of a 4 cell battery commonly deployed on robotic platforms, whilst also being close to common “wall-supplied” 12 V that is often used.

It was noted there would be a variation in TID between the first and last load of the test piece in the series, however, this would be a constant offset dose that was taken into account when averaging the output voltage measurement samples for each cycle of the system.

No Load Experiments

It was thought that a possible mitigation technique against radiation degradation would be to include redundant systems onto the robotic platform to activate when primary systems failed. Therefore, the reaction of the devices to radiation exposure whilst switched off was considered useful to determine if this method could be deployed. Baseline experiments were conducted with no load applied to each of the test circuits. During these irradiation experiments, no current was passed through the devices and all pins were grounded. A measurement of output voltage was taken before and after

the irradiation.

4.3 Initial Results

This section presents the results gathered from the first round of experiments conducted following the procedures outlined in Section 4.2.2.

4.3.1 Device Descriptions

The COTS devices chosen for experimentation are outlined in Table 4.1. Three voltage references and one linear voltage regulator were chosen initially.

Table 4.1: Devices Chosen for Experimentation.

Part Number	Device	V_{out}	Tolerance	Package
Fairchild Semiconductor LM336Z5	Voltage Reference	5 V	1%	TO-92
Texas Instruments LM336Z5	Voltage Reference	5 V	1%	TO-92
Texas Instruments LM4040DIZ5	Voltage Reference	5 V	1%	TO-92
Fairchild KA7805AETU	Linear Voltage Regulator	5 V	5%	TO-220-3

Voltage references are often used as part of a voltage regulator to maintain a consistent value at limited current for the voltage regulator to amplify. Analysis of their degradation modes may suggest a degradation mode for linear voltage regulators.

The linear voltage regulator chosen has a maximum output current of 1 A and is typical of many COTS regulators deployed in embedded systems. Both are of utmost importance in the power management of an embedded system.

Characterisation of all of these devices is imperative during design of a robotic platform designed to function in a high dose-rate radioactive environment, such as nuclear decommissioning.

4.3.2 Voltage References

This section describes the experimental results gathered regarding the radiation tolerance of voltage references. Fig. 4.4 displays a photograph of a voltage reference test circuit that was placed on the switching circuit as discussed in Section 4.2.2.

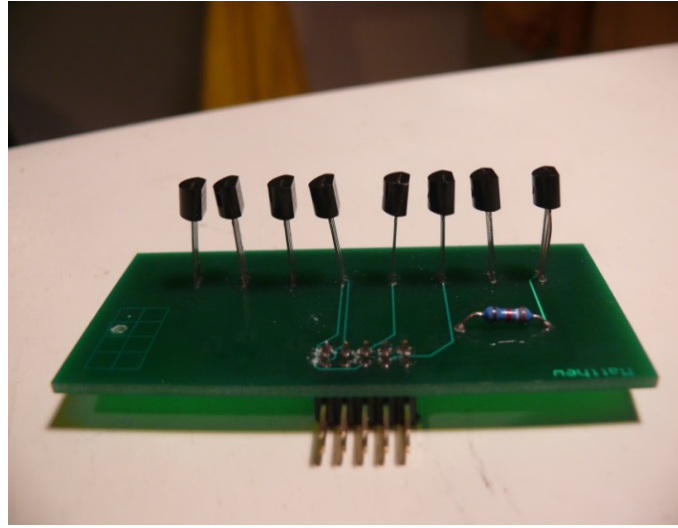


Figure 4.4: Voltage reference test circuit photograph.

Four test boards, each containing eight voltage references were used for each chosen voltage reference. Two for variable load experiments and two for no load experiments.

4.3.3 Variable Load Experiments

This section presents the data gathered from the variable load experiments of each chosen voltage reference. It was found that there was no change in output voltage degradation dependent on the load drawn. Therefore, the results presented in this section are of the voltage reference drawing a load of 10 mA, which can be considered the same as all load currents.

Fairchild LM336Z5

The output voltage degradation of the Fairchild LM336Z5 voltage reference can be seen in Table. 4.2. The figure represents the average of 8 voltage references with an increasing dose at a load current of 10 mA.

Table 4.2: The average output voltage of the Fairchild LM336Z5 voltage reference at intervals up to a TID of 5 kGy(Si)

Output Voltage (V)	Dose (Gy(Si))
4.960	385
4.983	1,540
5.008	2,700
5.032	3,850
5.056	5,000

The output voltage of the LM336Z5 increased by approximately 0.1 V after a TID of 5 kGy(Si), equalling the specified manufacturer's tolerance range. The temperature of the voltage reference increased by 10 degrees Celsius during irradiation, which could lead to a maximum change in output voltage of 0.02 V due to temperature drift. This suggests that the majority of degradation witnessed was due to the exposure to γ -radiation.

The increase of output voltage appears consistent between equal TID intervals, suggesting that a predictable further increase in output voltage is likely with larger doses, moving the output voltage outside manufacturers' tolerances, for example +0.12 V after a further 1.2 kGy(Si).

Texas Instruments LM336Z5

The degradation of the Texas Instruments LM336Z5 voltage reference output voltage up to a TID of 5 kGy(Si) is shown in Fig. 4.3. The data represents an average of 8 voltage references from one board at a current draw of 10 mA.

Table 4.3: The average output voltage of the Texas Instruments LM336Z5 voltage reference at intervals up to a TID of 5 kGy(Si)

Output Voltage (V)	Dose (Gy(Si))
5.018	385
5.021	1,540
5.035	2,700
5.055	3,850
5.079	5,000

As with the Fairchild LM336Z5 voltage reference, the output voltage rises with an increasing dose, however, the magnitude of change is approximately 0.06 V after a TID of 5 kGy(Si). This is a very small change in output voltage and is only 0.01 V greater than the manufacturers' tolerance of ± 0.05 V. The temperature during irradiation increased by 10 degrees Celsius, leading to a potential increase of 0.01 V due to temperature drift. Therefore, as with the Fairchild LM336Z5 voltage reference, the magnitude of degradation due to γ -exposure was approximately 5 times the temperature drift expected.

Unlike the Fairchild LM336Z5 voltage reference, the degradation rate of the output voltage appears to increase with each step in TID. This creates a larger change in

output voltage magnitude for each 1.2 kGy(Si) of dose making predictability of future output voltage unreliable.

Texas Instruments LM4040DIZ5

Fig. ?? outlines the degradation of the Texas Instruments LM4040DIZ5 voltage reference output voltage up to a TID of 5 kGy(Si). The data represents the average of 8 voltage references at a load current of 10 mA.

Table 4.4: The average output voltage of the Texas Instruments LM4040DIZ5 voltage reference at intervals up to a TID of 5 kGy(Si)

Output Voltage (V)	Dose (Gy(Si))
5.030	385
5.040	1,540
5.049	2,700
5.058	3,850
5.061	5,000

The Texas Instruments LM4040DIZ5 voltage reference shows the least degradation of output voltage in comparison to the previous voltage references with a magnitude of 0.030 V to 0.035 V after a TID of 5 kGy(Si). This is almost negligible degradation and is within the manufacturer's tolerance of ± 0.05 V. The magnitude of output voltage degradation is also only marginally greater than an expected temperature drift of approximately 0.025 V, suggesting that the LM4040DIZ5 is the most radiation tolerant out of the three references tested.

4.3.4 Annealing

After irradiating each of the voltage references, the output voltage was monitored for 3 weeks to determine if any room temperature annealing was observed, resulting in the device output voltage recovering. Table 4.5 summarises the output voltage of each reference at 3 days, 1 week and 3 weeks, post-irradiation.

Table 4.5: Output voltage of references monitored for 3 weeks post-irradiation.

Voltage reference	Post-irrad.	3 days	1 week	3 weeks
Fairchild Semiconductor LM336Z5	5.055 V	5.113 V	5.125 V	5.054 V
Texas Instruments LM336Z5	5.080 V	5.065 V	5.063 V	5.059 V
Texas Instruments LM4040DIZ5	5.061 V	5.074 V	5.080 V	5.078 V

The Fairchild LM336Z5 voltage reference sees a rise in output voltage of 0.070 V over the first week before recovering to approximately its final irradiation output voltage. It is possible that with more time left at room temperature the output voltage will decrease further to its original value. However, readings were not taken past this point so this remains unknown. It is also possible that natural temperature fluctuations within the storage room could lead to natural fluctuations in output voltage up to 0.03 V.

The Texas Instruments LM336Z5 voltage reference sees a decrease across all measurements resulting in a drop of output voltage of 0.02 V from the irradiated value. This is a third of the damage caused by irradiation, but does not return the output voltage to the pre-irradiation value. This value could also be equivalent to the natural drift in output voltage dependent on the temperature with a predicted drift of 0.01 to 0.02 V, suggesting that a room-temperature anneal has little to no effect on the recovery of the device.

The Texas Instruments LM4040DIZ5 voltage reference exhibits a similar response to the Fairchild LM336Z5 voltage reference as the measurements on day 3 and week 1 show an increase in output voltage, with a magnitude of 0.019 V, before a decrease after 3 weeks. However, the voltage changes are in the magnitude 0.005 V this is almost negligible and may be caused by fluctuations in temperature causing a drift in output voltage, suggesting that a room-temperature anneal has negligible effect on the LM4040DIZ5 device.

4.3.5 Voltage Regulator

This test is focused on the failure mechanism of a standard linear voltage regulator when exposed to irradiation. The linear voltage regulator irradiated during this test was the Fairchild Semiconductor KA7805AETU [94]. This is a fixed output 5 V, 1 A regulator, typical of many commercially available linear voltage regulators on the market. Fig 4.5 outlines a photograph of the test circuit before and after irradiation.

The change in output voltage of the Fairchild KA7805 linear voltage regulator up to a TID of 5 kGy(Si) can be seen in Fig. 4.6. The change in output voltage is represented by an average of all 8 regulators on the test circuit during irradiation with each line representing a different load current. A standard deviation of 0.065 V between the

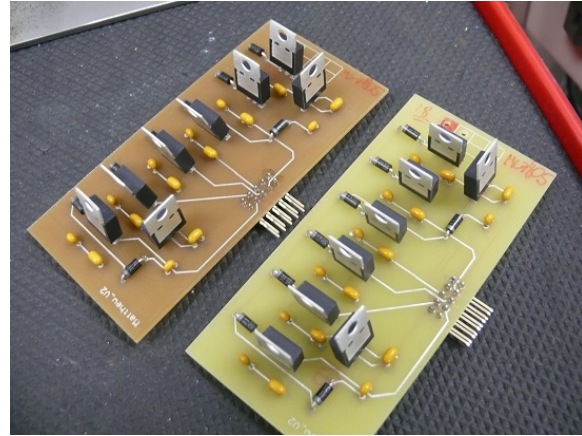


Figure 4.5: Outline of voltage regulator circuit before and after irradiation.

measured output voltages of all eight individual regulators was calculated, suggesting that the results are reliable.

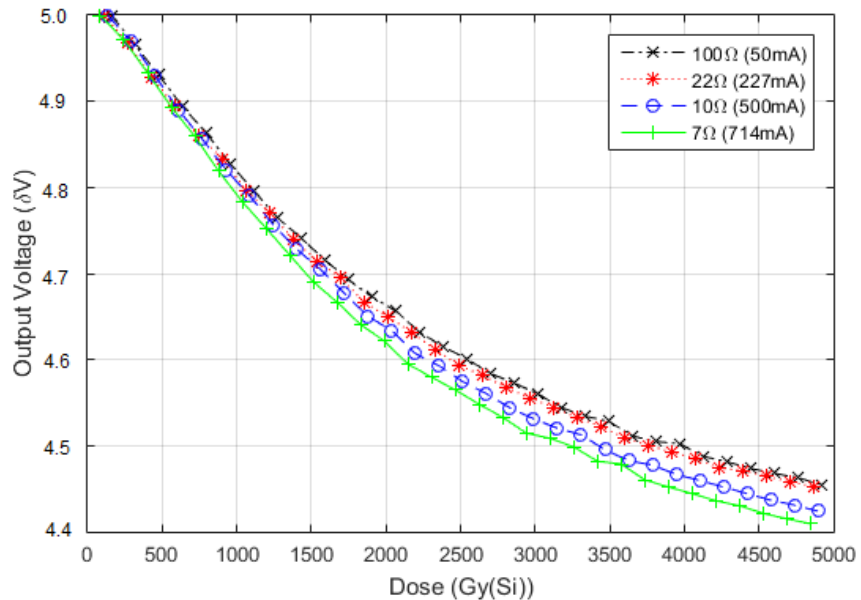


Figure 4.6: Degradation of the Fairchild KA7805 voltage regulator during an irradiation with a TID of 5 kGy(Si). Showing change in output voltage with an increasing dose.

The output voltage decreased with an increased dose leading to a change of approximately -0.5 V to -0.6 V. This was outside the manufacturers' tolerances of ± 0.2 V and larger than an expected temperature drift of approximately 0.1 V. This decrease in output voltage would be expected based on the review of the literature, which suggests a reduction in the gain of transistors exposed to gamma radiation. A reduction in the gain of the main output pass transistor of the voltage regulator would result in

a reduced output voltage.

The output voltage exhibited a small variation in degradation rate dependent on load current. When drawing the greatest load of 700 mA, the device degradation was larger than when drawing the smallest load of 50 mA. This could be due to the load regulation of the regulator that has a maximum value of 0.1 V, however, there was little difference in output voltage before irradiation, with a difference in output voltage dependent on load occurring during irradiation. This suggests it was an effect caused by the exposure to γ -radiation.

4.3.6 No Load Experiments

The KA7805 voltage regulator was exposed to a TID of 7 kGy(Si) without drawing a load current. Fig. 4.7 shows the drop in output voltage exhibited at a TID of 5 kGy(Si) and 7 kGy(Si). The output voltage was measured at the four different load currents used during the load variation experiment.

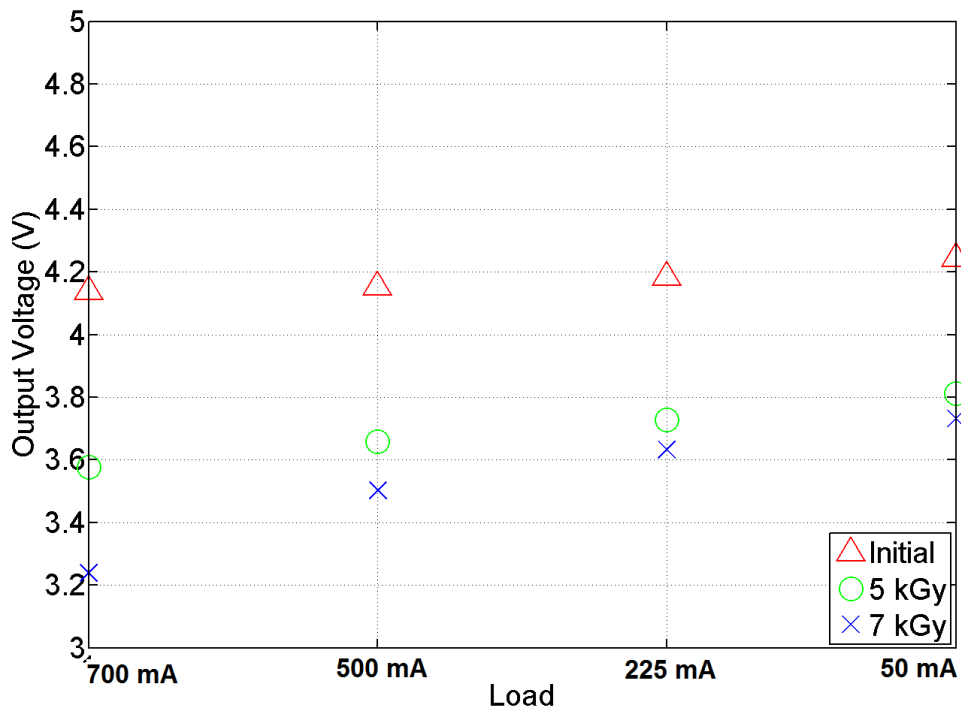


Figure 4.7: Degradation of a grounded Fairchild KA7805 COTS voltage regulator before and after irradiation with a TID of 10 kGy(Si).

The change in output voltage is similar to that of the variable load experiments with a drop in voltage of approximately 0.6 V for the largest load of 700 mA and 0.4 V at the smallest load of 50 mA. This follows the same patterns as the variable load test

and suggests that redundant voltage regulators cannot be placed on the board to be used when the biased voltage regulator fails.

4.3.7 Annealing

Having irradiated the Fairchild KA7805, the output voltage was monitored for the following 3 weeks to determine if an annealing took place at room temperature. Table 4.6 summarises the change in output voltage of the voltage regulator after 4 days, 1 week and 3 weeks.

Table 4.6: Output voltage of KA7805 regulator monitored for 3 weeks post-irradiation.

Load	Post-irrad.	4 days	1 week	3 weeks
700 mA	4.41 V	4.22 V	4.24 V	4.31 V
500 mA	4.43 V	4.24 V	4.27 V	4.32 V
225 mA	4.46 V	4.26 V	4.29 V	4.32 V
50 mA	4.46 V	4.35 V	4.37 V	4.41 V

It can be seen that the output voltage at all load currents exhibit an initial decrease in value in comparison to the end of the irradiation. However, they exhibit an increased output voltage after this. The initial fall in output voltage is correlated with the magnitude of load current. The biggest magnitude fall in output voltage of 0.19 V was seen for the 700 mA load and the smallest fall of 0.11 V was seen for the 50 mA load. The increase in voltage over the next 3 weeks appears to equal half of this initial drop. For example, the 700 mA load exhibits an increase of 0.09 V and the 50 mA 0.06 V. These values are approximately half the initial respective falls in output voltage.

It is unlikely that naturally occurring temperature drift of the output voltage would cause the increase and decrease in output voltage seen over the course of 3 weeks, however, the load regulation of the device could mask some of the change in output voltage.

4.3.8 Analysis of Results

After initial experiments on the radiation tolerance of COTS components it was shown that voltage references experienced an increase in output voltage with an increasing dose. However, variations in the magnitude of output voltage degradation were observed across each different voltage reference. The Fairchild LM336Z5 output voltage

increased the most at 0.1 V and the Texas Instruments LM4040DIZ5 the least at 0.03 V after a TID of 5 kGy(Si).

Naturally occurring temperature drifts in the output voltage cause a portion of the output voltage increase, however, the majority of output voltage magnitude change is due to gamma exposure. It is also likely that a voltage reference placed on a robotic platform will experience an increase in operating temperature of 10 degrees Celsius, suggesting that the gathered results are representative of a real-world deployment.

All references experienced a change in output voltage within the manufacturers' tolerances of ± 0.05 V up to a TID of 5 kGy(Si) suggesting these references are suitable for deployment in the defined nuclear decommissioning environment. However, although the change in output voltage was less than the manufacturer's tolerance, the initial output of some of the voltage references was close to the upper limit of 5 ± 0.05 V. For example, the Texas Instruments LM336Z5 pre-irradiation output voltage was 5.017 V. An increase of 0.06 V moves the output voltage to 5.077 V, outside manufacturers' tolerances.

It is suggested therefore, that voltage references are very tolerant to radiation, but an initial measurement of the starting output voltage is required in case it is near the upper limit of manufacturing tolerances as this will be increased by incident radiation taking it outside of the required output voltage range.

Monitoring of the output voltage over the course of 3 weeks post-irradiation found an initial increase of output voltage for the Fairchild LM336Z5 and Texas Instruments LM4040DIZ5 before all exhibited a decrease in output voltage. It is conceivable, room temperature anneals could be used to return the device to its initial output voltage, however, more than 3 weeks would be required and a cost analysis of storage of multiple annealing parts must be undertaken as this may not be viable. All references cost between £0.50 - £0.70, which could be considered disposable.

The Fairchild KA7805 voltage regulator experienced a drop in output voltage with the magnitude of output voltage change dependent on the load current. This fall in output voltage is likely due to the gain degradation of the output pass transistor [96]. The degradation appears consistent and therefore predictable. This could lead to the replacement of the regulator in an embedded system before degradation reaches a critical state of possible loss of embedded system.

As with the voltage references, when the output voltage is monitored over the 3 weeks after irradiation, an increase in degradation is first witnessed before a recovery. In this case, decreases in output voltage of between 0.2 V and 0.1 V are witnessed dependent on load value. After 3 weeks, half of this fall is recovered, but this is still less than post-irradiation values. This would suggest that room temperature annealing is not a viable option for these devices. A higher temperature anneal could be attempted with these devices to determine if this would encourage annealing. This was not conducted in this study as the equipment required was not available.

Due to the large degradation witnessed for the Fairchild KA7805 voltage regulator, two more linear voltage regulators were chosen to complete further analysis on this part. As variation was seen between the degradation mode of each voltage reference, it was considered necessary to determine if this was the same for COTS linear voltage regulators. Voltage regulators are an important part of a robotic platform and their degradation modes must be characterised robustly to determine correct usage in a nuclear decommissioning environment. The following section outlines the devices and experiments conducted to further understand the radiation tolerance of COTS linear voltage regulators.

4.4 Further Experimentation on COTS Linear Voltage Regulators

The additional linear voltage regulators were chosen to have the same output voltages and similar maximum current tolerance to the Fairchild KA7805. Different manufacturers were used to determine if there was a correlation in the effects of radiation across different manufacturers or if the effects were random. This section outlines the results of further radiation tolerance experimentation.

4.4.1 Device Descriptions

The components chosen were the ON Semiconductor MC7805ACTG [97] and STMicroelectronics L4941BV [98]. The TO-220-3 package was used for both devices. Both

manufacturers stated output voltage tolerances of $\pm 0.2V$ under output current conditions of 5 mA to 1 A with input voltages of 7.5 V to 20 V for the On Semiconductor regulators and 6 V to 14 V for the STMicroelectronics regulator. These regulators are similar in output voltage, tolerance and maximum current, but being manufactured by different companies may outline different degradation modes dependent on the manufacturer.

Each test circuit consisted of eight COTS voltage regulators of the same manufacturer. A protection diode was placed on the output of each package to avoid reverse polarity on the output transistor of each regulator during operation of the other regulators. Only the STMicroelectronics stated their device incorporated reverse polarity protection, therefore, this was considered a necessary precaution.

The diode was positioned within the irradiator and characterised before and after irradiation to determine the degradation characteristics of the diode. It was found there was no change in diode forward voltage, regardless of load current, during irradiation. Therefore, any change in output voltage observed was due to the voltage regulator. The diode was therefore discounted as a reason for decreasing output voltages.

The input voltage to the regulators was kept constant at +14 V to remain consistent with the previous test during irradiation and the control system was as discussed in 4.2.2.

4.4.2 Variable load experiments

ON Semiconductor MC7805

As with the Fairchild KA7805 voltage regulator, the MC7805 output voltage decreased with an increasing dose. This change in output voltage can be seen in Fig. 4.8 .

The degradation mode is similar to the Fairchild KA7805 as it also shows a decrease in output voltage, however, the change in magnitude is only 0.08 V, which is still within the manufacturers tolerance. A temperature change of 10-20 degrees Celsius would result in an approximate drift in output voltage of 0.03 to 0.06 V suggesting that much of the change in output voltage could be attributed to a change in temperature during irradiation.

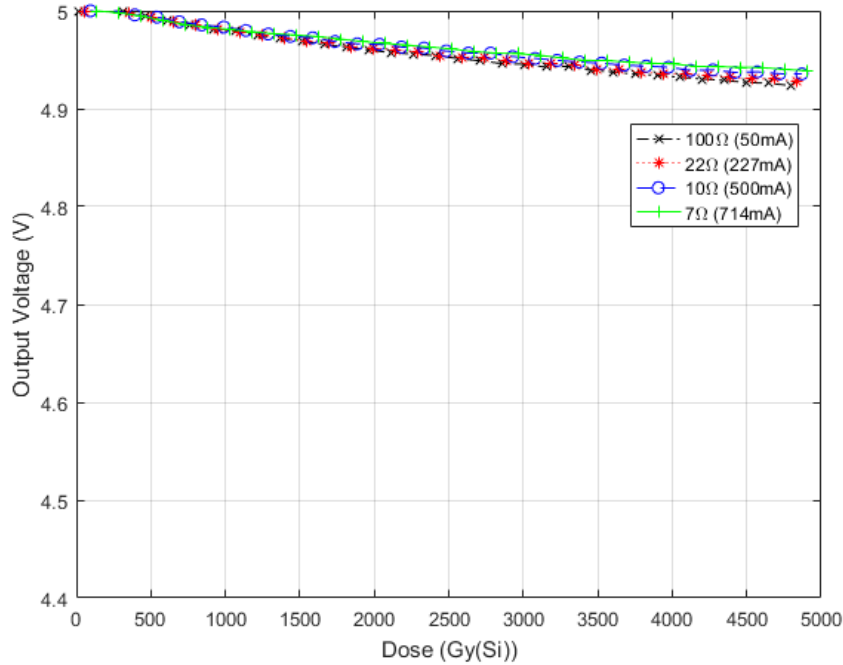


Figure 4.8: Change in output voltage of the ON Semiconductor MC7805 voltage regulator during irradiation with a TID of 5 kGy(Si).

There is a difference in degradation magnitude for each load current as can be seen by the spread in magnitude of degradation. This resulted in a difference of output voltage of approximately 0.02 V between the largest and smallest load, however, this is within the load regulation of the voltage regulator so could be caused by this inherent tolerance.

STMicroelectronics L4941BV

The degradation of the output voltage of the L4941BV up to a TID of 5 kGy(Si) can be seen in Fig. 4.9.

A large degradation of output voltage regulation was witnessed at the lowest current, however, the regulator continued to regulate within the manufacturer's tolerance of ± 0.2 V at higher currents with a degradation of approximately 0.09 V for all other loads. Unlike either the KA7805 or MC7805, a small increase of 0.02 V in output voltage up to a TID of 1 kGy(Si) was witnessed. This initial rise could be due to a temperature drift of the output voltage with the final degradation of 0.09 V outside the expected temperature drift of 0.03 to 0.06 V, implying competing mechanisms in the change of output voltage.

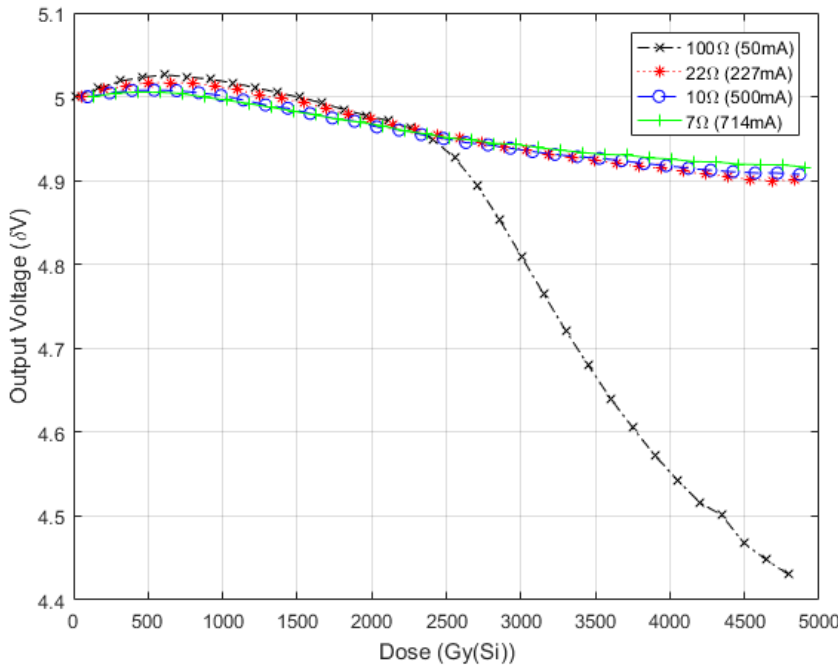


Figure 4.9: Degradation of the ST Microelectronics L4941BV voltage regulator during irradiation with a TID of 5 kGy(Si).

Other than the lowest current, this degradation mode is similar to the Fairchild KA7805 and ON Semiconductor MC7805 voltage regulators. Suggesting a decrease in output voltage with an increasing dose is common for voltage regulators. However, due to the variation in magnitude of degradation and the unexpected but repeatable nature of the STMicroelectronics L4941BV failure at low currents, the degradation mode of COTS voltage regulators can be considered inconsistent between devices, therefore, there is no way to predict when a different voltage regulator would fail.

Table 4.7 summarises the degradation of each manufacturer's COTS voltage regulator.

Table 4.7: Change in output voltage of COTS Voltage Regulators After a TID of 5 kGy(Si).

Regulators	Load Currents			
	700 mA	500 mA	225 mA	50 mA
Fairchild KA7805	-0.46 V	-0.45 V	-0.41 V	-0.40 V
ON Semiconductor MC7805	-0.08 V	-0.07 V	-0.05 V	-0.05 V
STMicroelectronics L4941BV	Failure	-0.10 V	-0.08 V	-0.08 V

4.4.3 No Load experiments

The same COTS voltage regulators were exposed to a TID while all pins were grounded as discussed in Section 4.2.2. Table 4.8 shows the drop in output voltage for a no load irradiation of the MC7805 and L4941BV regulators up to a TID of 3 kGy(Si).

Table 4.8: Change in output voltage of COTS Voltage Regulators After a TID of 3 kGy(Si)

Regulators	Load Currents			
	700 mA	500 mA	225 mA	50 mA
ON Semiconductor MC7805	-0.032 V	-0.027 V	-0.023 V	-0.021 V
STMicroelectronics L4941BV	-0.314 V	-0.071 V	-0.054 V	-0.043 V

A degradation of 0.314 V in the output voltage for the L4941BV at its greatest load was witnessed with all other values remaining within the manufacturers tolerance. This suggests that these devices are negligibly effected by a no load irradiation at low load currents whilst the degradation can still be unpredictable with large decreases in output voltage witnessed with the largest load current.

4.4.4 Anneal of voltage regulators

As with the Fairchild KA7805, the output voltage of the MC7805 and the L4941BV were monitored over a 3 week period. The change in output voltage is summarised in Table 4.9.

Table 4.9: Output voltage of MC7805 and L4941BV regulators monitored for 3 weeks post-irradiation.

Regulator	Load	Post-irrad.	4 days	1 week	3 weeks
MC7805	700 mA	4.95 V	4.76 V	4.78 V	4.80 V
	500 mA	4.95 V	4.72 V	4.73 V	4.75 V
	225 mA	4.96 V	4.66 V	4.67 V	4.68 V
	50 mA	4.92 V	4.61 V	4.62 V	4.63 V
L4941BV	700 mA	4.91 V	4.73 V	4.77 V	4.79 V
	500 mA	4.93 V	4.74 V	4.77 V	4.79 V
	225 mA	4.87 V	4.64 V	4.65 V	4.66 V
	50 mA	4.19 V	4.62 V	4.63 V	4.64 V

Both regulators see a decrease in output voltage over the first 4 days before an increase from this point onwards. However, the increase is almost negligible in comparison to the decrease in output voltage. This suggests that no annealing took place

at room temperature for the voltage regulators. An anneal at a higher temperature should be completed to determine if this would result in the regulator recovering.

4.4.5 Analysis of Results

As confirmed by previous research discussed in Chapter 2, the output voltage of the COTS voltage regulators fell with an increased dose. This was due to gain degradation of the output pass transistor.

Testing also highlighted large variations in the magnitude of device degradation observed in COTS linear voltage regulators that was dependent on the manufacturer. Furthermore, differences were seen within the same batch and test. For example, Fig. 4.10 shows the variation between the 8 individual Fairchild KA7805 voltage regulators at a load of 700 mA that were on the same test circuit and averaged together in Fig. 4.6.

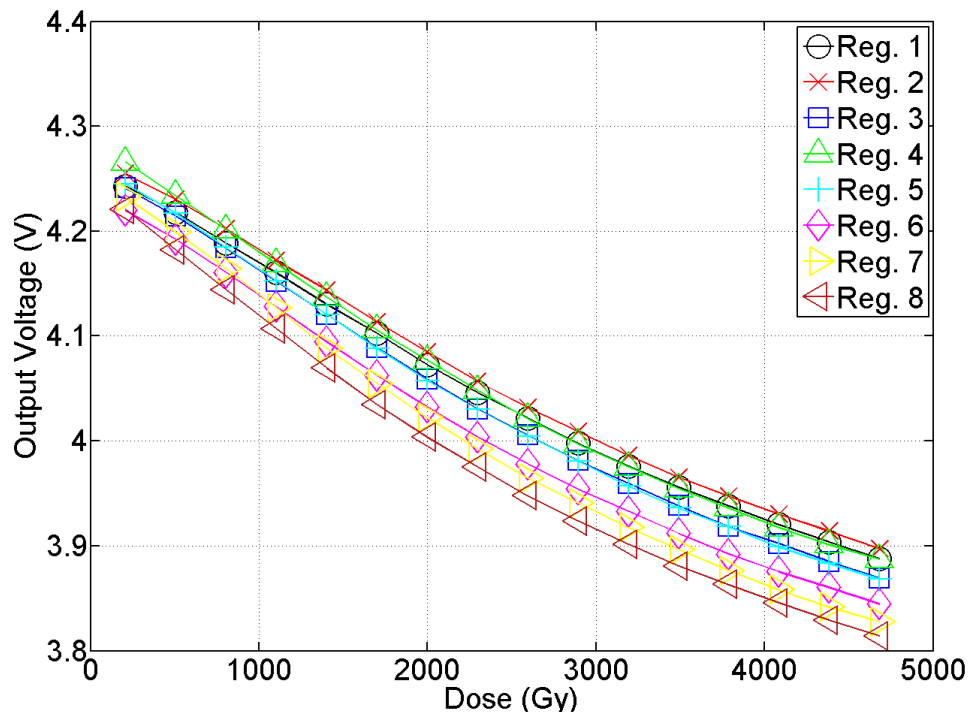


Figure 4.10: Degradation of eight separate Fairchild KA7805 COTS voltage regulators during an irradiation with TID of 5 kGy(Si). Only the 700 mA load is shown.

Before irradiation, the variation of output voltage was approximately +0.5 V, and after irradiation the variation of output voltage was approximately +0.9 V. The output voltage variation almost doubled as each regulator degraded at a different rate.

Also, a second test circuit for the Fairchild KA7805 regulator reached the same magnitude of device degradation at a TID of 3.75 kGy(Si) rather than 5 kGy(Si), with a second STMicroelectronics L4941BV test circuit showing a reduced degradation with a magnitude of -0.6 V in comparison to Fig. 4.9 showing a decrease of -0.85 V.

It was also found that the magnitude of degradation was dependent on the load current applied to the regulator. Larger currents resulted in greater degradation in all except the ST L4941BV which showed a large degradation at low load. Differences between load variation and no load results also indicated that degradation increased when there was any flow of current through the regulators.

No load tests suggested that the MC7805 and L4941BV voltage regulators were not susceptible to radiation damage, when non biased, except at the largest load current of 700 mA for the L4941BV. Unfortunately, as there was still an unexpected failure, the response of COTS voltage regulators are considered unpredictable.

Monitoring of the output voltage from the regulators for 3 weeks post-irradiation suggests that devices degrade further after irradiation. It is suggested that due to the high dose-rates used within the experiments, some of the degradation may be masked and only exhibited after a “settling” period.

The large differences observed between these regulators suggest that similar degradation characteristics may be expected to occur in other linear ICs. This means the degradation modes are likely to be inconsistent across multiple devices and hence their use in radioactive environments will be difficult to validate.

Full characterisation of any COTS component used in an embedded system is ideally required, but in the case of linear voltage regulators this appears to be extremely difficult to determine. This leads to prolonged and expensive testing periods, even though there is potential for low-cost, low-dose applications.

The inability to fully analyse the complex behaviour of linear ICs when exposed to radiation makes potential mitigation techniques difficult. Therefore, if it was possible to reduce the complexity of the device by using discrete components, a potentially more radiation tolerant component could be created that is better suited to nuclear decommissioning environments.

An alternative to a COTS voltage regulator was suggested to determine if a discrete voltage regulator could exhibit greater radiation tolerance at a greater consistency

than COTS voltage regulators. The design and experimental results are described in Section 4.5.

4.5 Discrete Voltage Regulator

Due to the inconsistent degradation of the output voltage of COTS linear voltage regulators, an alternative low-cost discrete linear voltage regulator was designed and its tolerance to radiation analysed. If radiation tolerance or degradation predictability increased, the techniques used in designing a discrete regulator could potentially be applied to other components found in embedded systems that are susceptible to the current gain degradation of transistors as a failure mode.

4.5.1 Device Descriptions

The initial design suggests an appropriate process to develop voltage regulators for specific design cases with increased radiation tolerance. Therefore, it cannot be treated as an exact replacement for the COTS voltage regulators described previously. The discrete voltage regulator device was constructed from six components. The schematic of the device can be seen in Fig. 4.11.

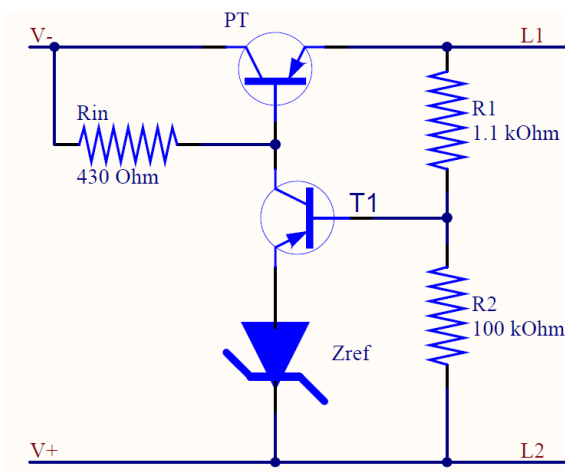


Figure 4.11: Schematic of discrete voltage regulator designed for decreased device degradation. Transistors are PNP BJTs as opposed to common NPN types.

Initial requirements of the discrete voltage regulator included outputting a voltage of +6.5 V within a 5% tolerance. This value was obtained with a +5.6 V zener

diode (which can be altered to change the necessary output voltage) and the base-emitter voltage of the 2N9306 transistor. Two PNP BJTs (chosen for their greater tolerance than NPN BJTs) controlled the output voltage. These transistors were the Multicomp 2N9306 TO-92 packaged switching transistor (T1) and a pass transistor (PT) for current flow of the required rating were the two PNP BJTs.

COTS linear voltage regulators such as the Fairchild KA7805 contain many additional components, which enable current limiting, thermal protection, short-circuit protection and more. These are required in COTS components due to the unknown final application of the device, supplying a part to end-users that could be applied to multiple products.

It is suggested, that for development of a nuclear decommissioning robotic platform, variables such as input voltage, load conditions and operating temperature would be known, therefore the addition of these extra components is not required and the base components could be specifically chosen dependent on these known conditions. This should increase the radiation tolerance of the device as there are less components that could potentially degrade and affect the operation of the device.

Three separate pass transistors were used to create three separate versions of the discrete voltage regulator whilst all other components remained the same. This was because they were found to be the most susceptible component in the circuit. They were the STMicroelectronics TIP2955, the Multicomp TIP36c, and the Multicomp BD250C. All were in the TO-247 package and PNP pass transistors with similar maximum value electrical characteristics but with variations in maximum current capacity.

They were chosen to determine the difference in degradation characteristics of transistors manufactured for varying rated currents. These are vertical structure PNP transistors, which were discussed in Chapter 2 as having greater tolerance than NPN, lateral PNP and substrate PNP transistors.

The output voltage was required to remain stable with a changing load current similar to the COTS voltage regulator's range of 0 to 1 A. Therefore, a measured load and line regulation of 0.2 V, which is similar to the output voltage tolerance of the Fairchild KA7805 regulator, was considered sufficient for use in a robotic platform.

Nine discrete voltage regulator circuits were constructed for each pass transistor and tested as described in Sections 4.6.1 and 4.2.2.

4.6 Discrete regulator Results

This section first presents the results of the variable load experiments before displaying the no load experimental results.

4.6.1 Variable load experiments Alterations

The discrete voltage regulator, shown in Fig. 4.11, was also connected to the radiation tolerant switching circuit described in Section 4.2.2, however, the magnitude of the load currents were changed as the BJTs had a greater maximum current than the linear regulators. One discrete voltage regulator was tested at a time.

The load values chosen were 80 mA, 0.7 A, 1.4 A and 2 A. The 2 A load moves the output voltage away from initial specified tolerance, however, it was considered relevant for a case where a constant load is known in a design, such as powering headlights on a moderately sized ROV. Therefore, the characterisation of degradation modes for this load current was undertaken. These are larger than for the COTS voltage regulators due to the greater maximum tolerance of the discrete voltage regulator whilst also covering a similar range of loads that the COTS regulators were subjected to.

TIP2955 Discrete Voltage Regulator

An initial TID test of 10 kGy(Si) was completed on the TIP2955 discrete voltage regulator after an initial pause in irradiation highlighted an unexpected temperature dependency, with a subsequent purposeful stoppage conducted to determine if a repeated effect was witnessed. The load current was turned off during each stoppage. Fig. 4.12 shows the result of this experiment.

The output voltage of the discrete voltage regulator remained unchanged throughout irradiation with a load current below 1.4 A. However, in the case of the largest load current of 2.0 A, an initial fall in output voltage of approximately 2.25 V was observed before settling at a constant output voltage. Two sudden drops in output voltage followed by immediate recoveries were observed after each break in irradiation.

The changes in circuit conditions during the interruptions were the circuit temperature and current draw. Current flowing through the regulator caused an increase in

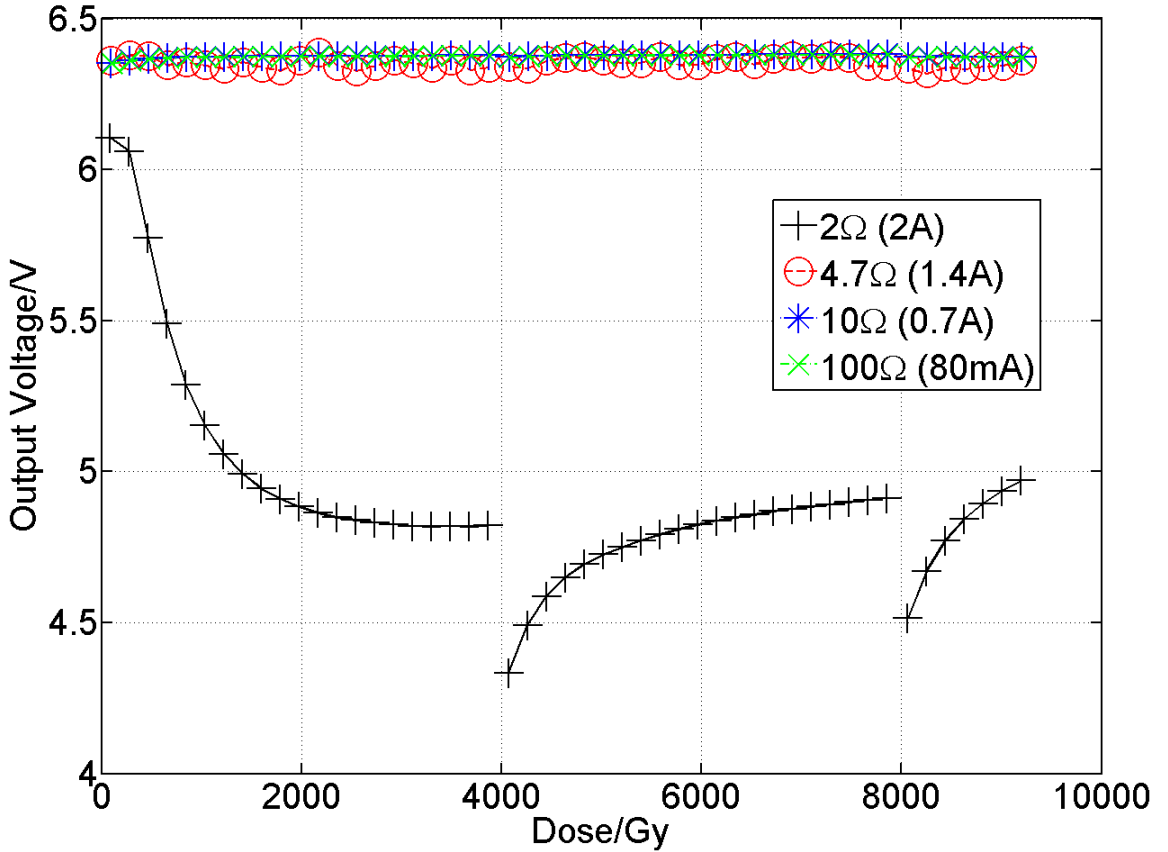


Figure 4.12: Degradation of TIP2955 discrete voltage regulator during an irradiation with a TID of 10 kGy(Si) and 5 minute no load interruptions at 4 kGy(Si) and 8 kGy(Si).

circuit temperature due to the increased power output as heat. During the interruption in irradiation, the temperature of the package decreased to room temperature. On restart, with the 2.0 A load drawn, an increase in output voltage was witnessed. This suggests that operating the discrete voltage regulator at an increased temperature could enable the degradation of the output voltage to be minimised. Further tests to validate this hypothesis will be discussed in Section 4.7.

TIP36C Discrete Voltage Regulator

Having decided to determine the temperature dependency of the 2.0 A condition in Section 4.7, the TIP36C discrete voltage regulator was exposed to a continuous dose of 5 kGy(Si), representative of a year's dose in the Sellafield legacy ponds, as seen in Fig. 4.13. There was no observable degradation at currents below 1.4 A with an initial increase in output voltage for the highest current before saturation of the output voltage after 3 kGy(Si).

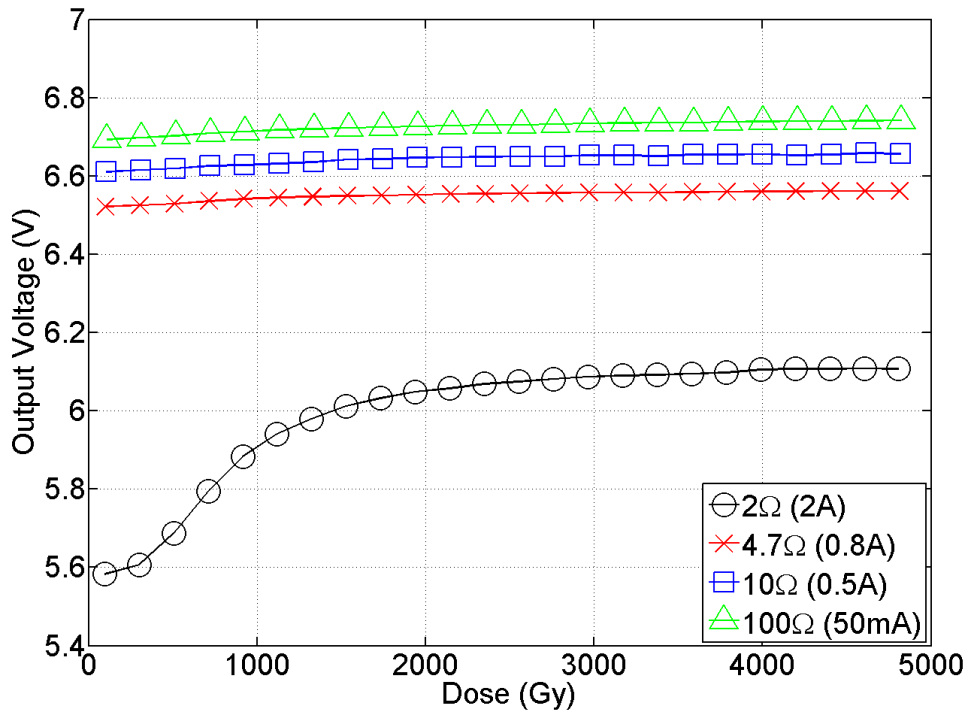


Figure 4.13: Degradation of TIP36C discrete voltage regulator during an irradiation with a TID of 5 kGy(Si).

BD250C Discrete Voltage Regulator

The BD250C discrete voltage regulator was also exposed to a TID of 5 kGy(Si) with the results shown in Fig. 4.14. As with the TIP36C discrete voltage regulator, there was no observable decrease in output voltage for currents below 1.4 A, but there was an initial increase in output for the largest load, before saturation of the output voltage after 2 kGy(Si).

4.6.2 No load experiments

As with the COTS voltage regulators, multiple samples of the discrete linear voltage regulators were exposed to a TID of 5 kGy(Si) whilst all the pins were grounded. The output voltage of the regulator was measured before irradiation at all four current loads discussed in section 4.6.1 and after the irradiation with the same test conditions.

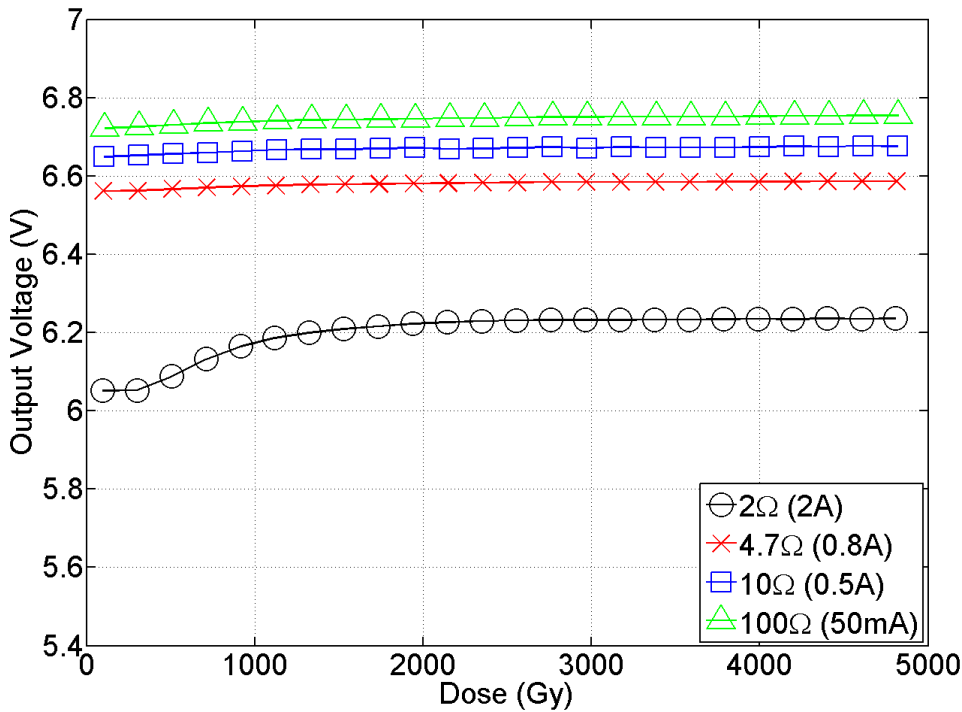


Figure 4.14: Degradation of BD250C discrete voltage regulator during an irradiation with a TID of 5 kGy(Si).

TIP2955

Fig. 4.15 indicates a large degradation of the device occurred for the largest load (2.0 A). Smaller currents are not included, as they showed a similar degradation pattern, but with a much smaller magnitude.

This figure also highlights an increase in output voltage during the experiment. As the discrete voltage regulator was connected to the 2 A load, the output voltage increased with time. This was true of all discrete voltage regulators measured after a no load irradiation.

Before irradiation, this represents an increase in the current gain of the main pass transistor due to the increase in junction temperature caused by the large load current. A constant junction temperature, therefore constant output voltage, was achieved after approximately 100 s.

Following irradiation, a greater increase in output voltage over the same time period is observed suggesting that the effect seen is not purely an increase in gain due to junction temperature, but an annealing effect. This was true of all discrete voltage regulators measured after a no load irradiation.

This increase with time exhibits, on a small scale, the possibility of self-annealing.

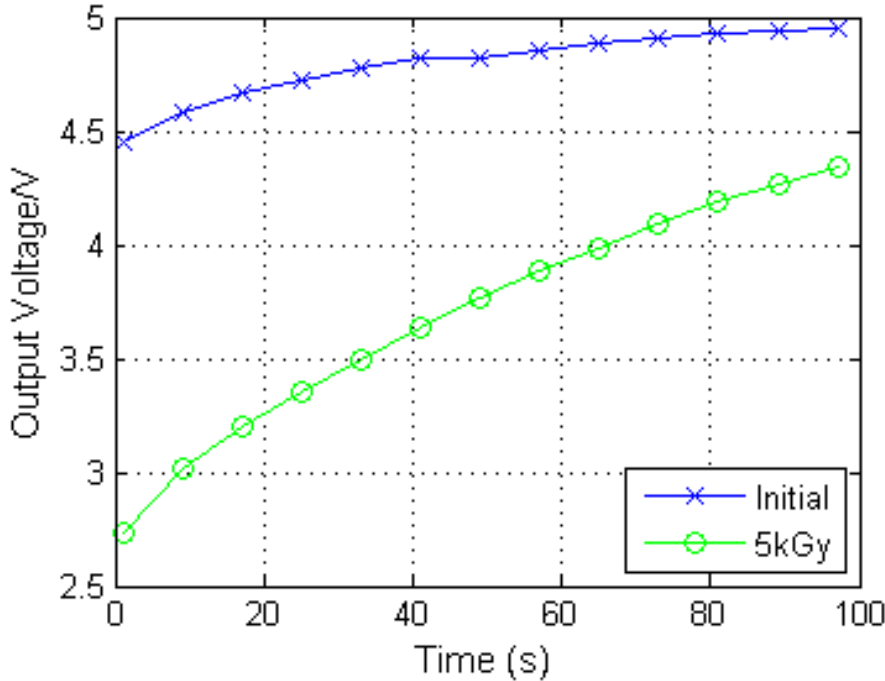


Figure 4.15: Degradation of a no load TIP2955 discrete voltage regulator before and after an irradiation with a TID of 5 kGy(Si). Only the 2 A load is shown as all other currents show lesser or minimal degradation.

This self-annealing effect was explored in greater detail during further irradiation experiments and is discussed in Section 4.7.

TIP36C and BD250C Discrete Voltage Regulators

Table 4.10 adds the no load experimental results for the BD250C and TIP36C to compare with the TIP2955 up to a TID of 5 kGy(Si).

Table 4.10: Change in Output Voltage of Discrete Voltage Regulators After a TID of 5 kGy(Si).

Discrete BJT	2 A	1.4 A	0.7 A	0.080 A
TIP2955	-1.765 V	-0.114 V	-0.084 V	negligible
BD250C	-1.440 V	-0.125 V	-0.040 V	negligible
TIP36C	-1.141 V	-0.079 V	-0.017 V	-0.031 V

As with the variable load experiments, there are decreases in output voltage of up to 1.765 V for the greatest load current of 2 A, but smaller decreases in output voltage for current draws below 1.4 A, with a maximum degradation of 0.125 V. The magnitude of change is also greater than the load variation experiments suggesting that these devices are more susceptible, especially at high currents, to a no load irradiation.

4.6.3 Analysis of Results

Initial testing of the discrete voltage regulators showed radiation tolerance up to a TID of 5 kGy(Si) at currents below 1.4 A with negligible output voltage degradation observed. A current of 1.4 A is larger than the 1.0 A rated COTS voltage regulators discussed in this study and therefore this negligible degradation occurs over a comparable current load.

The load regulation that was observed for the discrete circuits, although a larger range than the COTS regulators, are within the manufacturers' output voltage tolerances of the COTS devices. Therefore, with no device degradation of the output voltage for the discrete voltage regulator, it will operate within the output voltage tolerance of the COTS regulators. The load regulation of the discrete voltage regulator was obtained over the same range as noted in the datasheets of the COTS linear voltage regulators, however, in a bespoke robotic platform, the range of input voltages and output currents will be known with less variation, meaning the load regulation over that range will be reduced.

When connected to the largest load current of 2.0 A, the output voltage exhibited the largest degradation of up to 1.765 V, which suggests there may be a threshold load current at which degradation occurs between 1.4 A and 2.0 A. A temperature dependency was also witnessed, during an initial irradiation, resulting in falls of output voltage when the irradiation was interrupted, with an immediate increase in output voltage following restart of the irradiation, as shown in Fig. 4.12. An initial increase in output voltage in Fig. 4.13 and Fig. 4.14 for large currents until saturation of the output voltage, also suggests temperature dependencies.

An initial fall in output voltage of the device that then saturates to a constant suggests that pre-deployment irradiation of the component is possible. This would enable currents above 1.4 A to be available if this device is deployed in an embedded system.

Many of the discrete voltage regulator irradiations also highlight an initial degradation response up to 1 kGy(Si) that then reduces in magnitude or saturates. This would suggest that it is possible to pre-expose some technologies, prior to deployment, to reduce degradation during operation. For example, the proposed discrete voltage regulator shows degradation of the output voltage up to 1 kGy(Si) as a reduction

(TIP2955) or increase (TIP36C and BD250C) of the output voltage to a saturation level and then remains consistent during further irradiation. Further analysis of this effect could be performed in the future.

The proposed discrete voltage regulator is not without its limitations. For example, the current footprint of the discrete voltage regulator is 4 times that of the COTS voltage regulator. However, size was not something that was considered in this work and it is anticipated that the size and power requirements to introduce a temperature controlled block could be reduced if necessary.

Based on these observations, a controlled temperature irradiation was conducted to distinguish the degradation effects of current size and temperature. The results are discussed in Section 4.7.

4.7 Temperature Controlled Experiments

For this work, the COTS voltage regulator that showed the greatest degradation in the earlier experiments (Fairchild KA7805) and all three of the discrete voltage regulator circuits were attached to a temperature controlled block made from aluminium, which could hold a temperature to a tolerance of $\pm 2^\circ\text{C}$.

As discussed in Chapter 2, Elevated Temperature Irradiations (ETIs) have shown maximum degradation at temperatures of up to 100°C and therefore, temperatures of 50°C , 65°C and 80°C were chosen to be well within manufacturing tolerances and highlight any ELDRS effects hidden due to the high dose-rate. The output voltages of all circuits were measured up to a TID of 5 kGy(Si).

Further load variation tests as discussed in Section 4.2.2 were conducted with this temperature controlled block, for both the COTS voltage regulators and the designed discrete voltage regulators.

4.7.1 Fairchild KA7805

The Fairchild KA7805 linear voltage regulator's output voltage degradation can be seen in Fig. 4.16.

The figure shows the KA7805 voltage regulator experienced greater total degradation of the output voltage (compared to non-temperature controlled exposure), but

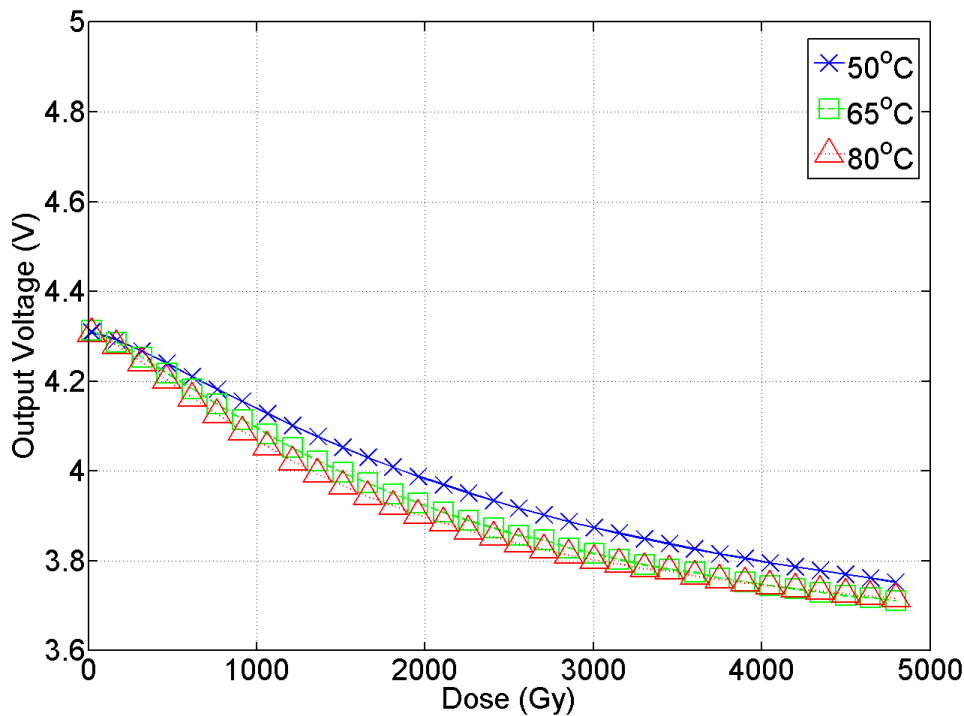


Figure 4.16: Degradation of COTS voltage regulator KA7805 at temperatures of 50°C, 65°C and 80°C.

an increase in uniformity of distribution across the different loads. Only the values for the 50 mA current (100Ω) load is shown as all other currents exhibited similar degradation effects.

4.7.2 Discrete regulators

Figures 4.17-4.19 show that all the discrete voltage regulators experienced an increase in output voltage after an initial drop in output with an increase in temperature.

An increase in temperature from 50 to 80°C reduced device degradation by approximately 0.9 V for the TIP2955, 1 V for the TIP36C regulators and 0.4 V for the BD250C regulator. This suggests there is an annealing effect for the discrete device that is controllable with circuit operating temperature.

This annealing effect returned the output voltage of the TIP36C to within the desired tolerance of the starting output of the circuit suggesting the annealing effect could be used in-situ for self-repair to a fully functional state. Only the largest load of 2 A is shown as there was minimal to negligible device degradation for lower currents during irradiation.

The possibility of annealing a device during operation was explored in further

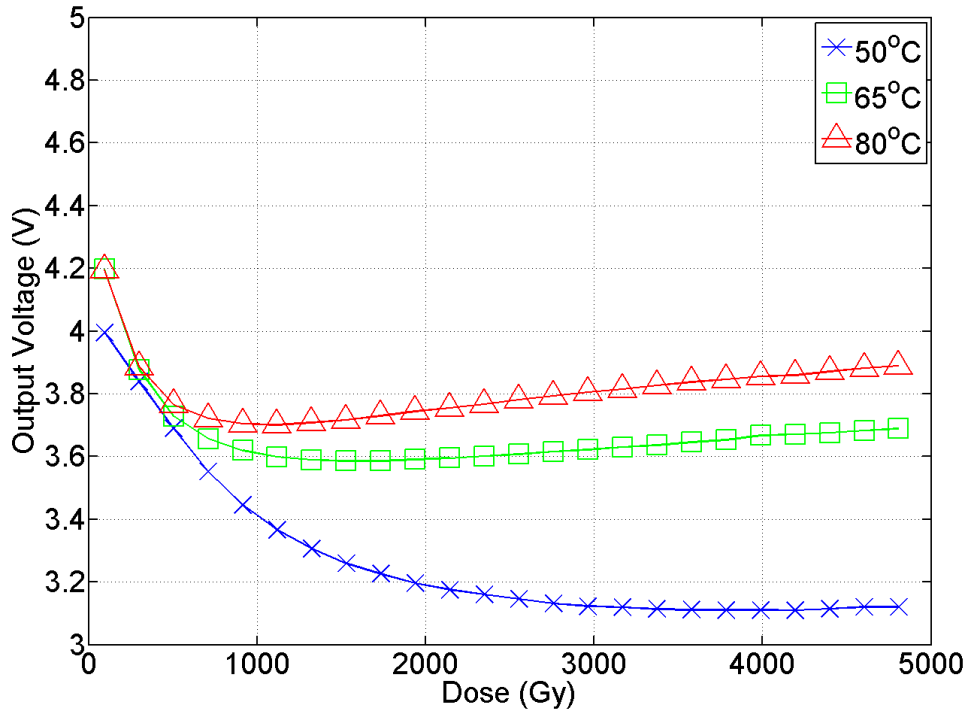


Figure 4.17: Degradation of TIP2955 discrete voltage regulator during an irradiation with a TID of 5 kGy(Si) at temperatures of 50°C, 65°C and 80°C.

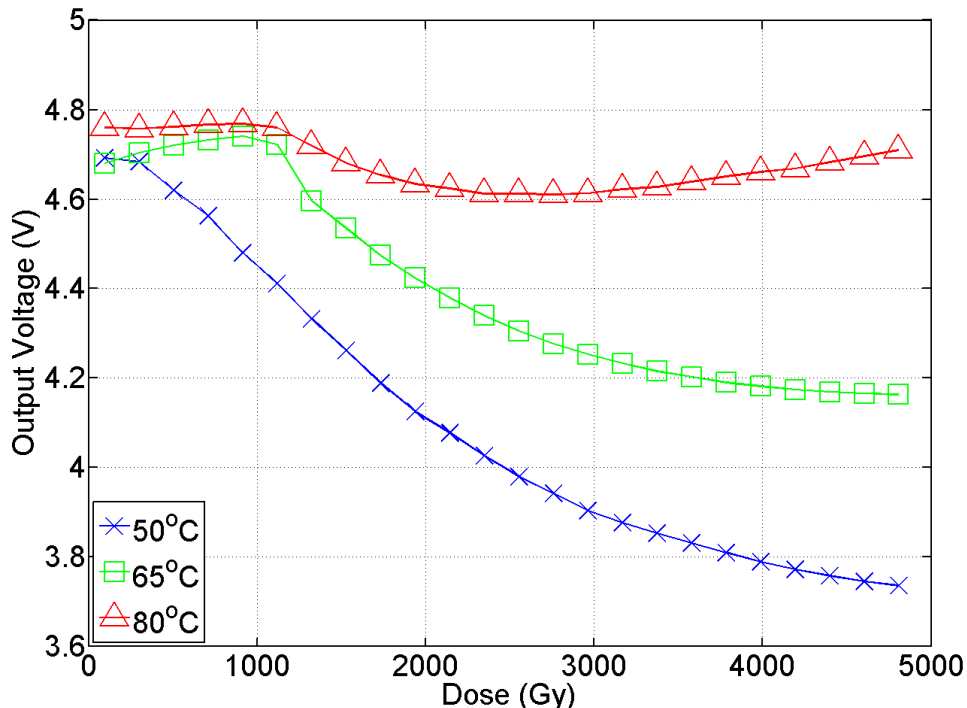


Figure 4.18: Degradation of TIP36C discrete voltage regulator during an irradiation with a TID of 5 kGy(Si) at temperatures of 50°C, 65°C and 80°C.

irradiations to determine if the device could be left to degrade, then recover and so on. The results are displayed in Section 4.8.

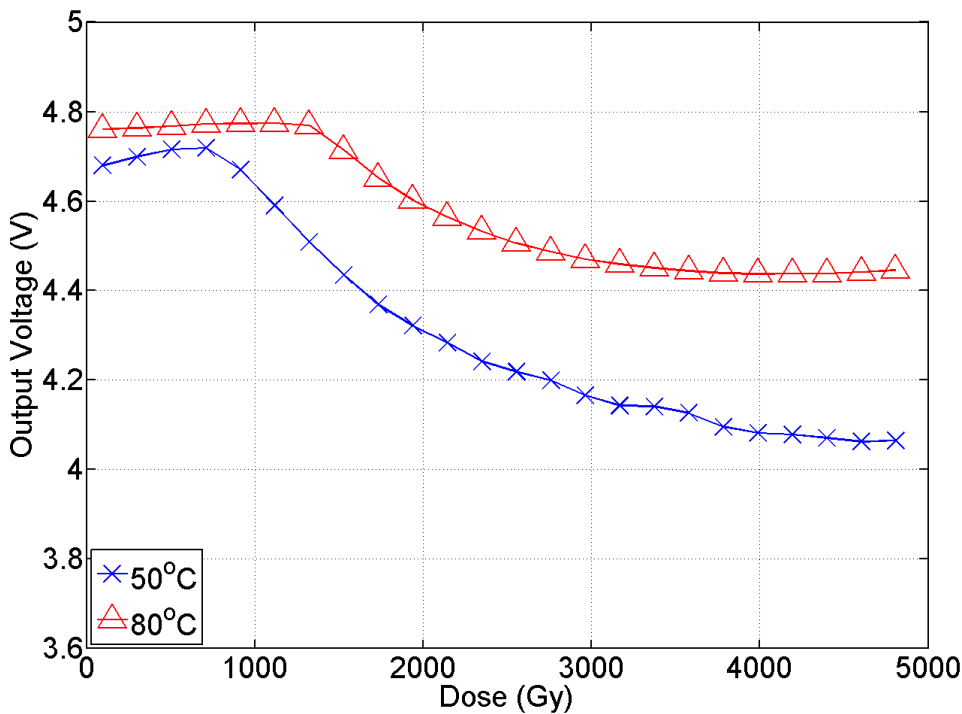


Figure 4.19: Degradation of BD250C discrete voltage regulator during an irradiation with a TID of 5 kGy(Si) at temperatures of 50°C and 80°C.

4.8 Interrupted Irradiation Thermal Anneal

For these experiments, a discrete voltage regulator of each pass transistor type, was placed in the irradiator and allowed to degrade for 25 mins at a dose-rate of 140 Gy(Si).min⁻¹, equivalent to a TID of approximately 3.5 kGy(Si). Then the irradiation was altered whilst the temperature of the circuit was raised to 80°C, for 10 minutes, before continuing the irradiation for a further 10 minutes, up to a total TID of 5 kGy(Si). Due to time constraints, the timings of each segment could not be increased.

Figures 4.20-4.22 show the change in output voltage of the TIP2955, TIP36C and BD250C respectively.

Fig. 4.20 shows the TIP2955 discrete regulator output voltage degrading to saturation with a drop of 0.8 V, similar to non-temperature controlled experiments. The sudden jump witnessed just before a TID of 3.5 kGy(Si) exhibits the annealing effect of increasing the temperature to 80°C for 10 minutes before restarting the irradiator. An increase in output voltage of 0.3 V suggests that annealing takes place, but it does not return the output voltage to pre-irradiation levels.

Fig. 4.21 outlines the interrupted thermal anneal for the TIP36C discrete voltage

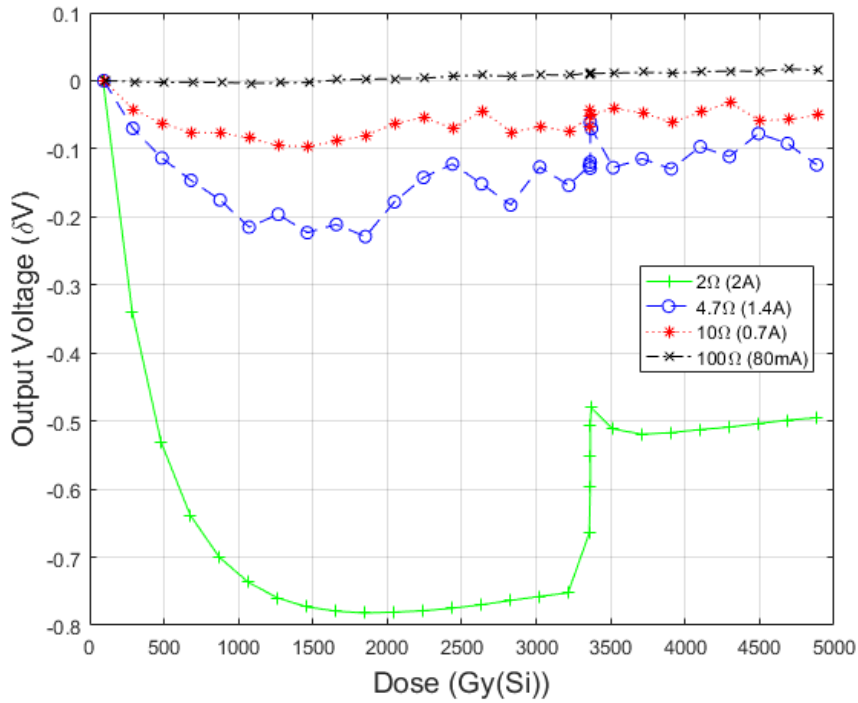


Figure 4.20: Interrupted irradiation with thermal anneal for the TIP2955 discrete voltage regulator.

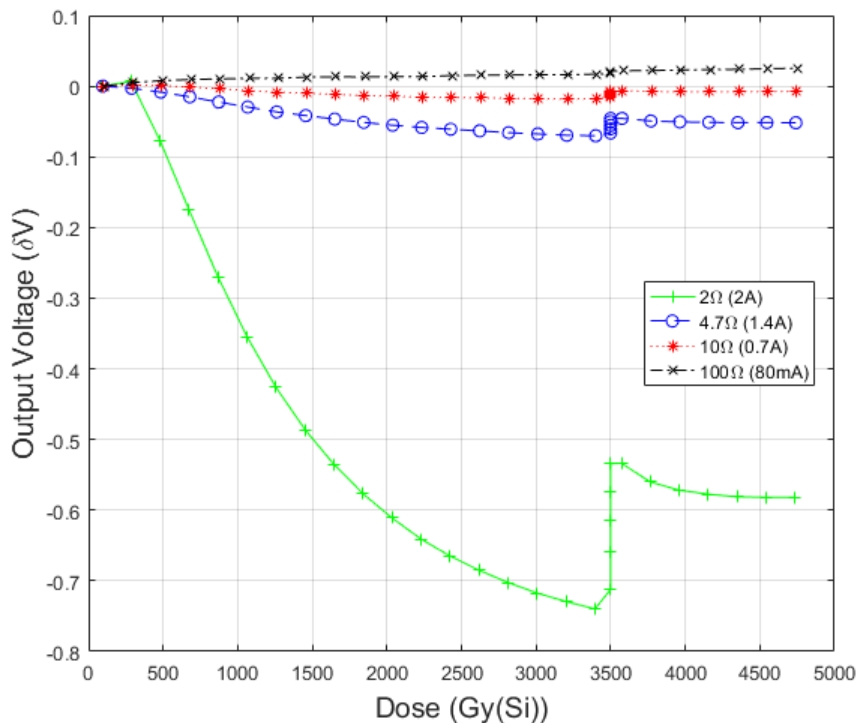


Figure 4.21: Interrupted irradiation with thermal anneal for the TIP36C discrete voltage regulator.

regulator. As with the TIP2955, a degradation in output voltage of approximately 0.8 V is allowed before the irradiation is stopped and temperature raised. It can be seen that the output voltage recovered approximately 0.26 V within this time before degrading after the irradiator was restarted.

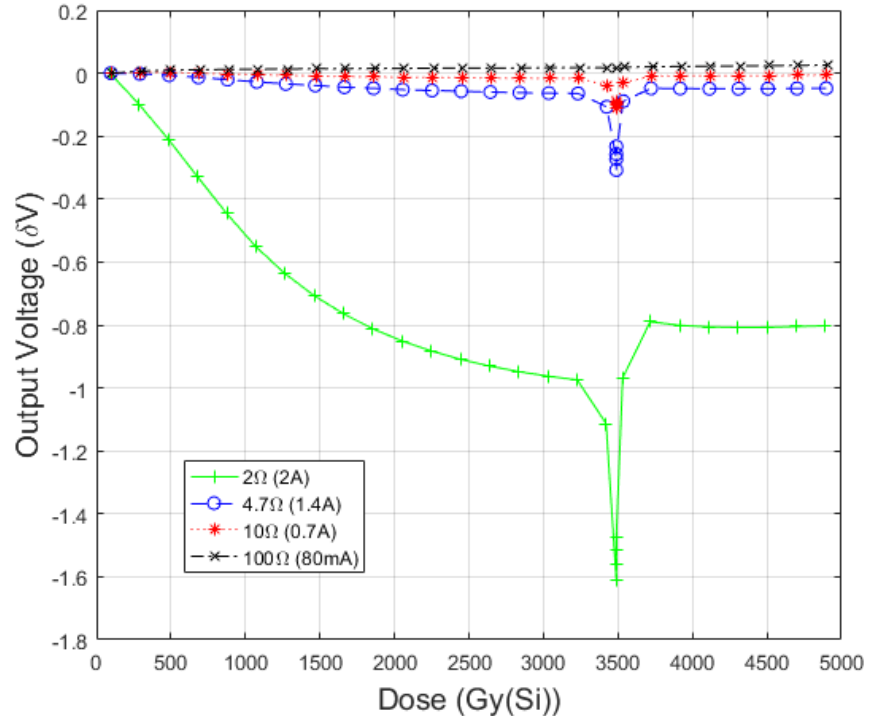


Figure 4.22: Interrupted irradiation with thermal anneal for the BD250C discrete voltage regulator.

Fig. 4.22 shows the output voltage degradation during the interrupted thermal anneal experiment of the BD250C discrete regulator. In this instance, after an initial degradation, further degradation is witnessed when the irradiator was turned off before a recovery is witnessed with thermal annealing. It was thought this drop may have been caused by an unforeseen pause before thermal annealing was begun.

4.8.1 Results Analysis

It can be seen in all the results that there is a temperature dependency on output voltage degradation magnitude. It appears that some control of the degradation can be achieved with the aid of a temperature controlled circuit to encourage annealing, as can be seen through spikes in the output voltage after the temperature is applied. Due

to time constraints, it is impossible to be sure if annealing would recover the device to its initial operating voltage.

If it is possible to temperature anneal these devices, then in-situ recovery can be conducted via the deployment of an artificial load placed on their output to encourage a rise in junction temperature. Performed at intervals throughout an operational year, this could allow the robotic platform to remain active throughout required missions.

4.9 Conclusions

COTS components used within robotic platforms are varied. This work has attempted to understand the radiation response of multiple voltage references, linear voltage regulators and a bespoke discrete linear voltage regulator design.

All voltage references showed an increase in output voltage, although there were differences in the magnitude of change dependent on manufacturer. This inconsistency suggests that any COTS voltage reference requires irradiation testing before incorporation into an embedded system design, even though these results suggest the effects of a high dose-rate environment are tolerable across multiple different references.

The degradation of the Fairchild KA7805 regulator highlighted a vulnerability in the power management system of an embedded system due to a large decrease in output voltage. This encouraged testing of a further two voltage regulators which showed varied degradation modes to gamma exposure.

This led to the development of a low-cost discrete voltage regulator, which was designed and tested. The design exhibited reduced degradation at a load level below 1.4 A across all devices with varied degradation magnitudes above this load. This offers a potential solution for use at room temperature in low load systems. In such systems, the output voltage can be altered with the size of the Zener diode allowing relatively straight forward adaptability dependent on each circuit's requirements.

The experimental results showed a strong correlation between discrete regulator output voltage at a load of 2.0 A and the temperature at which the device was operated. An annealing effect was observed for the discrete voltage regulators drawing a current of 2.0 A that enabled the devices to recover between 0.20 and 0.25 V of the output voltage degradation. In certain circumstances, this may extend component operational

life-time.

The temperature was also controlled for the COTS voltage regulators. The magnitude of output voltage degradation increased with an increased temperature. This suggested that the elevated temperature, as discussed in Chapter 2, increased the degradation of the linear IC, highlighting ELDRS effects. This could be due to the complex circuit behaviour of the linear IC as well as the different technology used to manufacture transistors in ICs (i.e. lateral PNP transistors), which have been shown to be more sensitive to radiation [99]. Whereas the discrete voltage regulator exhibited either the absence of ELDRS effects or an increase in annealing effects at the elevated temperature.

Having discovered the temperature dependency of the discrete voltage regulators, an attempt to control the annealing effect was completed with results suggesting that annealing of the largest load output voltage is possible but it could not be confirmed if complete recovery is possible.

It is suggested that the power regulation circuitry of a robotic system in a nuclear decommissioning environment will always draw current. Controlling the temperature of the device using an appropriate temperature controlled block/heat-sink has the potential to allow annealing during operation and hence reduced radiation damage. Alternatively, by switching in an additional load, the temperature could be controlled to anneal the device once a pre-determined threshold on output voltage was reached. Such a solution would be more applicable for low dose-rate environments. Mechanical degradation due to increased temperature still needs to be explored, however, the temperatures discussed are within manufacturers tolerances and should therefore have minimal effect on the capabilities of the devices.

It is possible that the approach of simplifying circuits using individual radiation tolerant discrete components could be applied to a large range of components, such as motor drivers. However, work is required to experimentally validate this hypothesis. This would offer the potential for a new approach to developing electronic systems with greater tolerance to radiation for use in embedded systems in decommissioning environments that is viable and affordable.

It is hoped that this work will lead to new possibilities for designing embedded systems with increased tolerance to radiation that can be used with greater reliability

in the nuclear decommissioning industry, avoiding common mode failure mechanisms due to the parallel connections between regulators and multiple devices.

4.10 Initial results on COTS microcontroller radiation tolerance

One of the most important components of a robotic device is its microcontroller(s). If this fails then the robotic device could become unpredictable or uncontrollable. Therefore, an initial study of the radiation tolerance of the flash memory of the Microchip PIC18F4520 was undertaken. This microcontroller was chosen for its similarities to many controllers used within embedded systems and robotic platforms. The flash memory was chosen as a starting point to determine the degradation mode of microcontroller memory as the robotic platform's control software would be placed here.

4.10.1 Microcontroller testing

The flash memory was filled with a “0101010...” pattern and read before and after an irradiation. This pattern was used to determine if neighbouring bits experienced alternate degradation modes or if they were independent of each other with changes of memory in only one direction, for example, only 0’s to 1’s rather than 1’s to 0’s. The pattern is represented by the hexadecimal “AAAA” in the Opcode column as seen on the left of Fig. 4.23.

A total of eight microcontrollers were exposed to TIDs ranging from 300 Gy(Si) to 1500 Gy(Si). A sudden degradation was observed at 1.2 kGy(Si), with the memory read back from the flash memory shown on the right of Fig. 4.23.

Before this TID, no degradation of the memory was observed with the ability to return and program the correct values into the PIC18F4520 flash memory. After a TID of 1.2 kGy(Si), the microcontroller was unable to return the correct values or be re-programmed. An all ‘1111...’ pattern returned or ‘FFFF...’ in hexadecimal.

If the bits in the flash memory of a robot flipped during deployment, the device

Line	Address	Opcode	Disassembly	Line	Address	Opcode	Disassembly
1	0000	AAAA	BTFSS 0xfaa, 0x5, ACCESS	1	0000	FFFF	GOTO 0x1ffffe
2	0002	AAAA	BTFSS 0xfaa, 0x5, ACCESS	2	0002	FFFF	NOP
3	0004	AAAA	BTFSS 0xfaa, 0x5, ACCESS	3	0004	FBEF	NOP
4	0006	AAAA	BTFSS 0xfaa, 0x5, ACCESS	4	0006	BFFF	BTFSC 0xff, 0x7, BANKED
5	0008	AAAA	BTFSS 0xfaa, 0x5, ACCESS	5	0008	BBFF	BTFSC 0xff, 0x5, BANKED
6	000A	AAAA	BTFSS 0xfaa, 0x5, ACCESS	6	000A	FFBF	NOP
7	000C	AAAA	BTFSS 0xfaa, 0x5, ACCESS	7	000C	FFFF	NOP
8	000E	AAAA	BTFSS 0xfaa, 0x5, ACCESS	8	000E	FFEF	NOP
9	0010	AAAA	BTFSS 0xfaa, 0x5, ACCESS	9	0010	FFFFB	NOP
10	0012	AAAA	BTFSS 0xfaa, 0x5, ACCESS	10	0012	FFFF	NOP
11	0014	AAAA	BTFSS 0xfaa, 0x5, ACCESS	11	0014	EBFF	
12	0016	AAAA	BTFSS 0xfaa, 0x5, ACCESS	12	0016	BFFF	BTFSC 0xff, 0x7, BANKED
13	0018	AAAA	BTFSS 0xfaa, 0x5, ACCESS	13	0018	EAFF	
14	001A	AAAA	BTFSS 0xfaa, 0x5, ACCESS	14	001A	FFFF	NOP
15	001C	AAAA	BTFSS 0xfaa, 0x5, ACCESS	15	001C	AFFF	BTFSS 0xff, 0x7, BANKED
16	001E	AAAA	BTFSS 0xfaa, 0x5, ACCESS	16	001E	FFFF	NOP
17	0020	AAAA	BTFSS 0xfaa, 0x5, ACCESS	17	0020	AFFF	BTFSS 0xff, 0x7, BANKED
18	0022	AAAA	BTFSS 0xfaa, 0x5, ACCESS	18	0022	FFFE	NOP
19	0024	AAAA	BTFSS 0xfaa, 0x5, ACCESS	19	0024	FFFE	NOP
20	0026	AAAA	BTFSS 0xfaa, 0x5, ACCESS	20	0026	FFFF	NOP
21	0028	AAAA	BTFSS 0xfaa, 0x5, ACCESS	21	0028	FFFE	NOP
22	002A	AAAA	BTFSS 0xfaa, 0x5, ACCESS	22	002A	AFFEF	BTFSS 0xef, 0x7, BANKED
23	002C	AAAA	BTFSS 0xfaa, 0x5, ACCESS	23	002C	EFFF	GOTO 0x1ffffe
24	002E	AAAA	BTFSS 0xfaa, 0x5, ACCESS	24	002E	FFFF	NOP
25	0030	AAAA	BTFSS 0xfaa, 0x5, ACCESS	25	0030	EFFA	GOTO 0x1ffdf4
26	0032	AAAA	BTFSS 0xfaa, 0x5, ACCESS	26	0032	BFFE	BTFSC 0xfe, 0x7, BANKED
27	0034	AAAA	BTFSS 0xfaa, 0x5, ACCESS	27	0034	FFEF	NOP
28	0036	AAAA	BTFSS 0xfaa, 0x5, ACCESS	28	0036	AFBF	BTFSS 0xbf, 0x7, BANKED
29	0038	AAAA	BTFSS 0xfaa, 0x5, ACCESS	29	0038	FBEF	NOP

Figure 4.23: The memory of the Microchip PIC18F4520 before (on the left) and after (on the right) irradiation with a TID 1.2 kGy(Si).

could become unstable with some loss of control. In a nuclear decommissioning environment this poses a contamination hazard.

Analysis of each of the other 7 test samples showed no degradation of the flash memory prior to 1.2 kGy(Si), with complete degradation after this TID.

4.10.2 Microcontroller Results analysis and conclusions

The microcontroller flash memory appears to reach a threshold of degradation that deteriorates the memory beyond repair at 1.2 kGy(Si). Before this point, the memory could be read and re-programmed correctly, but after this threshold, the memory became corrupted. This could lead to unexpected movements of a robotic platform or complete loss of control. This must be avoided in a nuclear environment to avoid contamination of the device or surrounding area and to reduce risk to workers.

A consistent threshold value for degradation suggests that it would be possible to replace the microcontroller before total failure if designed as a modular component easy to remove and replace. Further experimentation on microcontroller flash memory

was not possible during this study, however, this study suggests that it may be possible to use this specific device up to a threshold of 1.2 kGy(Si) minus a safety factor before replacement is required.

Chapter 5

Current Underground Robotic Platforms and Environment

Having discussed the effects of radiation on COTS components and attempts to mitigate the degradation, we required robotic platforms to implement these findings within a decommissioning environment. As previously discussed, an area of concern during decommissioning of the Sellafield site is the current maintenance of the legacy storage ponds and the sub-soil environment surrounding them. These ponds were constructed to be temporary but have long out-lived their initial lifetime.

The requirement for nuclear power plants to produce more power during the coal mine strikes of the 1970s/80s, meant that improper procedures were followed [100]. Waste was placed inside the pond without proper inventories and slow re-processing has meant that the ponds were required for longer.

Many of the storage facilities are now 60-70 years old. They are concrete lined and there is a danger that leaks have formed in the concrete lining, allowing radioactive substances to escape. They can then travel further throughout the environment.

Currently, boreholes are used to monitor the ground for radioactive leaks and their propagation through the soil. They are dug at intervals throughout the site and periodically visited with sensing units, which are lowered into the borehole. The measurements taken are compared with a neighbouring borehole to develop an idea of the flow of radioactive material. It is, however, possible to miss radioactive isotopes between boreholes. It also requires further excavations for exploration of a new area. This is time intensive and costly.

Radioisotopes likely to be found in the ground after leakage from the storage ponds include tritium (^3H), Strontium-90 (^{90}Sr), Technetium-99 (^{99}Tc) and Caesium-137 (^{137}Ce) [101]. The highest annual measured activity of beta-emitting radionuclides from boreholes on site was 111.5 kBq.l^{-1} in 2013 [102]. This is above WHO guidelines and suggests leaks on-site.

A device capable of burrowing beneath and around the Sellafield Legacy ponds would aid in the characterisation of the sub-soil environment. It could offer in-situ readings whilst adding the capability to explore hard to reach or previously uncharacterised areas. The robotic platform would be required to burrow up to 5 m underground, withstand radiation up to a TID of 5 kGy(Si) and be able to change direction whilst underground.

This chapter outlines current research on underground burrowing robots and the geology/environment around the Sellafield legacy ponds. Challenges facing such a mechanical device and current solutions used in industry will be discussed as well as a summary highlighting deficiencies in current literature, determining the path of research to be taken in this project.

Due to time constraints inherent in the research project, progress was initially focussed on the mechanical design of the robotic platforms with integration of circuitry designed in Chapter 4 suggested for incorporation in future iterations of the embedded system.

5.1 Environment of Sellafield

This section outlines currently available information on groundwater location, top-soil ratios and bedrock characteristics of the Sellafield site. It is necessary to know the geology of the surrounding area to aid in device development.

5.1.1 Soil Composition

There is a variety of superficial deposits on top of the bedrock in and around the Sellafield work-site. They include sand, gravel, clay, silt and diamicton. Fig. 5.1 shows the location of the superficial deposits overlaid on an ordnance survey map of the area.

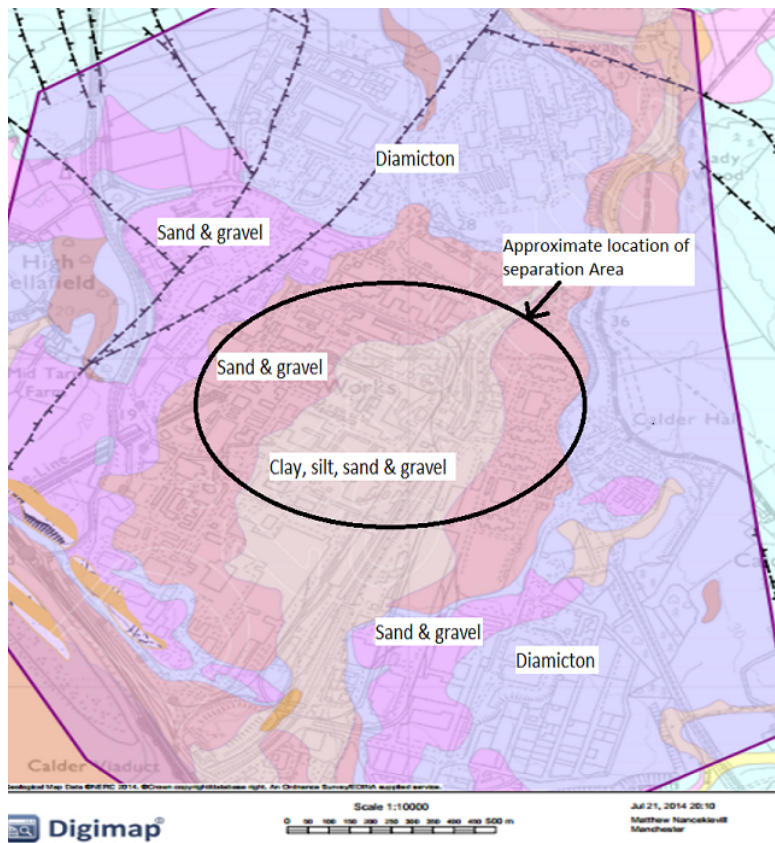


Figure 5.1: Overview of the superficial deposits on top of the bedrock at the Sellafield site

The purple outline marks the boundary of the Sellafield site. The superficial deposits within this outline rest on top of sandstone bedrock at a depth of approximately 25 m. The Sellafield legacy ponds were built on a layer of concrete that is 5 m from the surface. This means there is approximately 20 m between the bedrock and the bottom of the ponds. This can be considered the available working envelope to a device designed to burrow beneath the Legacy ponds.

Table 5.1 indicates the post glacial drifts (Quaternary drift) that comprise the natural ground up to a maximum thickness of 60 m (dependent on altitude) beneath the Separation Area [103]. Made ground represents a man-made area of land where an artificial fill has been used to reclaim areas of marshes, lakes or shorelines.

Understanding the location of each type of soil and the approximate ratio of one type to another will allow for targeted development and also deployment. If one soil type is easier to burrow through than the others, initial deployment could occur there.

Table 5.1: Subdivision of the Quaternary Drift in the Sellafield Buried Channel [103]

Geological Unit	Elevation (m)	Lithology
Q1	Base of Made Ground to +10 m	Predominantly sands and gravels, 20% silt and clay. Clays and silts thin (<5 m) and persistent over tens of metres
Q2	+10 m to -5 m	Predominantly sands and gravel; 30% silt and clay. Clays and silts thicker (<15 m) and persistent up to 100 m
Q3	-5 m to top of sand-stone bedrock	Reduced proportion of silt and clay. Silt and clay absent below -16 m

5.1.2 Radioactive leak pathways

The Sellafield site consists of 3 km² of industrial buildings set on a slight incline. The site altitude ranges from sea-level to 50 m above at its highest point. The River Calder travels through the site, with the site mostly surrounded by farmland [104]. This has created natural paths for radiation leaks to leave the site and contaminate the surrounding area. Fig. 5.2 outlines the contoured environment, and therefore, an overview of the radiation leak paths.

Fig. 5.3 outlines the groundwater movement on-site and the paths that radioactive leaks could take. It can be seen that, as well as a generally homogeneous groundwater level, there are elevated peaks and also buried channels that collect contaminants. A device to monitor this area would need to be able to navigate through or around groundwater as well as avoiding any utility pipes, boreholes and bedrock channels.

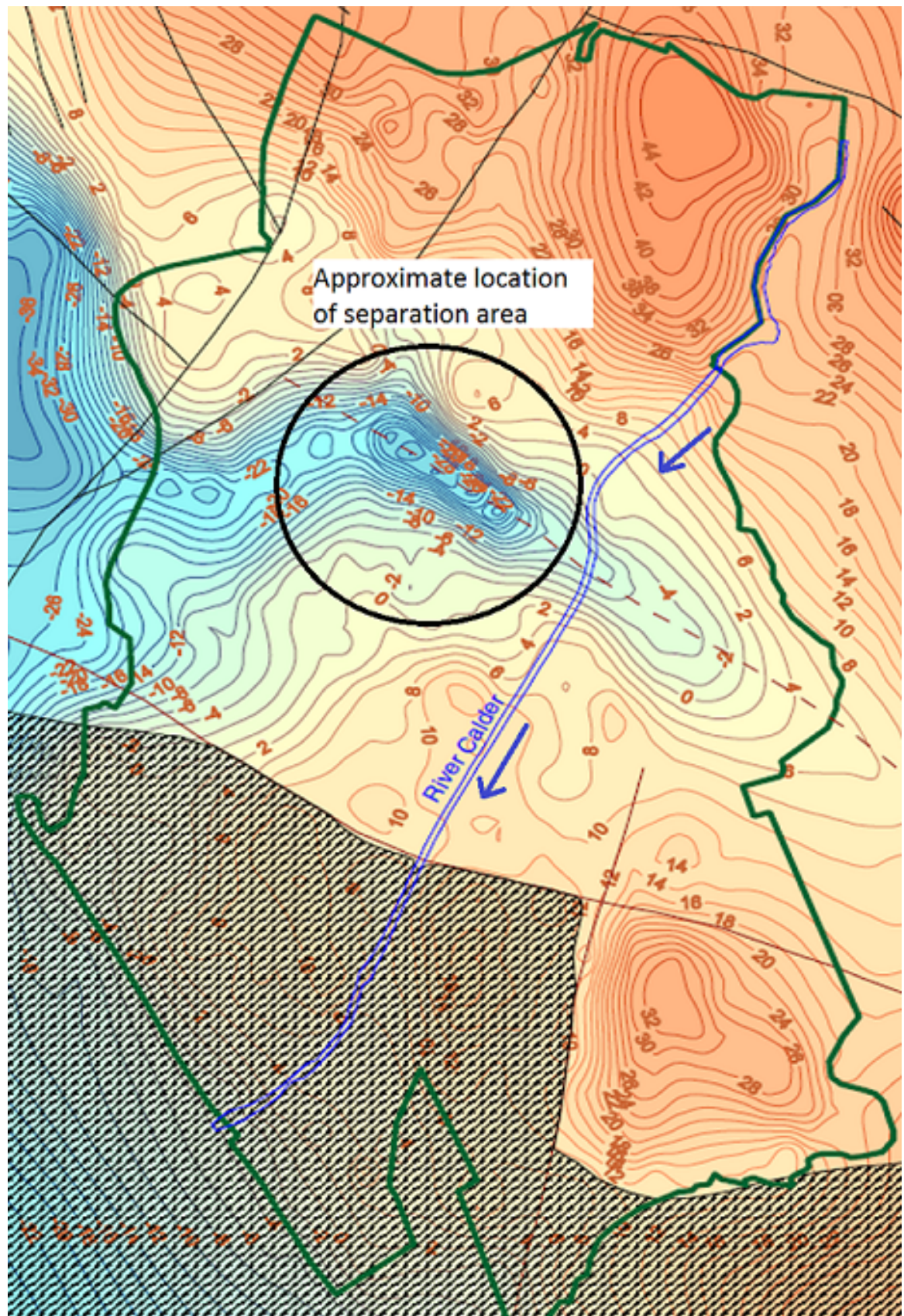


Figure 5.2: Contour map of the Sherwood Sandstone Rockhead Surface (mAOD) [104].

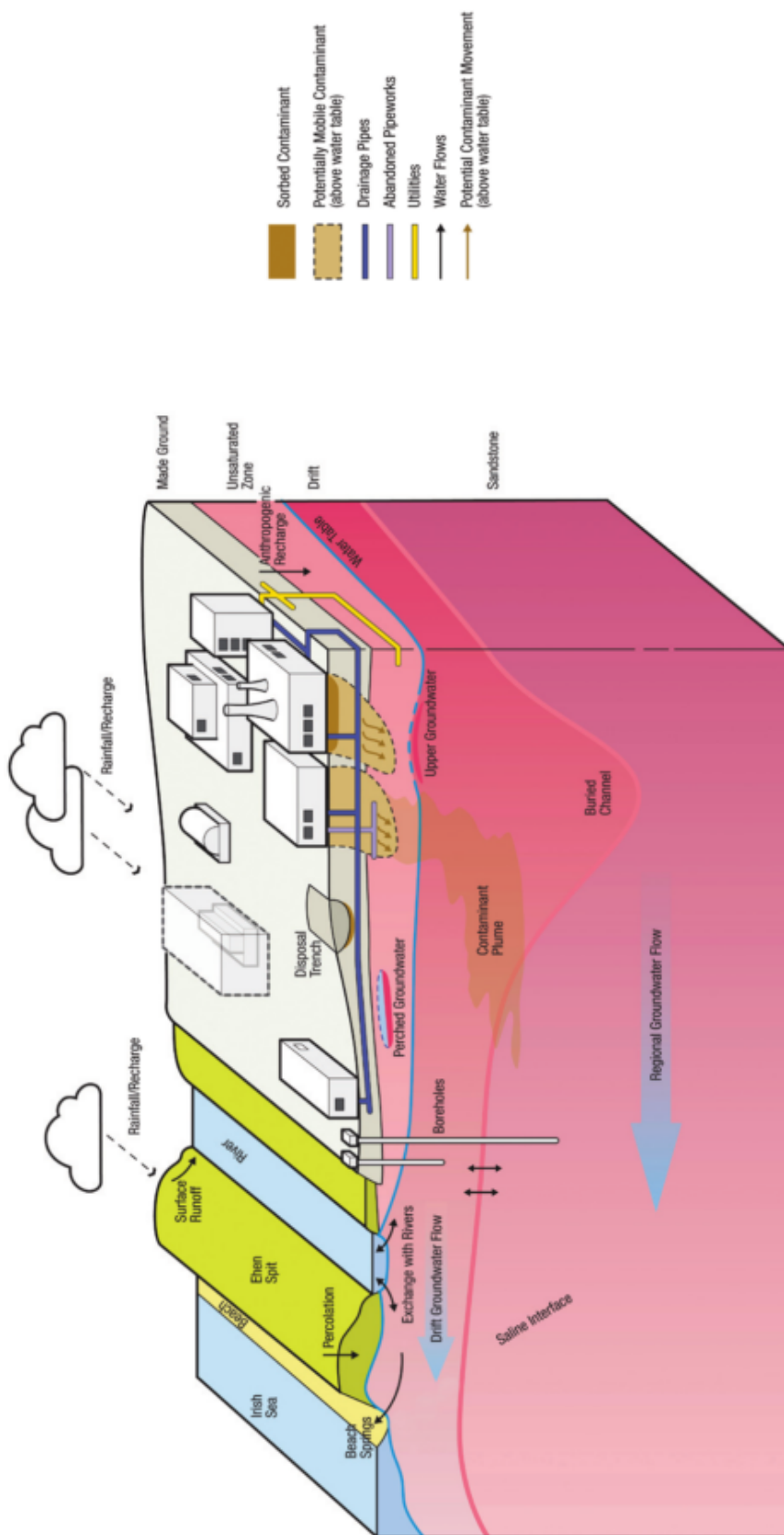


Figure 5.3: Overview of potential leaks and groundwater movement [102].

The variable geology in and surrounding the Sellafield site complicate the design and development of a robotic platform for underground characterisation.

5.1.3 Radionuclide Information

Throughout its history there have been radionuclide leaks at the Sellafield legacy site [105]. Fig. 5.4 shows the predicted radionuclides beneath the Sellafield site and their travel velocities.

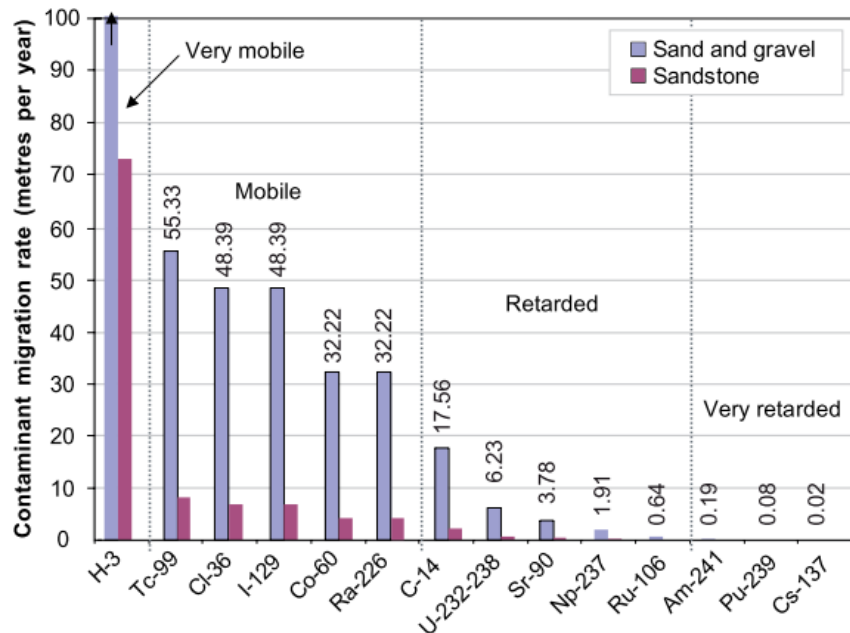


Figure 5.4: List of radionuclides found beneath the Sellafield site and their predicted travel velocities [101].

It can be seen that there are many different predicted radionuclides. Their travel velocities' away from the storage facilities and through the environment are varied in different mediums. Any device designed to monitor for radiation within the Sellafield area must be capable of detecting these radionuclides and determine their location relative to the surrounding geology.

A radionuclide such as Co⁶⁰ travels eight times quicker in sand and gravel than in sandstone. This suggests the need for a priority list in localisation and removal of radionuclides for those that move quickly away from site.

As well as travel velocity difficulties, characterisation of independent sources is not trivial. Tc⁹⁹ has a half-life of 212,000 yrs and has been observed in multiple well

samples. It is predicted that multiple Tc⁹⁹ sources are the cause of multiple readings, however, this is not certain [101].

The activity level of the detected Sr⁹⁰ has been measured at up to 111.5 kBq.l⁻¹ [102], whereas Tc⁹⁹ is a maximum of 230 Bq.l⁻¹. This compares to the World Health Organisations' guideline of 100 Bq.l⁻¹ [101]. The inability to be able to determine whether the source of a radionuclide is from multiple locations or one as well as where the sources are in relation to their leak point, outlines the requirement for a device capable of sub-soil characterisation.

Much of the information on the contamination of the Sellafield site comes from studies conducted in the last 10-15 years. Leaks or radioactive plumes that originated before this date are therefore very difficult to characterise. Recent information on the discharges from the Sellafield site in 2011 can be found [102], [106]. These reports give a good indication of the nature of radioactive activity on the Sellafield site, but due to the inherent security involved in keeping the Nuclear site safe, some information would not be released to the public and it is therefore difficult to definitively understand the conditions within the sub-soil radiation environment.

5.1.4 Dose-rates

It is difficult to estimate the radiation levels of ground contamination around the Sellafield site. Current information suggested that the surrounding marine life and agriculture does not contain radiation levels above the classified limit [106]. Therefore, exact levels of ground contamination are not known. This is a large instigator in the motivation for this project.

Figures reported [107], suggest that doses at the bottom of the Sellafield legacy ponds range from 0.05 - 1 Gy.h⁻¹, these will be used as a representation of the dose levels likely to leak into the surrounding area.

Table 5.2 shows that doses range from 1.2 Gy - 8 kGy over the course of a year. With limited access to facilities for long periods of testing, this range needs to be narrowed for investigation. To start, it is suggested to expose components to a constant exposure of 5 kGy and after analysis of the results determine if this remains a suitable TID.

Assuming the device would not be deployed 24/7 all year round, 5 kGy(Si) was used

Table 5.2: Summary of radiation dose-rates and total doses of a representative nuclear environment [107].

Time spent in environment	TID (Gy) for dose-rate of 0.05 Gy.h ⁻¹	TID (Gy) for dose-rate of 0.5 Gy.h ⁻¹	TID (Gy) for dose-rate of 1 Gy.h ⁻¹
1 day	1.2	12	24
1 week	8.4	84	168
1 month	33.6	336	672
6 months	201.6	2016	4032
1 year	403.2	4032	8064

as an upper estimate of the TID to direct the radiation levels at which characterisation of electronic components would be undertaken. If the components passed this original benchmark, they can then be tested against higher dose levels.

5.2 Underground Burrower Requirements

Having discussed the projected environment for an underground burrower, a set of requirements were created through discussions with operations staff at Sellafield and Nuclear Decommissioning Authority (NDA). This allowed a targeted approach to research and development of a prototype device. These included, but are not limited to;

1. To be able to burrow up to 5 m underground through sand.
2. Controllable via a surface base station and tether.
3. Withstand radioactive contamination up to 5 kGy(Si).
4. Low-cost, <£200.
5. Be able to change direction whilst underground.
6. Be adaptable to changeable geology.

There are currently no devices capable of meeting all of these requirements, therefore, an understanding of how current research projects could be combined into a new and improved device was necessary. Prototype manufacturing was undertaken at the University of Manchester's mechanical workshop and with University 3D printing technology.

5.3 Current Robotic Technology

Many of the current underground robotic platforms are found in tunnelling and excavation projects. Development of devices within these fields of expertise has allowed the technology to be applied to space exploration and deep underground mapping [108–110].

Each research project was mainly designed to tunnel in a straight line or excavate a site. Currently, there is little research into underground automation or monitoring techniques in a small environment. Examples of bespoke research projects attempting to achieve underground monitoring or geological sampling are presented in the following sections.

5.3.1 Regolith Advanced Surface Systems Operations Robot

RASSOR (pronounced razor) is a robot that was designed by NASA for lunar mine excavation. They were tasked with creating a robot that could mine materials on the moon whilst retaining ruggedness and combating the lack of gravitational pull that excavators on Earth receive.

The drums, as seen on the end of each arm in Fig. 5.5 rotate in opposite directions to create traction at one end to allow the other to mine. It can right itself, is “relatively” light, and can traverse most terrains [111]. However, it is unlikely this technology could burrow itself multiple metres underground or change direction whilst sub-surface.



(a) RASSOR deployed on a lunar slope



(b) Example RASSOR excavation technique

Figure 5.5: NASA’s RASSOR robot used for lunar excavation and geological sampling [111].

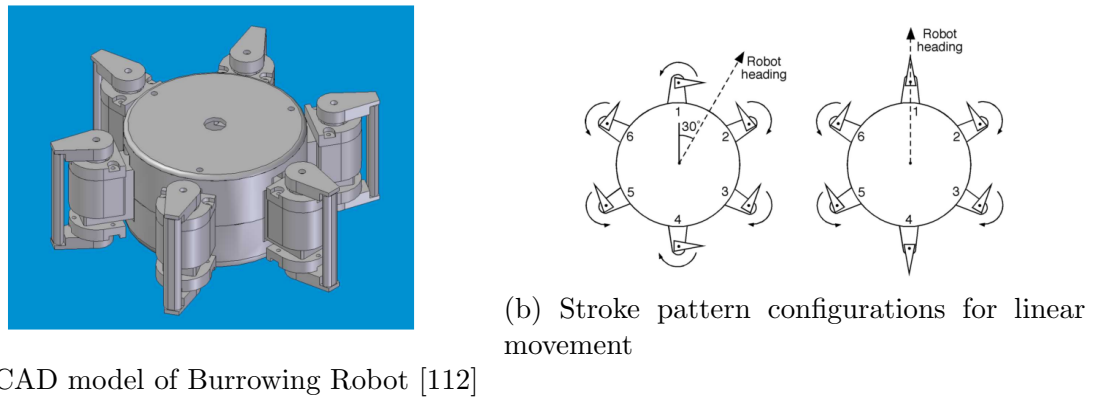


Figure 5.6: An Agile Burrowing Robot for Underground Chemical Source Location [112]

5.3.2 An Agile Burrowing Robot for Underground Chemical Source Location

This research project outlined the design of a robot for burrowing underground to determine the source of a specific chemical location [112]. A long thin robot increased drag when turning underground, therefore, a short cylindrical body was proposed.

Fig. 5.6 shows the CAD model of the proposed design and the movement of the paddles required for linear movement. With each paddle controlled individually it was possible to travel in multiple directions.

This robot was tested in sand and was found to be able to move in a plane parallel to the surface. It was unable to move up and down and is therefore limited in its avoidance of obstacles and application for underneath a Sellafield legacy pond.

The same research group developed a device that navigated on the surface towards the highest concentration of an underground chemical source before penetrating the ground with a sensor node to gather data [113]. The prototype can be seen in Fig. 5.7

This type of design could be used with any prototype as a way of directing the original area of investigation and transporting the device into a hazardous zone before burrowing underground.

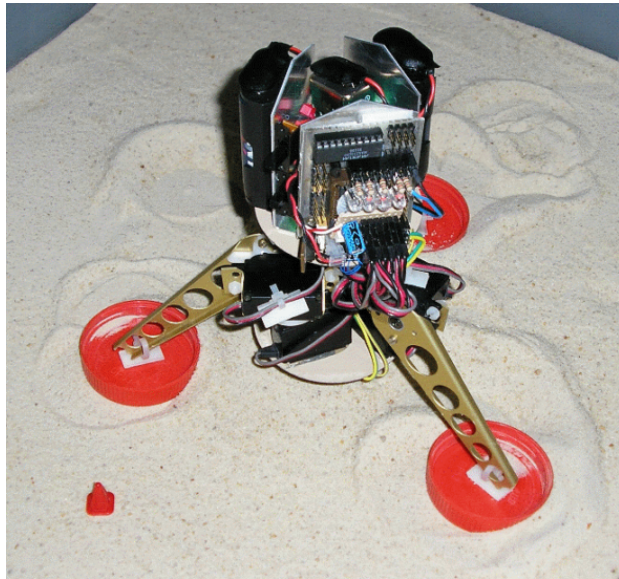


Figure 5.7: Device used to deploy sensor node as close to chemical source as possible [113].

5.3.3 Autonomous Burrowing Robot for Lunar Subsurface Exploration

An autonomous burrowing robot for lunar subsurface exploration has been developed [114]. Different drilling mechanisms and propulsion systems were analysed for optimum lunar subsurface exploration. It was the research groups' aim to be able to bury a long-term seismometer under the lunar surface.

The team simulated and tested three varying screw mechanisms with the contra-rotor screw seen in Fig. 5.8 found to be most suitable for lunar excavation. The opposing movement of the forward and rear sections, negate the reaction forces on the body. This stopped the body rotating instead of the drill-head [115].

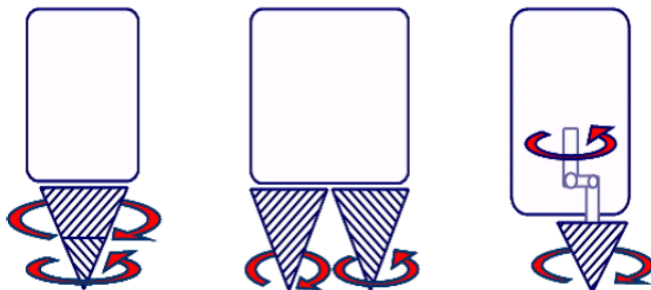


Figure 5.8: Screw mechanisms prototyped to find optimum solution [115].

It was found that the body still experiences rotational forces if not configured

correctly. Imbalance in the weight distribution and the relative speed of each element of the contra-rotor screw to the other also contributed to vibration if not balanced.

Although designed for a specialised operation in lunar excavation, similarities can be drawn with the design of a robot for underground sensor deployment in a nuclear decommissioning site. Major differences to take into account between these environments include the manoeuvrability of the device and its adaptability to varying geology. Lunar regolith is homogeneous in nature, whereas sub-soil environments vary, therefore, the ratio in speeds of the front and back half may need to be adaptable. This makes design and manufacture complicated.

5.3.4 DigBot

DigBot was created to investigate geological conditions and ground pollution after disasters such as earthquakes and tsunamis [116]. As was suggested by [115], it implemented a contra-rotor drilling mechanism to burrow and therefore avoid reaction forces on the main body. A prototype of DigBot can be seen in Fig. 5.9.



Figure 5.9: DigBot prototype demonstrating contra-rotor screw [116]

The authors found that DigBot was capable of burrowing up to 38 cm [116], with further work to be done on the propulsion system and waterproofing.

As with many current underground products, researchers concentrated on digging in a straight line rather than changing direction of travel whilst underground. Therefore, the current prototype was not considered fully suitable for this research project's requirements. It also struggled to burrow past 38 cm in sand, this suggested that it would struggle further in soil.

5.3.5 The Mars Underground Mole

The Mars Underground Mole (MUM) was a device that was developed to enable subsurface measurements on Mars [117]. The European Space Agency incorporated

the Mole device, which was initially called the Planetary Underground Tool (PLUTO), onto the beagle 2 lander launched in 2003 [117]. The landing was not successful and so the device was not deployed on Mars.

The burrowing technique was based on a hammering mechanism. A mass was connected by a spring to a motor gearbox. This compressed the spring until a release point was reached. This then pushed the mass and created forward momentum. A secondary spring absorbed the recoil at a reduced energy to avoid movement backwards. An outline can be seen in Fig. 5.10.

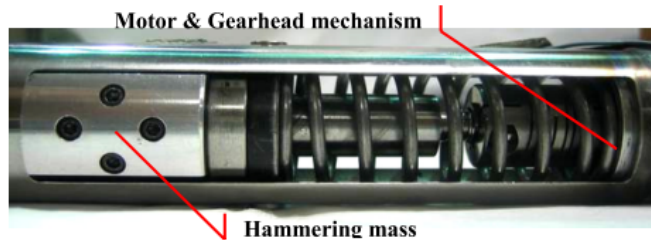


Figure 5.10: Mars Underground Mole hammering mechanism.

This was a simple approach and also energy efficient as the required motor torque remained constant during operation, however, it was unable to alter its direction of movement. It was twinned with a tether that could transfer sensor data back to the surface whilst also enabling the device to be winched out of the ground if required. The technical specifications of the MUM can be seen in table 5.3.

Table 5.3: MUM specifications [118].

Parameter	Value
Mass Mole (actual mass)	2000 g
Mole Diameter	4 cm
Mole Length	60 cm
Peak Power Draw	10 W
Maximum Penetration Depth	2 m
Speed	1 m.hr ⁻¹
Retraction mechanism	Surface Winch
Retraction force capability	2.5 kN

The size, power requirements and achievable depth suggest that this device could be successfully adapted and improved for a sub-soil environment. Power on lunar missions, especially to Mars, is limited by the amount that can be harvested via solar panels, therefore, without this limitation on Earth, a more powerful device could be manufactured.

5.3.6 Puncturing Mud Robot

A team from the Harbin Engineering University in China have attempted to take an air-powered soil penetrator, used by civil engineering contractors to place pipes under gardens and highways, and developed a mechanism to allow shallow burrowing curves to be achieved [119]. Fig. 5.11 highlights the structure of the turning mechanism.

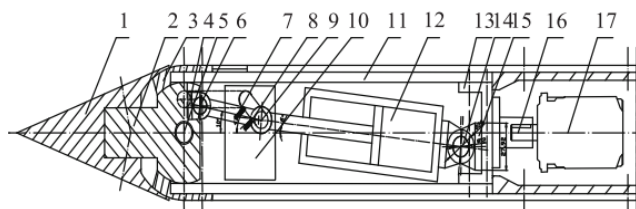


Figure 5.11: Turning device of puncturing mud robot [119].

The main working principle is the change in angle of the nose-cone, creating an angled hammer forward. Over time this creates a curved trajectory. Simulations run by the group suggested it could be a viable design as long as the air pressure was high enough [119]. Modifying a solution already used in existing civil engineering techniques reduced development time and increased ruggedness. This would be a sensible approach for research conducted within this project.

5.3.7 Further Techniques Considered

As well as the bespoke devices already discussed, there are many projects that contain useful information on possible mechanisms to be prototyped and tested. This will aid further in development of a robotic platform.

A robotic mole called Bidi-bot was designed for a search and rescue environment (Fig. 5.12). It uses paddles to remove debris in its way following the same trajectory as a mole. It can propel itself forward on debris or clear a path for it to travel through [120].

Analysis and prototyping showed that the use of paddles allowed excavation of debris, however, the torque required is large. Attempting paddle movement underground would require large, powerful motors and a device capable of removing debris created. It is, therefore, unlikely that a paddled device in this arrangement is a viable option. It would require a modification of structure and operation.

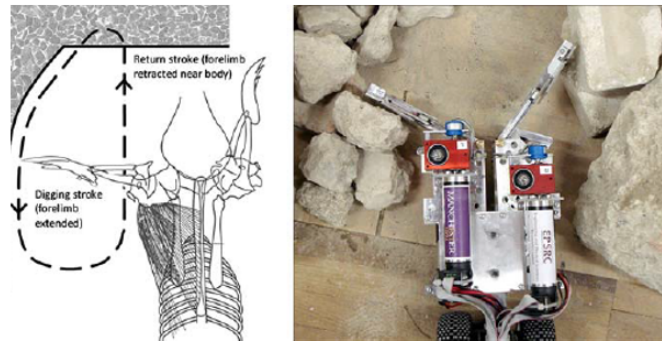


Figure 5.12: Side-by-side comparison of mole morphology and robot design [120].

CRABOT [121] was based on the mole crab and used paddles to pull itself through sand as outlined in Fig. 5.13. It combined a comb structure with a flexible vane to create drag in one direction and reduce drag in the other [121].

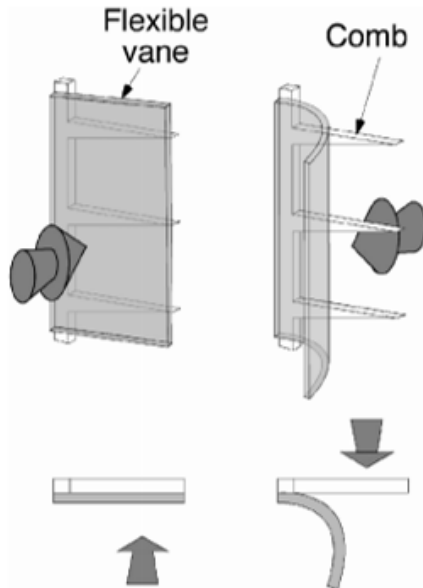


Figure 5.13: Deployment of a feather vane [121].

This solved the problem of debris jamming the paddles, but does not solve the problem of large torque forces required to enable such movement. Limited success was achieved with this set-up.

An artificial bivalve has also been created to replicate the movement of a clam in underwater sediment as seen in Fig. 5.14. It protrudes a valve that becomes an anchor in the sand, before pulling itself toward the anchor [122].

Analysis of its success suggested that it is able to move in small marine environments with a loose sediment but would not have the required energy or body shape to

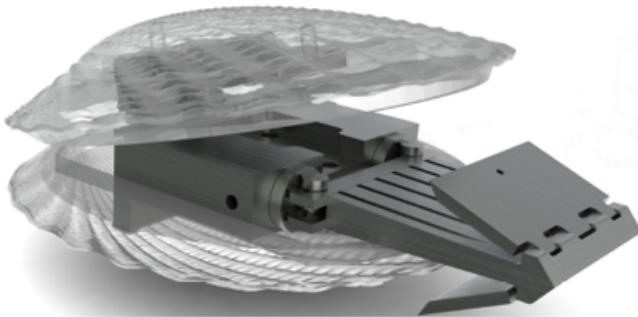


Figure 5.14: Bivalve configuration for anchoring a device [122].

manoeuvre through a sub-soil environment.

Inclusion of these techniques has highlighted techniques that may have been considered during development but due to limited success in these research projects should not be considered during development of a sub-soil robotic platform.

5.3.8 Summary of Current Robotic Platforms

Having analysed the state-of-the-art surrounding the development of underground robotic platforms, it is important to develop an understanding of the best possibilities for further development. The techniques best-suited to the target environment of this project.

Table 5.4 summarises the important data gathered about current research projects developing underground devices and the applicability of each one to this project. Manoeuvrability is quantified through number of degrees of freedom, which is represented by the acronym d.o.f.

It was decided to explore the possibility of a contra-rotating screw, such as the ones developed for DigBot and the Autonomous Burrowing Robot for Lunar Subsurface Exploration. Simulations and prototyping suggested that this is a viable option for lunar excavation and it was hoped this could be transferred to a soil based environment.

Many of the discussed research projects implemented a hammering mechanism to burrow underground. The MUM uses springs and motors, whereas the Puncturing Mud Robot uses pneumatic power. For a combination of size and power constraints, a hammering mechanism appears to be a good choice to further develop and was considered the priority for improvement due to its easier manufacture and control.

Table 5.4: Summary of the main specifications of literature research projects.

Design	Manoeuvrability	Size	Applicability
RASSOR	Minimal	Large	Too big and does not serve the same purpose as required
Lunar sub-surface	1 d.o.f	Small	Good size and mechanism but can only travel in one direction
Dig-Bot	1 d.o.f	Small	Good size but limited depth achievable and can only travel in one direction
MUM	1 d.o.f	Medium	Good size and achievable depth but can only travel in one direction
Puncturing Mud-Robot	2 d.o.f	Medium	Big, and expensive air compressor equipment required, however, 2 d.o.f.
Paddle designs	1 plane	Medium	Limited in movement, limited depth and slow
Bi-valve	1 plane	Small	Limited in environment, achievable depth and only 1 d.o.f

None of the discussed research projects met the requirements set-out for this research project. Therefore, a collaboration of ideas may be required, such as a contra-rotating screw in front of a hammering mechanisms body, or paddles to the side of the device to direct movement. Further discussions would take place after initial prototyping.

5.4 Summary and Evaluation of Current Research

Currently there is no device capable of sub-soil characterisation to the requirements outlined in Section 5.2. Much of the current literature has been focussed on lunar regolith sampling and excavation. This means device operation is specific to one goal, reducing the likelihood that in their current form they could be used for sub-soil characterisation on Earth.

Analysing the current state-of-the-art suggested that the use of a hammering mechanism and/or a contra-rotating screw head would be the best starting point for initial prototyping and manufacture. Once a device capable of burrowing using one of these techniques or a combination was devised, a turning mechanism could be added.

There appears to be a lack of knowledge on how best to manoeuvre the device

once underground, as no repeatable and robust method exists to allow a device to turn underground. Physically altering the shape of a device such as the MUM robot into a curved shape would allow “trench runs” to be performed underneath the ponds. This would allow the collection of invaluable data from beneath the pond.

The environment our device would be required to navigate through consisted mostly of clay, sand and silt. The working envelope of the device is between the bottom of the ponds (5 m deep) to bedrock (approx. 25 m deep), therefore, a steering device would require a turning radius of less than 10 m.

Chapter 6

Development of Underground Burrower

A review of the current literature highlighted that there was no device capable of burrowing beneath the Sellafield Legacy ponds to characterise the environment. Therefore, a collaboration of techniques were required to develop a novel underground burrower.

Two techniques were considered for development. The contra-rotor screw mechanism used within the DigBot platform and lunar sub-surface device and the hammering mechanism used within the MUM device. Progress developing these ideas is discussed in this chapter with the hammering mechanism prioritised for development after initial testing of the contra-rotor mechanism.

Areas for improvement are discussed and an analysis of the applicability of the device for the required nuclear decommissioning environment is presented with suggestions for deployment techniques.

6.1 Contra-rotor screw mechanism development

Many articles have explored the equations that dictate the operation of a sub-surface screw [123–125]. In short, a screw can be considered an inclined plane wrapped around a cylinder. However, in this instance, the screw must be considered around a conical surface with the angle of this surface altering the force required to screw within the same material. The contra-rotor screw system has been modelled by Nagaoka et

al. [126]. They determined the performance of their design via the index of “Specific Energy”, often used in industry [127]. The required energy per minute for drilling, E , ($D.J.\text{min}^{-1}$), is calculated as follows:

$$E = W \times \pi D \times f \times 10^{-9} \quad (6.1)$$

$$W = w_1 \times g + w_2 \quad (6.2)$$

D is the diameter of the drilling hole in mm, f is the rotation speed in rpm, W is the propulsive force in N, w_1 is the robot mass in kg, g is gravitational acceleration and w_2 is all the external force without robot weight in N. By using a speed of penetration (PR , m.hr^{-1}) the magnitude of soil removed (V , $\text{m}^3.\text{min}^{-1}$) can be calculated as follows:

$$V = \pi \times \left(\frac{D \times 10^{-3}}{2} \right)^2 \times \frac{PR}{60} \quad (6.3)$$

Therefore, the specific energy, SE , can be calculated as;

$$SE = \frac{E}{V} = \frac{0.24 \times f}{D \times PR} \times (w_1 g + w_2) \quad (6.4)$$

We can also calculate the equivalent angular velocity, w_s , of the contra rotating screw through analysis of the speeds of rotation of each moving part. The total energy of rotation can be defined as;

$$\frac{1}{2}I_1w_1^2 + \frac{1}{2}I_2w_2^2 = \frac{1}{2}(I_1 + I_2)w_s^2 \quad (6.5)$$

I_1 , g.m^2 , is the inertia of the front screw and I_2 is the inertia of the rear screw. w_1 , rad.s^{-1} , is the angular velocity of the front screw, with w_2 representing the rear screw angular velocity. Therefore, the equivalent angular velocity of the system, w_s equates to;

$$w_s = \sqrt{\frac{I_1w_1^2 + I_2w_2^2}{I_1 + I_2}} \quad (6.6)$$

Fig. 6.1 outlines the structure of a contra-rotor mechanism and the terms used to describe each part. The front half of the contra-rotor spins anti-clockwise, with the back-half spinning clockwise. This is enabled via the implementation of a planetary gearbox.

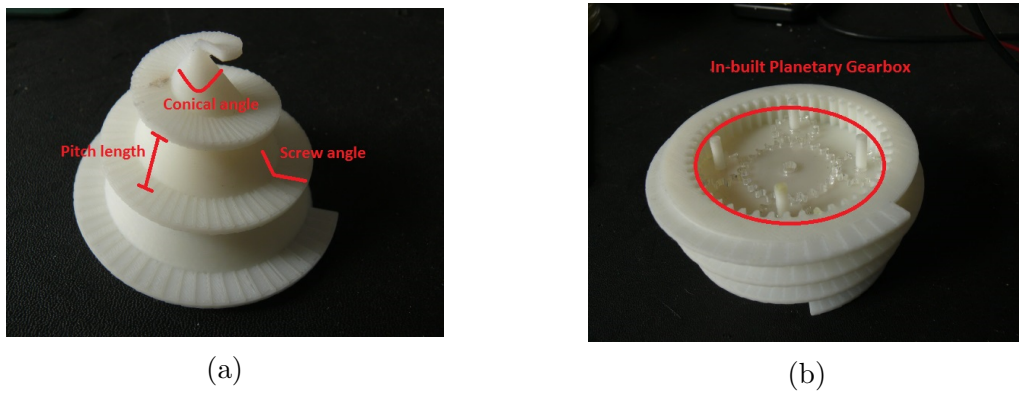


Figure 6.1: a) Front half of contra-rotor screw, b) back half of contra-rotor screw with in-built planetary gearbox.

Prototypes of many different halves with varying pitch lengths, screw angles and conical angles were designed to determine the optimum design for sub-soil penetration. Example technical drawings of the contra-rotor screw mechanism can be seen in Figures 6.2 and 6.3.

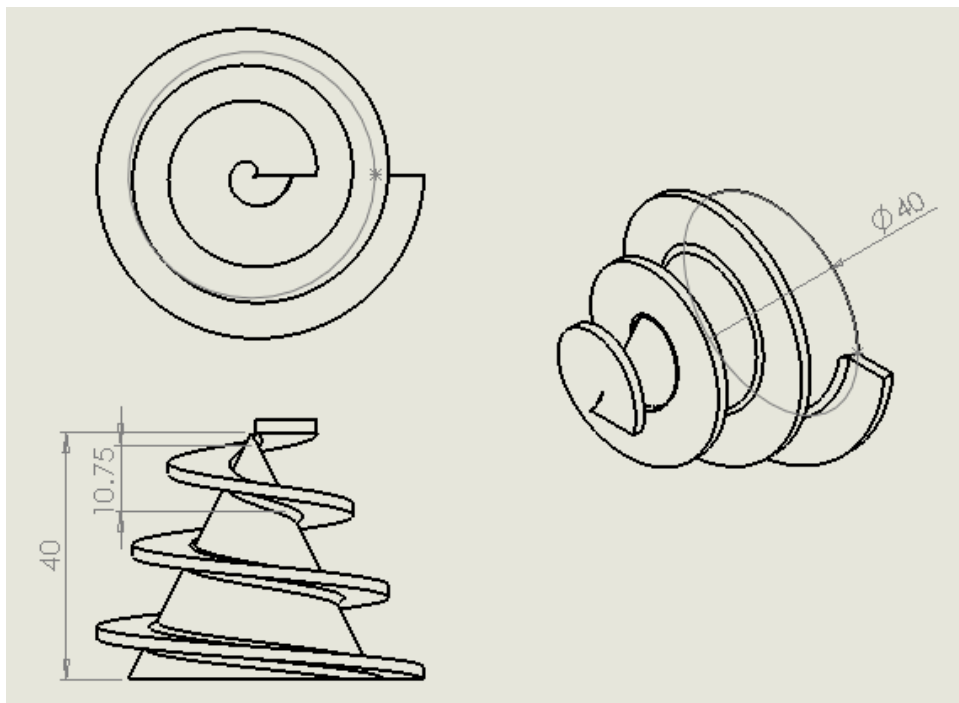


Figure 6.2: Technical drawing of the front half of a contra-rotor screw.

It was hoped these designs would then be further developed into a mechanically robust system. If this was successful, changes in design to attempt underground cornering would be applied. Fig. 6.4 displays an example of the initial contra-rotor prototype, which was 3D-printed using a MakerBot PLA thermal extrusion 3D printer.

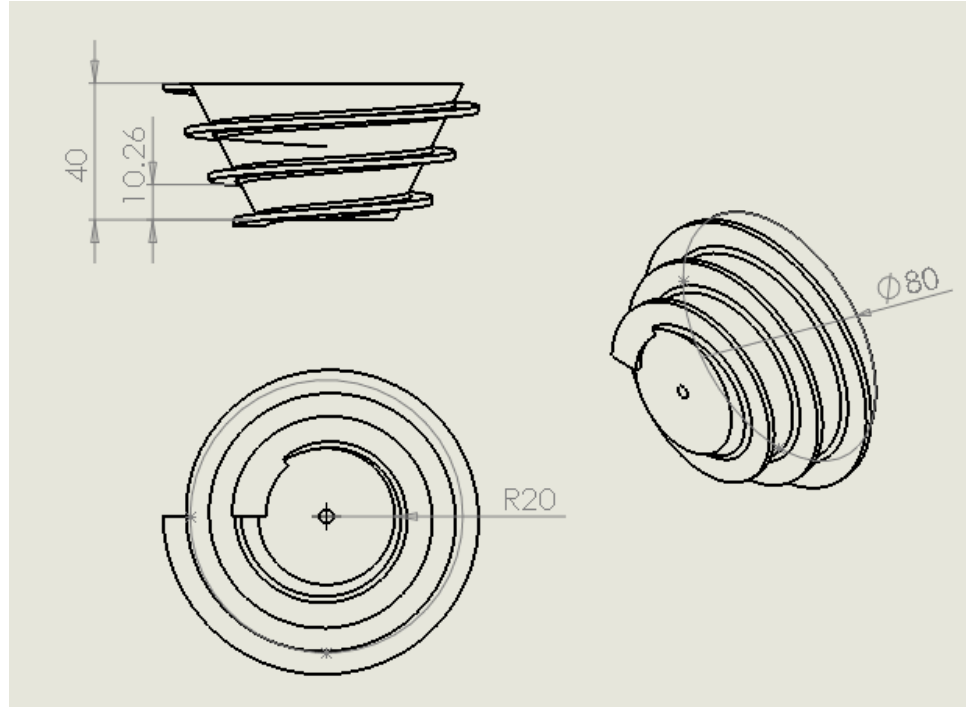


Figure 6.3: Technical drawing of the back half of a contra-rotor screw.

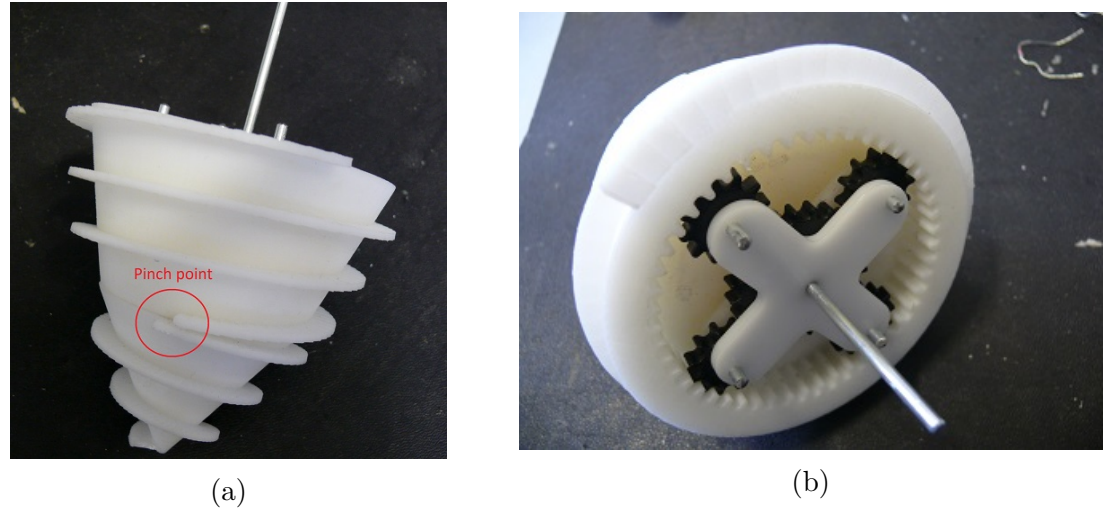


Figure 6.4: a) Side view of the initial contra-rotor prototype, b) rear-view showing the planetary gearbox used to rotate the halves in different directions.

The in-built planetary gearbox seen in Fig 6.4b can be modified to change the angular rotation of each half. For example, it may be beneficial to have the front half spin twice as fast as the back half. This can be adjusted in the 3D model of the back half for each iteration of the device.

3D-printing allows for quick re-design and manufacture but it is not without disadvantages. The material used has low strength, approximately 50 MPa tensile strength

in comparison to 2,100 MPa for steel, with differences in mechanical properties dependent on orientation during printing, therefore, many iterations were required to determine the optimum configuration.

Original designs were difficult to assemble with many time-consuming iterations for further development required. For example, the clamping mechanism to connect each half to the axle, failed when a torque less than required for penetration of the soil was applied. This resulted in the axle spinning without rotating either screw halves.

A further iteration highlighted the need to leave a space between the end of the bottom thread and start of the top thread. A pinching effect caused by the opposite rotation resulted in trapped soil and a screw unable to rotate. Fig. 6.4a highlights the area of this pinching effect.

Another area of concern was the expulsion of soil from the screw mechanism. Fig. 6.5 highlights the effect a conical shaped screw has on the direction and therefore forces of expelled soil. This is important when discussing the compressive forces acting upon the device underground.

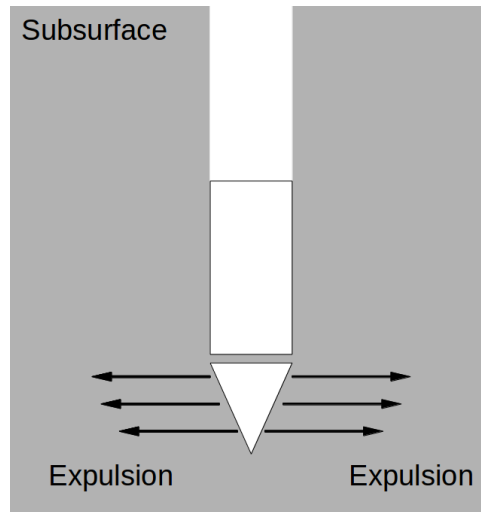


Figure 6.5: Direction of soil expulsion of a conical shaped screw during sub-surface locomotion [128].

Due to this effect, a contra-rotor screw with a cylindrical back half rather than conical was also manufactured to determine if there was a difference in overall penetration and propulsion performance due to the direction of soil expulsion. This can be seen in Fig. 6.6.

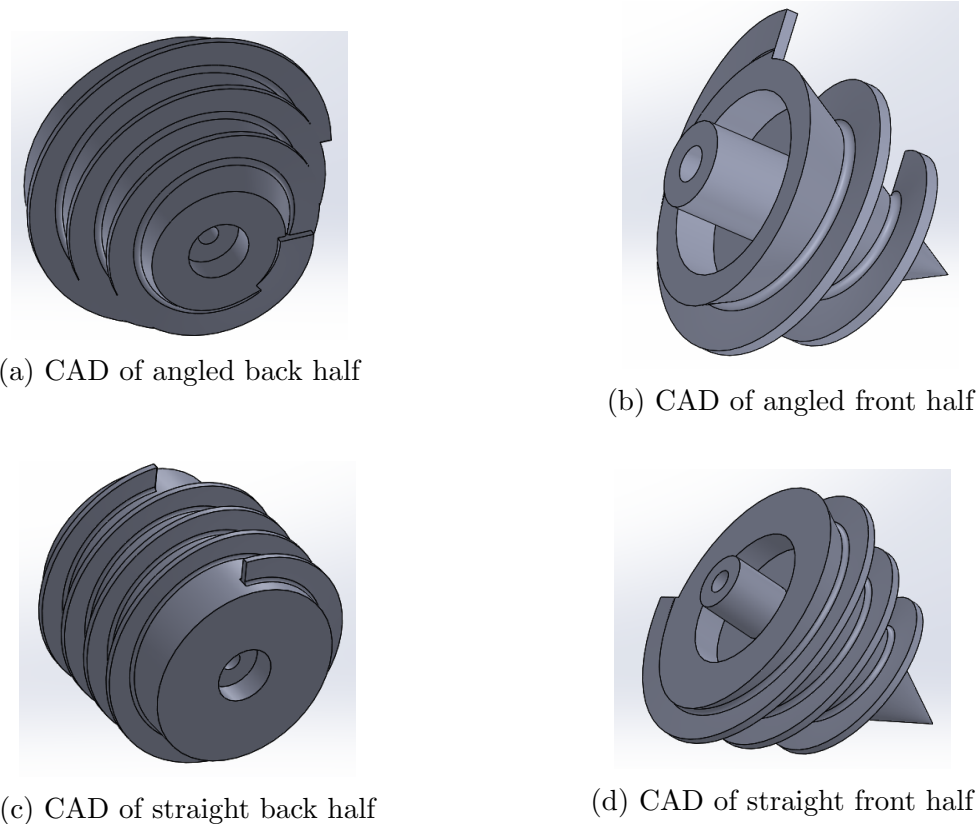


Figure 6.6: CAD models of example contra-rotor mechanism prototypes.

6.1.1 Contra-rotor testing

To test the contra-rotor screw design, a cordless drill capable of torque up to 41 Nm, was used to drive the contra-rotor axle. The success of the design would be determined by the time it took to become fully submerged in a container of sand, 400 mm in diameter and 300 mm deep.

Unfortunately, it became apparent during experimentation that there were many flaws with the development of contra-rotor screw mechanism. Ingress of soil between the two rotating halves created a large frictional force that could not be overcome by the motor torque. The further the device travelled through the soil, the greater torque required with the stall torque of the motor reached within only a few centimetres of soil.

Due to these fundamental flaws of the contra-rotor design and large manufacturing times, it was decided that the contra-rotor screw was not a viable option for the requirements specified for this device such as burrowing up to 5 m underground. Therefore,

the design would not be recommended for a similar environment and was not pursued further. The development of a hammering mechanism device was prioritised for further study.

6.2 Hammer mechanism development

This section outlines the development of a hammering mechanism robotic platform. Initially, the forces required to enable operation are calculated before a summary of the progress completed towards development of a prototype system.

6.2.1 Hammering mechanism structure

The hammering mechanism consists of a mass attached to the end of a spring that is compressed before suddenly being released. To transform the rotational force from a DC motor into a linear force, a cam was developed. This structure can be seen in Fig. 6.7.

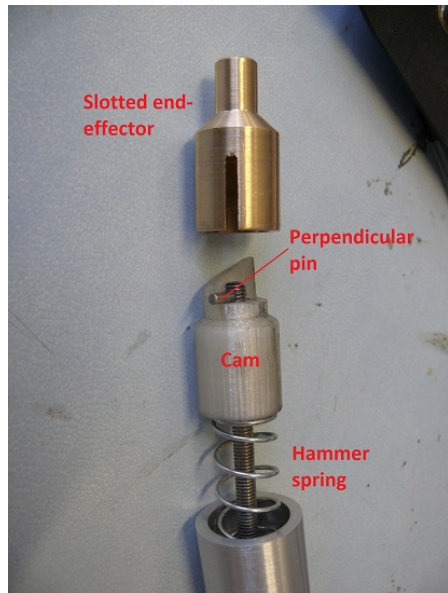


Figure 6.7: Example of cam system used

An axle in the centre of the cam is connected to a pin that sits perpendicular to the axle. This rests on the edge of the cam. The motor then rotates this axle through a slotted end effector. The slot is the width of the pin allowing it to be held, whilst also allowing a vertical movement. This forces the pin to rise, compressing the hammer spring to the designed height, before suddenly releasing at the end of the slope.

6.2.2 Force calculations

The force required to raise a mass attached to a spring is calculated via Hooke's Law [129];

$$F = -kx \quad (6.7)$$

F is the force required to compress the spring, k is the spring constant and is determined by the material, shape and size of the spring, x is the displacement from the at rest state. Fig. 6.8 outlines the model of the system highlighting the mass attached to the end of a spring.

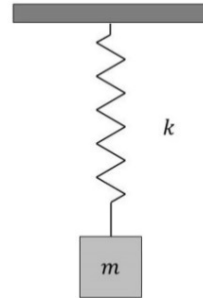


Figure 6.8: Simplified model of internal hammering mass attached to spring

The force required to lift the spring needs to be combined with the force to rotate the pin connected to the axle. To calculate the required motor force the shape of the cam needs to be considered. A cam can be modelled as an inclined plane wrapped around a cylinder. This presents us with the system shown in Fig. 6.9.

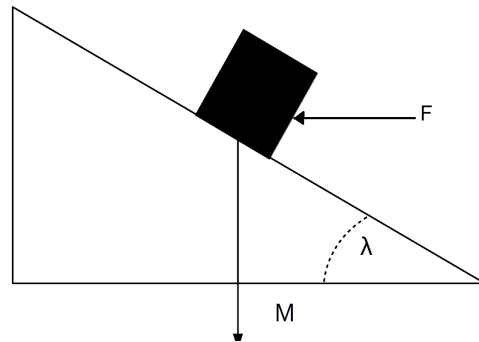


Figure 6.9: Model of an inclined plane, representative of a cam.

From first principles, there are three forces that are required to be taken into account. The friction force, the mass acting parallel to the plane and the force imparted

onto the mass. This gives the net force parallel to the plane as;

$$F\cos(\theta) = mg\sin(\theta) + \mu mg\cos(\theta) + \mu F\sin(\theta) \quad (6.8)$$

$$F(1 - \mu\tan(\theta)) = mg(\tan(\theta) + \mu) \quad (6.9)$$

This gives the force required to move the load up the incline as [124];

$$F \geq \frac{\mu + \tan(\lambda)}{1 - \mu\tan(\lambda)} Mg \quad (6.10)$$

F is the force required to lift the mass M , μ is the coefficient of friction between the wedge and weight, g is the force of gravity and λ is the incline angle.

Although conventionally this models the force required to push the mass up the inclined plane, it can also be considered as a wedge being pushed underneath the mass. This would equate to the apparent rotation of the cam underneath the mass. This gives us the torque required to rotate the pin around the cam as;

$$T \geq \frac{\mu + \tan(\lambda)}{1 - \mu\tan(\lambda)} r Mg \quad (6.11)$$

T is the torque and r is the distance from the centre of rotation to the mid-point of the weight.

The required torque of the motor can be calculated by combining equations 6.7 & 6.11. The mass on the inclined plane will appear to increase due to an increased compression in the spring. Therefore, the maximum torque will occur at the moment of greatest compression at the top of the cam incline.

The maximum torque required can be calculated by modelling the maximum weight observed by the motor when the spring is most compressed. This is done by substituting equation 6.7 for Mg in equation 6.11 and adding the weight of the hammer due to gravity, giving us the equation;

$$T \geq r \frac{\mu + \tan(\lambda)}{1 - \mu\tan(\lambda)} [(-kx) + (mg)] \quad (6.12)$$

6.3 Initial hammering mechanism prototype

Having discussed the process used to choose the correct specification motor for a specified spring, an initial prototype was constructed to determine feasibility of the design. Fig. 6.10 outlines the initial design of the device.

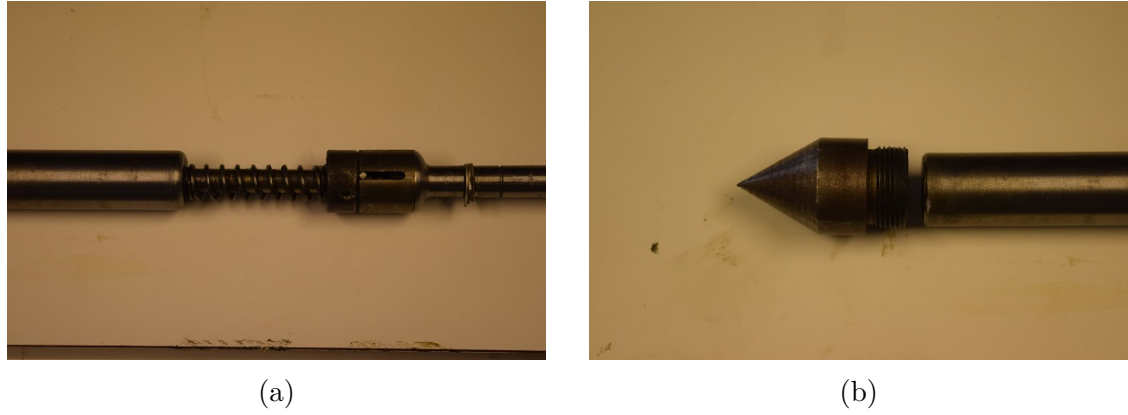


Figure 6.10: a) Outline of internal hammering mechanism, b) removable nose cone that can be replaced with different end effectors.

The cam and motor were attached to the outer body of the device, with the mass and axle allowed to freely move. The slotted end effector was driven by a cordless drill motor to rotate the axle. The initial device had an outer diameter of 35 mm and was 300 mm long.

6.3.1 Initial Test Results

The mole was tested in a container of sand, which had a diameter of 400 mm with a depth of 250 mm. Marks were added to the body of the prototype every centimetre. The time in-between each centimetre of penetration into the sand was measured to determine penetration rate. Fig. 6.11 outlines the average depth reached over time for ten test-runs.

It was found that a maximum depth was reached of 220 mm over the course of 1 hr. It was assumed it did not travel to the full depth of 250 mm due to compression of the sand near the base of the container.

The penetration rate also slowed as the device depth became greater. The increased friction of sand acting upon a greater surface of the device slowed progress. It also became apparent that the device would oscillate slightly after every impact. Therefore,

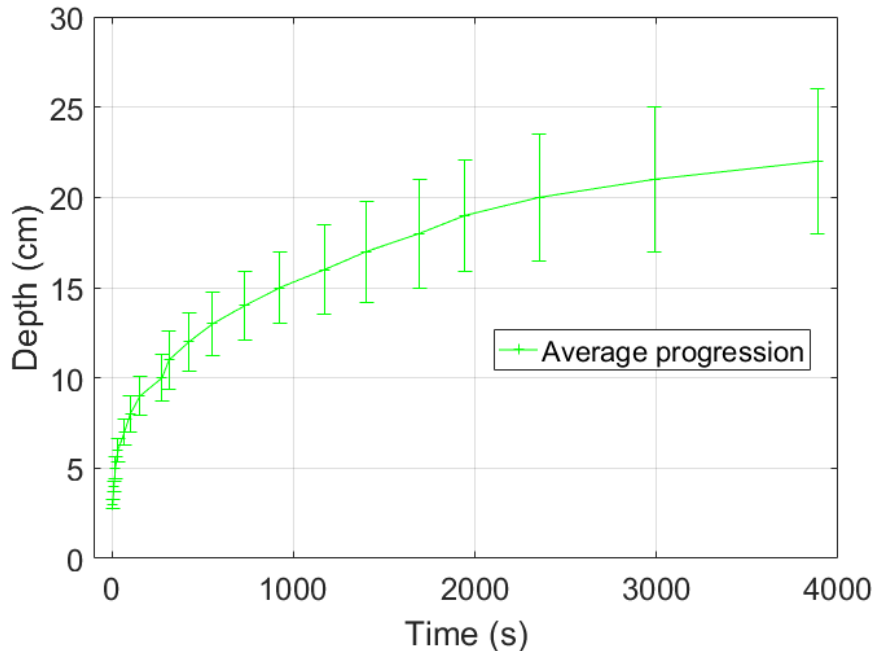


Figure 6.11: Average of ten attempts of the device to penetrate to a depth of 250 mm.

much of the forward force was rebounded and wasted resulting in the device “bouncing” in place. At shallower depths, this oscillatory motion combined with the weight of the device was enough to allow penetration but further progress was hampered by this motion as the sand became more compressed.

6.4 Developed Prototype

Having witnessed an oscillatory action reducing the forward momentum of the hammering mechanism, a further iteration of the device was developed. A suppressor mass was included within the design as seen in Fig. 6.12.



Figure 6.12: Motor now encased in a brass housing acting as suppressor mass.

Technical drawings of the suppressor housing, cam, axle rotator and hammering mass can be seen in Figs. 6.13 - 6.16.

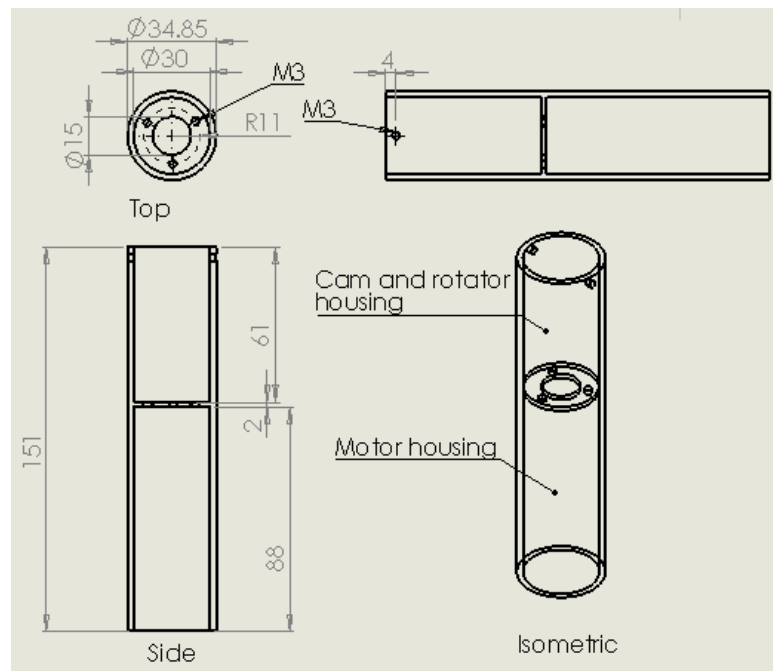


Figure 6.13: Housing for the motor, cam and axle rotator in the developed hammering prototype

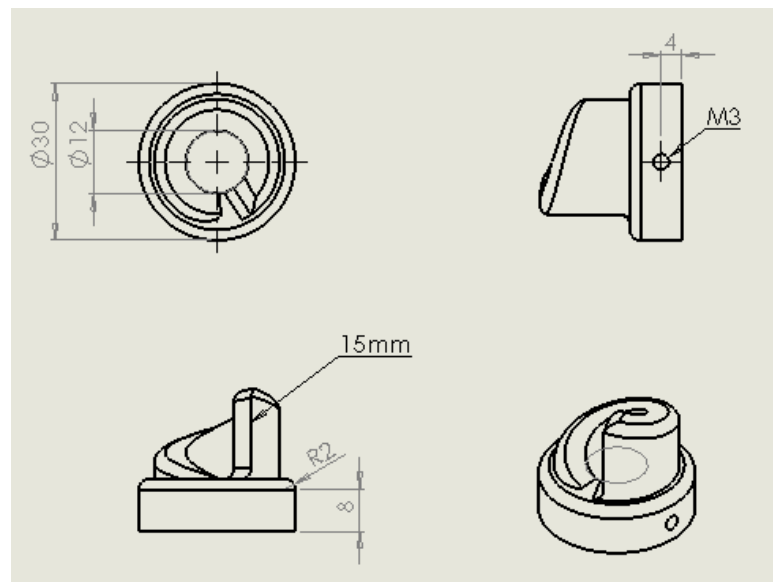


Figure 6.14: Technical drawing of cam manufactured for developed prototype

In the initial design, as the main hammer mass impacted the back of the nose cone and rebounded, a backwards force was re-absorbed by the spring and impacted on the fixed cam in the opposite direction.

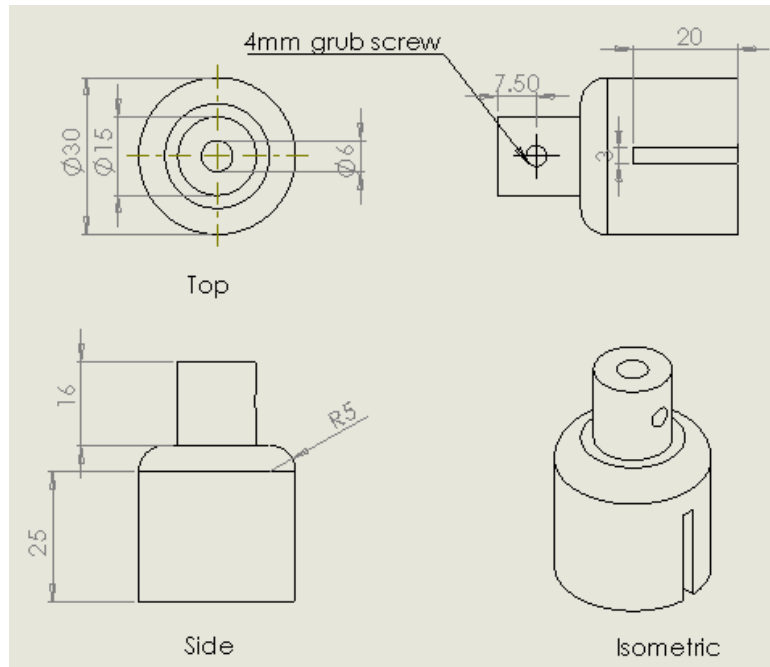


Figure 6.15: Technical drawing of axle rotator mounted above the cam.

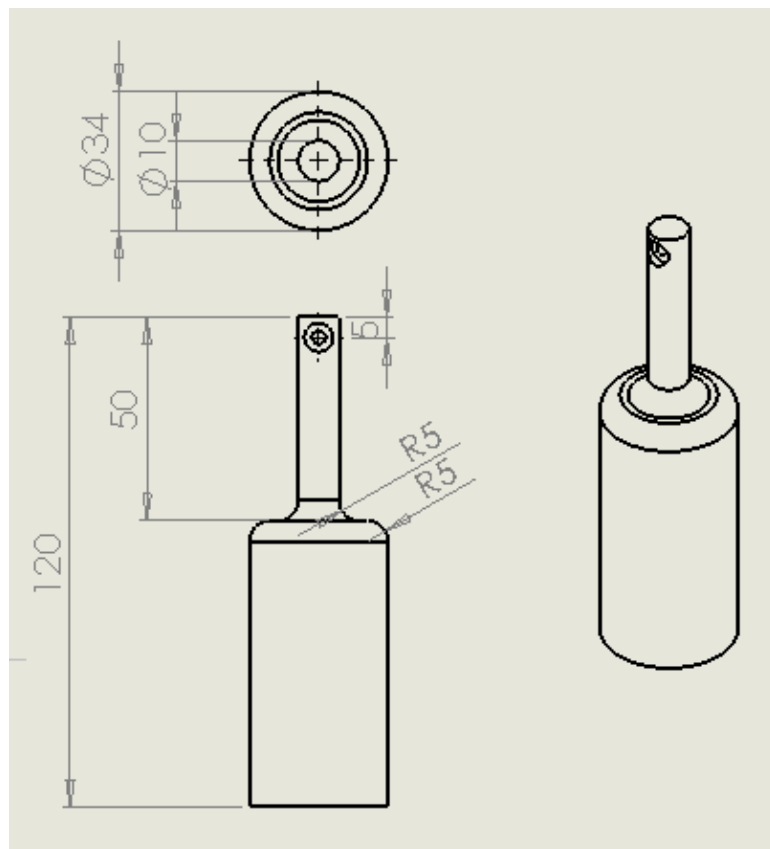


Figure 6.16: Technical drawing of the hammer mass developed for the hammering prototype.

To avoid this opposing force, the motor and cam were encased in a brass housing

that could freely move within two end-stops. This design enables the same impact force to result in a backward motion of the motor and cam housing, which can be “absorbed” by a suppressor spring. This reduces the magnitude of the reactionary force experienced by the device in the opposite direction.

Due to the increase in mechanical complexity inside the device, the overall size of the device increased to 45 mm in diameter and a length of 450 mm. The major factors causing the increase in size are motor diameter and thickness tolerances of the component parts.

The diameter could be reduced to approximately 35 mm rather than 45 mm with a more expensive motor such as those provided by Maxon, which could cost over £600, whilst the motor used in this study was the McLennan PS150-24-125 that cost £54.08, had a torque of 75 Ncm, maximum torque rpm of 34, mass of 85 g and a maximum current draw of 0.44 A. Machining of each constituent part to a thinner overall diameter is also possible but not completed during this project for robustness during prototyping. The decrease in diameter would reduce the exterior friction of the geology on the device, increasing the rate of penetration and achievable depth.

6.4.1 Optimisation of spring combinations

Before further tests were conducted in sand, as in Section 6.3.1, a series of tests to determine the optimum combination of main compression spring, suppressor spring and starting distance between the end of the mass and nose cone were conducted.

The device was placed horizontally on a laboratory bench-top with two markers 50 mm apart. The time it took to reach the second marker and also the number of impacts required were measured. Table 6.1 outlines the test results gathered for spring and starting distance optimisation. k_h is the spring constant of the hammer spring and k_s is the spring constant of the suppressor spring.

It can be seen that as the initial starting space between the mass and the nose cone increased, the average time taken to reach the 5 cm marker decreased. This is due to finding the optimum point of impact for the mass being released and the opposing force caused by this release forcing the mass away from impact.

The larger hammer spring with the greatest spacer sees the smallest time and number of beats to reach 50 mm. This combination of suppressor spring and hammer

Table 6.1: Summary of spring optimisation

Spring Constant	Spacer (mm)	Average time (s)	Average number of strikes
$k_h = 4.04 \text{ N.mm}^{-1}$ $k_s = 0.99 \text{ N.mm}^{-1}$	2	51.5	42
	3	39.6	33
	4	43.5	36
	5	39.6	33
$k_h = 6.69 \text{ N.mm}^{-1}$ $k_s = 0.99 \text{ N.mm}^{-1}$	2	45.4	30
	3	38.6	25
	4	33.2	21
	5	29.5	20

spring was used for all future tests.

6.4.2 Resultant burrowing penetration results

Having decided upon the optimum spring combination, a series of penetration rate tests were conducted. Due to the increased size in device, a clear perspex tube, 150 mm in diameter and 600 mm in length was used as the sand container with the device placed in the centre. Fig. 6.17 outlines this set-up.



Figure 6.17: Overview of the test set-up for the hammering mechanism device.

Marks were added at regular intervals of 10 mm to the exterior of the mole and the time to move from one to the next was measured. This was then noted and analysed over the length of time it took to reach 250 mm. Fig. 6.18 shows the average time taken for four separate burrowing attempts to reach a depth of 250 mm.

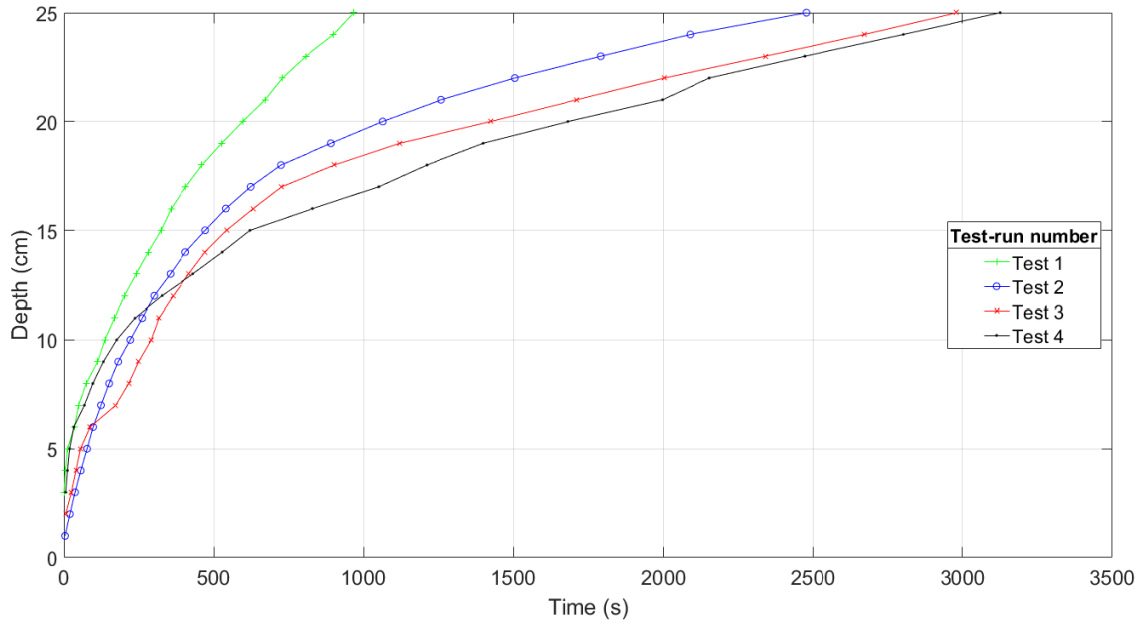


Figure 6.18: Outline of the average time taken for the device to reach a depth of 25 cm.

There was some variation during each of the tests with each subsequent test exhibiting slower penetration rates to the previous experiment. This was attributed to the compacting of the sand in the enclosed pipe. The increased compression slowed the progression of the mole due to a larger impact force being required to penetrate the sand.

6.4.3 Eccentric motor

Having tested the device's burrowing capabilities, further ideas to maintain the consistency of burrowing penetration rate and increase the peak penetration depth were investigated.

A technique used in civil engineering projects to burrow piles into the ground for building foundations, is vibratory pile drilling [130]. This is the process of integrating a vibration onto the pile, which excites the particles surrounding the pile, which then start behaving as a liquid. This allows the pile to "sink" into the ground.

This technique has been used in a research project conducted by Sellafield for a sludge sampler [131–133]. This added eccentric motors (a dc motor with an off-centred mass placed on the drive shaft) to a long cylindrical device that with no external forces was able to sample sludge up-to 1 m in depth.

To determine the applicability of this technique on the device in sand, two eccentric motors were mounted within the main body. These were the Precision Microdrives™ model:324-401 and 312-107. The 324-401 has a diameter of 24.3 mm, length of 12.5 mm, rated rpm of 5,700 and a typical normal amplitude of 21 G. This compares to the 312-107, which has a diameter of 12 mm, length of 15.1 mm, rated vibration of 6,400 rpm and typical normal amplitude of 14.3 G.

The two motors were mounted perpendicular to each other and controlled separately to determine which mounting arrangement was optimum. Fig. 6.19 outlines the two eccentric motors chosen that were mounted to the outer casing. The motor on the left outputs a force in the same direction of hammering movement and the motor on the right outputs a force perpendicular to the outer casing.

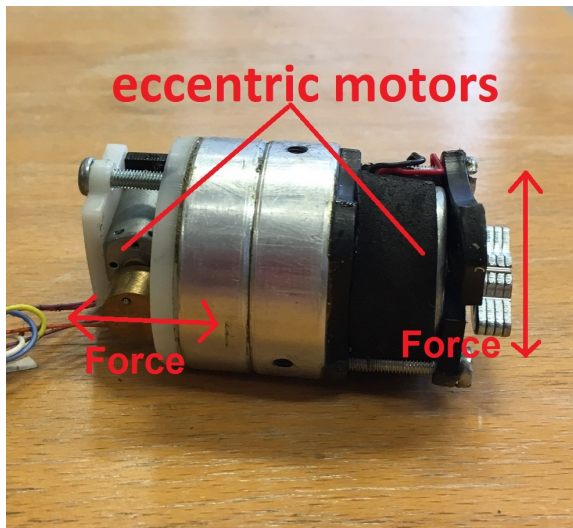


Figure 6.19: Outline of eccentric motor size and mounting structure. The two threaded holes mounted the motors to the outer casing.

The use of the eccentric motors appeared to increase the speed of penetration of the underground burrower. The change in penetration speed was determined by the magnitude of vibration with either a perpendicular to forward motion, or, forward motion vibration, effecting the speed of the device equally.

When the vibration motor speeds were increased to maximum available power, the

underground burrower began to oscillate in the same position with no progression on each hammer stroke. It is thought this is due to a similar effect as witnessed with the initial hammering mechanism. The vibration begins to actively work against forward motion by imparting a backwards force equal to the forwards force.

The optimum value of the vibration motor power may change with varying geology and soil compression. The ability to change the power of the vibration motors during operation, separately to the main hammering frequency, means that this can be taken into account with maximum power available if the device becomes lodged.

6.5 Analysis of device development

A major benefit of the hammering mechanism in comparison to the contra-rotor mechanism is the motor torque required remains constant no matter the depth of the device. All actuation happens internally within the mole with changes in geology not effecting this internal mechanism, which reduces the likelihood of motor mechanical failure. This makes the hammering mechanism a very reliable system that can be used repeatedly without failure although regular inspections must be taken at the impact point of the main mass and surface of the cam slope.

Results gathered during development suggested that a device based on a hammering mechanism with the addition of eccentric motors is worth further study and development. Long manufacturing lead-times limited the progress possible for continued improvements in this study, however, a prototype has been constructed that highlights the design of the most appropriate mechanism to meet the specified requirements.

The addition of a vibration motor aided in the penetration rate of the device as it dislodged the immediately surrounding geological material, thus reducing friction of the soil on the burrower. Care must be taken when increasing the strength of the vibration with a large vibration actively acting against the force to move the burrower further into the soil. Further analysis of orientation and strength is required to suggest an optimal performance of the vibration motors.

Through observations of the devices during experimentation, a number of deployment options were considered to help inform appropriate applications of the device. Initial requirements outlined through discussions with technicians from Sellafield and

the NDA included the ability to navigate underground with the implication that this would be in any direction. It has been found that this desire may be unnecessary and reduce robustness for a low-cost robotic platform. An alternative idea to create a device capable of a curved path is suggested. This would enable “trench-runs” that could be repeated from one side to the other parallel to the edge of a storage pond.

As the device will be tethered for power and communication, the tether could be equipped with sensing units placed along the length of the cable. A “trench-run” conducted by the device could then enable this cable to be left in the ground with as many sensing units required connected along its path enabling 24/7 monitoring of areas beneath the Sellafield legacy ponds as seen in Fig. 6.20.

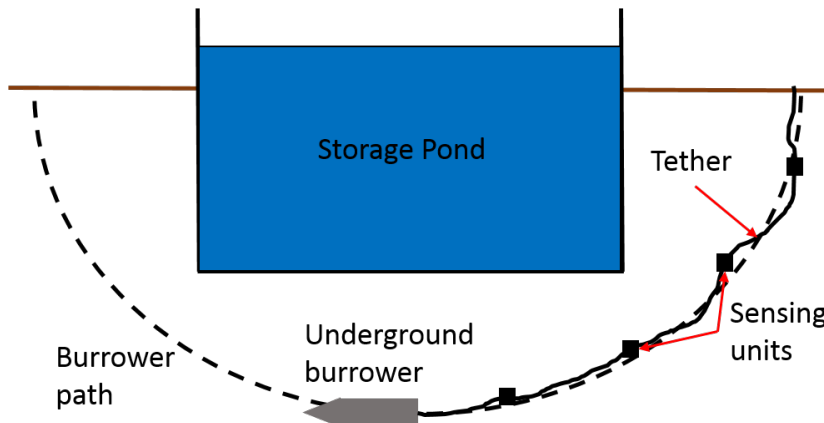


Figure 6.20: Sensing unit application suggestion.

It is thought a curved path could be achieved through use of an angled nose cone, shortening of the main body and addition of a curve in the rear of the main body. Through a combination of these techniques, it should be possible to develop a device capable of creating a curved trajectory.

6.6 Summary

This chapter has discussed the progress made in developing a prototype for underground burrowing and characterisation of the geological environment surrounding the Sellafield Legacy ponds. Multiple techniques have been trialled with the preferred hammering mechanism method suggested over any development of a contra-rotor screw.

Initial prototyping of 3D printed contra-rotor screws suggested that the torque required to screw through the geology surrounding the legacy ponds was unmanageably

high, with additional difficulties in manufacturing a part which did not allow ingress of soil between the individual rotation sections. Therefore, this system was deemed inappropriate for further study and would not be recommended for a project with similar requirements.

Through multiple iterations of the hammering mechanism design, a suppressor mass was introduced that reduced recoil forces on impact with a solid ground. This increased penetration rate and also maximum penetration depth.

Improvements to the manufacturing process would increase efficiency by reducing friction between the suppressor mass and the outer casing, whilst decreasing the outer diameter of the mole. This in turn reduces the friction of the mole to the surrounding geology, increasing penetration rate and depth.

An alternative application of the device has also been suggested by industrial collaborators in Japan. Adaptation of the device to burrow through sludge of 300 to 1000 mm at the bottom of the Fukushima Pressure Containment Vessel (PCV) in a similar way to the Sellafield sludge sampler [131–133] but with a different method of sampling the sludge.

Chapter 7

A Review of Current Submersible Robotic Platforms

There are many submerged nuclear facilities that require surveillance and monitoring. This is especially true in nuclear decommissioning scenarios such as the Sellafield legacy ponds and Fukushima nuclear accident. In both cases, there are radioactively contaminated areas that have been flooded with water for cooling and moderation.

Whilst water is a good radioactive shield and moderating agent, it leads to difficulties in determining the location and state of radioactive objects. It is difficult to visually inspect the environment, therefore, a submersible device capable of navigating hard-to-reach and dangerous areas would aid in characterisation of the environment.

A large strain was placed upon the Sellafield legacy ponds in the 1980s during the coal miners strike. Nuclear power plants were required to increase production of electricity resulting in a higher rate of nuclear fuel processing occurring at the Sellafield site [100]. Waste was created at a rate faster than it could be processed and the exact inventory of some materials in the ponds is uncertain. They are considered an “intolerable risk” [134], requiring decommissioning. To safely and efficiently achieve decommissioning, a complete inventory is required with the exact location and radioactive properties of all contents to be known.

Another area of interest for deployment of a submersible is the Fukushima Nuclear Power Plant (NPP), which presents a similar problem to the site in Sellafield. Due to the tsunami and subsequent evacuation and explosion at Fukushima, the fuel left in the reactor became molten and is believed to have fallen from the bottom of the

reactor and into the pedestal.

Dose-levels were too high for workers to get close enough to characterise the fuel location and the reactors and suppression chambers were flooded for cooling and moderation. A submersible is now required to characterise the flooded regions.

This chapter outlines the current submersible Remotely-Operated vehicles (ROVs) used in industry and research, it then evaluates where improvements are required for a system to be deployed in the proposed environments of the Sellafield Legacy ponds and Fukushima Daiichi.

7.1 Environment

The motivation for developing a submersible ROV is to characterise nuclear decommissioning environments with unknown location of nuclear waste. An overview of the environments of the Sellafield Legacy ponds and Fukushima Daiichi helps to define the parameters for operation. As discussed previously, the two examples of a nuclear decommissioning environments prioritised within this project are the Sellafield legacy ponds and Fukushima Daiichi.

7.1.1 Sellafield Environment

The Nuclear Decommissioning Authority (NDA) estimate the cost of nuclear clean-up in the UK to be in excess of £100bn over the next 120 years [2]. Much of this money will be spent on the decommissioning of the Sellafield site. Fig. 7.1 highlights the challenges facing an underwater ROV [135] in one of the Sellafield legacy ponds, which contains closely spaced compacted crates, some of which have fallen over, filled with sometimes unknown objects.

A submersible ROV capable of navigating between each of the crates could output valuable data on the mechanical state of the crate (whether it needs to be replaced due to rust or mechanical fault), whilst also locating unknown items of radioactive debris and waste.

Targeted removal of the debris could then take place with new crates properly installed and maintained, capable of storing the material until it can be completely decommissioned.

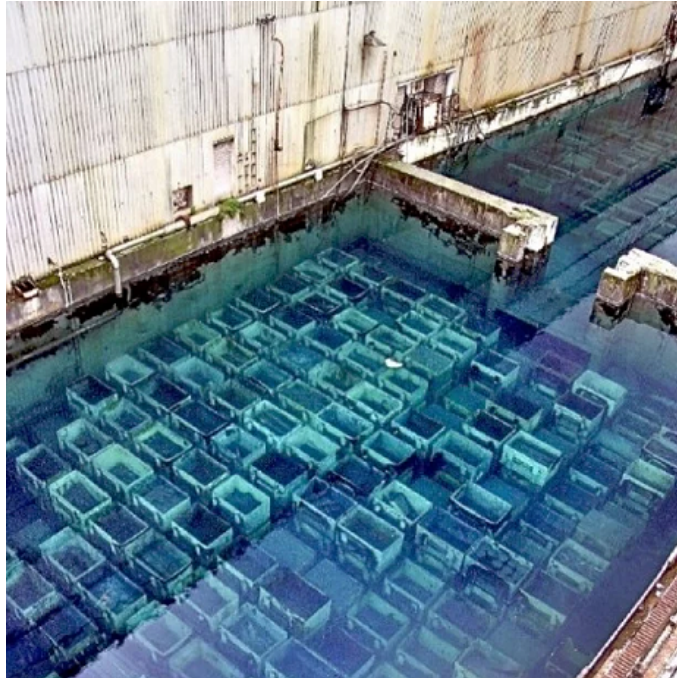


Figure 7.1: The current state of one of Sellafield's storage ponds [135]

While there are many problems facing the Sellafield site requiring a submersible ROV, much of the work in this project has focussed on a specific deployment case for Fukushima Daiichi. Therefore, the device must be capable of deployment within Fukushima with any deployment in Sellafield requiring only minor modifications.

7.1.2 Fukushima Environment

Six years after the Fukushima accident, much is still unknown about the internal state of the reactor. Fuel that was within the reactor during the explosion, is believed to have become molten and fallen through the bottom of the pressure containment vessel (PCV) and into the pedestal. It is possible that it remains within the reactor, however, or has fallen out of both the PCV and pedestal, or a combination of all three. Fig. 7.2 highlights the predicted environment and the area of deployment for a submersible ROV.

A shape changing robot was deployed by Hitachi in April 2015 [5]. Fig 7.3 outlines the robot and it's two main configurations. It is able to become one long shape to be passed through an access port and then bend to allow it to drive around an area of investigation.

This is the closest that a robotic platform has been to the PCV and centre of

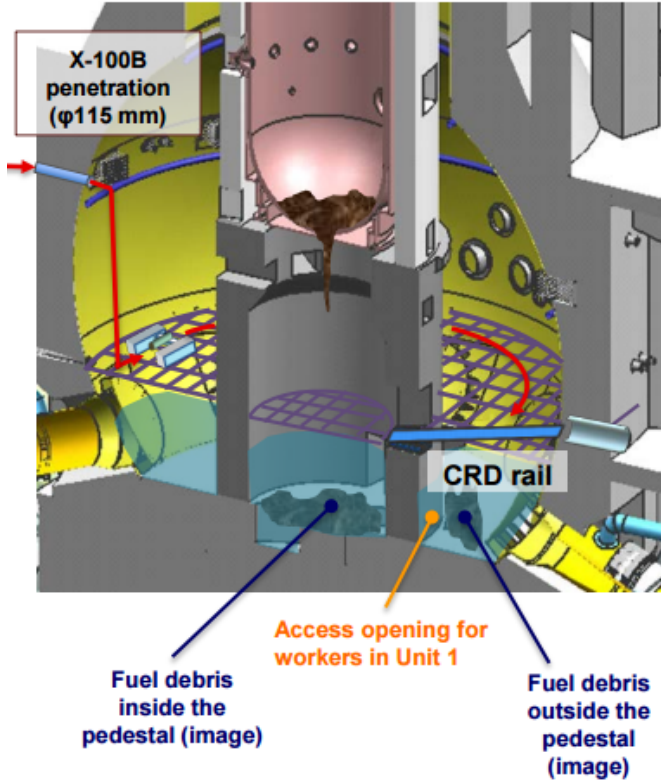


Figure 7.2: CAD overview of PCV, pedestal, grating and predicted fuel debris location [136].

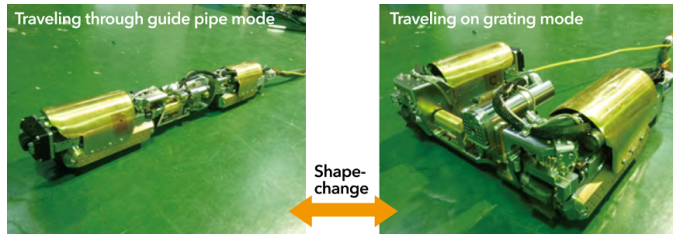


Figure 7.3: Shape changing robot developed and deployed by Hitachi [137].

the NPP. Two devices were deployed and tasked with moving around the grating in opposite directions. When one became stuck (see Fig. 7.4), the other one travelled to determine what had happened to it after characterising its side of the grating.

Fig. 7.5 shows a buckle on the grating whilst Fig. 7.6 shows a piece of grating that has fallen through its support.

This robot also discovered that the dose-rate within this area of the NPP was approximately 4 to 10 Gy(Si).h⁻¹. The operational lifetime of the shape changing robot was designed to be approximately 8 hrs requiring a TID tolerance of 80 Gy(Si), which it successfully survived. This dose-rate is approximately 16 times the values



Figure 7.4: One of the shape-changing robots stuck in grating gap.



Figure 7.5: Visual inspection of grating surrounding the pressure containment vessel [138].

seen in the Sellafield legacy ponds.

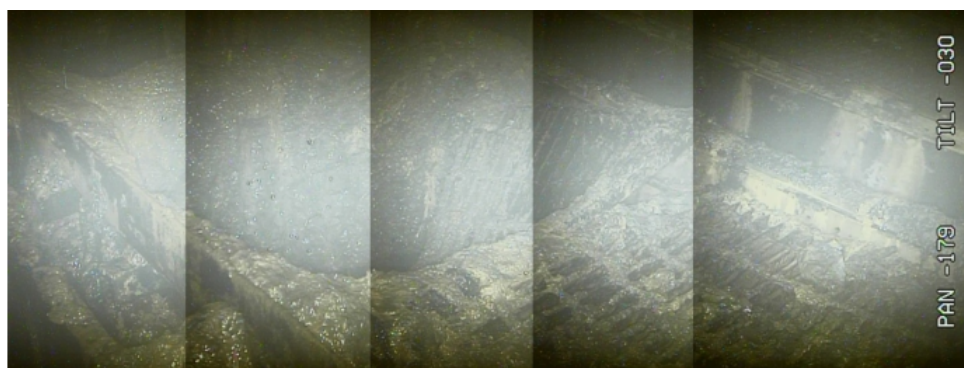


Figure 7.6: Collapsed grating within the Fukushima Power Plant [138].

Fig. 7.7 shows the deployment of Hitachi's swimming robot [136] within the suppression chamber around the PCV. It can be seen that the visibility is poor with very murky waters due to sludge and debris surrounding the Fukushima PCV. It is also

important to notice the amount of mechanical structures located within the water creating a cramped and cluttered environment for a submersible to navigate. It is likely to be more cluttered and have less visibility inside the PCV.



Figure 7.7: Footage of Hitachi's "swimming robot" deployed in Fukushima Daiichi Torus room [136].

Fig. 7.8 shows debris that has fallen into the suppression chamber. This debris highlights that the environment is unknown due to the mechanical failure of many structures during the reactor explosion and fire. It also indicates the build-up of sediment. This sediment is likely to have been caused from sand ingress after the tsunami and rust/dust build-up from the building remaining flooded for many years.

The movement of this sediment due to the recycling of water and thrusters from the ROV causes the water to become murky and have low visibility. It also should be considered a risk to any external actuators of the deployed submersible as it could clog thrusters or pumps and limit movement of the ROV.



Figure 7.8: Fallen debris within the flooded suppression chamber [138].

7.2 Submersible ROV Requirements

Many industrial solutions are not suitable for deployment in a small and cluttered environment consisting of radioactive debris. For example, any autonomous or tetherless devices cannot be deployed. This is because a tele-operator must be in full control of the robotic platform in a hazardous environment and conventional wireless communication techniques do not satisfactorily operate in a nuclear contaminated area [139]. Tethered systems also allow control of the robot many orders of magnitude further away from the hazardous environment in comparison with wireless techniques with less latency in communication [139].

Larger ROVs used for marine research or the oil and gas industry are also not suitable for deployment in the PCV. Fig. 7.7 highlights the cluttered environment in the suppression chamber surrounding the PCV with the PCV interior half as tall and wide. As with the shape changing robot, any submersible placed inside the interior of the PCV is likely to be sacrificial with size of the robot effecting number of deployments and ease of future investigations. Therefore, the presented ROVs were chosen for analysis due to their similarities with the requirements of this project.

The requirements for a submersible device to be deployed in the Sellafield legacy ponds or Fukushima Daiichi's Pressure Containment Vessel (PCV) were discussed with technicians from both facilities and included, but were not limited to;

1. Must be a tethered system.

2. Capable of carrying a payload of up to 1 kg.
3. Fit through a 150 mm (6") access pipe.
4. At least 3 degrees of freedom (d.o.f), forward/backwards, up/down and left/right.
5. Ability to interface with bespoke radiation detectors.
6. Ability to add physical characterisation sensors such as a sonar.
7. Adaptability to robustly integrate a range of as yet undetermined detectors
8. No battery.
9. Low-cost, with the constituent parts costing <£200.
10. Operating lifetime of 10 hours.

There are no submersible ROVs currently available that have the capability of meeting each of these requirements. The closest submersible to meeting this combination of requirements has been developed concurrently with this project and is dubbed the “little sunfish” designed and manufactured by Toshiba [140]. Currently, the payload of detectors is not known with the device recently deployed (Summer 2017) so will not be included in the main body of literature review, however, Fig 7.9 outlines the ROV and an image taken from within the PCV of Unit 3 in Fukushima.

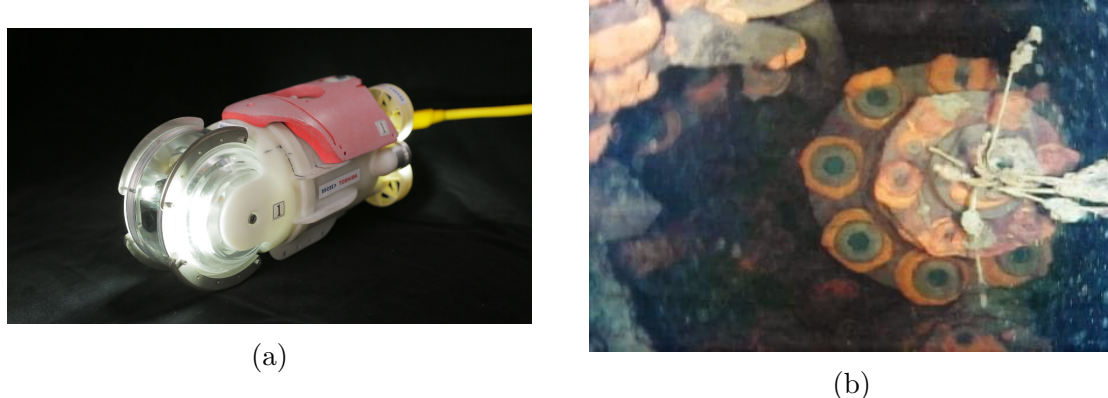


Figure 7.9: a) Outline of developed “little sunfish” and b), photo taken by the ROV from inside the PCV [140, 141].

7.3 State-of-the-art Research

A review of the state-of-the-art devices capable of meeting some of these requirements are discussed in this chapter. An evaluation of their specifications, as well as adaptability to a nuclear decommissioning environment is included and used to aid the

development of a robotic platform.

7.3.1 Ellipsoidal Vehicle for Inspection and Exploration (EVIE)

EVIE is a tether-less submersible ROV that was developed at the MIT, USA to inspect and explore in environments such as nuclear reactors, water pipelines, oil pipelines and submarine hulls [142]. Therefore, the design is very small as can be seen in Fig. 7.10.

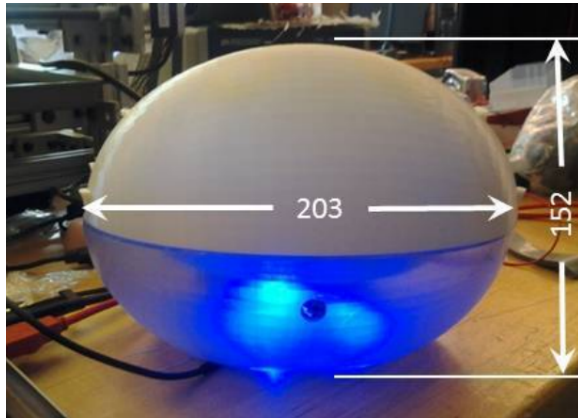


Figure 7.10: Dimensions of the EVIE robotic platform project [142].

The device utilises six water-pumps that allow the device to move in 5 d.o.f. and the hull is 3D printed meaning the constituent parts are low-cost. However, the control system governing movement is not stable due to the ellipsoid shape of the robot [142]. Future work intends to resolve this issue. EVIE is slightly too big for the requirements of this project and is not capable of a payload of 1 kg, but orientation of the water pumps could be utilised within a new design.

7.3.2 The Eyeball ROV

A spherical underwater ROV has been developed, in part supported by Mitsubishi Heavy Industries [143]. Fig. 7.11 outlines the shape and orientation of the ROV.

It can be seen that there are two fixed thrusters on either side of the ROV with a camera fixed to the exterior. The direction of motion is controlled by an internal eccentric mass. This rotates the main body of the ROV changing its heading, with the thrusters pushing the ROV in that direction.

With an external diameter of 120mm it is within this study's requirements, however, the spherical design can lead to difficulties during manufacture. Keeping the

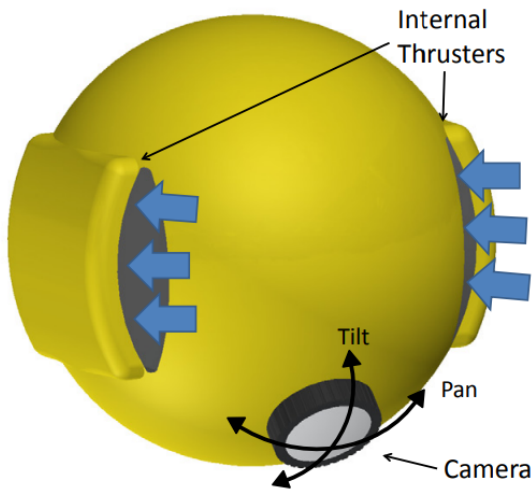


Figure 7.11: Overview of spherical robot with camera fixed on the exterior surface of the robot [143].

ROV water-tight has been problematic and this would be exacerbated with the addition of a tether mounting point. The small form factor also suggests the capable payload of the device is less than 1 kg.

7.3.3 EU-funded CoCoRo project

The Collective Cognitive Robotics research consortium [144] is funded by the EU 7th Framework program [145]. Their aim is to develop collaborative swarms of underwater ROVS capable of working together autonomously to achieve a pre-determined task.

There are two main underwater ROVs developed via this consortium. These are the JEFF ROV [146] and the Lily ROV [147]. They communicate via flashing blue LEDS and use these to position themselves relative to each other to act as a swarm. The two ROVs can be seen in Fig. 7.12.

Lily is primarily designed as a stationary marker within the swarm with almost negligible drift in open water. This is so they can relay communications from a base-station to all the constituent members of the swarm. It has dimensions of 130x100x70 mm. This means it has a diagonal dimension of 164 mm making it too large for our requirements. Two thrusters at the rear of the ROV and a central thruster enable movement in 3 d.o.f.

JEFF acts as a high-speed and manoeuvrable complimentary design to the Lilly ROV. Developed to speed up search-route success in conjunction with other JEFF

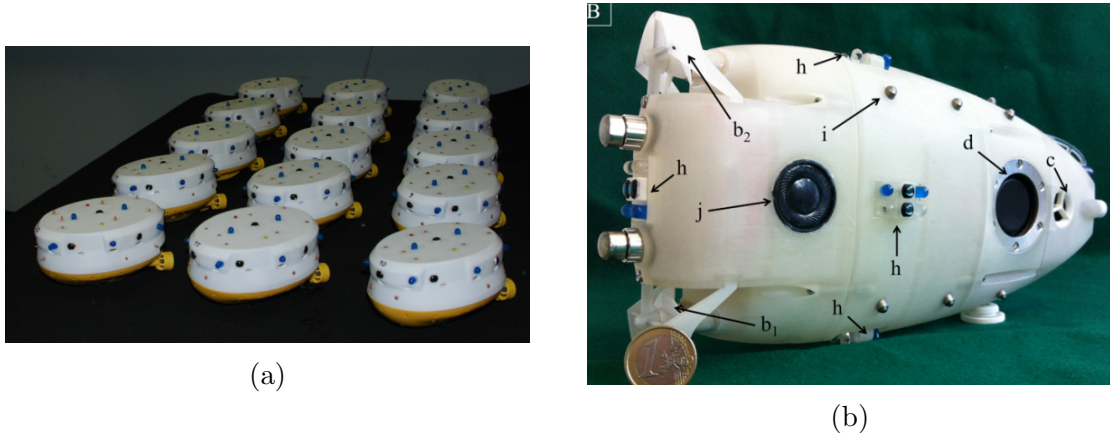


Figure 7.12: a) Overview if Lily robot design [147] and b), overview of Jeff robot design [146].

ROVs and the Lily ROVs it is powered with two rear facing propellers and a lateral propeller. The buoyancy is controlled via two pistons that alter the volume of the robot whilst using membranes to maintain water-tightness [146]. The letters in figure 7.12b represent a. shell, b. aft propulsion units, c. bow thruster unit, d. buoyancy system, e. control and power management PCBs, f. battery pack, g. expansion connector for sensors, h. blue lights, k. underwater docking station, l. microphone.

The size, payload and wireless communication protocols mean that these devices could not be deployed within Fukushima. However, the buoyancy system of the JEFF robot and manoeuvrability of the Lily robot should be considered in the design of a robotic platform.

7.3.4 Swimming Robot

Submersible robots have already been deployed at Fukushima to gather information on the internal state of the power plant. Fig. 7.13 highlights Hitachi's "swimming robot" that has been deployed in the Fukushima Daiichi suppression chamber [136].

The submersible consisted of three thrusters, two at the rear and one in the middle. This created left, right, up, down and forward movements. High powered lights and a camera were also used for visual inspection. The approximate size of the ROV is 700 mm x 500 mm x 500 mm.

Visual inspection was completed and analysis of the water flow was tested with the use of a tracer placed in the water by the submersible. This tracer was then monitored



Figure 7.13: Hitachi’s submersible robot for surveying of leakage points from PCV [136]

via an ultrasonic sonar system on a separate submersible to determine if there were unknown leaks of the coolant [136].

This solution was designed for deployment inside the suppression chamber outside the PCV and was successful in characterising that environment. However, it is too big and cumbersome to be deployed through an access port for further characterisation of the internals of the PCV.

7.3.5 Deep Trekker (DTG2)

The deep trekker comes in many formats. Fig. 7.14 outlines the starter package that costs approximate \$4,500 at time of writing [148]. This increases with the addition of manipulators or thrusters.

The movement of the deep trekker is controlled via two thrusters at the rear, whilst an internal mass rotated by a motor alters its centre of gravity. This pitch control directs the front of the ROV in an almost 180° arc from straight down to straight up. The thrusters then push the DTG in the direction it is pointing.

It is battery powered (up to 8 hours), with an HD camera and neutrally buoyant tether. Mounting points facilitate the addition of further sensors or manipulators dependent on the requirements [148].

The DTG2 is battery-operated and 325 mm x 258 mm x 279 mm, which is larger



Figure 7.14: Deep Trekker (DTG2) starter pack [148].

than the 150 mm diameter access port into Fukushima or Sellafield. However, the direction control is of interest to reduce the number of actuators and power requirements of an ROV design.

7.3.6 Video Ray

The VideoRay is an ROV that has been used by customers such as the U.S. Navy and coast guard as well as by James Fisher Nuclear to explore the First Generation Magnox Storage Pond (FGMSP) [149]. Therefore, it has experience deployed in a nuclear decommissioning environment. A photograph of the ROV can be seen in Fig. 7.15.



Figure 7.15: VideoRay voyager submersible [150].

The VideoRay consists of three thrusters, two at the rear and one in the middle for depth control. It offers an HD camera, depth sensor and a compass [150]. It also offers customisable features and modular replacements for parts.

The size of the video ray is 375 mm x 289 mm x 223 mm which is larger than the required diameter. However, the power for the ROV is transmitted through the tether and it is capable of interfacing multiple sensors. The communication protocol and power circuitry were considered relevant for further analysis.

7.3.7 AC-ROV

The AC-ROV 100 is a submersible ROV manufactured by AC-CESS [151]. It has a very small form factor, able to pass through a pipe of diameter 190 mm and is very mobile. It is primarily used as a visual inspection tool for hard to reach and cramped spaces. Fig. 7.16 shows its small and compact design.



Figure 7.16: AC-CESS AC-ROV submersible ROV [151].

The AC-ROV is powered by four lateral thrusters that are offset to enable movement in any lateral direction. It also has two vertical thrusters that allow tilting at the front and rear. Unlike many commercially available ROV units it is powered via the tether and therefore, does not rely on a battery. However, it can only carry a payload of 200 g and fit through a 190 mm diameter pipe meaning it could not be deployed in Sellafield or Fukushima. The 5 d.o.f movement makes it the most manoeuvrable

of the ROVs discussed and should be considered during actuator layout design of our ROV.

7.3.8 OpenROV

The OpenROV 2.8 kit is an open-source project designed for a community to help improve the design and functionality [152]. It has gone through many editions with the current one at time of writing the 2.8. It features three brushless thrusters, two at the rear and one for depth control, as can be seen in Fig. 7.17.



Figure 7.17: OpenROV v2.8 kit [152].

The ROV is neutrally buoyant, streams HD video, has the capability to attach more sensor units and has a neutrally buoyant tether. One of the most relevant features is the web interface and control, which condenses the tether into two thin wires. This greatly improves manoeuvrability, decreases cost and entanglement from unknown objects. It also means the communication speed is very high. This was integrated within our robotic platform and is discussed in greater detail in Chapter 8.

The size of the OpenROV is 300 mm x 200 mm x 150 mm, which is larger than the 150 mm diameter required and due to the orientation of the thrusters, it is not as manoeuvrable as the AC-ROV.

7.3.9 Forth AVEXIS

Forth engineering have developed an underwater submersible, based off the lessons learned in their partnership with the University of Manchester called the Forth AVEXIS [153]. Fig. 7.18 outlines the design.



Figure 7.18: FORTH AVEXIS [153].

It is one of the fastest underwater submersibles currently available, with a maximum speed of 0.5 m.s^{-1} , and has both a front and rear facing camera to allow visual inspection to occur simultaneously in two directions, thus avoiding entanglement with unknown obstacles behind the submersible.

It contains three thrusters, two at the rear and one in the middle for depth control and is mainly cylindrical in shape. At 450x145 mm, it is one of the biggest submersibles and at 8 kg it is also one of the heaviest, however, it meets the requirements of the outer diameter and also has mounting points for additional sensors or payloads. The manoeuvrability is limited though due to its long cylindrical shape and only 3 actuators. It also requires a battery for operation.

7.3.10 AVEXIS

The Aqua Vehicle EXplorer for In-situ Sensing (AVEXIS) was initially constructed as part of a PhD thesis at the University of Manchester [154]. Fig. 7.19 outlines the orb shape and six propeller thrusters used for omnidirectional control.

Designed to be a low-cost solution to monitoring the Sellafield Legacy ponds, the original AVEXIS was able to show proof-of concept design with a few reliability problems concerning the actuators and water sealing design.

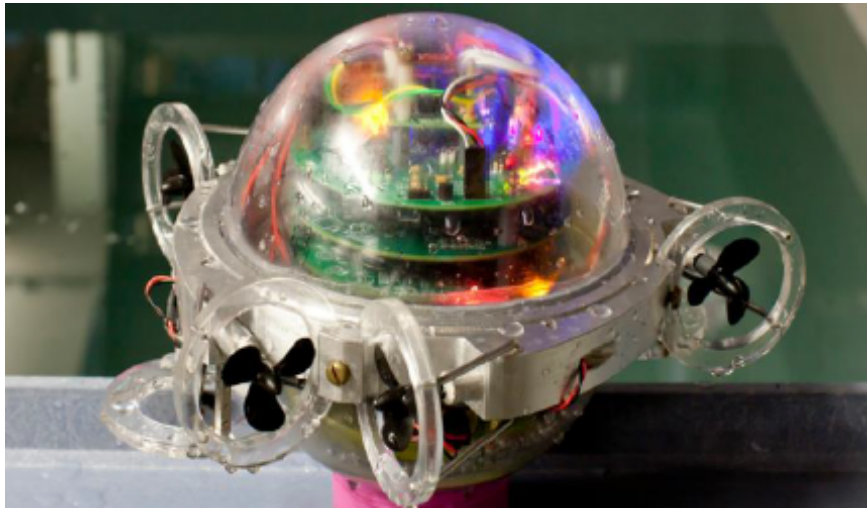


Figure 7.19: The University of Manchester's original concept AVEXIS [154].

The AVEXIS has been improved further resulting in a change of design. Thrusters were replaced with pumps, the orb was replaced by a cylindrical tube and difficult to manufacture CNC machined aluminium collars were replaced by 3D printed hulls [4]. Fig. 7.20 shows the current state of the AVEXIS. Capable of a payload approximately 500 g and more powerful pumps (93 mN in comparison to 26 mN for the original thruster concept [4, 154]).



Figure 7.20: The University of Manchester's AVEXIS [4].

This design is not without its drawbacks. The 3D printed hulls were very difficult to waterproof due to the layering technique of 3D printing whilst also being slightly

porous in nature. To achieve neutral buoyancy the weight must be kept constant and an increase due to absorbed water in the hulls led to the submersible sinking.

The tether was also cumbersome as it was stiff, which effects the manoeuvrability of the ROV, and it was heavy, making it difficult to propel forwards.

7.3.11 Evaluation of current Technology

Development of a suitable submersible to characterise the internals of the Fukushima NPP requires a combination of multiple technologies. Table 7.1 combines the important information from each of the ROVs discussed.

Table 7.1: Summary of the main specifications of discussed submersible ROVs.

ROV	Payload	Size	d.o.f	Sensor Integration	Battery or tether	Cost
EVIE	Not known	203 x 152 (mm)	5	Ultrasonic sensor	Battery	N/A
Eyeball ROV	Not known	120 (mm) diameter	3	Camera	Battery	N/A
Lily	Not known	130 x 100 x 70 (mm)	3	Temp, chemical and camera	Battery	N/A
JEFF	Not known	250 x 120 x 50 (mm)	3	Temp, chemical and camera	Battery	£1,100
Swimming Robot	>1 kg	N/A	3	Dose-rate, camera	Tether	N/A
DTG2	approx 500 g	325 x 258 x 279 (mm)	2	Adaptable	Tether	\$6,000
Video Ray	Not known	375 x 289 x 223 (mm)	3	Adaptable	Tether	\$5,000
AC-ROV	200 g	190 mm dia.	5	Adaptable	Tether	N/A
OpenROV	<500 g	300 x 200 x 150 (mm)	3	Camera	Tether	\$1,000
Forth AVEXIS	Not known	450 x 145 (mm)	2	Camera	Battery	£10,000
AVEXIS	<500 g	150 mm diameter	3	Camera, depth	Tether	£200

As can be seen, many of the devices lack the ability to carry a payload of >1 kg, the only exception is the large Hitachi swimming robot. The Forth AVEXIS and eyeball ROV represent the only ROVs with the required diameter, but they do not

have enough d.o.f in comparison to the AC-ROV and AVEXIS.

Sensor integration varied with the bigger and more expensive ROVs being capable of adaptable sensing units, while the smaller and cheaper units had very limited potential for sensor integration.

It can also be seen that many of the ROVs operate with batteries. This introduces a hazard in a nuclear environment with the possibility of production of noxious gases from the materials within the batteries, as well as increasing the weight of the ROV, reducing the payload of the ROV.

The cost of the ROVs varies widely, with some values unobtainable due to unavailability in the literature. All devices are more expensive than the AVEXIS with the most comparable the OpenROV project, which has a value of \$1,000. This is 5 times the amount required to spend on the ROV.

These properties result in the unsuitability of each of the discussed ROVs for deployment within Fukushima. However, lessons can be learned from these devices that allow the development of an improved device capable of meeting the specifications of both Sellafield and Fukushima. For example, the communication protocol deployed in the OpenROV and the manoeuvrability of the AC-ROV.

7.4 Sensor Instrumentation

To complete the design of a suitable robotic platform, sensors used for characterisation must be integrated. The major sensor suites required in a nuclear decommissioning robotic platform are;

1. A gamma detector for dose-rate monitoring and isotope identification.
2. A sonar for physical characterisation.
3. A neutron detector to determine neutron flux. (This is not included in this work)

Radioactive isotope identification is important to determine the location of the fuel debris, the primary target for decommissioning, whilst dose-rate monitoring analyses the safety of the environment. Sonar data would be invaluable in location and characterisation of debris.

This project includes collaboration with the University of Lancaster. This relationship means that they provide radiation detectors, which the University of Manchester

were tasked with integrating within their ROV, whilst also devising a way to pass the data from the detector to the surface for analysis. The chosen radiation detectors will be discussed in Chapter 8.

Another set of collaborators linked with this project are the National Maritime Research Institute, the Japan Atomic Energy Agency and Nagaoka University, all based in Japan. They were tasked with procurement and development of a sonar for physical characterisation of Fukushima Daiichi. Full integration of the sonar including the communication protocol and data analysis was undertaken by the University of Manchester. The sonar will be discussed in Chapter 8.

7.5 Summary and Evaluation of Current Research

There are many submersible ROVs currently in the market, however, none of them meet the requirements outlined at the beginning of this chapter. It was thought that a combination of some of the ROV specifications can be developed into one deployable robotic platform.

To increase speed of development, work will concentrate on improvements to the current AVEXIS project at the University of Manchester. It meets the cost, size and d.o.f requirements with improvements required to the tether system for manoeuvrability, as well as sensor integration and general ruggedness of the design to meet stringent controls for deployment within the Fukushima PCV.

Analysis of the environment has highlighted the cluttered and low visibility nature of the PCV. Whilst dose-rate monitoring suggested dose-rates of up to 10 Gy(Si).h^{-1} . If dose-rates stay consistent this would require the AVEXIS to be tolerant to a TID of up to 100 Gy(Si), but it is possible that the dose-rate will increase within the PCV by up to ten times. This must be taken into consideration during the design.

The work completed to develop the AVEXIS project for suitable deployment within Fukushima is outlined in Chapter 8.

Chapter 8

Development of a Submersible ROV

Characterisation of nuclear decommissioning environments is required to enable safe and efficient dismantling. With many submerged nuclear waste facilities, an ROV capable of monitoring and locating both gamma and neutron radiation sources whilst also detecting unknown debris is desirable.

To develop a device with these capabilities, a set of redevelopments were required to be made to the University of Manchester’s AVEXIS vehicle [4]. This was to produce a robust robotic platform to allow the integration of detectors. The redevelopments chosen included; a new design for the communication protocol, to enable integration of a more sophisticated range of detectors that require high throughput data streams whilst using a smaller, more flexible tether, that can also provide the required power supply. Re-development of the hull to increase the payload up to 1 kg, whilst refining water-proofing techniques and making improvements to the electronic design.

Following implementation of the new designs, the capability of the ROV to characterise unknown nuclear waste was analysed through the integration of a gamma detector and sonar. Adaptability of the device to enable the addition of a neutron detector during the next iteration of the ROV was also completed. The aim of these additions was to enable technical demonstrations of the fully integrated device to our collaborators.

To permit complete localisation of radioactive waste and debris, a new positioning system was developed to integrate with the measurements gathered from the gamma

detector and sonar. An initial prototype of a vision based localisation system is discussed in this chapter.

This chapter outlines work completed towards the development of the AVEXIS to be deployed in Fukushima Daiichi and also includes analysis of technical demonstrations conducted in the UK and Japan.

8.1 Development and Integration of New Designs

Initial work concentrated on the improvement of the mechanical and electronic design of the AVEXIS. Areas highlighted for improvement from previous versions of the AVEXIS were;

- Waterproofing.
- End-caps that became heavier due to absorbed water and cause the device to sink.
- Electronics reliability.
- Noisy camera feed.
- Difficult to maintain.

By improving these areas, a robust platform for integration of the required sensors could be achieved. This would allow radioactive isotope characterisation and construction of an underwater 3D-point cloud visualisation. These capabilities would aid in the complete characterisation of the PCV at Fukushima.

8.1.1 Waterproofing and assembly

The initial AVEXIS used thermally extruded plastic hulls made from a 3D printer to allow quick prototyping and to keep the system low-cost. However, thermally extruded 3D printed parts are not inherently waterproof due to the layered nature of printing.

To attempt to improve water-tightness of the 3D printed hulls, a double hull design was used with space for a polyurethane layer between each hull to create a watertight barrier. This was accompanied by silicon sealant to cover any leak points. Unfortunately, this was not entirely watertight.

A new design was developed and implemented as a direct replacement. Polyvinyl chloride (PVC) plastic endcaps were manufactured with two grooves for two 5.6 mm diameter o-rings. This created a double seal between the inside of the tube and the endcap, which can be seen in Fig. 8.1. This allowed easy assembly and dis-assembly whilst retaining a watertight seal. Fig. 8.2 outlines the dimensions of the AVEXIS.

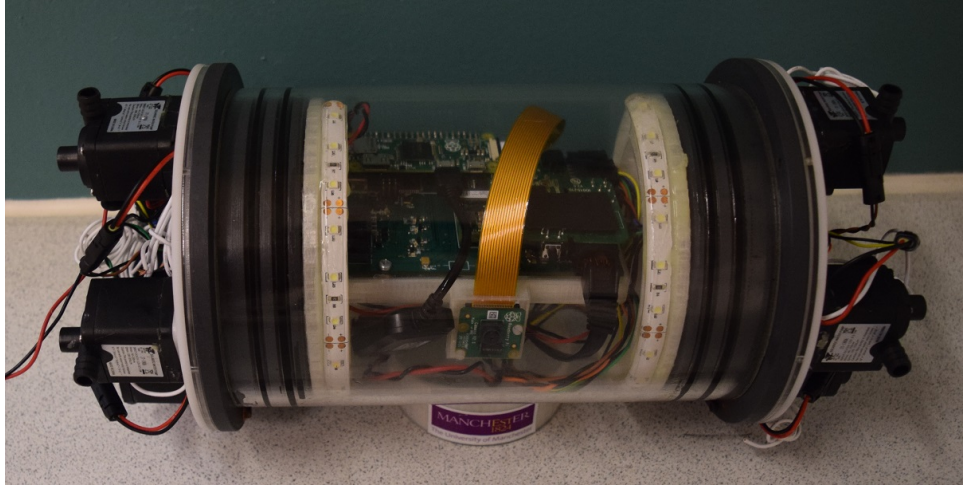


Figure 8.1: End-caps made from PVC with two o-rings for waterproofing.

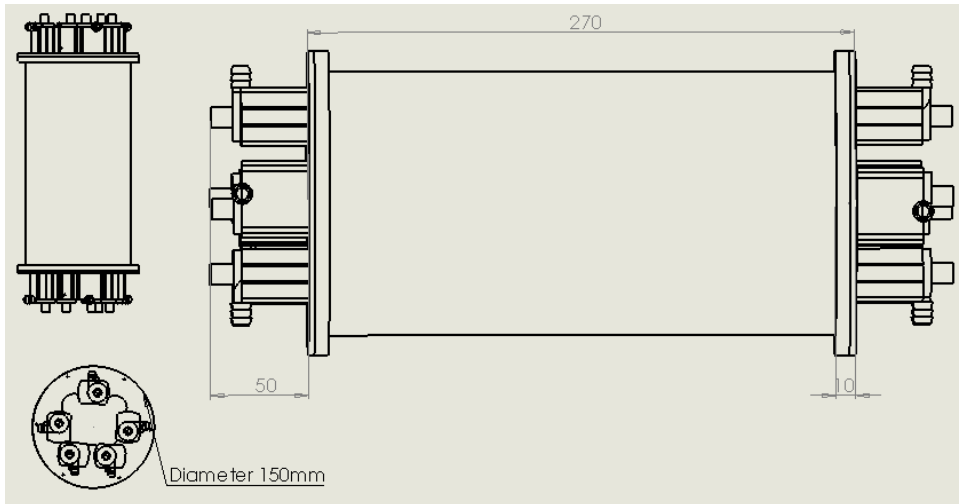


Figure 8.2: Dimensions of AVEXIS ROV

This type of design has previously been tested for waterproofing to a depth of 100 m [155]. However, due to limited access to equipment capable of simulating 100 m depth at the University of Manchester, a depth of 10 m was tested with no leakage found. The depth of the water in Fukushima Daiichi is known to be approximately 5 m and therefore this design was considered suitable.

PVC has been shown to produce HCl when exposed to gamma irradiations, but it is believed that the dose required to produce HCl is more than received during the operational lifetime. However, if the device is deployed in Fukushima, other materials would be explored to replace the PVC end-caps and reduce this likelihood.

Another cause of water-leaks was the entry point of external wires. A set of “cable penetrators” were manufactured based on a similar design used by blue robotics [156]. The design consists of a metal bolt with a bore that wires can be passed through. A mould was then manufactured to submerge the gaps between the wires and casing with epoxy. This created a watertight seal in-between each of the wires through a penetrator that can be unscrewed for maintenance. Fig. 8.3 outlines this structure.

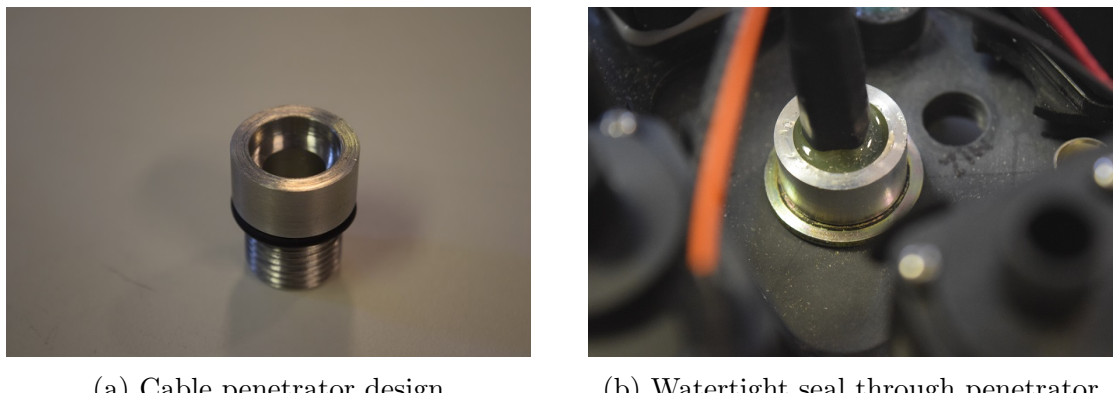


Figure 8.3: Outline of cable penetrators manufactured for watertight seal around entry cables.

A test was conducted to determine the water tightness of the cable penetrators when combined with the PVC endcaps. A vacuum tube was placed in an IP69 cable gland with a vacuum pump removing all air from inside the AVEXIS. This simulated water pressure from the outside pushing in. An air valve monitor was read to determine if there was any loss of pressure with none witnessed up to the required 10 m depth measurement.

8.1.2 Communication Protocol

It was decided to change the communication protocol to allow the reduction in size of the tether. This section outlines the initial constraints of the previous system before discussing the changes made and how it was integrated into the system.

Tether

A major problem of the initial tether was the flexibility. The tether resisted movement in every direction due to the rigidity of the cable. It was also relatively large (12 mm diameter) making it difficult to drag when in a large pond. Fig. 8.4 shows the turning radius and size of the tether relative to the AVEXIS.

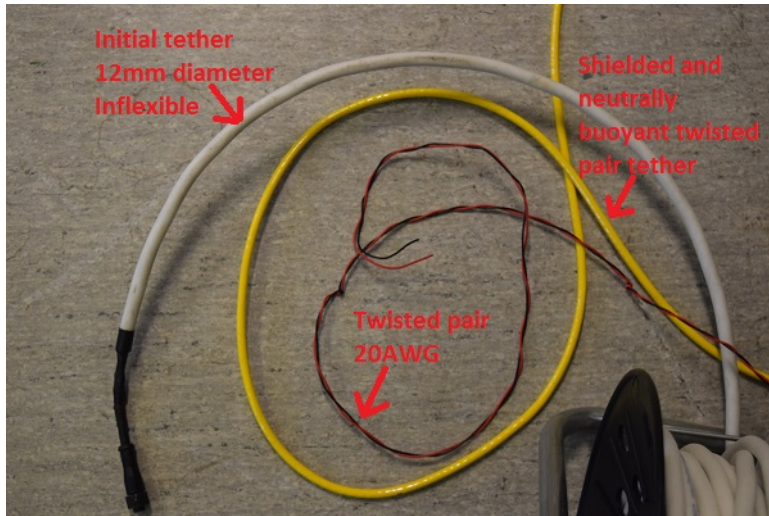


Figure 8.4: The outer white tether was the initial design. A twisted pair of 20 AWG can be seen in the centre for comparison.

The OpenROV open source community have developed a two-wire tether system based on powerline home adaptor technology [157]. An overview of a home-based powerline system can be seen in Fig. 8.5. This works by transmitting an Ethernet signal from the home's router, to a powerline adaptor plugged into the mains cabling, which overlays the Ethernet signal to all the plug sockets in the house. This allows a powerline adaptor plugged into any other plug socket to provide an Ethernet signal to any attached device. For example, a smart TV in the lounge or a desktop computer in the study.

This technology was implemented onto the AVEXIS using the Tenda home plug adaptor [159] and a Raspberry Pi Zero as the interface to the control board within the AVEXIS. Fig.8.6 shows the flow of communication and power for the system.

An Ethernet powerline adaptor placed inside the surface power supply overlays the signal onto the two power wires leaving the power supply at 48 V and GND. Within the ROV is another Ethernet powerline adaptor to retrieve the signal from the power wires. An Ethernet cable is then connected to the Pi Zero via a micro-usb to Ethernet

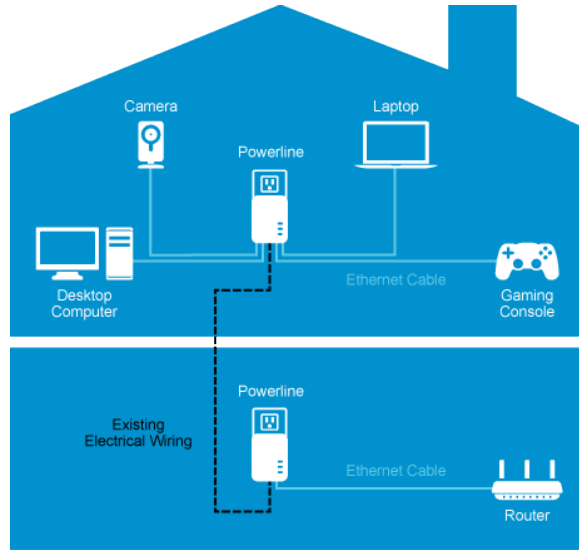


Figure 8.5: A local network is created from a surface laptop and multiple devices can attach to the same network through multiple powerline adaptors [158].

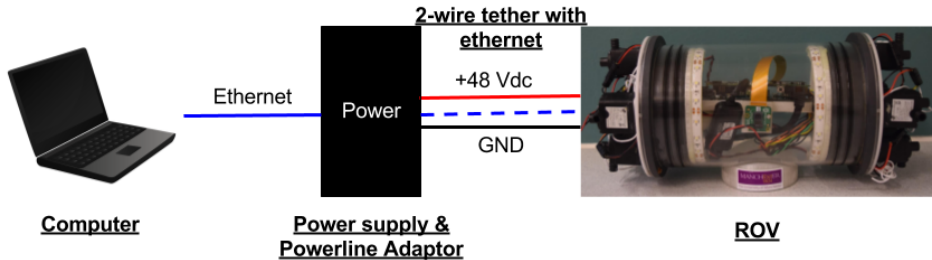


Figure 8.6: Overview of the communication from a surface based computer to the submersible.

adapter.

Fig. 8.7 shows the initially deployed tether incorporating this system. It was made from two individual 20 AWG wire twisted into a pair. It can be seen that the size is much smaller than the original tether seen in Fig. 8.4 and it is more flexible.

Although it worked as a proof of concept, it was not neutrally buoyant, and therefore caused the ROV to sink once more than 5 m of tether was released. Therefore a neutrally buoyant tether was acquired and swapped for the two-wire tether.

The new tether was neutrally buoyant, encapsulated with a strong exterior plastic and is made of 6 x 26 AWG wires that can be combined into two sets of 3. One set for +Vd.c. and the other for GND. The communication system was unaffected by the change in tether.

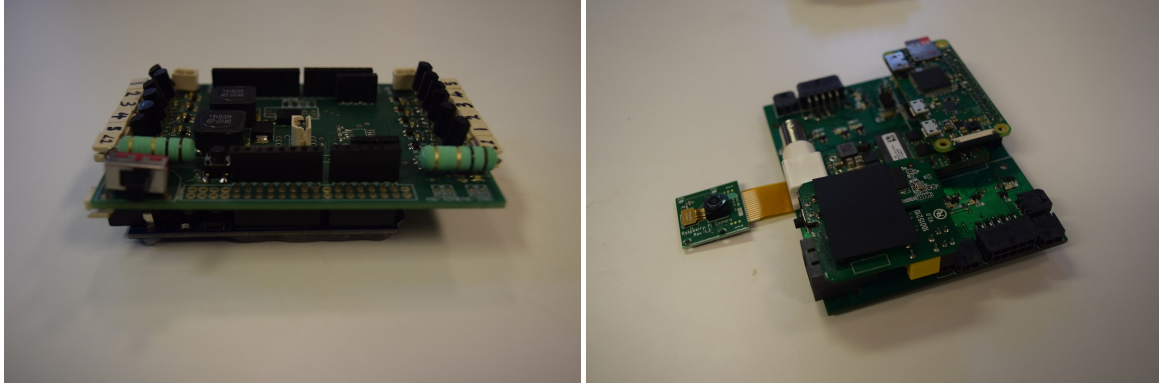


Figure 8.7: Initial two-wire tether prototype.

8.1.3 Electronic Design

The main power and control board required redesigning to manage the new communication protocol and improve reliability issues with the original electronic system.

The new power system was based off an industry standard power brick (General Electric EVK011A0B41Z [160]) with space made for the powerline adaptor and pi zero for communication. Fig. 8.8 outlines the circuit board prior to development and after.



(a) Initial circuit board

(b) Newly designed circuit board

Figure 8.8: A comparison of new and old boards showing the modifications in terms of size and robustness.

Figure outlines the block diagram of the PCB with the incoming communication and power passing through the powerline block, which enables the Pi Zero to be accessible via the base station. Instructions can then be passed from the Pi Zero to the Atmega32U4 that interfaces all I/O components such as the pumps, depth sensor and IMU.

Temperature tests were conducted on the main drivers and power brick with 3

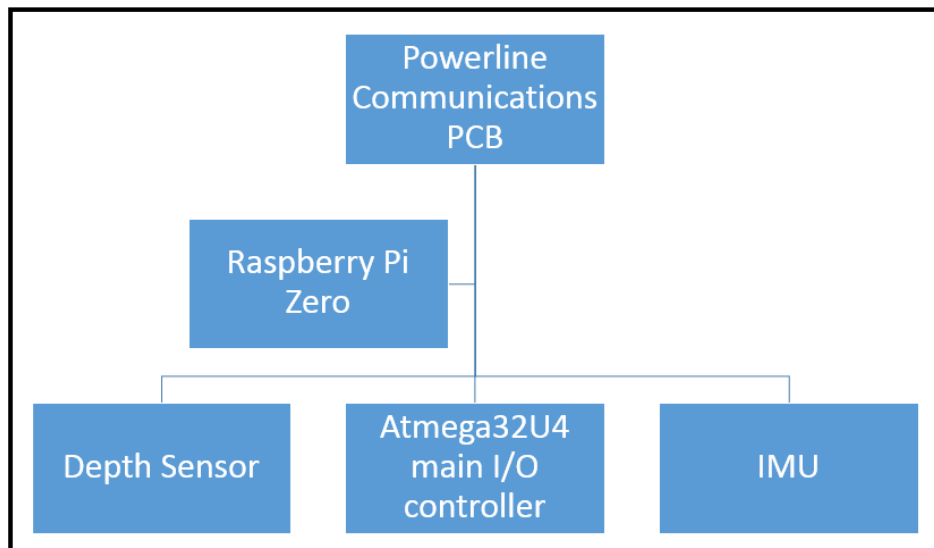


Figure 8.9: Block diagram of the ROV's PCB.

pumps on both side fully on and the LEDS on. Temperatures were taken from the motor drivers and power brick. After 30 minutes the temperature of the motor drivers had reached 45 degrees Celsius while the power brick had reached 55 degrees Celsius. These values remained the same for the next half an hour, at which point the test was stopped.

It is thought these conditions of 6 pumps on at the same time constantly for 1 hour is much more power intensive than a realistic operation where no more than 4 pumps are on at the same time and are only operated intermittently.

The new circuit design also integrated all constituent parts onto one circuit board, making it a lot more rugged with no loose connections due to placement on top of each other or unwanted shorts. It also leaves more space for air to travel over the PCB keeping it cool during operation rather than enclosed by an arduino.

8.1.4 Control Interface

With the introduction of Ethernet as the communication medium, a Pi Camera could be used at full High Definition resolution to transmit a live video feed from the AVEXIS. This is an improvement on the noisy camera feed of the previous design due to the use of Ethernet communication, unaffected by the switching power supply, in comparison to an analogue communication protocol used previously.

The Raspberry Pi Zero could also act as a web server that could be accessed from

any web browser on the same network. Therefore, joystick and keyboard control could be implemented through a web page that the video feed was being transmitted too. This is seen in Fig. 8.10.

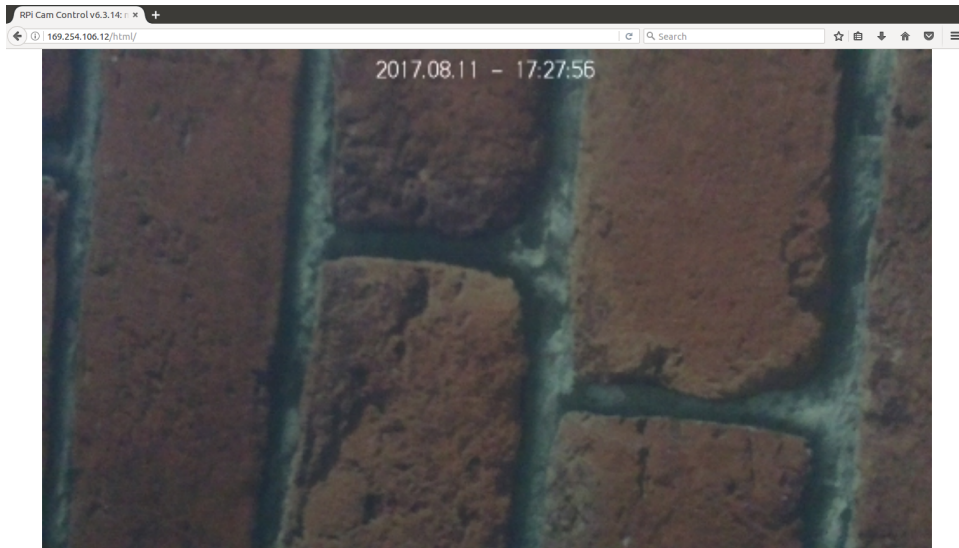


Figure 8.10: Screenshot of the camera feed as seen in a web browser.

This also aids portability of operation with any computer able to control the AVEXIS reducing base station size and cost outlay. The addition of any web-enabled sensor is also possible on the same two wire tether as long as further powerline adaptors are added. This means each device is assigned a separate IP address and can be accessed individually.

8.2 Radiation Sensor Integration

The radioactive environment within Fukushima consists mainly of melted nuclear fuel. This debris acts as both a gamma and neutron radiation source. Therefore, integration of gamma and neutron detectors capable of dose-rate monitoring and radioactive isotope identification are important for full characterisation of the environment. This work concentrates on the integration of a gamma detector, with work on integrating a neutron detector required in future work.

This section outlines the work conducted to integrate a gamma detector into the AVEXIS with the systems put in place also applicable to a neutron detector, which is therefore not discussed in this study. Tests conducted to evaluate the sensor output are discussed.

8.2.1 CeBr₃ detector implementation

As part of the collaborations involved with this project, the University of Lancaster procured a gamma detector based on Cerium Bromide (CeBr₃) to measure gamma dose-rates and also enable isotope identification. An overview of the detector can be seen in Fig. 8.11.

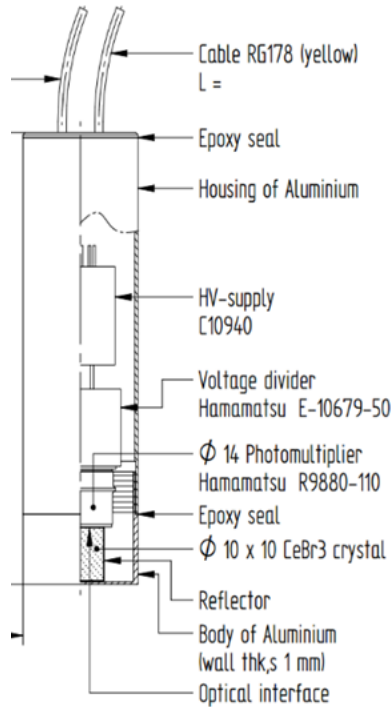


Figure 8.11: Overview of the CeBr₃ gamma detector.

To integrate this detector within the AVEXIS, changes to the power board were required to produce power for the detector whilst a further connection to the surface was required for the detectors signal to the surface.

Fig. 8.12 outlines the size of the detector in relationship to a 1p coin whilst also showing a casing that was manufactured to protect the detector in the unlikely event of a complete failure of the AVEXIS hull.

Initially, it was hoped to gather the data in the ROV and transmit along the two-wires, but this was considered infeasible within the time-frame required. Therefore, a RG178 coaxial cable was bought to be used as an auxiliary signal tether when the detector was in use. This was attached to the exterior of the tether and had a negligible effect on the drag. Future editions of the tether could include this coaxial cable within a protective sheath to reduce the possibility of entanglement.



(a) CeBr₃gamma detector from SCIONIX [161]. (b) Watertight container for the CeBr₃ detector

Figure 8.12: CeBr₃ detector and bespoke water-tight container.

Water tank testing

Having integrated the detector within the ROV, tests were required to validate operation. The combined system was initially tested on a laboratory benchtop to ensure suitability of the ROV power supply when the detector was operational. This also confirmed that the detector signal was transmitted successfully over the 50 m RG178 tether without degradation or noise overpowering the signal. The set-up is shown in Fig. 8.13.

The response of the detector to a 10-minute exposure of a 330 kBq ¹³⁷Cs source located outside the ROV was analysed and found to be suitable for correct identification of the radioactive source. Fig. 8.14 outlines the gamma spectrum observed during the 10 minute exposure.

This test outlined the ability of the ROV to detect a radiation source with the gamma detector powered via the ROV and the signal returned via a 50 m tether. This suggests that the same could be achieved underwater. It is also worth noting that it is unlikely a tether this long will be deployed, therefore, attenuation experienced through the tether will be reduced with a shorter cable.

The ROV was then tested using a tank located at Lancaster University. The same



Figure 8.13: Exposure of the CeBr₃ gamma detector integrated within the ROV to a Cs¹³⁷ source on a lab bench-top.

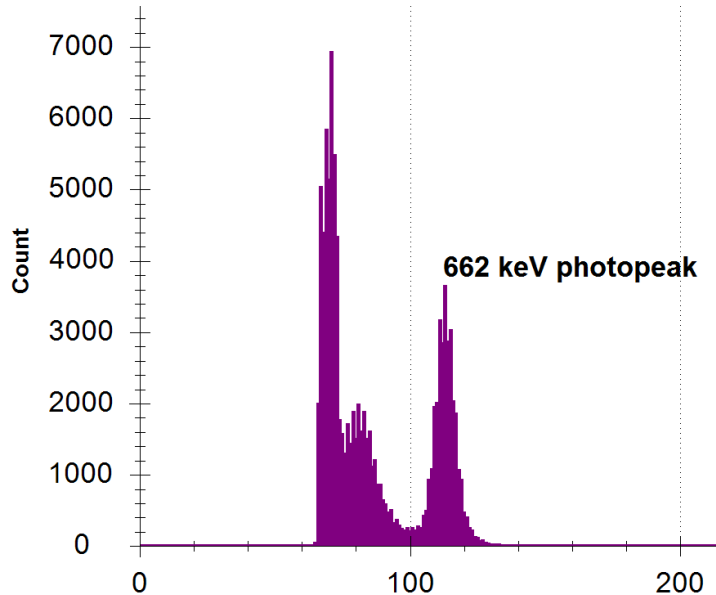


Figure 8.14: Initial measurement of radioactive counts exposed on a lab benchtop whilst integrated within the ROV for 10 minutes.

¹³⁷Cs source was placed on the side of the tank. Fig. 8.15 outlines the set-up of the experiment.

Initial tests involved submerging the ROV at two specific distances. The first distance was as close to the tank edge as possible, whilst the second was with the ROV at a distance of 0.5 m from the side of the tank. The tank wall was made from approximately 25 mm thick glass. A 10-minute exposure at each position was taken with the spectra received seen in Figs 8.16 and 8.17.

The experiments found that the same radioisotope could be identified through a

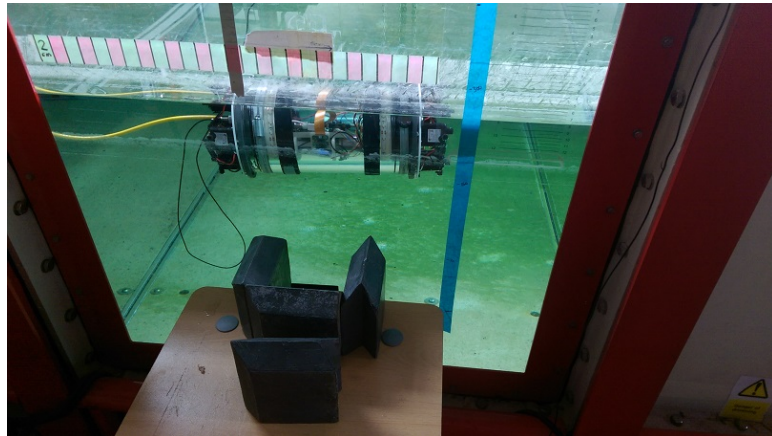


Figure 8.15: Exposure of the CeBr₃ gamma detector integrated within the ROV to a Cs¹³⁷ source whilst submerged.

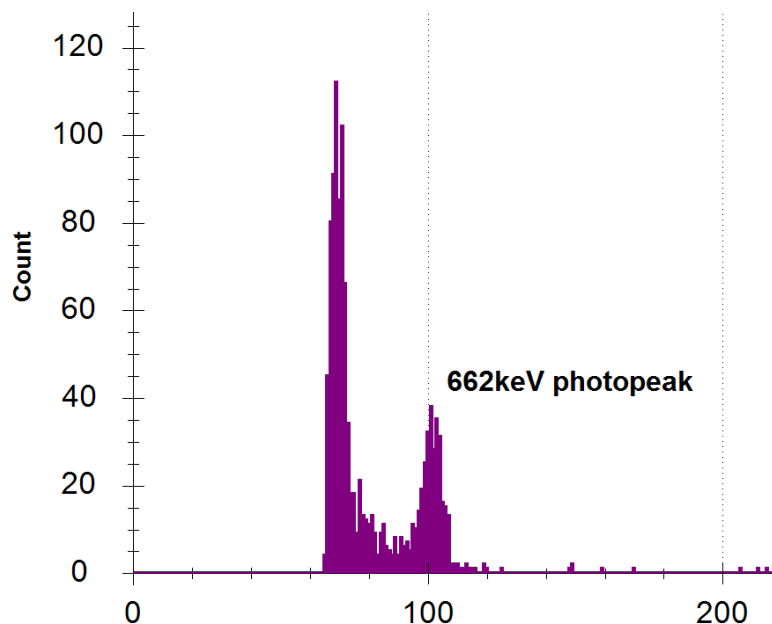


Figure 8.16: Counts observed with the ROV submerged but as close as possible to the source for 10 minutes.

medium of water. However, due to the minimal activity of the source, it was difficult to gather a distinct gamma spectrum with the ROV 0.5 m from the tank wall during a 10-minute exposure. The shape of the gathered spectrum was apparent and it is believed that a longer exposure or source of higher activity would output a clearer gamma spectrum. This suggests that the ROV is capable of underwater radioisotope identification.

Whilst submerged, it is possible that the CeBr₃ gamma detector could determine the location of gamma sources by collecting the number of counts over a set time period at pre-determined positions. The ROV could then be positioned so that the detector is

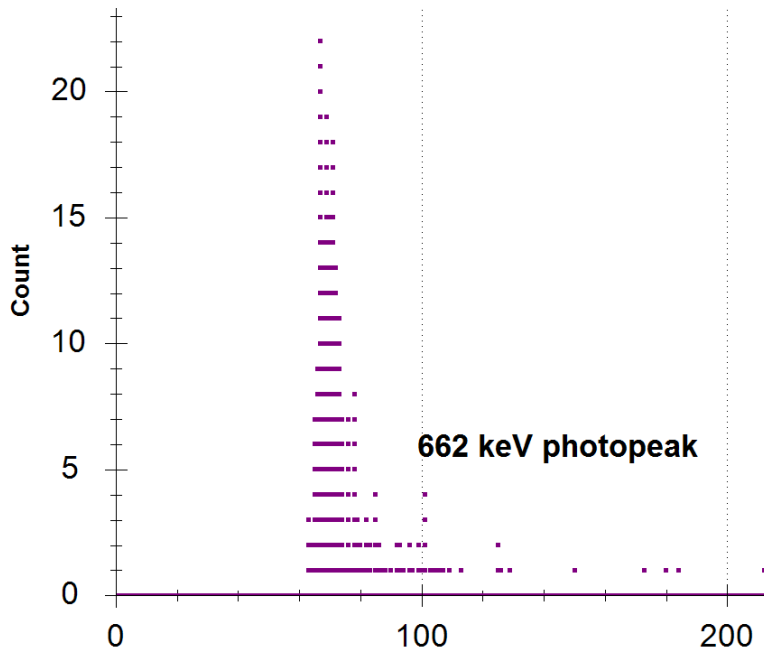


Figure 8.17: Counts observed with the ROV 50 cm from the tank edge and radioactive source for 10 minutes.

exposed to the higher counts required to carry out the more detailed spectral analysis for identification purposes.

This two-stage analysis would allow the detector to work with a greater accuracy and reliability, whilst reducing the radiation damage to the ROV with movement capable to first avoid, and then characterise, each gamma source closer.

These tests demonstrated the detector is able to operate and provide data that can be used to identify a radioactive source whilst submerged and in very close proximity to a weak ^{137}Cs source. However, source identification from a greater distance in a submerged state was not possible.

8.2.2 Sonar implementation

Collaborators from the National Maritime Institute, Nagaoka University of Technology and the Japan Atomic Energy Agency were interested in using the AVEXIS to locate physical debris inside the Fukushima Daiichi plant. To do this, they wanted to attach a sonar to the bottom of the AVEXIS to characterise the physical layout of the unknown areas beneath the PCV in the pedestal.

The sonar suggested was the IMAGENEX 831L [162], which was believed to be suitable, due to its design for use in enclosed pipe systems. This meant the device is

small and relatively light, allowing for integration onto an ROV to detect debris below the system.

The sonar was loaned to the author for integration within the AVEXIS. Fig. 8.18 shows the suggested sonar with Table 8.1 outlining the specifications.



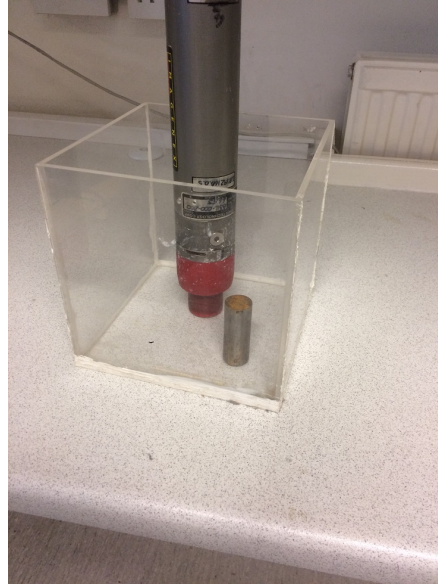
Figure 8.18: IMAGENEX 831L pipe profiling sonar [162].

Table 8.1: Summary of IMAGENEX 831L specifications.

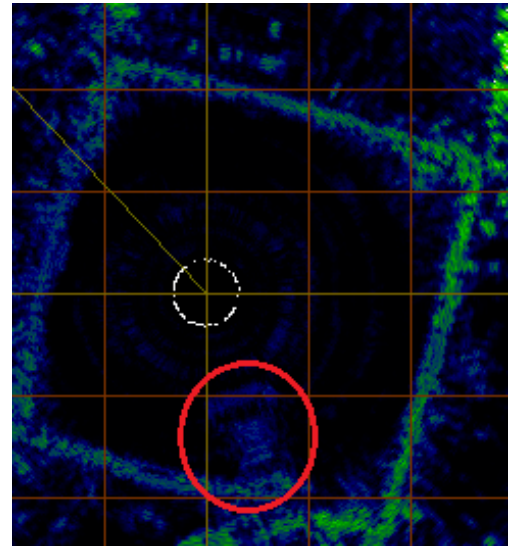
Frequency	2.25 MHz
Transducer	Profiling type, fluid compensated
Transducer Beam Width	1.4° conical
Range Resolution	1/250 of full scale range (e.g. 1 mm at 250 mm)
Min. Detectable Range	50 mm (approx. 2")
Max. Operating Depth	1000 m
Max. Cable Length	Standard: 100 m on CAT5e
Interface	Standard: 10 Mbps Ethernet TCP/IP
Connector	Subconn MCBH-8M-SS
Power supply	20-32 Vd.c. at less than 5 W
Dimensions	61 mm diameter x 343 mm length
Weight: In Air	1.2 kg
In Water	0.4 kg
Materials	6061-T6 Aluminium & Polyurethane
Finish	Hard Anodize

It can be seen that the communication protocol is Ethernet TCP/IP, therefore it is possible to use the same powerline technology as discussed in Section 8.1.2. Communication with the sonar can be conducted over the same two lines that the AVEXIS is controlled and powered from with no additional wires required.

To determine how the sonar worked, an initial test to validate the sonar output was completed. The sonar was placed in a small container filled with water and connected to a laptop with a static IP address running IMAGENEX's software. Fig. 8.19a shows the test set-up, while Fig. 8.19b shows the software output.



(a) Experimental set up of initial sonar communication.



(b) Output of IMAGENEX sonar software.

Figure 8.19: Initial sonar communication testing.

The shape of the box can be clearly seen in Fig. 8.19b. The small darkened area highlighted by the red circle shows the small metal cylinder placed in the container with the sonar in Fig. 8.19a.

The range of the sonar was set to 0.125 m highlighting the detail that can be achieved on a small-scale. This suggested that the sonar could characterise debris which may be small and hard to detect when a greater range is used. An example use-case of the sonar integrated within the ROV would be to set a large range, such as 5 m, when the ROV is shallowest in the water to highlight areas for further characterisation. It could then move closer with a smaller more detailed range capable of complete characterisation. However, further experimental validation of the sonar output when fully submerged was required.

To integrate the sonar into the current AVEXIS set-up, a PCB was designed and manufactured that converted the 48 V from the tether to 24 V required for sonar operation. An additional powerline adaptor power circuit was also integrated within

the same PCB. Therefore, the sonar power PCB could be replaced and removed if required, allowing easy integration and editing for future generations of the device.

Due to the inability to change anything on the sonar as it did not belong to the University and was very expensive, a cable was ordered from the manufacturer of the sonar connector and an equivalent panel connector.

This was attached to the sonar, and the end-cap of the AVEXIS. The sonar was then powered and communicated to from within the AVEXIS, which was subsequently controlled via the two wire tether to the surface. This layout can be seen in Fig 8.20.



Figure 8.20: Sonar integrated with the AVEXIS.

Having completed this, a test was completed to determine if the addition of the sonar to the two-wire tether created degradation of camera output or control inaccuracies. There was no noticeable degradation of either the camera output, the AVEXIS control or the sonar output when all were placed on the same two-wires. Therefore, the communication system was considered capable of withstanding all devices.

Water tank testing

Having validated the operation of the sonar on the laboratory benchtop, submerged tests were undertaken to obtain mock tank data. Forth Engineering, Maryport, own a mock decommissioning pond. It is approximately 8 m wide, 25 m long and 6 m deep.

This is representative of a Sellafield legacy pond, whilst the depth is representative of the PCV found at Fukushima.

The AVEXIS with the sonar attached was placed inside the tank with the output of the sonar gathered. A screenshot of the sonar data is shown in Fig. 8.21.

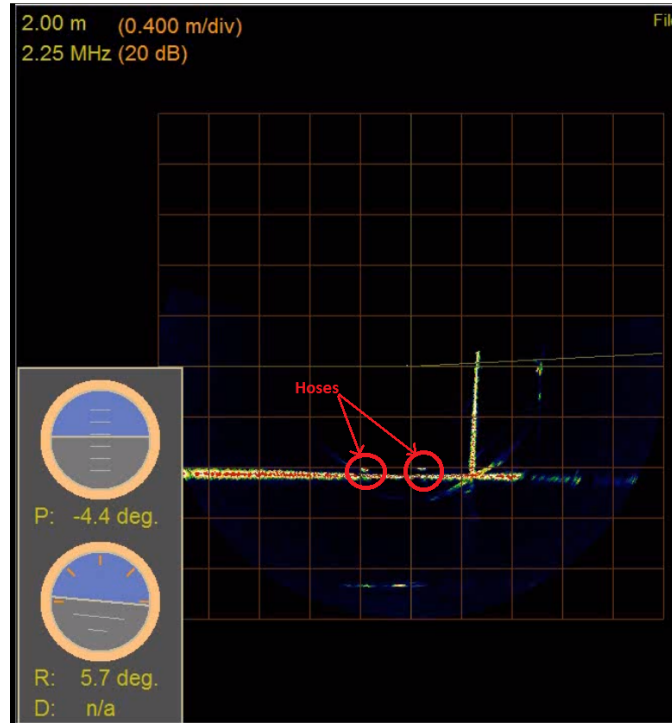


Figure 8.21: Screenshot of sonar output from Forth test. The two shapes represent a hose on the bottom of the tank.

It shows the corner of the tank with the AVEXIS approximately 0.5 m away from the tank wall and 0.8 m from the bottom. The two small shapes at the bottom of the tank represent a drainage hose placed on the bottom of the tank. The ability to output the shapes of these two hoses indicate the suitability of the ROV for characterising debris at the bottom of the PCV in Fukushima. Broken piping or cylindrical fuel rods are likely debris that require localisation.

From these tests, it was determined that the sonar data could be accurately retrieved allowing characterisation of an underwater environment in a 2D plane. This was the stage of work required for a technical demonstration to our collaborators in Japan.

8.3 Technical Demonstration NMRI, Japan

A visit to the NMRI in Japan with the AVEXIS was conducted to showcase the integration of the sonar and CeBr₃ gamma detector and to discuss future work. This was required to generate confidence within our collaborators that it was desirable to continue development of the AVEXIS system for deployment at Fukushima.

The industrial visit was a success with the AVEXIS detecting simulated debris at the bottom of the water tank owned by the NMRI. Fig. 8.22 shows an overview of the testing facility at the NMRI.



Figure 8.22: NMRI water tank, dimensions 8 m x 50 m x 6 m (w x l x d).

Initially, the NMRI placed simulated debris at the bottom of the tank. The simulated debris was representative of what might be expected at Fukushima and can be seen in Fig. 8.23. A layer of sand was placed over this debris to represent sediment that has built up in the PCV over the course of the last 6 years whilst submerged for cooling and radiation moderation purposes.

A member of the Japan Atomic Energy Agency attended the main technical demonstration. The AVEXIS was tasked with detecting the simulated debris and outputting the data to a screen for observation. Fig. 8.24 shows the AVEXIS deployed within the tank during the test with the pole seen in the foreground a camera for media purposes.

The AVEXIS displayed its manoeuvring capabilities and collected sonar data of the simulated debris. A screenshot of this data is shown in Fig. 8.25.

It is possible to see a general domed shape as expected from Fig. 8.23 covered in simulated sediment. Although the sonar did not penetrate through the sand, sharp

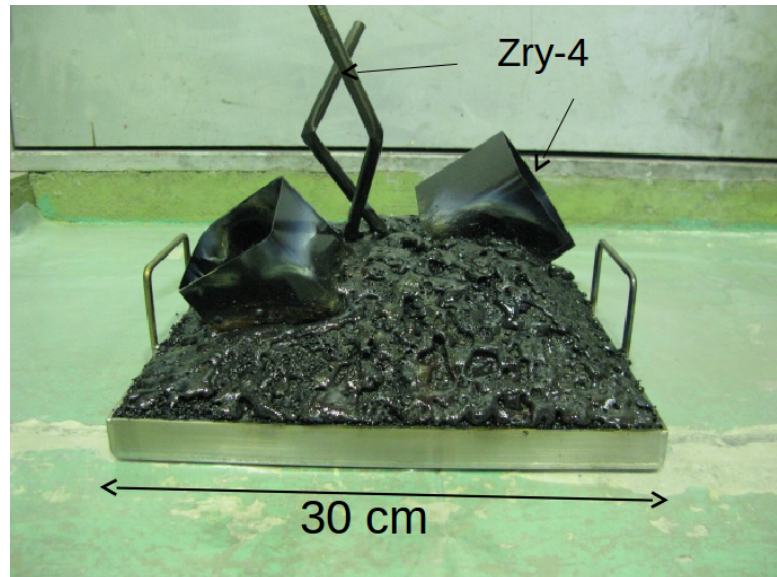


Figure 8.23: Simulated debris placed at the bottom of the tank.

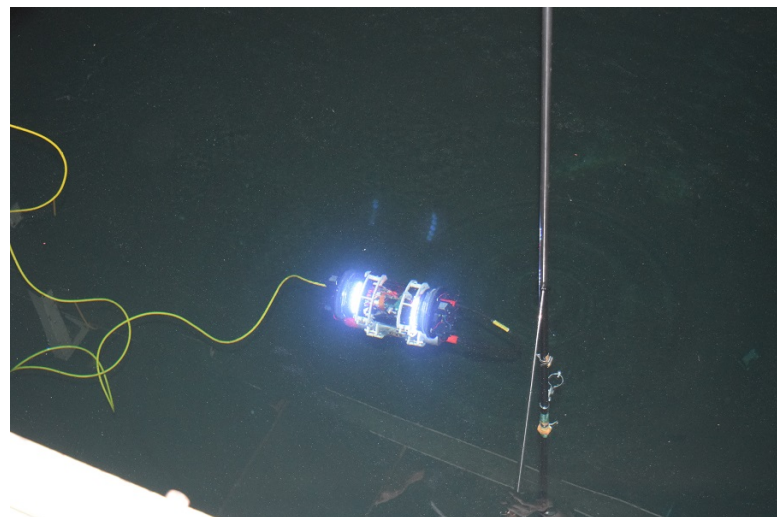


Figure 8.24: AVEXIS deployed within NMRI tank.

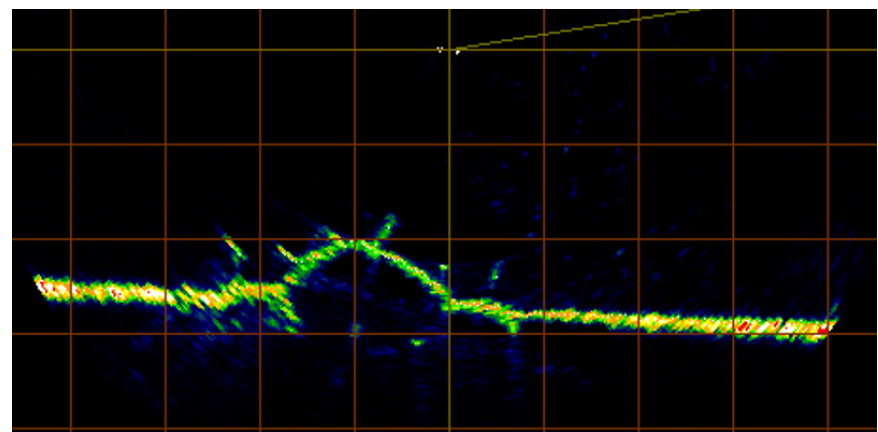


Figure 8.25: Sonar output over simulated debris.

edges were detected of the mock broken girders and debris leading to a detailed view of the debris. It was hoped further testing could increase the accuracy and resolution of the sonar output further, however, this was impossible due to time constraints of the technical demonstration. Plans were then made for a future demonstration in Japan October 2017.

The experimental verification of the AVEXIS to detect the representative debris generated confidence within our collaborators in Japan to continue the project for further development and eventual deployment within Fukushima.

Fig. 8.26 shows the capability of the on-board camera of the AVEXIS to see a metal pole placed approximately 2 m away in low-light conditions. Improvements can also be made to this with use of a camera without an infrared filter, larger and brighter LEDs for illumination and a clean of the lenses before deployment.



Figure 8.26: Screenshot of on-board camera taking a picture of a pole placed approximately 2 m away in poor lighting.

It is important to note for future international technical demonstrations that minor issues were caused due to mishandling from the airport baggage handlers resulting in loose connections and compressed plastic. However, there were enough spares and the damage superficial enough to allow on-site repair and deployment.

8.4 Software Development

Having completed the first technical demonstration of the AVEXIS in Japan, objectives to undertake for further demonstrations were discussed. These included;

1. Development of a positioning System.
2. Ability to output 3D point cloud data of sonar.
3. Integrate a neutron detector.
4. Complete further electronic component irradiation testing.

To allow localisation of radioactive waste and debris, a positioning system is required to relate the data gathered from the on-board detectors to the real-world position. Therefore, development of a positioning system and the ability to create a 3D reconstruction of sonar data using this positioning system were prioritised.

8.4.1 Positioning system

There are many techniques that can be used to create a positioning system. For example, above ground, GPS is often used for real world positioning. Indoor applications deploy RF transmitters and receivers at known locations and measure the “time of flight” that can achieve accuracies in the magnitude of ± 2 cm. Acoustic positioning is also used over long distances underwater in submarines.

The use of GPS or RF signals is difficult underwater, with the cluttered environment of the PCV in Fukushima making acoustic systems un-reliable. Therefore, after discussions with technicians from the NMRI and Fukushima, a vision system was considered the most viable option to contend with the constraints of a cluttered environment and the time constraints of the project.

An initial feasibility study was completed to determine if a vision system was plausible. A prototype of the system can be seen in Fig. 8.27.

A camera was placed above a small tank with a “dummy” AVEXIS placed inside. Green LEDs were placed on the left and red LEDs on the right. The camera could then track the AVEXIS via colour recognition of the light given off by the LEDs, with orientation also possible due to the use of a different colour on each side. This returned an x and y pixel value of the AVEXIS relative to four blue markers on the corners of the tank. These pixel values could then be scaled to the real distance per pixel as



Figure 8.27: Screenshot of prototype vision positioning system showing a mock AVEXIS and tank.

the size of the top of the tank is known. A depth sensor on the AVEXIS returned the depth giving a 3D position.

As can be seen in Fig. 8.27, the bottom rectangle of the tank appears smaller than the top of the tank outlining the change in distance per pixel measurement dependent on the depth of the AVEXIS. This can be taken into account via a transformation of one plane to another. This is possible as the camera position does not change during deployment and the smaller rectangle is known to be the same physical size as the larger rectangle.

Another issue that may cause problems within a vision based system is the refraction of light when transferring from air to water. This should be possible to take into account if the camera is placed directly in the centre of the image looking down with the equation of refraction well known.

Progress on a vision-based positioning system was started with feasibility of the system proven. Future work must be conducted to improve robustness of the system but each improvement is plausible.

8.4.2 3D point cloud construction

To develop the capability to construct a 3D map of the submerged environment. A technique to receive the data transmitted by the sonar and display it was required.

It was decided to use the Robot-Operating-System (ROS) to create this environment. ROS is fundamentally a communication protocol allowing easy portability of code from one system to another as well as sensors of many different types to communicate with each other. ROS nodes can be written in either python or C.

A ROS node was developed to display the sonar output data in real-time. This initially consisted of imitating the same 2D images received from the IMAGENEX sonar software discussed previously. Having completed this task, an example of the positioning system discussed in Section 8.4.1 was used to give the device real-world position within the tank at Lancaster University. This enabled the 2D data gathered from the sonar to be placed relative to each other dependent on the calculated real-world position. An example of a 3D image can be seen in Fig. 8.28.

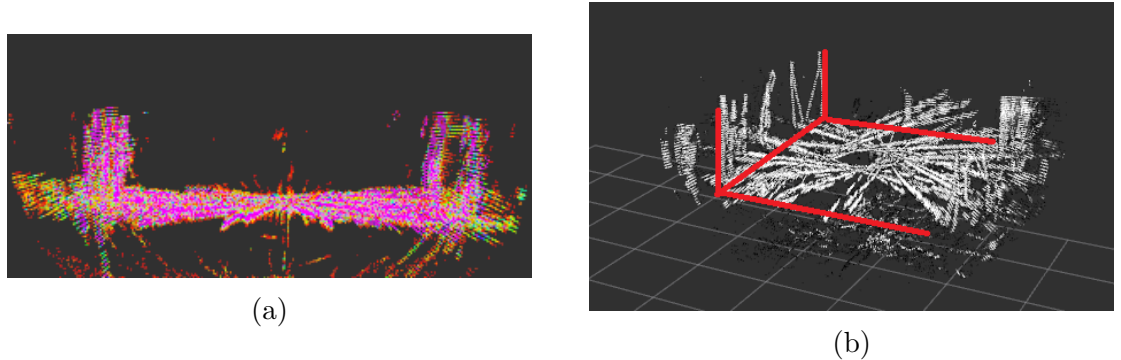


Figure 8.28: a) Side-on view of 3D reconstruction from water tank and b) isometric view with colour removed and annotation added to highlight the 3D image.

Fig. 8.28a shows the side-on view of the tank which can be identified with the two edges of the tank wall and the base of the tank. Fig 8.28b shows the same image but rotated to an isometric view to highlight the 3D view. The colour was changed to aid visualisation of the data.

It can be seen that an image of the tank is being developed, but there are areas where the tank wall appears to shift in relation to a neighbouring 2D-splice. This was due to incorrect calibration of the vision system resulting in small jumps of the outputted real-world position. Improved calibration will improve the stitching of the sonar data.

The feasibility to use the positioning system and sonar images in conjunction with each other to position the AVEXIS in the Fukushima PCV and output the internal state has been proven. Further development will allow for greater accuracy and

robustness and the overlay of radio-isotope localisation.

8.5 Summary

Development of the AVEXIS into an ROV capable of characterising the internal state of Fukushima Daiichi has been achieved. Improvements to the robotic platform to enable integration of detectors included the implementation of a new communication system reducing the required number of wires for the custom tether improving manoeuvrability and reducing drag and entanglement.

Further improvements have been made to the hull and sealing design with the removal of 3D printed hulls that increased in weight during operation, causing loss of device. These have been replaced by PVC end-caps with o-ring grooves cut into their exterior, allowing for improved water tightness and re-movability if a change in design is required.

Integration of multiple sensors has also been achieved. The addition of the University of Lancaster's CeBr₃ gamma detector has enabled radioactive isotope identification and characterisation with submerged and bench-top tests undertaken at the facilities at the University of Lancaster proving feasibility.

The IMAGENEX 831L sonar has also been added in conjunction with collaborators at the NMRI, Nagaoka University and the Japan Atomic Energy Agency. This has enabled physical layout characterisation of simulated debris. Tests conducted at the NMRI in Japan showcased the abilities to interested parties and has resulted in a further test to be undertaken in October 2018 at the Naraha facility in Fukushima prefecture, Japan.

Initial prototyping of a vision-based positioning system and 3D reconstruction of sonar data has also been undertaken with initial experimentally gathered results suggesting the applicability of these techniques to implementation within Fukushima.

Chapter 9

Conclusions and Future Work

9.1 Research Outcomes

This chapter presents the outputs from this research project. Important conclusions to be taken from each chapter are discussed and summarised with an analysis of the contribution to knowledge of this work. Suggested future work is also outlined in the hope of directing successful future research in this area.

The conclusions are discussed in order of the suggested research outcomes from Chapter 1.

Experimental validation of the degradation modes COTS IMUs experience when exposed to γ -radiation

It was found that many COTS IMUs are susceptible to gamma radiation exposure. The only exception to show no degradation up to a TID of 1 kGy(Si) was the one-axis ENC-03R gyroscope.

As all devices degraded in different modes, it is impossible to tell without further experimentation and analysis of the silicon structure exactly what the degradation mechanisms are. However, it is likely that charge build-up on the silicon changes the mechanical properties of the MEMS or the digital output circuitry.

If included in a robotic platform the most radiation tolerant gyroscope, the ENC-03R, would be suggested whilst either the ADXL335 or MPU-6050 would be suggested for an accelerometer. This is due to their consistent output before a sudden degradation at a threshold. If replaced regularly, these devices could be deployed in a nuclear

decommissioning environment.

A key point to be taken from these tests is the need for tests to be undertaken for each different IMU that is desired to be deployed within a nuclear decommissioning robotic platform. Without testing the desired IMU, it is difficult to predict how they will degrade and exactly when. It also highlights the relatively low TID tolerance of the devices with respect to the expected yearly TID of 5 kGy(Si) expected in the Sellafield legacy ponds, with the only current mitigation techniques available either increasing shielding around the component, or periodically replacing them.

Analysis of the observed degradation modes of COTS power regulation components

Experimental verification of the radiation tolerance of common COTS components such as a microcontroller, voltage references and linear voltage regulators outlined varying degradation modes that were inconsistent across each component family. Voltage reference testing suggested that the versions tested were relatively tolerant to radiation and could be deployed within a radioactive field.

The MC7805 voltage regulator degraded the least within the COTS voltage regulator devices. This suggested that this specific device may be deployable in a nuclear decommissioning environment. The variation seen in degradation modes for each of the other devices tested, suggest that a prediction of how any other COTS linear voltage regulator would degrade is unreliable.

It is suggested that by screening components known to show inconsistencies in radiation degradation modes, it may be possible to determine the most radiation tolerant devices. This is time-consuming, however, and is why work was undertaken on the development of a more radiation tolerant device development technique.

Investigation into the radiation tolerance of a bespoke discrete voltage regulator

The development and testing of a discrete linear voltage regulator device suggested that a greater radiation tolerance and consistency in degradation modes could be achieved in specific operating conditions such as load current magnitude. Each discrete regulator tested exhibited negligible degradation at load currents below 1.4 A with

varying magnitudes of degradation above this value.

Temperature dependencies suggested that it may be possible to anneal the devices during irradiation, but this was not fully explored within this work due to time constraints with access to the irradiator.

The use of discrete components to replace a COTS device may be possible across multiple ICs with this work suggesting that it is worth investigation.

Analysis of appropriate underground burrowing techniques

An underground burrower was researched and prototyped. After exploring the literature, two mechanisms for burrowing underground were chosen for further study. A contra-rotor screw mechanism and a hammering mechanism.

After initial testing it became apparent that the contra-rotor system was not suitable for the environment required and would become stuck easily with a large torque requirement for any motor used within it. Therefore, work concentrated on the hammering mechanism.

The hammering mechanism was shown to be a plausible device for underground burrowing with tests conducted in sand outlining the potential for further development and improvements to the capability of the device.

The addition of two eccentric motors also increased penetration speed with the vibration dislodging the sand surrounding the hammering mechanism allowing easier penetration of the device into the sand.

Development of an ROV capable of characterising submerged nuclear decommissioning environments

The AVEXIS was further developed from its original form to create a more rugged, waterproof, easier to control robotic platform that enabled integration of a CeBr₃ gamma detector and an IMAGENEX 831L sonar.

Important updates were the switch to a two-wire tether, removal of external 3D printed parts that soaked up water increasing the weight of the AVEXIS during operation, addition of depth and IMU sensors to allow localisation and changing the camera to an HD version with no interference apparent from the power supply for the pumps.

Integration of these sensors and improvements in general design meant the AVEXIS

successfully demonstrated that it is capable of locating radiation sources suggesting it is suitable for deployment in Fukushima.

9.2 Suggested Future Work

Future work that could be undertaken to further progress each area of research conducted are discussed in this section.

9.2.1 Radiation tolerance of COTS components

IMUs

There are many sensing element structures that can be incorporated within an IMU as discussed in Chapter 3. Testing the radiation tolerance of a range of these varying sensing elements would aid in determining different degradation modes for different technologies or whether there are common groups of degradation modes.

The temperature dependency of each IMU during irradiation would also be helpful to determine as large effects were witnessed in power regulation components.

Movement of the IMU in a pre-determined pattern to observe if this movement results in variable degradation modes may be of interest. The irradiator contains a turntable, which with the use of a slip ring connector would allow constant rotation of the IMU during irradiation.

Power regulation components

The temperature dependence witnessed for the discrete voltage regulators should be investigated further to determine if the degradation seen at the highest current could be annealed further than was possible in this study. Also, tests to determine if discrete regulators, with different output voltages and devices used as voltage references, would indicate if this design would work for multiple device loads.

Developing on the idea of discrete linear voltage regulators, design and testing of other linear ICs using discrete components could be of interest. For example, COTS motor drivers may be susceptible to radiation, but a discrete H-bridge configuration may show greater radiation tolerance.

9.2.2 Robotic platforms

Underground Burrower

Future work for the underground burrower includes multiple minor design and manufacturing alterations to increase the efficiency of the main hammering mechanism. This would allow a greater transmission of power to the body of the device for increased penetration-rates into the sub-soil environment.

Addition of a sampling mechanism and a gamma detector would increase the usability of the underground burrower. As it is cylindrical in shape, a detector such as the CeBr₃ gamma detector used within the AVEXIS, could be adapted for integration within the underground burrower. Changes in the length of the robot will be required to house the detector, however, it could lead to radioactive isotope identification and dose-rate mapping.

A priority for future work however, should aim to add the ability to controllably change directions underground. This could be achieved with an angled nose cone and main body or a rigid and curved tether casing like those found in curved drilling techniques.

AVEXIS

Many of the AVEXIS systems are ready for deployment, however, there are some key areas to address to avoid any unforeseen complications during use.

One example is the integration of more powerful thrusters that can overcome small increases or decreases in weight of the ROV. Currently, the pumps used are not powerful enough for this, leading to instances where a small change in ROV weight results in the inability to control the ROV either up or down.

For further adaptation of the AVEXIS for characterisation of the Fukushima Daiichi nuclear power plant, increased radiation tolerance testing of the on-board electronics should take place. Importantly the communication circuitry and camera. These remain, as yet, untested to gamma exposure.

Improvements to the positioning system will also aid in the localisation of radiological sources and physical debris to enable safer and more efficient decommissioning.

9.3 Summary

This thesis has outlined the many challenges facing the development of robotic platforms for nuclear decommissioning. Accidents, such as Fukushima, and the prolonged use of the originally temporary storage ponds at Sellafield, highlight the need for such devices.

All nuclear decommissioning robotic platforms must be able to sustain exposure to radiation for the duration of their operational lifetime. Therefore, radiation tolerance investigations of common components must continue to be conducted.

Areas that are either not safe, or too difficult to reach for human workers, necessitate the continued development of existing and novel robotic platforms to aid in the effort of nuclear decommissioning.

It is hoped that the work presented in this thesis on the radiation tolerance of electronic components, and the development of prototype robotic platforms, will aid in the nuclear decommissioning effort at sites in the UK and across the globe in Japan.

References

- [1] S. J. Palethorpe, B. Bowen, J. J. Hastings, P. E. Mort, and G. Askew, “Technical challenges, needs and opportunities in decommissioning of the Sellafield Site,” Sellafield, Seascale, UK, Tech. Rep. Oct., 2013.
- [2] Nuclear Decommissioning Authority, “Nuclear Decommissioning Authority Strategy,” Nuclear Decommissioning Authority, Cumbria, Tech. Rep. March, 2016.
- [3] S. Kawatsuma, M. Fukushima, and T. Okada, “Emergency response by robots to fukushima-daiichi accident: summary and lessons learned,” *Industrial Robot: An International Journal*, vol. 39, no. 5, pp. 428–435, 2012.
- [4] A. Griffiths, A. Dikarev, P. Green, B. Lennox, X. Poteau, and S. Watson, “AVEXIS-Aqua Vehicle Explorer for In-Situ Sensing,” *IEEE Robotics and Automation Letters*, vol. 3766, pp. 282–287, jan 2016.
- [5] Tokyo Electric Power Company, “Development of a technology to investigate inside the Reactor Primary Containment Vessel (PCV),” Tech. Rep., 2015.
- [6] S. N. Ahmed, *Physics and engineering of radiation detection*, 2nd ed., 2015. [Online]. Available: <http://www.sciencedirect.com/science/book/9780128013632>
- [7] D. Makowski, “The Impact of Radiation on Electronic Devices With the Special Consideration of Neutron and Gamma Radiation Monitoring,” Ph.D. dissertation, Technical University of Lodz, 2006.
- [8] G. S. Was, *Fundamentals of Radiation Materials Science*. Springer Science+Business Media, LLC, 2007.

- [9] S. Battisti, “Radiation Damage to Electronic Components,” *Nuclear Instruments and Methods*, vol. 136, pp. 451–472i, jan 1976.
- [10] H. Kvedalen, “Study of radiation effects in COTS semiconductors for use in high energy physics experiments,” Ph.D. dissertation, University of Oslo, 2002.
- [11] S. F. Jackson, S. D. Monk, and Z. Riaz, “An investigation towards real time dose rate monitoring, and fuel rod detection in a First Generation Magnox Storage Pond (FGMSP),” *Applied Radiation and Isotopes*, vol. 94, pp. 254–259, sep 2014.
- [12] Tokyo Electric Power Company, “Development of a technology to investigate inside the Reactor Primary Containment Vessel (PCV),” TEPCO, Tokyo, Tech. Rep., apr 2015.
- [13] Texas Instruments, “TI Space Products,” Dallas, Tech. Rep., 2016.
- [14] G. Spiezia, M. Brugger, S. Danzeca, R. G. Alia, R. Gaillard, E. Fadakis, G. Foucard, R. Losito, J. Mekki, P. Oser, P. Peronnard, G. Ruggiero, and R. Secondo, “Compendium of Radiation-Induced Effects for Candidate Particle Accelerator Electronics,” in *Radiation Effects Data Workshop (REDW), 2014 IEEE*, 2014.
- [15] European Space Agency, “Eurpoean Preferred Parts List,” Tech. Rep. 32, jul 2016.
- [16] M. V. O. Bryan, K. A. Label, D. Chen, M. J. Campola, M. C. Casey, J. M. Lauenstein, J. A. Pellish, R. L. Ladbury, M. D. Berg, and A. T. Facilities, “Compendium of Current Single Event Effects for Candidate Spacecraft Electronics for NASA,” 2015.
- [17] M. J. Campola, D. J. Cochran, A. J. Boutte, D. Chen, R. A. Gigliuto, K. A. Label, A. Jonathan, R. L. Ladbury, M. C. Casey, E. P. Wilcox, M. V. O. Bryan, J.-m. Lauenstein, D. Violette, M. A. Xapsos, N. Goddard, and S. Flight, “Compendium of Current Total Ionizing Dose and Displacement Damage for Candidate Spacecraft Electronics for NASA,” 2015.
- [18] J. Saraiva and M. Brugger, “Radiation Environments and Their Impact at the Cern’s Injector Chain,” Tech. Rep., 2015.

- [19] Department of Defence, "MIL-STD-883K," Tech. Rep., jun 2016.
- [20] S. S. McClure, R. D. Harris, B. G. Rax, and D. O. Thorbourn, "Characterization of radiation hardened bipolar linear devices for high total dose missions," *IEEE Radiation Effects Data Workshop*, pp. 1–6, 2012.
- [21] S. Sze, *Semiconductor Devices Physics and Technology*. John Wiley & Sons, 1985.
- [22] A. Bar-Lev, *Semiconductors and Electronic Devices*, 3rd ed. Prentice-Hall, 1993.
- [23] C. Hanks and D. Hamman, "Radiation Effects Design Handbook," in *Radiation Effects Design Handbook*, 1971, p. Section 3.
- [24] A. Holmes-Siedle and L. Adams, *Handbook of radiation effects*. OXFORD University Press, 2002.
- [25] G. Dienes, "Radiation Effects In Solids," *Nuclear Science*, pp. 187–220, 1953.
- [26] ESA, "The Radiation Design Handbook," Tech. Rep., 1993.
- [27] K. Holbert, "Radiation effects and damage," Tech. Rep., 2008. [Online]. Available: <http://holbert.faculty.asu.edu/eee560/RadiationEffectsDamage.pdf>
- [28] ESA, "The Radiation Design Handbook," European Space Research and Technology Centre, Noordwijk, Tech. Rep., 1993.
- [29] F. Zandman, P. R. Simon, and J. Szwarc, *Resistor theory and technology*, revised ed ed. SciTech Publishing Inc, 2002.
- [30] S. Dorst and L. Wurzel, "The Effect of Radiation Environment on Film Resistors," *IEEEExplore*, pp. 206–214, 1963.
- [31] J. Fossum, H. Sander, and H. Gerwin, "The Effects of Ionizing Radiation on Diffused Resistors," *IEEE Transactions on Nuclear Science*, vol. NS-21, no. 6, pp. 315–322, dec 1974.
- [32] C. L. Bowman, "Magnetic Materials Suitable for Fission Power Conversion in Space Missions," Tech. Rep., dec 2012.

- [33] Nichicon, "General Description of Aluminum Electrolytic Capacitors," Tech. Rep., 2014.
- [34] ESA, "The Radiation Design Handbook," 1993.
- [35] C. L. Hanks and D. J. Hamman, "Radiation Effects Design Handbook: Section 3. Electrical Insulating Materials and Capacitors," Tech. Rep. July, 1971.
- [36] R. Roy and A. Pandya, "Evaluation of gamma and neutron irradiation effects on the properties of mica film capacitors," *Bulletin of Materials Science*, vol. 28, no. 7, pp. 719–724, dec 2005.
- [37] L. S. Salomone, F. Campabadal, M. I. Fernández, J. Lipovetzky, S. H. Carbonetto, M. A. G. Inza, E. G. Redin, and A. Faigón, "Radiation Effects in Al₂O₃ - based MOS Capacitors," pp. 3–7, 2012.
- [38] K. Sharashar and S. Kayed, "Experimental Study of Total Ionizing Dose Radiation Effects on MOS Capacitor," *IEEEExplore*, jan 2003.
- [39] C. Leroy and P.-G. Rancoita, "Particle interaction and displacement damage in silicon devices operated in radiation environments," *Reports on Progress in Physics*, vol. 70, no. 4, pp. 493–625, apr 2007.
- [40] W. Abare, F. Brueggeman, R. Pease, J. Krieg, and M. Simons, "Comparative Analysis of Low Dose-Rate , Accelerated , and Standard Cobalt-60 Radiation Response Data for a Low-Dropout Voltage Regulator and a Voltage Reference," in *Radiation Effects Data Workshop, IEEE*. IEEE, 2002, pp. 177–180.
- [41] V. Sukumar, "Power Transistors - Devices and Datasheets," Tech. Rep., 1999.
- [42] H. J. Krenz, *Electronic Concepts: An Introduction*, 1st ed. Cambridge University Press, 2000.
- [43] K. F. Galloway, R. L. Pease, R. D. Schrimpf, and D. W. Emily, "From Displacement Damage to ELDRS : Fifty Years of Bipolar Transistor Radiation Effects at the NSREC," *IEEE Transactions on Nuclear Science*, vol. 60, no. 3, pp. 1731–1739, jun 2013.

- [44] R. L. Pease, "Total Ionizing Dose Effects in Bipolar Devices and Circuits," *IEEE Trans. Nucl. Sci.*, vol. 50, no. 3, pp. 539–551, jun 2003.
- [45] R. N. Nowlin, E. W. Enlowff, R. D. Schrimpf, and W. E. Combsfff, "Trends in the Total-Dose Response of Modern Bipolar Transistors," *IEEE Transactions on Nuclear Science*, vol. 39, no. 6, pp. 2026–2035, dec 1992.
- [46] D. M. Schmidt, D. M. Fleetwood, R. D. Schrimpf, R. L. Pease, R. J. Graves, G. H. Johnson, K. F. Galloway, and W. E. Combs, "Comparison of Ionizing-Radiation-Induced Gain Degradation in Lateral, Substrate, and Vertical PNP BJTs," *IEEE Trans. Nucl. Sci.*, vol. 42, no. 6, pp. 1541–1549, dec 1995.
- [47] P. Fouillat, V. Pouget, D. McMorrow, F. Darracq, S. Buchner, and D. Lewis, *Radiation Effects on Embedded Systems*. Dordrecht: Springer Netherlands, 2007.
- [48] ECSS, *Space engineering: Calculation of radiation and its effects and margin policy handbook*. Noordwijk: ESA Requirements and Standards Division ESTEC, dec 2010.
- [49] Fairchild Semiconductor, "Understanding Latch-Up in Advanced CMOS Logic," Fairchild Semiconductor Corporation, Tech. Rep., apr 1999.
- [50] D. M. Fleetwood, "Total Ionizing Dose Effects in MOS and Low-Dose-Rate-Sensitive Linear-Bipolar Devices," *IEEE Trans. Nucl. Sci.*, vol. 60, no. 3, pp. 1706–1730, jun 2013.
- [51] J. R. Schwank, M. R. Shaneyfelt, and P. E. Dodd, "Radiation Hardness Assurance Testing of Microelectronic Devices and Integrated Circuits : Radiation Environments , Physical Mechanisms , and Foundations for Hardness Assurance," *IEEE Trans. Nucl. Sci.*, vol. 60, no. 3, pp. 2074–2100, jun 2013.
- [52] S. C. Witczak, R. C. Lacoe, D. C. Mayer, D. M. Fleetwood, R. D. Schrimpf, and K. F. Galloway, "Space Charge Limited Degradation of Bipolar Oxides at Low Electric Fields," *IEEE Transactions on Nuclear Science*, vol. 45, no. 6, pp. 2339–2351, dec 1998.

- [53] R. Schrimpf, "Recent Advances in Understanding Total-Dose Effects in Bipolar 'Transistors,'" *IEEE Transactions on Nuclear Science*, vol. 43, no. 3, jun 1996.
- [54] J. Titus, D. Emily, J. Krieg, T. Turflinger, R. Pease, and A. Campbell, "Enhanced Low Dose Rate Sensitivity (ELDRS) of Linear Circuits in a Space Environment," *IEEE Transactions on Nuclear Science*, vol. 46, no. 6, dec 1999.
- [55] R. L. Pease, S. Mcclure, J. Gorelick, and S. C. Witczak, "Enhanced Low-Dose-Rate Sensitivity of a Low-Dropout Voltage Regulator," *IEEE Transactions on Nuclear Science*, vol. 45, no. 6, dec 1998.
- [56] V. Ramachandran, B. Narasimham, D. M. Fleetwood, R. D. Schrimpf, W. T. Holman, A. F. Witulski, S. Member, R. L. Pease, G. W. Dunham, J. E. Seiler, and D. G. Platteter, "Modeling Total-Dose Effects for a Low-Dropout Voltage Regulator," *IEEE Transactions on Nuclear Science*, vol. 53, no. 6, pp. 3223–3231, 2006.
- [57] L. Leay, W. Bower, G. Horne, P. Wady, A. Baidak, M. Pottinger, M. Nancekievill, A. Smith, S. Watson, P. Green, B. Lennox, J. LaVerne, and S. Pimblott, "Development of irradiation capabilities to address the challenges of the nuclear industry," *Nuclear Instruments and Methods in Physics Research B*, vol. 343, pp. 62–69, 2015.
- [58] RAD, "Enhanced Low Dose Radiation Sensitivity (ELDRS) Testing," Radiation Assured Devices, Colorado Springs, Tech. Rep.
- [59] R. L. Pease, S. Mcclure, A. H. Johnston, J. Gorelick, T. L. Turflinger, M. Gehlhausen, J. Krieg, T. Carriere, and M. Shaneyfelt, "An Updated Data Compendium of Enhanced Low Dose Rate Sensitive (ELDRS) Bipolar Linear Circuits," *Radiation Effects Data Workshop*, 2001.
- [60] R. L. Pease, R. D. Schrimpf, and D. M. Fleetwood, "ELDRS in Bipolar Linear Circuits : A Review," *IEEE Transactions on Nuclear Science*, vol. 56, no. 4, pp. 1894–1908, aug 2009.

- [61] J. Boch, F. Saigné, R. D. Schrimpf, D. M. Fleetwood, R. Cizmarik, and D. Zander, "Elevated Temperature Irradiation at High Dose Rate of Commercial Linear Bipolar ICs," *IEEE Trans. Nucl. Sci.*, vol. 51, no. 5, pp. 2903–2907, oct 2004.
- [62] S. C. Witczak, R. D. J. Schrimpf, K. F. Galloway, D. M. Fleetwood, R. L. Pease, J. M. Puhl, D. M. Schmidt, W. E. Combs, and J. S. Suehle, "Accelerated Tests for Simulating Low Dose Rate Gain Degradation of Lateral and Substrate PNP Bipolar Junction Transistors," *IEEE Trans. Nucl. Sci.*, vol. 43, no. 6, pp. 3151–3160, dec 1996.
- [63] M. R. Shaneyfelt, J. R. Schwank, D. M. Fleetwood, R. L. Pease, J. A. Felix, P. E. Dodd, and M. C. Maher, "Annealing Behavior of Linear Bipolar Devices With Enhanced Low-Dose-Rate Sensitivity," *IEEE Trans. Nucl. Sci.*, vol. 51, no. 6, pp. 3172–3177, dec 2004.
- [64] D. Hughart, R. Schrimpf, D. Fleetwood, B. R. Tuttle, and S. T. Pantelides, "Mechanisms of Interface Trap Buildup and Annealing During Elevated Temperature Irradiation," *IEEE Trans. Nucl. Sci.*, vol. 58, no. 6, pp. 2930–2936, dec 2011.
- [65] K.-S. Chang-Liao, "A study of the anneal technique to recover the electrical characteristics of the packaged metaloxide semiconductor field effect transistors damaged by Co-60 irradiation," *Journal of Vacuum Science & Technology B: Microelectronics and Nanometer Structures*, vol. 10, no. 2, p. 744, mar 1992.
- [66] K.-S. Chang-Liao and C. Huang, "Anneal technique to recover the electrical characteristics of the packaged bipolar junction transistors damaged by Co-60 radiation," *Journal of Vacuum Science & Technology B: Microelectronics and Nanometer Structures*, vol. 12, no. 3, p. 1377, may 1994.
- [67] European Space Agency, "European Preferred Parts List," Tech. Rep. 32, 2016.
- [68] J. Beaucour, T. Carriere, A. Gach, and D. Laxague, "Total Dose Effects on Negative Voltage Regulator," *IEEE Transactions on Nuclear Science*, vol. 41, no. 6, pp. 2420–2426, 1994.

- [69] M. Álvarez, J. J. Jiménez, D. Escribano, P. Manzano, I. Arruego, V. Apéstigue, M. González-Guerrero, I. Martín, and D. M. González-Castaño, “Low Dose Rate Testing of ADXL327 Accelerometer for a Mars Mission,” in *IEEE Radiation Effects Data Workshop*, 2015.
- [70] F. Rudolf, S. Gonseth, R. Brisson, and P. Krebs, “New generation of high performance/high reliability MEMS accelerometers for harsh environment,” *Record - IEEE PLANS, Position Location and Navigation Symposium*, pp. 7–11, 2014.
- [71] A. Hartzell, M. da Silva, and H. Shea, *MEMS Reliability*. Wilmington, MA: Springer Science+Business Media, LLC, 2010.
- [72] H. R. Shea, “Radiation sensitivity of microelectromechanical system devices,” *Journal of Micro/Nanolithography, MEMS, and MOEMS*, vol. 8, no. 3, pp. 31 303–31 311, jul 2009.
- [73] Northrop Grumman, “LN-200S IMU,” Tech. Rep., 2013. [Online]. Available: www.northropgrumman.com
- [74] J. Fraden, *Handbook of Modern Sensors*, 5th ed. San Diego: Springer Science+Business Media, LLC, 2016, vol. 53, no. 9.
- [75] P. Qu and H. Qu, “Design and Characterization of a Fully Differential MEMS Accelerometer Fabricated Using MetalMUMPs technology,” *Sensors*, vol. 13, no. 5, pp. 5720–5736, may 2013.
- [76] Y. Xu, L. Zhao, Z. Jiang, J. Ding, N. Peng, and Y. Zhao, “A Novel Piezoresistive Accelerometer with SPBs to Improve the Tradeoff between the Sensitivity and the Resonant Frequency,” *Sensors (Switzerland)*, vol. 16, no. 2, feb 2016.
- [77] C. H. J. Fox and D. J. W. Hardie, “Vibratory Gyroscopic Sensors,” *Symposium Gyro Technology*, 1984.
- [78] L. P. Schanwald, J. R. Schwank, J. J. Sniegowski, D. S. Walsh, N. F. Smith, K. A. Peterson, M. R. Shaneyfelt, P. S. Winokur, J. H. Smith, and B. L. Doyle, “Radiation Effects on Surface Micromachined Comb Drives and Microengines,” *IEEE Transactions on Nuclear Science*, vol. 45, no. 6, pp. 2789–2798, dec 1998.

- [79] K. F. Man, "MEMS reliability for Space Applications by Elimination of Potential Failure Modes Through Testing and Analysis," in *SPIE*, vol. 3880, 1999.
- [80] H. R. Shea, "Reliability of MEMS for Space Applications," in *Proceedings of SPIE*, vol. 6111, no. 2006, 2006, pp. 61 110A–61 110A–10.
- [81] O. Coumar, F. Miller, N. Buard, P. Poirot, R. Gaillard, and L. Marchand, "Total Dose Effects and SEE Screening on MEMS COTS Accelerometers," in *Radiation Effects Data Workshop (REDW)*, 2004, pp. 125–129.
- [82] A. Knudson, S. Buchner, P. McDonald, W. Stapor, A. Campbell, K. Grabowski, and D. Knies, "The Effects of Radiation on MEMS Accelerometers," *IEEE Trans. Nucl. Sci.*, vol. 43, no. 6, pp. 3122–3126, dec 1996.
- [83] S. McClure, L. Edmonds, R. Mihailovich, A. Johnston, P. Alonzo, J. DeNatale, J. Lehman, and C. Yui, "Radiation effects in micro-electromechanical systems (MEMS): RF relays," *IEEE Transactions on Nuclear Science*, vol. 49, no. 6, pp. 3197–3202, dec 2002.
- [84] C. Lee, A. Johnston, W. Tang, C. Barnes, and J. Lyke, "Total dose effects on Microelectromechanical Systems (MEMS): accelerometers," *IEEE Transactions on Nuclear Science*, vol. 43, no. 6, pp. 3127–3132, dec 1996.
- [85] L. D. Edmonds, G. M. Swift, and C. I. Lee, "Radiation response of a MEMS Accelerometer: An Electrostatic Force," *IEEE Trans. Nucl. Sci.*, vol. 45, no. 6, pp. 2779–2788, dec 1998.
- [86] K. E. Holbert, J. A. Nessel, S. S. McCready, A. S. Heger, and T. H. Harlow, "Response of Piezoresistive MEMS Accelerometers and Pressure Transducers to High Gamma Dose," *IEEE Transactions on Nuclear Science*, vol. 50, no. 6 I, pp. 1852–1859, dec 2003.
- [87] S. Zhu, W. Huang, J. Wang, A. Li, S. Shen, and M. Bao, "Total dose radiation effects of pressure sensors fabricated on uni-bond-SOI materials," *Nuclear Science and Techniques*, vol. 33, no. 17, pp. 209–214, 2001.

- [88] S. S. McCready, T. H. Harlow, A. S. Heger, and K. E. Holbert, "Piezoresistive micromechanical transducer operation in a pulsed neutron and gamma ray environment," in *Radiation Effects Data Workshop*. IEEE, jul 2002.
- [89] T. F. Miyahira, B. G. Rax, and A. H. Johnston, "Total dose degradation of low-dropout voltage regulators," *IEEE Radiation Effects Data Workshop*, pp. 127–131, nov 2005.
- [90] Analog Device, "Data Sheet ADXL335," Tech. Rep., 2009. [Online]. Available: <https://www.sparkfun.com/datasheets/Components/SMD/adxl335.pdf>
- [91] Analog Devices, "Data Sheet ADXL345," Tech. Rep., 2015. [Online]. Available: <https://cdn-learn.adafruit.com/downloads/pdf/adxl345-digital-accelerometer.pdf>
- [92] D. L. Agency, "MIL-STD-883K," Tech. Rep., 2016.
- [93] Defense Logistics Agency, "MIL-STD-883F," Tech. Rep. March, mar 2003.
- [94] Fairchild Semiconductor, "KA78XXE / KA78XXAE 3-Terminal 1 A Positive Voltage Regulator," Fairchild Semiconductor Corporation, Tech. Rep., apr 2015.
- [95] National Instruments, "User Guide and Specifications: USB-6008/6009," Tech. Rep., 2008.
- [96] R. L. Pease, G. W. Dunham, and J. E. Seiler, "Total Dose and Dose Rate Response of Low Dropout Voltage Regulators," in *Radiation Effects Data Workshop, IEEE*. Ponte Vedra, FL: IEEE, jan 2007.
- [97] ON Semiconductor, "MC7800, MC7800A, MC7800AE, NCV7800," Tech. Rep., 2014.
- [98] STMicroelectronics, "Very low drop 1A regulator L4941," Tech. Rep., 2006.
- [99] D. M. Schmidt, D. M. Fleetwood, R. D. Schrimpf, R. L. Pease, R. J. Graves, G. H. Johnson, K. F. Galloway, and W. E. Combs, "Comparison of Ionizing-Radiation-Induced Gain Degradation in Lateral, Substrate, and Vertical PNP BJTs," *IEEE Transactions on Nuclear Science*, vol. 42, no. 6, pp. 1541–1549, 1995.

- [100] M. Hamer, "Delays in Nuclear Shutdown," *New Scientist*, p. 5, aug 1984.
- [101] Sellafield Ltd, "General Characteristics of the Principal Radioisotopes in Groundwater," Sellafield Ltd, Cumbria, Tech. Rep., 2012.
- [102] A. Stamper, D. Coughlin, A. Bowes, P. Ruddick, and F. Laws, "Groundwater Monitoring at Sellafield Annual Data Review 2013," Sellafield Ltd., Cumbria, Tech. Rep., 2013.
- [103] J. Cruickshank, I. Teasdale, and K. Eilbeck, "Findings of the Sellafield Contaminated Land & Groundwater Management Project and the Next Steps for the Land Quality Programme Report Number : MAN000405," Sellafield Ltd, Cumbria, Tech. Rep., feb 2012.
- [104] N. Smith and S. Cooper, "SCLS Phase 1 Sellafield Geological Conceptual Model," Sellafield Ltd, Tech. Rep., mar 2004.
- [105] J. Hunter, "SCLS Phase 1 Conceptual Model of Contamination Below Ground at Sellafield," Sellafield Ltd., Tech. Rep., mar 2003.
- [106] Sellafield Ltd, "Monitoring our Environment Discharges and Monitoring in the United Kingdom Annual Report 2011," Sellafield Ltd., Tech. Rep., 2012.
- [107] D. Majersky, "Removal and Solidification of the High Contaminated Sludges into the Aluminosilicate Matrix Sial During Decommissioning Activities," Tech. Rep., 1977.
- [108] H. Omori, T. Murakami, H. Nagai, T. Nakamura, and T. Kubota, "Development of a Novel Bio-Inspired Planetary Subsurface Explorer: Initial Experimental Study by Prototype Excavator With Propulsion and Excavation Units," *IEEE/ASME Transactions on Mechatronics*, vol. 18, no. 2, pp. 459–470, apr 2013.
- [109] R. Campaci, S. Debei, R. Finotello, G. Parzianello, C. Bettanini, M. Giacometti,

- G. Rossi, G. Visentin, and M. Zaccariotto, "Design and Optimization of a Terrestrial Guided Mole for Deep Subsoil Exploration - Boring Performance Experimental Analyses," in *The 8th International Symposium on Artificial Intelligence, Robotics and Automation in Space - iSAIRAS*. Munich: European Space Agency, sep 2005.
- [110] T. Kubota, K. Watanabe, S. Shimoda, and I. Nakatani, "Deep Drilling Robot for Subsurface Exploration," Ph.D. dissertation, The University of Tokyo, 2004.
- [111] S. Siceloff, "Engineers Building Hard-working Mining Robot," 2013. [Online]. Available: <https://www.nasa.gov/topics/technology/features/RASSOR.html>
- [112] R. A. Russell, "An agile burrowing robot for underground chemical source location," in *Proc. of Australian Conference on Robotics and Automation*, Melbourne, dec 2011.
- [113] R. Russell, "A ground-penetrating robot for underground chemical source location," *2005 IEEE/RSJ International Conference on Intelligent Robots and Systems*, pp. 175–180, 2005. [Online]. Available: <http://ieeexplore.ieee.org/lpdocs/epic03/wrapper.htm?arnumber=1545251>
- [114] K. Nagaoka, T. Kubota, I. Nakatani, and S. Tanaka, "Drilling Mechanism of Autonomous Burrowing Robot for Lunar Subsurface Exploration," Ph.D. dissertation, The graduate University for Advanced Studies, 2008.
- [115] K. Nagaoka, T. Kubota, M. Otsuki, and S. Tanaka, "Experimental study on autonomous burrowing screw robot for subsurface exploration on the Moon," *2008 IEEE/RSJ International Conference on Intelligent Robots and Systems*, pp. 4104–4109, sep 2008.
- [116] M. Hayashi and Y. Kawamura, "Development of DigBot for Surveying the Underground after the Disaster," University of Tsukuba, Tsukuba-city, Tech. Rep. 2, 2012.
- [117] C. Stoker, L. Richter, W. Smith, L. Lemke, P. Hammer, J. Dalton, B. Glass, and A. Zent, "The Mars Underground Mole (MUM): A subsurface penetration device

- with in situ infrared reflectance and raman spectroscopic sensing capability,” in *Sixth International conference on Mars*. NASA, jan 2003, pp. 2002–2004.
- [118] C. R. Stoker, A. Gonzales, and J. R. Zavaleta, “Moon / Mars Underground Mole,” NASA Ames Research Center, Moffett Field, CA, Tech. Rep., 2007.
- [119] Z. Zhang, L. Wang, and X. Ye, “General Capability Analyzing and Research on Puncturing Mud Robot,” in *International Conference on Mechanic Automation and Control Engineering*, jun 2010, pp. 3–6.
- [120] R. C. Richardson, A. Nagendran, and R. G. Scott, “Experimental Tests of Bidibot’: A Mechanism Designed for Clearing Loose Debris from the Path of Mobile Search and Rescue Robots,” *Advanced Robotics*, vol. 26, no. 15, pp. 1799–1823, oct 2012.
- [121] R. A. Russell, “CRABOT: A Biomimetic Burrowing Robot Designed for Underground Chemical Source Location,” *Advanced Robotics*, vol. 25, no. 1-2, pp. 119–134, jan 2011. [Online]. Available: <http://www.tandfonline.com/doi/abs/10.1163/016918610X538516>
- [122] D. P. Germann, W. Schatz, and P. E. Hotz, “Artificial Bivalves: The Biomimetics of Underwater Burrowing,” University of Zurich, Zurich, Tech. Rep., 2010.
- [123] R. F. Gillie, “Variable Pitch Screw Drives,” *Mechanism and Machine Theory*, vol. 13, pp. 523–531, apr 1978.
- [124] O. Vahid-Araghi and F. Golnaraghi, *Friction-Induced Vibration in Lead Screw Drives*. Springer Science+Business Media, LLC, 2011.
- [125] M. Neumeyer and B. Jones, “The Marsh Screw Amphibian,” *Journal of Teramechanics*, vol. 2, no. 4, pp. 83–88, 1965.
- [126] K. Nagaoka and T. Kubota, “Analytic study on screw drilling mechanism,” in *2009 IEEE International Conference on Robotics and Biomimetics (ROBIO)*. Guilin: Ieee, dec 2009, pp. 1579–1584.

- [127] H. Rabia, "Specific Energy as a Criterion for Drill Performance Prediction," *International Journal of Rock Mechanics and Mining Sciences and*, vol. 19, no. 1, pp. 39–42, 1982.
- [128] K. Nagatani, S. Kiribayashi, Y. Okada, K. Otake, K. Yoshida, S. Tadokoro, T. Nishimura, T. Yoshida, E. Koyanagi, M. Fukushima, and S. Kawatsuma, "Gamma-ray irradiation test of electric components of rescue mobile robot Quince - Toward emergency response to nuclear accident at Fukushima Daiichi Nuclear Power Station on March 2011," in *9th IEEE International Symposium on Safety, Security, and Rescue Robotics*, Kyoto, nov 2011, pp. 56–60.
- [129] D. Gross, W. Hauger, J. Schroder, W. Wall, and J. Bonet, *Engineering Mechanics 2: Mechanics of Materials*. Springer Science+Business Media, LLC, 2011.
- [130] D. Warrington, "Vibratory and Impact-Vibration Pile Driving Equipment," Tech. Rep., 1997. [Online]. Available: https://scholar.google.co.uk/scholar?hl=en&q=vibration+and+impact-vibration+pile+driving+equipment&btnG=&as_sdt=1%2C5&as_sdtp=#0
- [131] Nuclear Engineering International, "The cold probe for sampling at Sellafield," 2014. [Online]. Available: <http://www.neimagazine.com/features/featurethe-cold-probe-4163473/featurethe-cold-probe-4163473-3.html>
- [132] J. Erickson, C. Frigeo, S. Rostmark, and L. Sweden, "Sellafield Freeze Sampler," Sellafield Ltd, Cumbria, Tech. Rep., mar 2013.
- [133] J. Eriksson, N. Vyce, and A. Foster, "Freeze-Tec Sampling," Studsvik, Tech. Rep.
- [134] Nuclear Decommissioning Authority, *NDA Business Plan - Financial year beginning April 2014 to financial year ending March 2017*, 2014.
- [135] J. Vidal and R. Edwards, "Photographs of Sellafield nuclear plant prompt fears over radioactive risk," 2015. [Online]. Available: <https://www.theguardian.com/environment/2014/oct/29/sellafield-nuclear-radioactive-risk-storage-ponds-fears>

- [136] IRID, “Robots working inside the buildings at Fukushima Daiichi NPS(Part III),” 2016. [Online]. Available: http://irid.or.jp/en/research/gengorov_trydiver/
- [137] ——, “IRID Annual Research Report 2014,” Tech. Rep. March, 2015.
- [138] ——, “Survey Device (Shape-changing Robot) Deployed to Inspect Interior of Primary Containment Vessel (PCV),” 2015. [Online]. Available: <http://irid.or.jp/en/research/20150420/>
- [139] B. Siciliano and O. Khatib, *Springer Handbook of Robotics*, 2016.
- [140] Toshiba, “New Toshiba and IRID Robot Will Inspect Interior of Primary Containment Vessel at Fukushima Daiichi 3,” 2017.
- [141] Japan Press Network, “Unit3, severe damage in the containment vessel underwater robot survey, debris can not be confirmed,” 2017. [Online]. Available: http://www.47news.jp/news/2017/07/post_20170719203804.html
- [142] S. Bhattacharyya and H. H. Asada, “Control of a compact, tetherless ROV for in-contact inspection of complex underwater structures,” in *IEEE International Conference on Intelligent Robots and Systems*, no. Iros, 2014, pp. 2265–2272.
- [143] I. C. Rust and H. H. Asada, “The eyeball ROV: Design and control of a spherical underwater vehicle steered by an internal eccentric mass,” in *Proceedings - IEEE International Conference on Robotics and Automation*, 2011, pp. 5855–5862.
- [144] T. Schmickl, R. Thenius, C. Moslinger, J. Timmis, A. Tyrrell, M. Read, J. Hilder, J. Halloy, A. Campo, C. Stefanini, L. Manfredi, S. Orofino, S. Kernbach, T. Dipper, and D. Sutantyo, “CoCoRo - The Self-aware Underwater Swarm,” in *IEEE Conference on Self-Adaptive and Self-Organizing Systems Workshops, SASOW*, vol. 1, 2011, pp. 120–126.
- [145] U. Muldur, F. Corvers, H. Delanghe, J. Dratwa, D. Heimberger, B. Sloan, and S. Vanslembrouck, *A New Deal for an Effective European Research Policy*, 2006.

- [146] S. Mintchev, E. Donati, S. Marrazza, and C. Stefanini, “Mechatronic design of a miniature underwater robot for swarm operations,” in *Proceedings - IEEE International Conference on Robotics and Automation*, 2014, pp. 2938–2943.
- [147] D. Sutantyo, P. Levi, M. Christoph, and M. Read, “Collective-Adaptive Levy Flight for Underwater Multi-Robot Exploration,” in *IEEE International Conference on Mechatronics and Automation (ICMA)*, 2013, pp. 456–462.
- [148] Deep Trekker, “DTG2 Starter,” 2017. [Online]. Available: <https://www.deeptrekker.com/product/dtg2-starter/>
- [149] VideoRay, “VideoRay Case Study - James Fisher Nuclear,” 2015. [Online]. Available: <http://www.videoray.com/casestudies/download-cs-jfn.html>
- [150] ——, “VideoRay Voyager,” 2017. [Online]. Available: <http://shop.videoray.com/shop-front#!/product/category=10290101&id=52908730>
- [151] AC-CESS, “AC-ROV 100,” 2017. [Online]. Available: <http://ac-cess.com/index.php/gallery/ac-rov-100>
- [152] OpenROV, “OpenROV 2.8 Kit,” 2017. [Online]. Available: <https://www.openrov.com/products/openrov28/>
- [153] FORTH, “FE AVEXIS MICRO ROV,” Forth Engineering Ltd, Marport, CA, Tech. Rep., 2017.
- [154] S. A. Watson, “Mobile Platforms for Underwater Sensor Networks,” Ph.D. dissertation, University of Manchester, 2012.
- [155] BlueRobotics, “Watertight Subsea Enclosures,” 2017. [Online]. Available: <https://www.bluerobotics.com/store/watertight-enclosures/wte4-asmr1/#configuration>
- [156] ——, “Cable Penetrator for 6mm Cable,” 2017. [Online]. Available: <https://www.bluerobotics.com/store/connectors/penetrator-10-25-a/>
- [157] OpenROV, “OpenROV 2.8 kit,” 2015. [Online]. Available: <https://www.openrov.com/products/openrov28/>

- [158] LINKSYS, “LINKSYS PLSK400 POWERLINE 4-PORT FAST ETHERNET KIT,” 2017. [Online]. Available: <http://www.linksys.com/gb/p/P-PLSK400/>
- [159] TENDA, “200Mbps Powerline Adapter P200,” Tech. Rep., 2012.
- [160] GE, “EVK011A0B Series (Eighth-Brick) DC-DC Converter Power Modules,” Tech. Rep., 2013.
- [161] SCIONIX, “SCIONIX,” 2017. [Online]. Available: <http://scionix.nl/>
- [162] IMAGENEX, “IMAGENEX Model 831L Digital Pipe Profiling Sonar,” Tech. Rep., 2011.
- [163] ICRU, “Fundamental Quantities and Units for Ionizing Radiation (Revised),” Tech. Rep., 2011.
- [164] BIPM, “International System of Units (SI),” *Bureau International des Poids et Mesures, Le Systeme International d’Unites (SI)*, no. 8th ed, dec 2006.
- [165] National Radiological Protection Board NRPB, *Living with radiation*, 1973.

Appendix A

Radiation Unit Comparison

There are many different units used to describe radiation. This chapter describes the standard units with which the work was undertaken and the relationship to common alternatives. This will allow for any necessary calculations when given data in another format. This is normally applicable with old sets of data that use an older standard of unit.

The International Commission on Radiation Units and Measurements (ICRU) develops internationally acceptable units for radiation and radioactivity [163]. It is recommended to use the International System of Units (SI) [164]. There are no base SI units regarding radiation, however, there are derived SI units. These are the Becquerel, the activity of a radioactive source, equal to the reciprocal second. The gray, the absorbed dose, it is equivalent to joule per kilogram. The sievert, the personal dose equivalent or dose equivalent, equal to joule per kilogram. It is worth noting that the exposure, production of electrostatic positive or negative ionic charge in air, is measured in Coulombs per kilogram [163]. A summary can be seen in Table A.1.

Table A.1: Summary of derived SI units for radiation

Activity	Absorbed dose	Equivalent absorbed dose	Exposure
Becquerel (Bq) s^{-1}	gray (Gy) $J.kg^{-1}$	sievert (Sv) $J.kg^{-1}$	- $C.kg^{-1}$

It can be seen that the units of grays and sieverts are the same. To avoid confusion a recommendation was made in 1979 and updated in 2002 by The Comite International des Poids et Mesures to clarify the difference [164]. The quantity of an equivalent dose H is a product of the absorbed dose D and the quality factor Q [164].

$$H = QxD \quad (\text{A.1})$$

Q is dimensionless and is dependent on the material exposed, defined as a function of linear energy transfer by the ICRU. It will be different for example between skin and metal. Therefore the numerical value of H may differ from D dependent on Q . Sieverts is therefore used for the equivalent absorbed dose and grays are used for the absorbed dose.

The terms Becquerel and gray were accepted as derived SI units in 1976 and Sieverts were accepted in 1979. Other units of radiation were used prior to this and therefore are still very prevalent in many journals, reference papers and books. Examples of these units are the curie (Ci), the rad, the rem and the roentgen (R), sometimes spelt rntgen. A conversion and summary of each of these units compared with the SI units can be seen in Table A.2.

Table A.2: Summary of conversion from SI units to widely used units in literature

	Activity	Absorbed dose	Equivalent absorbed dose	Exposure
SI Units	Becquerel (Bq)	gray (Gy)	sievert (Sv)	C.kg ⁻¹
Common units	curie (Ci)	rad	rem	Roentgen (R)
Conversions	1 Bq 2.7x10 ⁻¹¹ Ci	= 1 Gy = 100 rad	1 Sv = 100 rem	1 C.kg ⁻¹ = 3,880 R

This study used the SI units for radiation. Where a journal or paper is referenced containing other units, a conversion was administered for consistency throughout the study. The quality factor of gamma rays is 1 [165], therefore, the value of the equivalent dose measured in sieverts, using equation A.1, can be assumed to be the same as that of the absorbed dose in grays. Therefore grays will be used to describe dose and can be assumed to equal the equivalent dose unless otherwise stated.

Appendix B

Further IMU data

B.1 Additional LSM9DS0 IMU test sample results

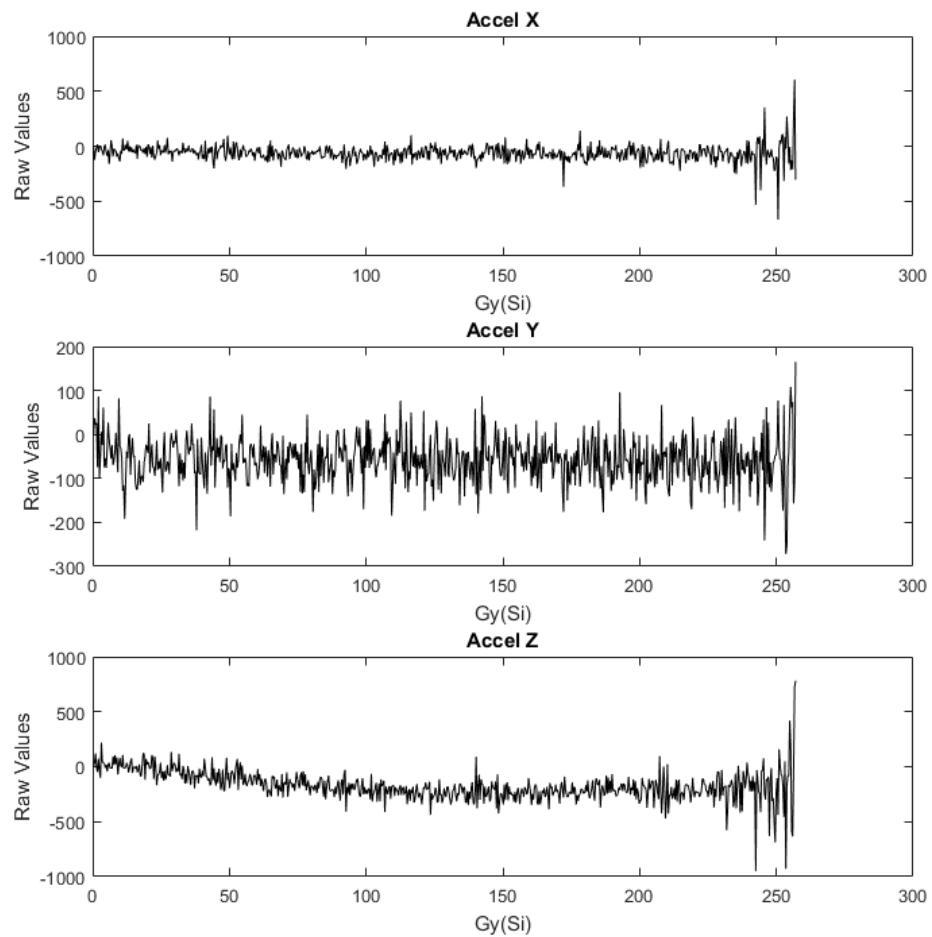


Figure B.1: Further test sample of LSM9DS0 showing accelerometer degradation

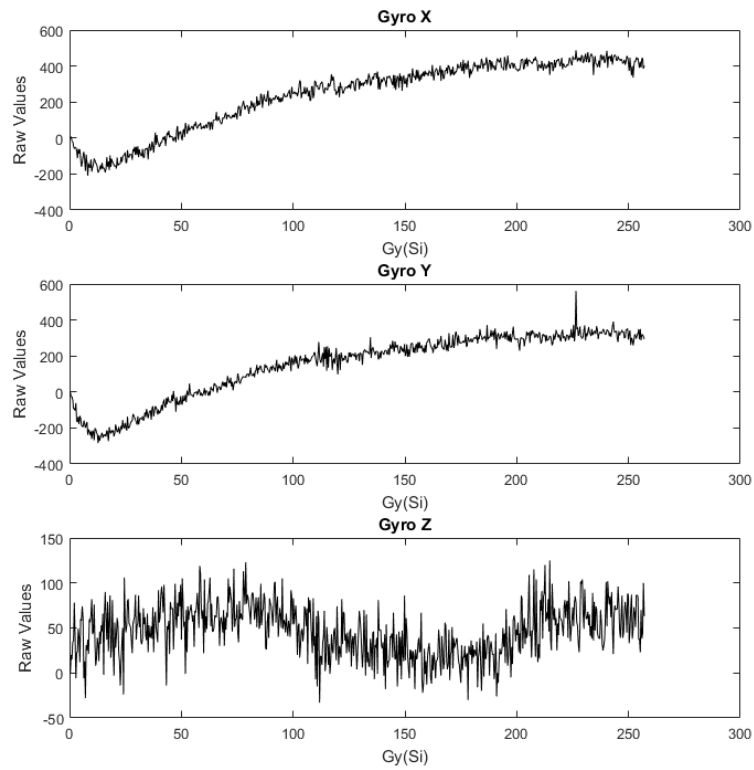


Figure B.2: Further test sample of LSM9DS0 showing gyroscope degradation

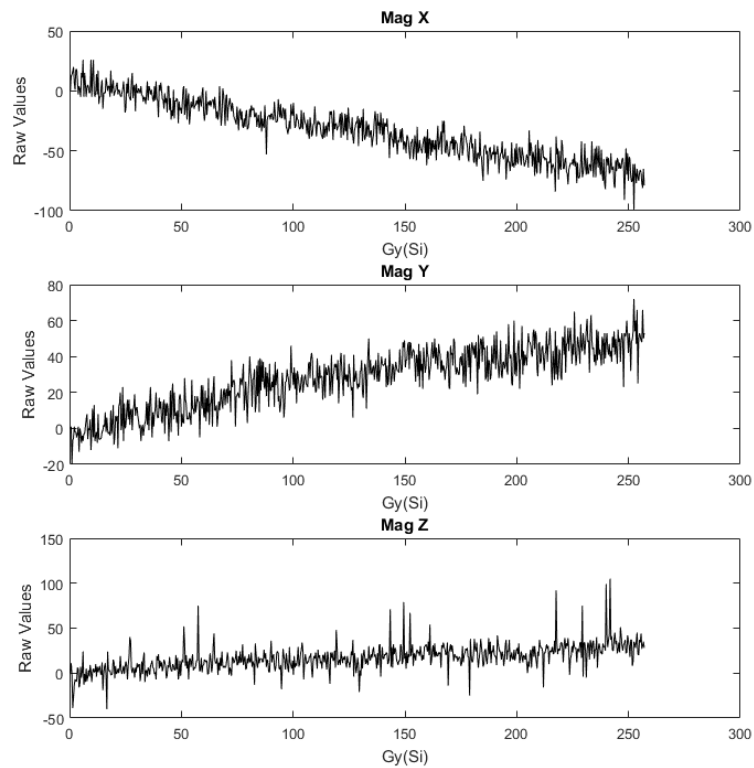


Figure B.3: Further test sample of LSM9DS0 showing magnetometer degradation

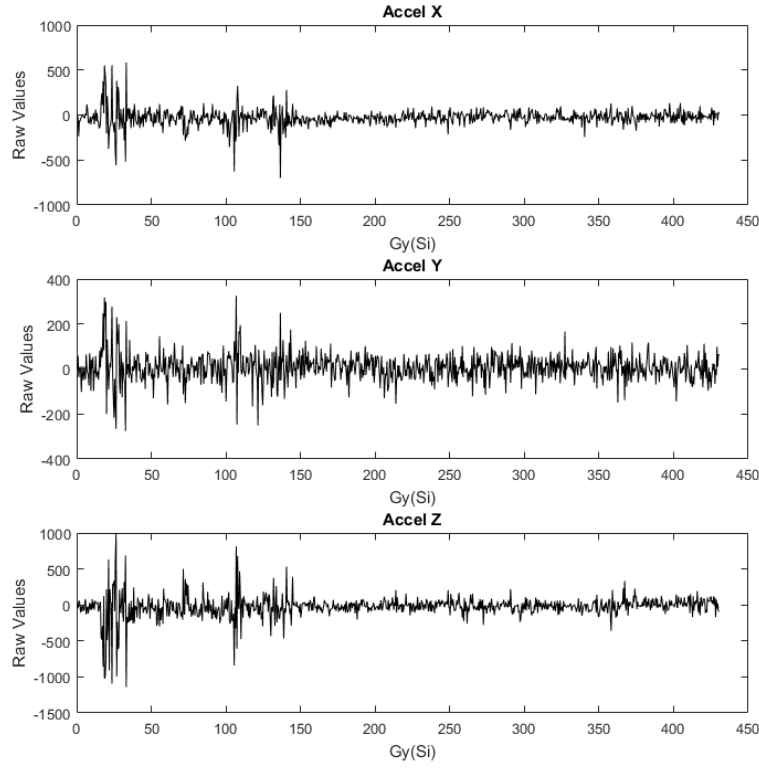


Figure B.4: Further test sample of LSM9DS0 showing accelerometer degradation

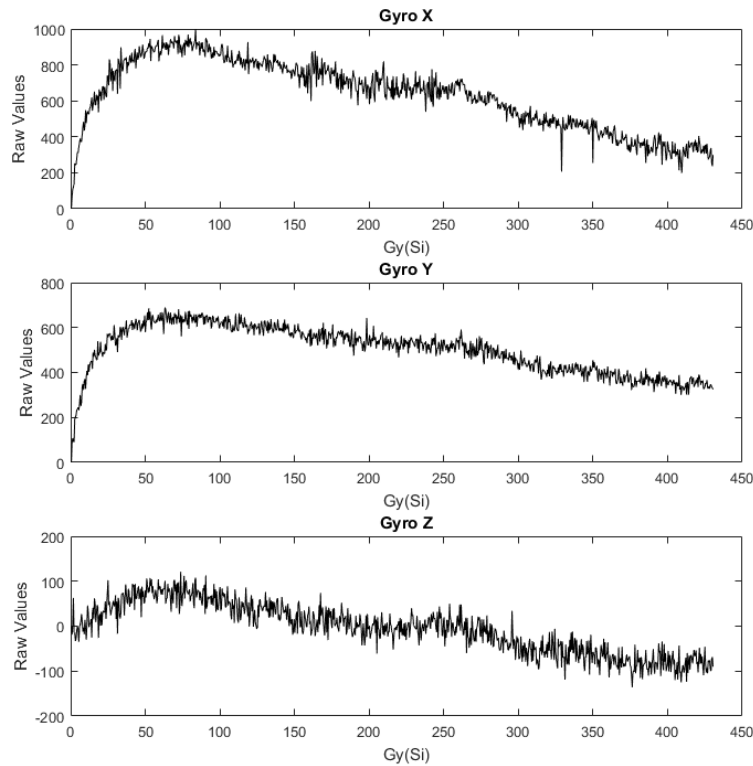


Figure B.5: Further test sample of LSM9DS0 showing gyroscope degradation

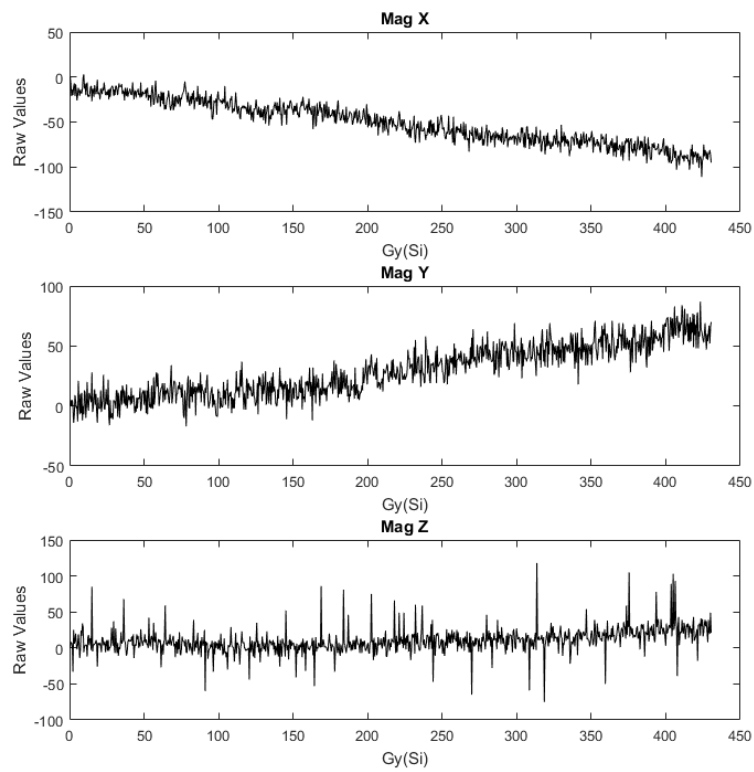


Figure B.6: Further test sample of LSM9DS0 showing magnetometer degradation

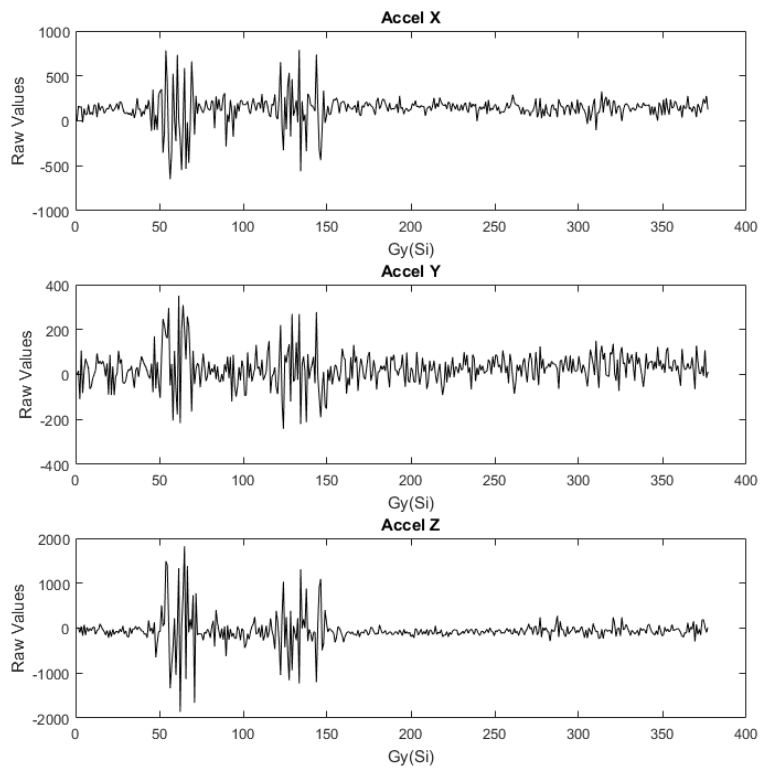


Figure B.7: Further test sample of LSM9DS0 showing accelerometer degradation

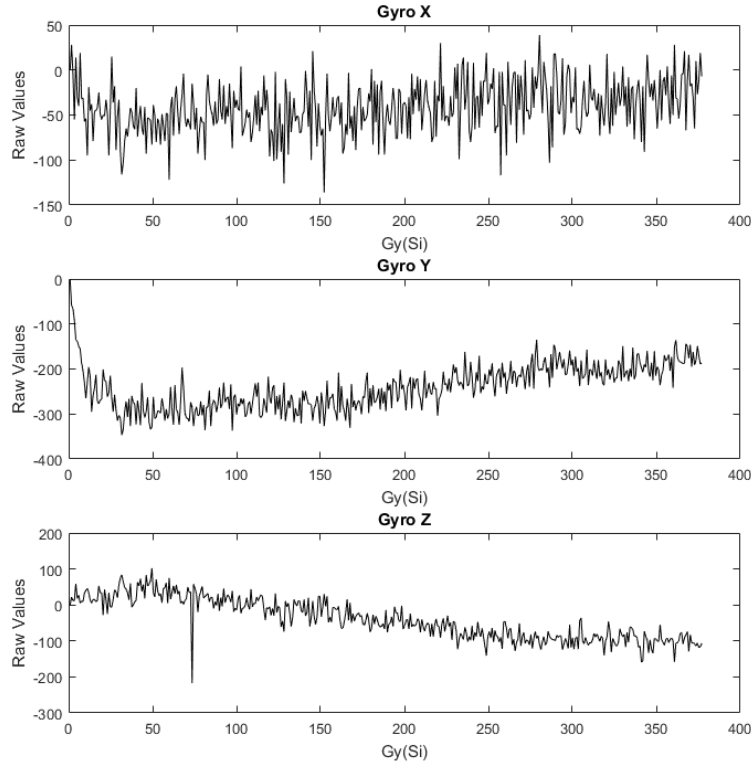


Figure B.8: Further test sample of LSM9DS0 showing gyroscope degradation

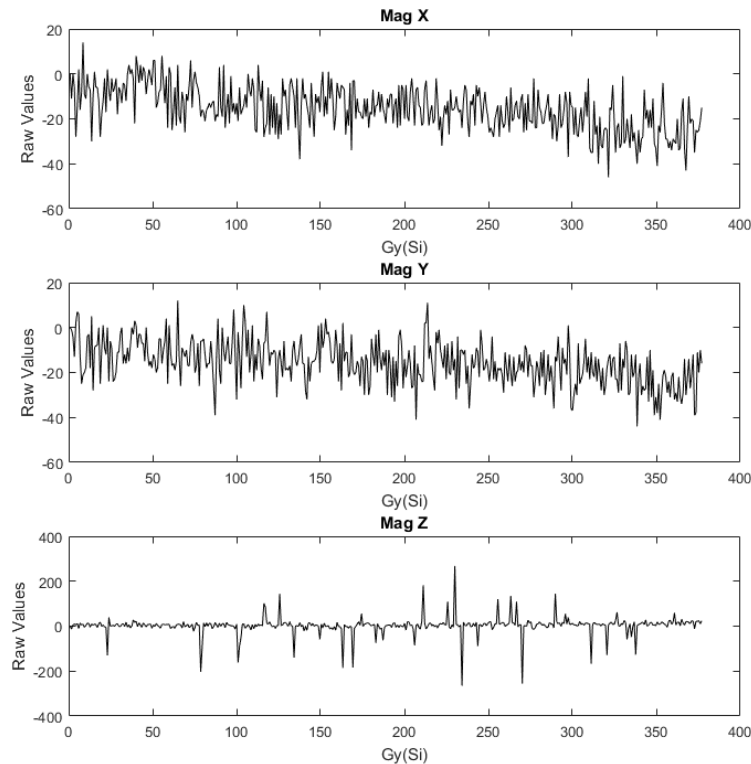


Figure B.9: Further test sample of LSM9DS0 showing magnetometer degradation

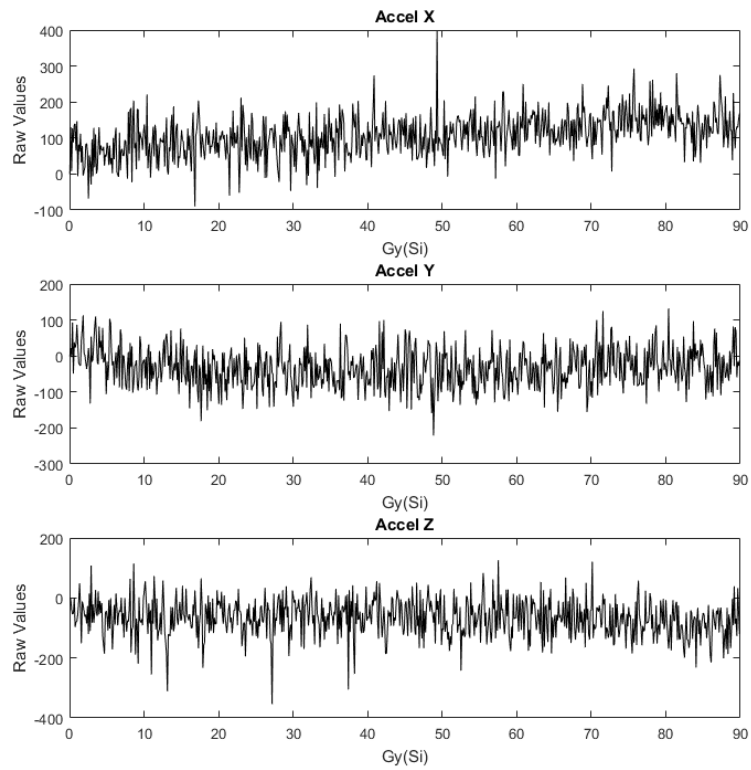


Figure B.10: Further test sample of LSM9DS0 showing accelerometer degradation

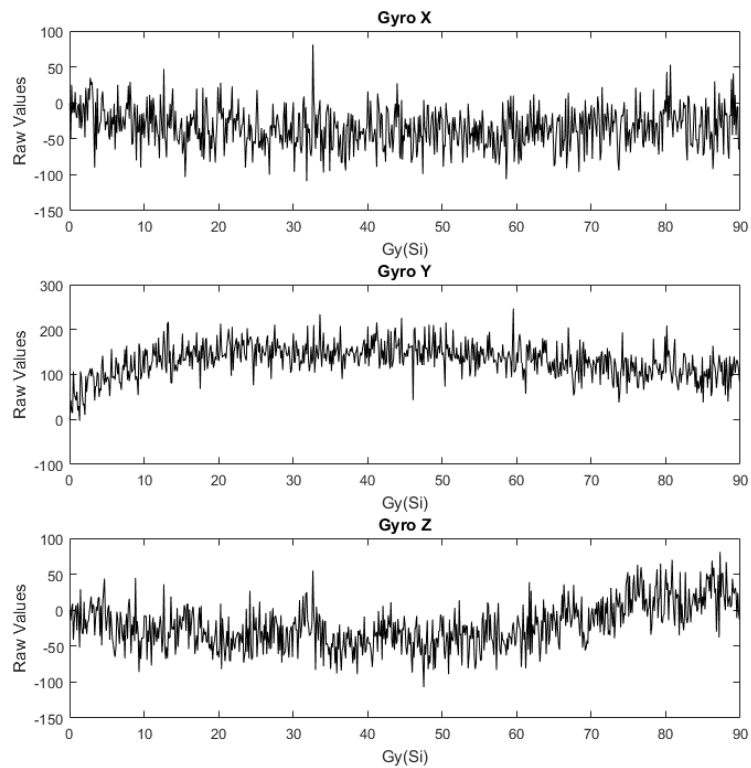


Figure B.11: Further test sample of LSM9DS0 showing gyroscope degradation

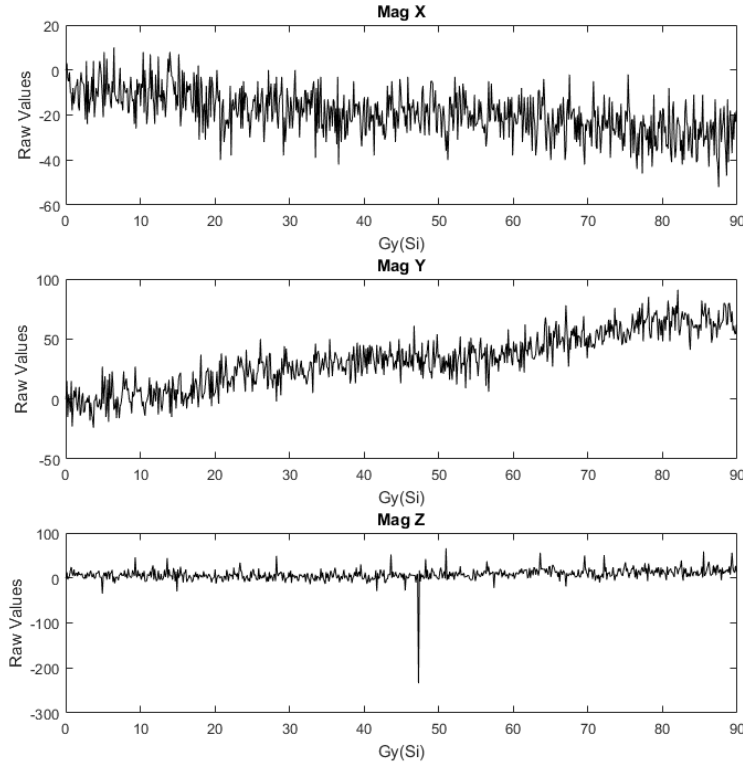


Figure B.12: Further test sample of LSM9DS0 showing magnetometer degradation

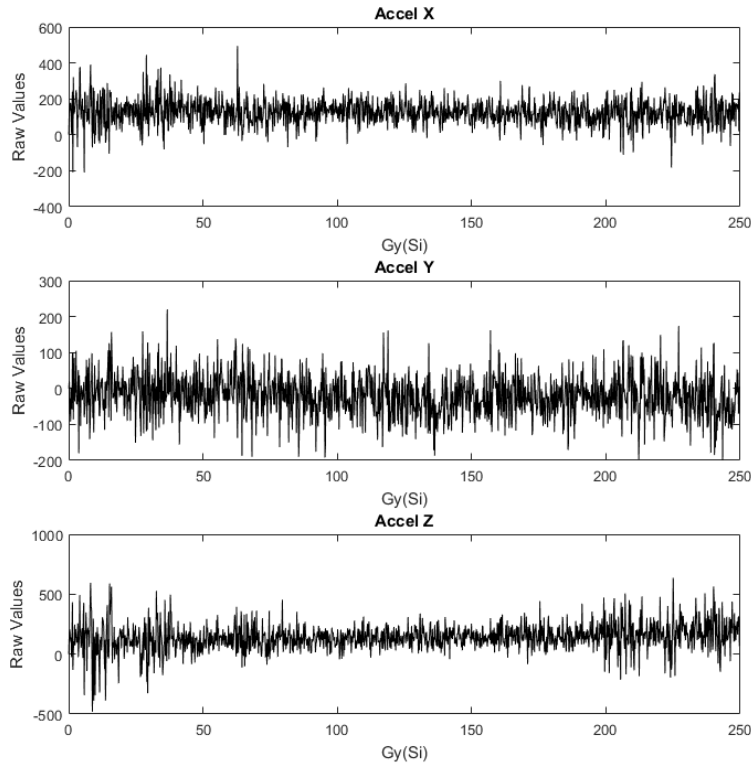


Figure B.13: Further test sample of LSM9DS0 showing accelerometer degradation

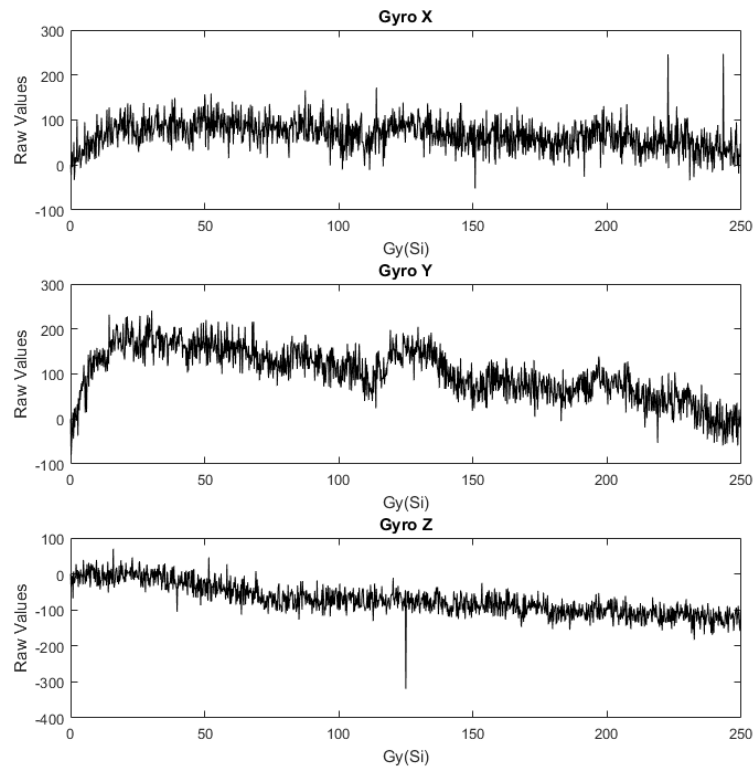


Figure B.14: Further test sample of LSM9DS0 showing gyroscope degradation

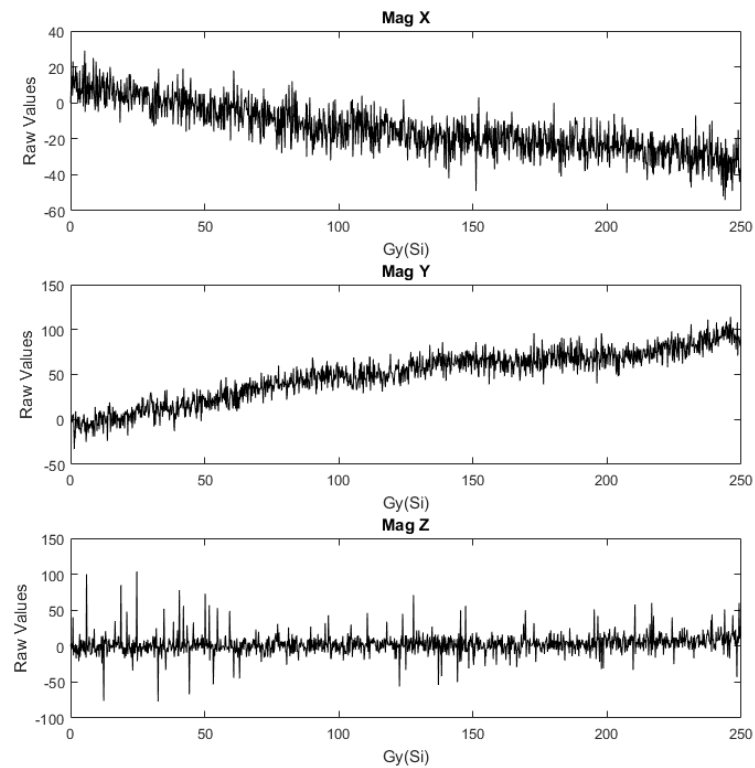


Figure B.15: Further test sample of LSM9DS0 showing magnetometer degradation

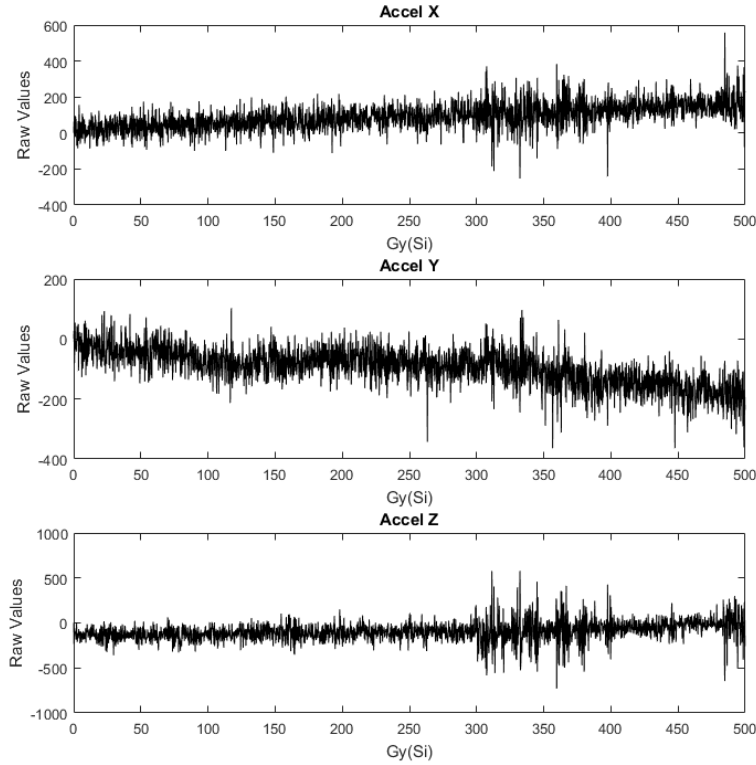


Figure B.16: Further test sample of LSM9DS0 showing accelerometer degradation

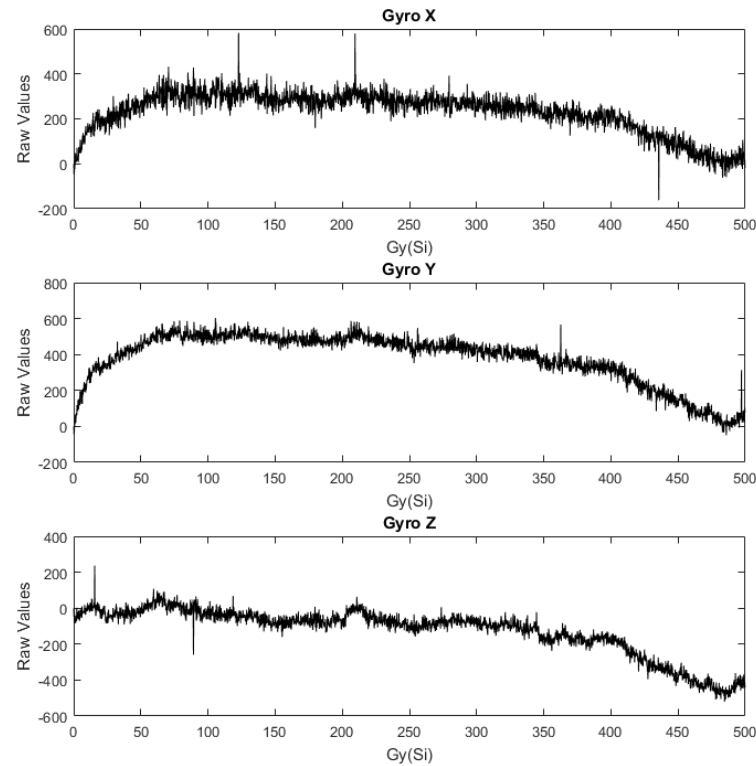


Figure B.17: Further test sample of LSM9DS0 showing gyroscope degradation

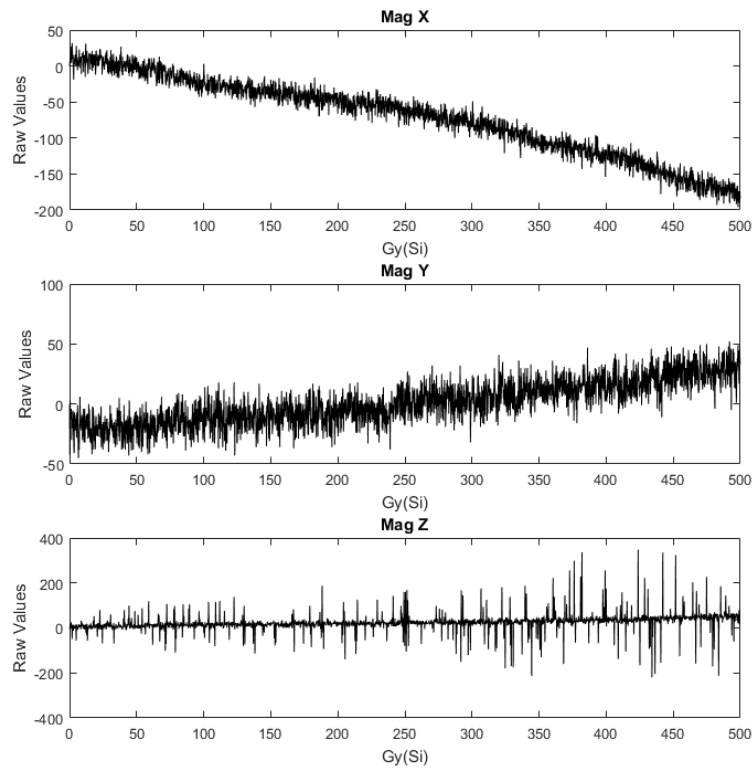


Figure B.18: Further test sample of LSM9DS0 showing magnetometer degradation

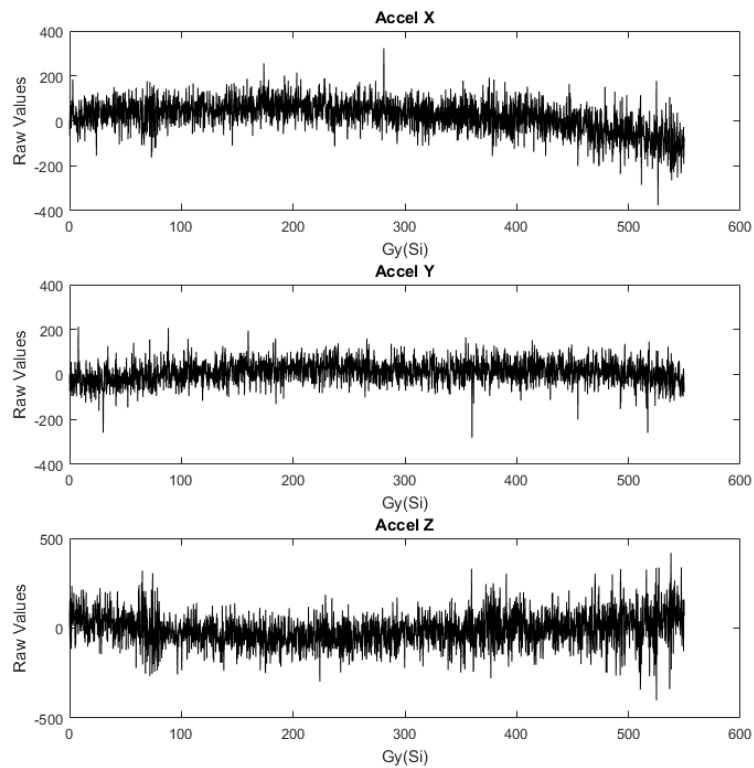


Figure B.19: Further test sample of LSM9DS0 showing accelerometer degradation

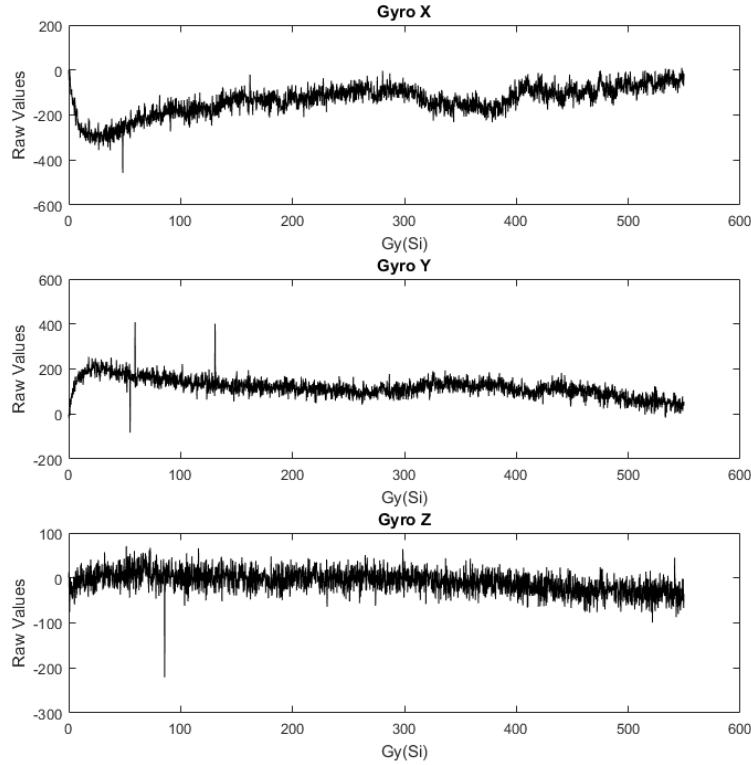


Figure B.20: Further test sample of LSM9DS0 showing gyroscope degradation

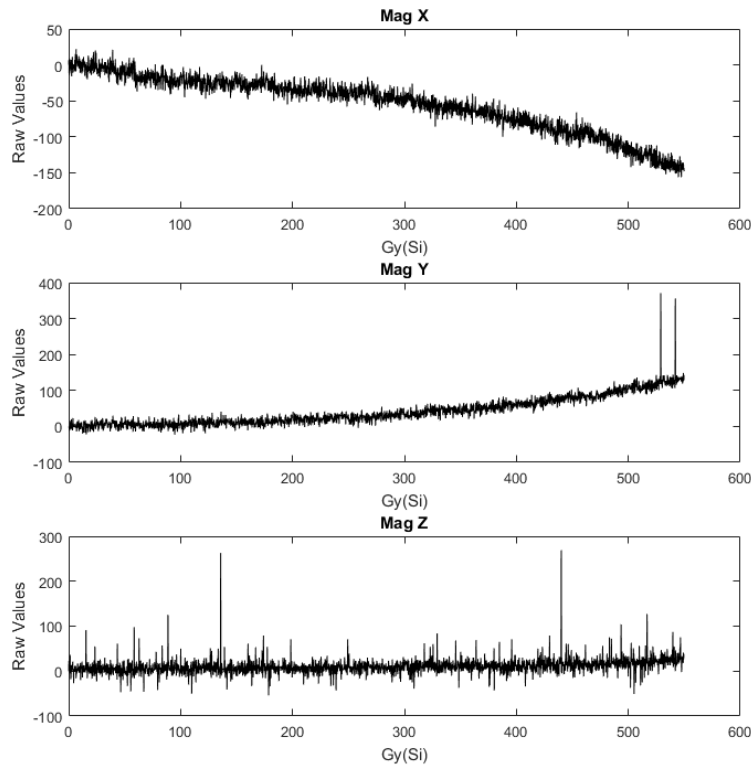


Figure B.21: Further test sample of LSM9DS0 showing magnetometer degradation

B.2 Additional MPU-6050 IMU test sample results

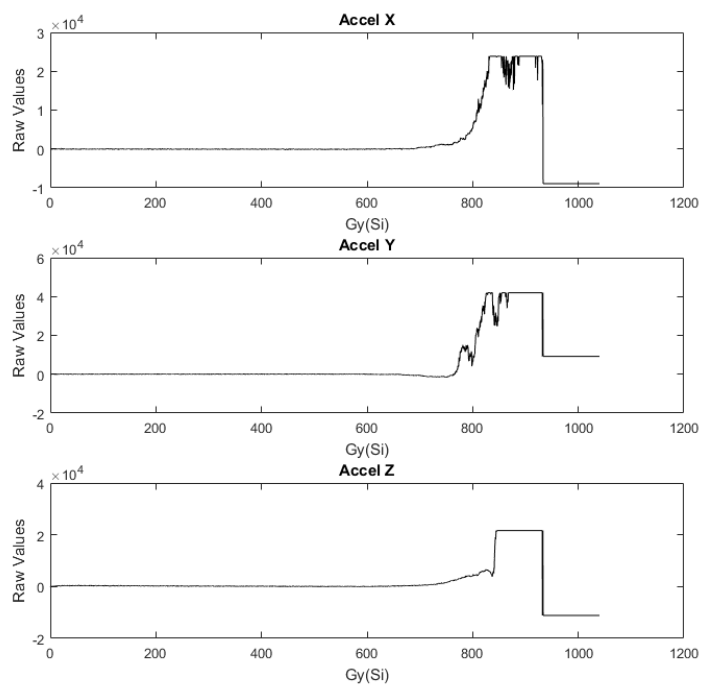


Figure B.22: Further test sample of MPU-6050 showing accelerometer degradation

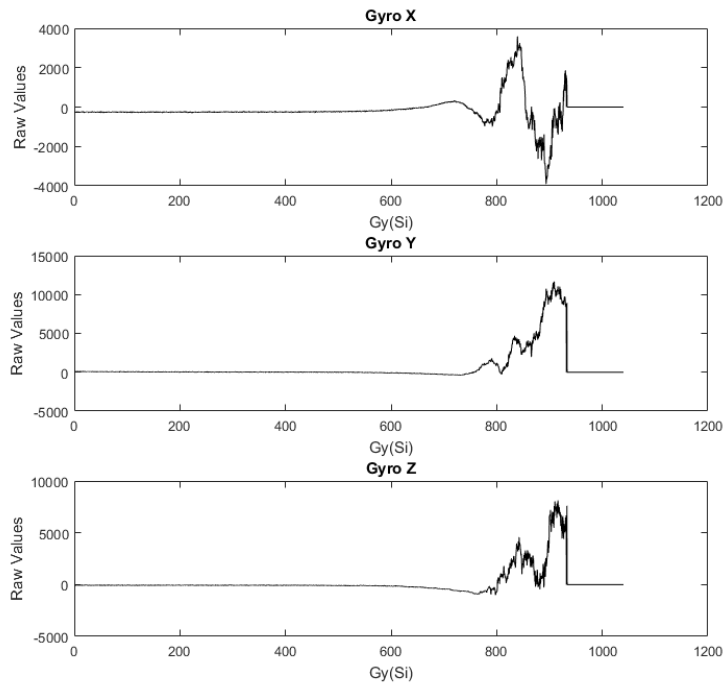


Figure B.23: Further test sample of MPU-6050 showing gyroscope degradation

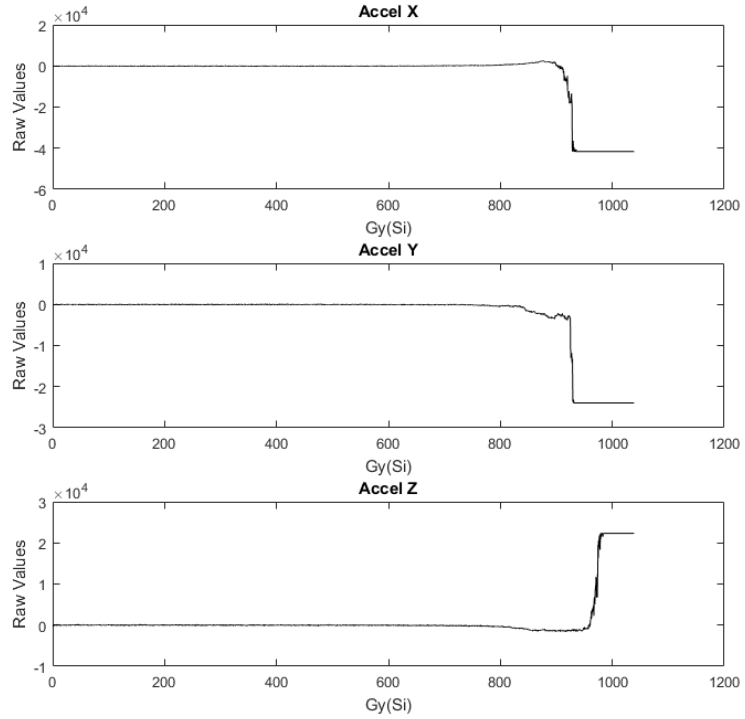


Figure B.24: Further test sample of MPU-6050 showing accelerometer degradation

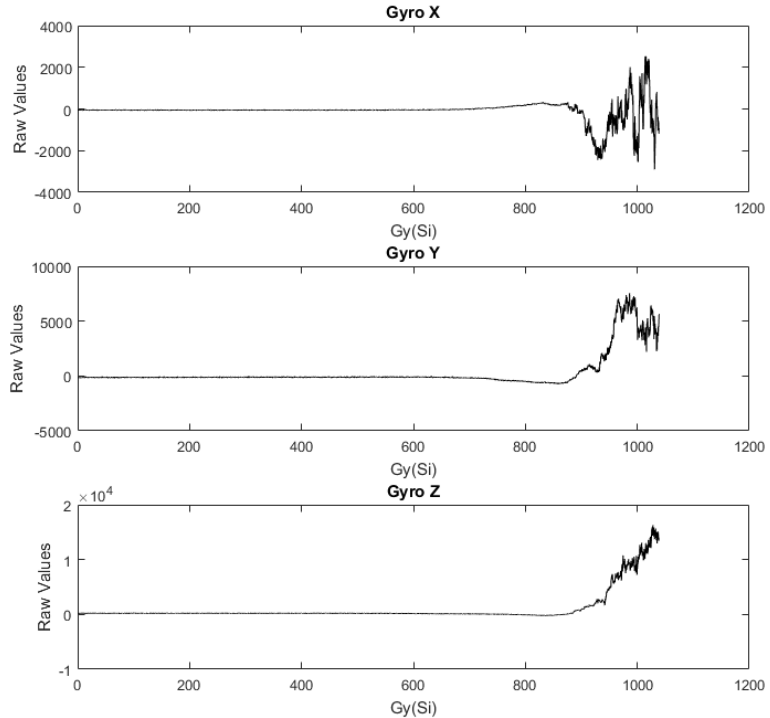


Figure B.25: Further test sample of MPU-6050 showing gyroscope degradation

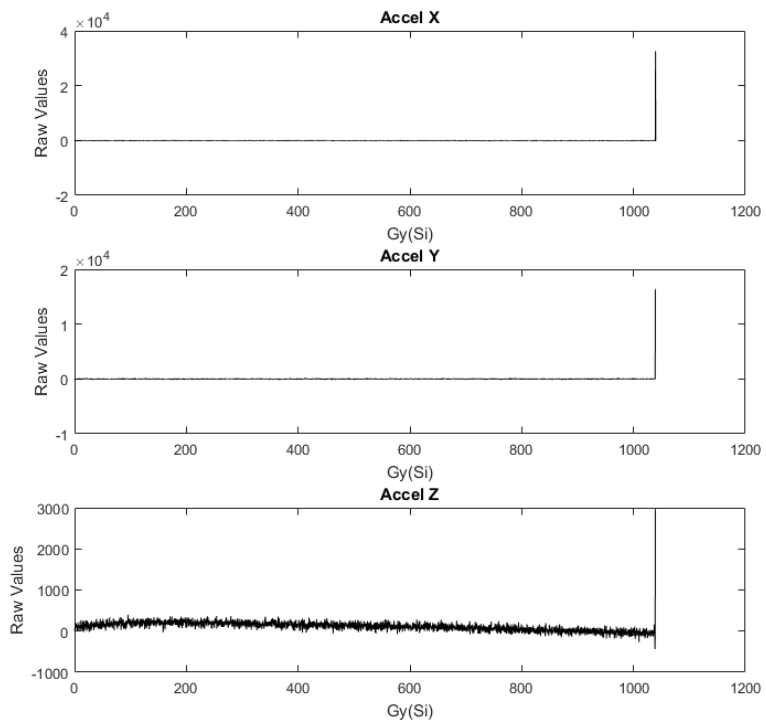


Figure B.26: Further test sample of MPU-6050 showing accelerometer degradation

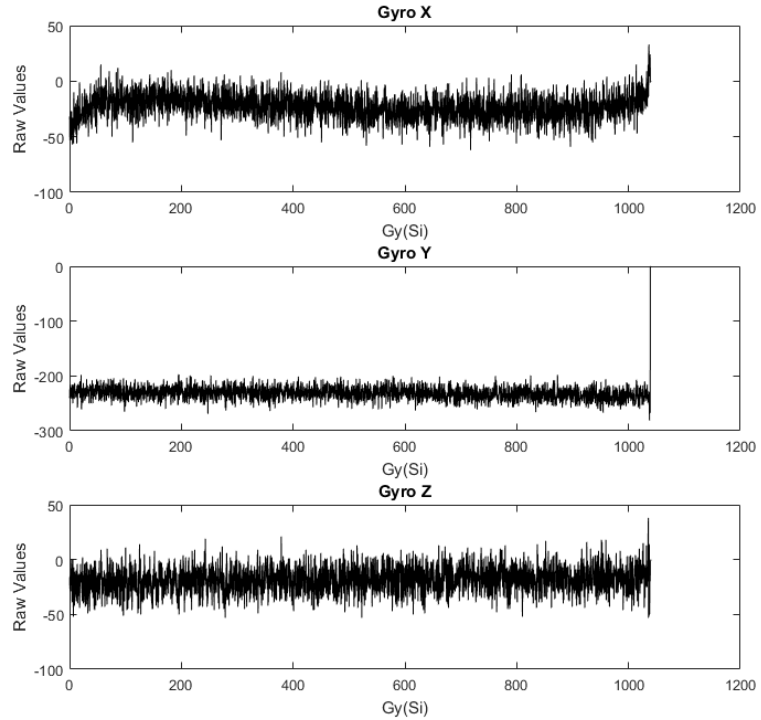


Figure B.27: Further test sample of MPU-6050 showing gyroscope degradation

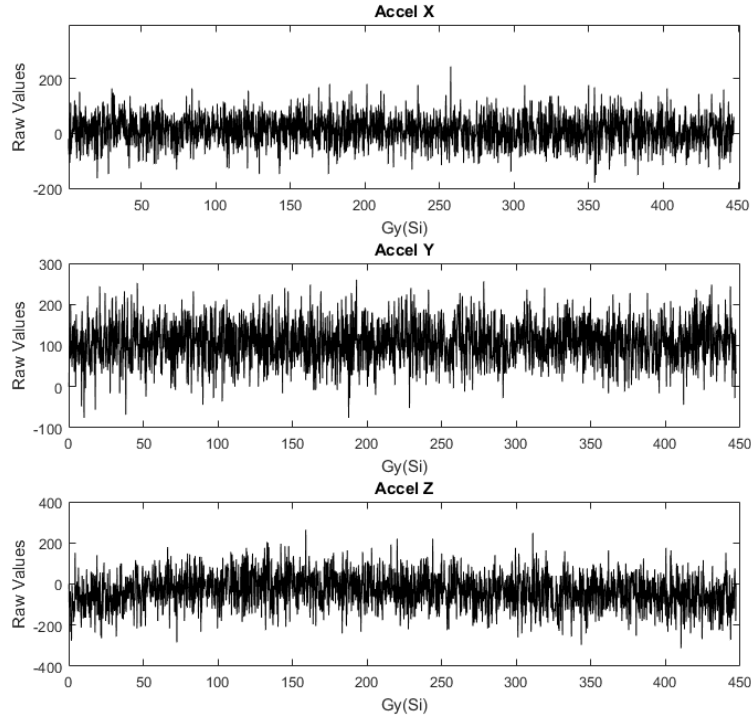


Figure B.28: Further test sample of MPU-6050 showing accelerometer degradation

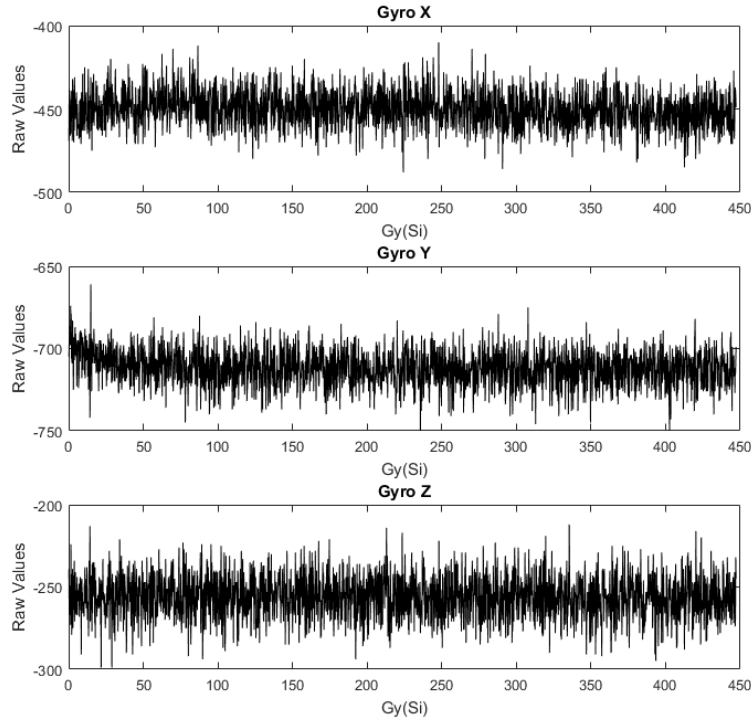


Figure B.29: Further test sample of MPU-6050 showing gyroscope degradation

B.3 Additional SEN-10121 IMU test sample results

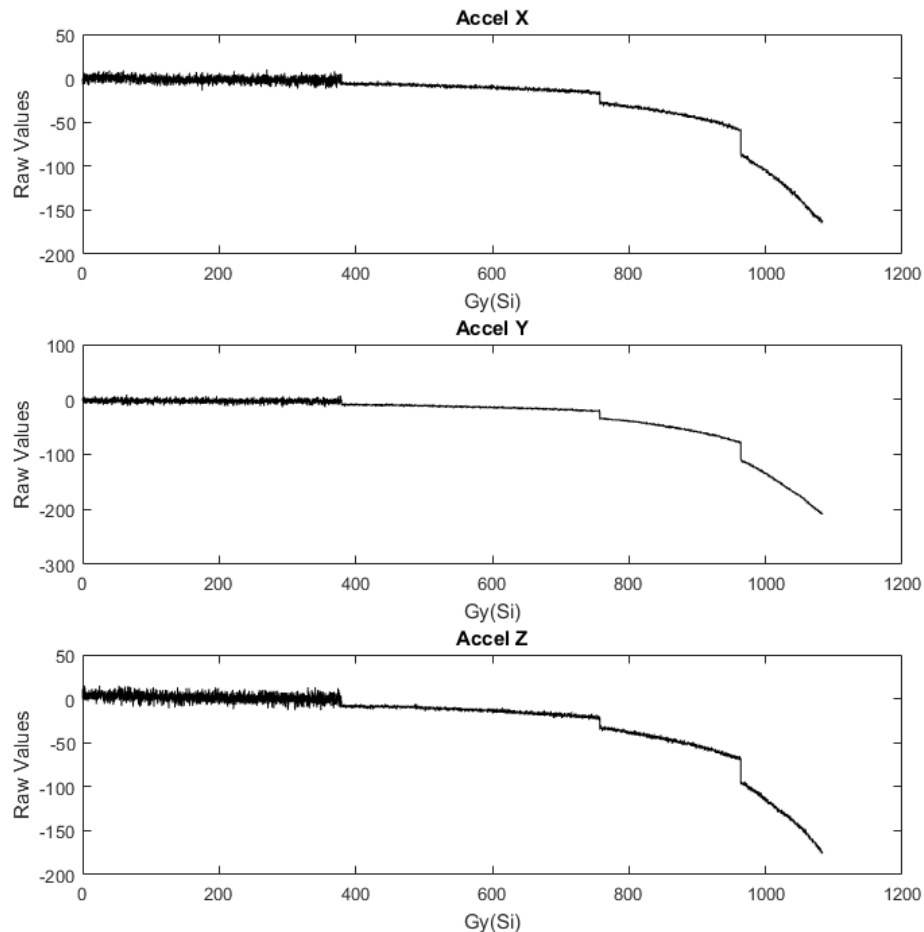


Figure B.30: Further test sample of SEN-10121 showing accelerometer degradation

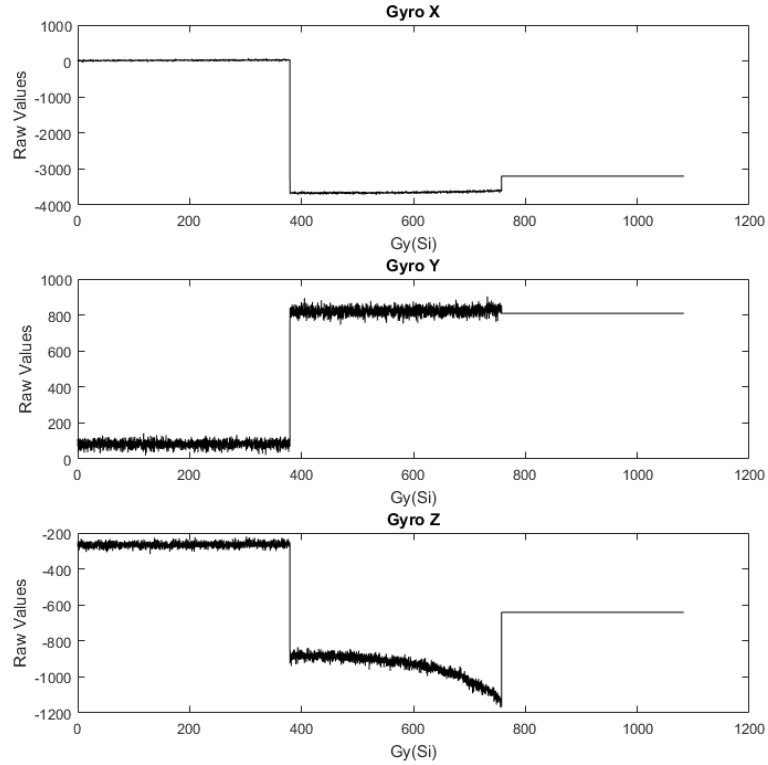


Figure B.31: Further test sample of SEN-10121 showing gyroscope degradation

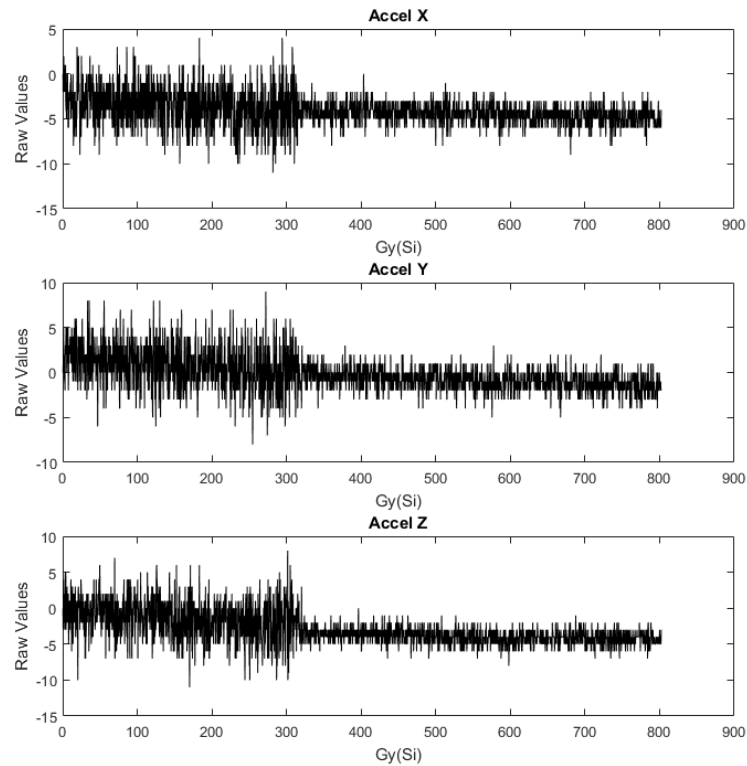


Figure B.32: Further test sample of SEN-10121 showing accelerometer degradation

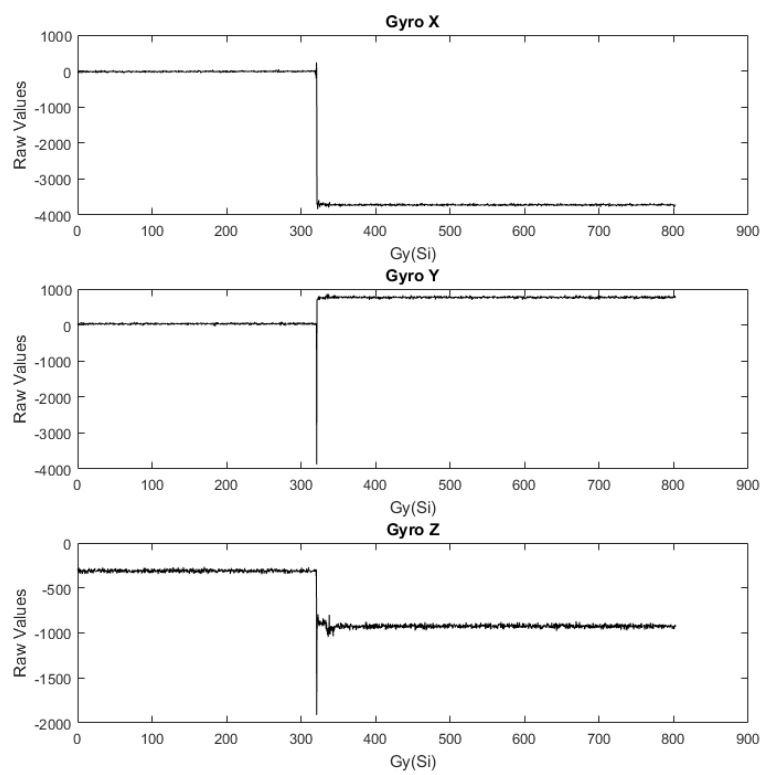


Figure B.33: Further test sample of SEN-10121 showing gyroscope degradation

B.4 Additional ADXL335 IMU test sample results

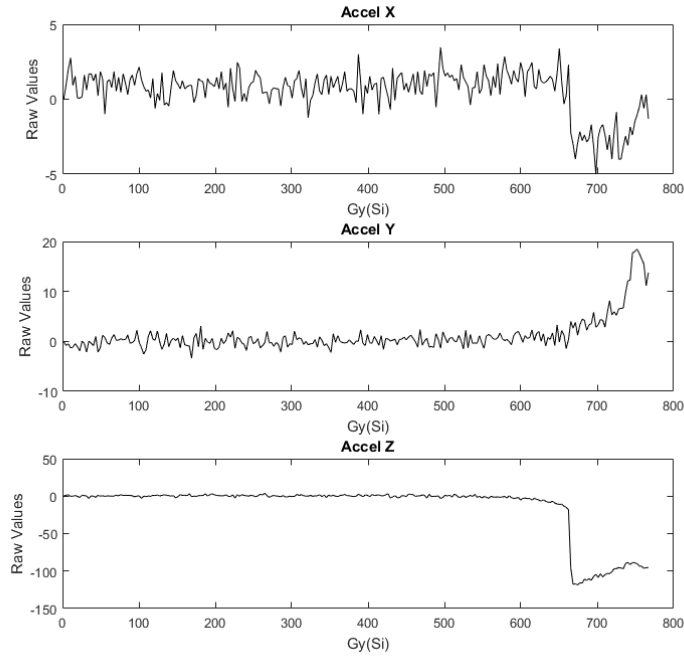


Figure B.34: Further test sample of ADXL335 accelerometer showing degradation with an increasing dose

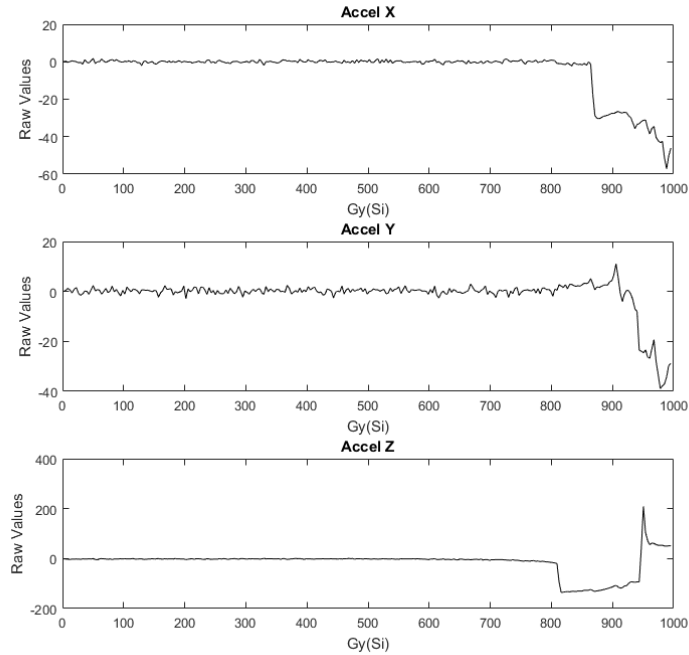


Figure B.35: Further test sample of ADXL335 accelerometer showing degradation with an increasing dose

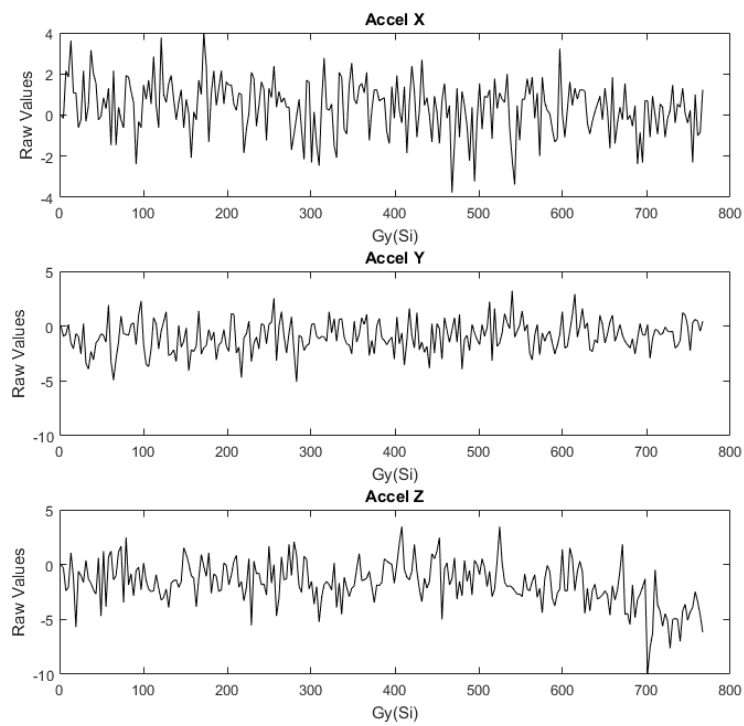


Figure B.36: Further test sample of ADXL335 accelerometer showing degradation with an increasing dose

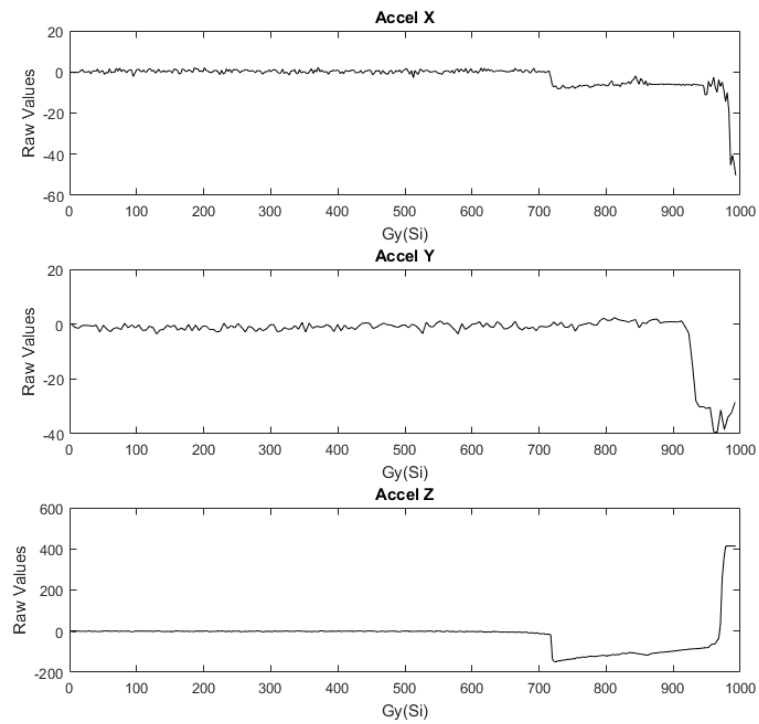


Figure B.37: Further test sample of ADXL335 accelerometer showing degradation with an increasing dose

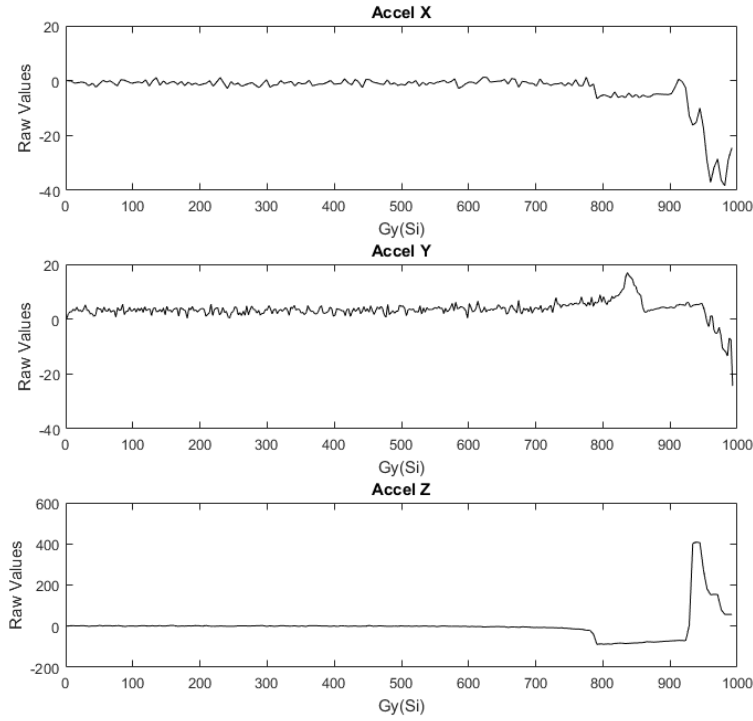


Figure B.38: Further test sample of ADXL335 accelerometer showing degradation with an increasing dose

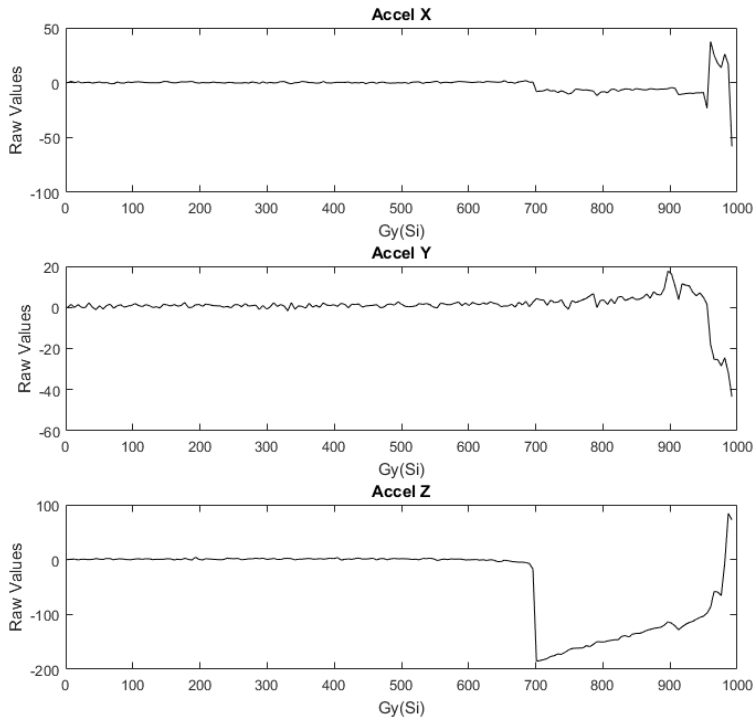


Figure B.39: Further test sample of ADXL335 accelerometer showing degradation with an increasing dose

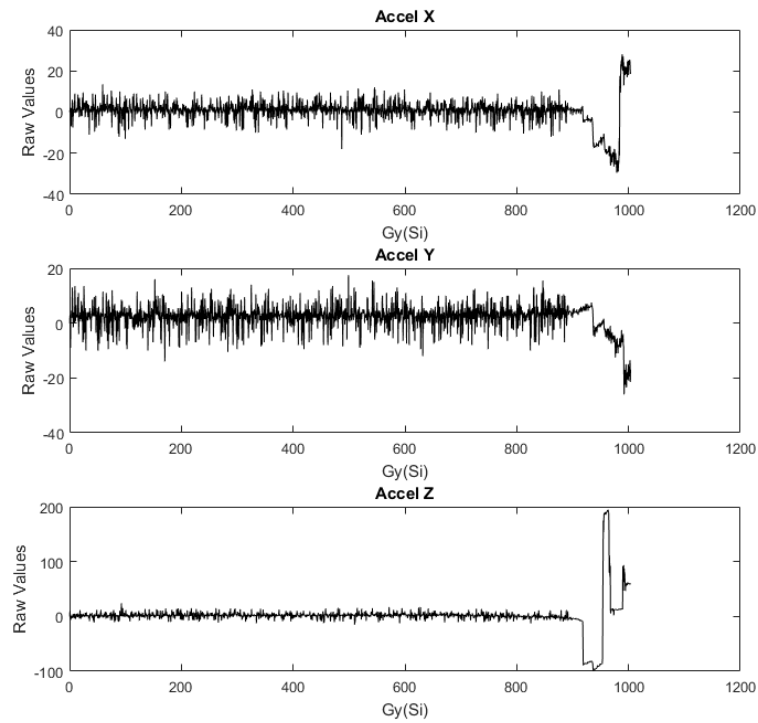


Figure B.40: Further test sample of ADXL335 accelerometer showing degradation with an increasing dose

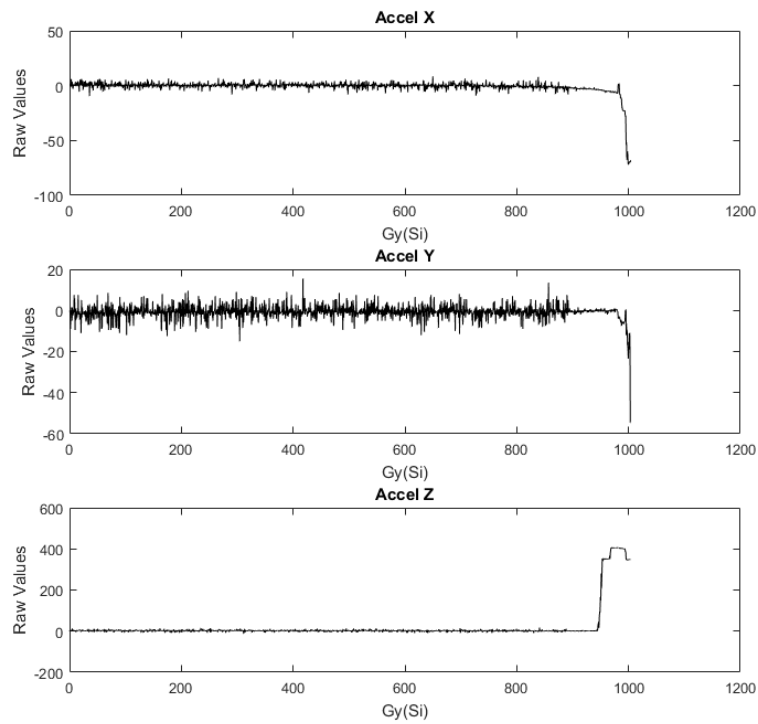


Figure B.41: Further test sample of ADXL335 accelerometer showing degradation with an increasing dose

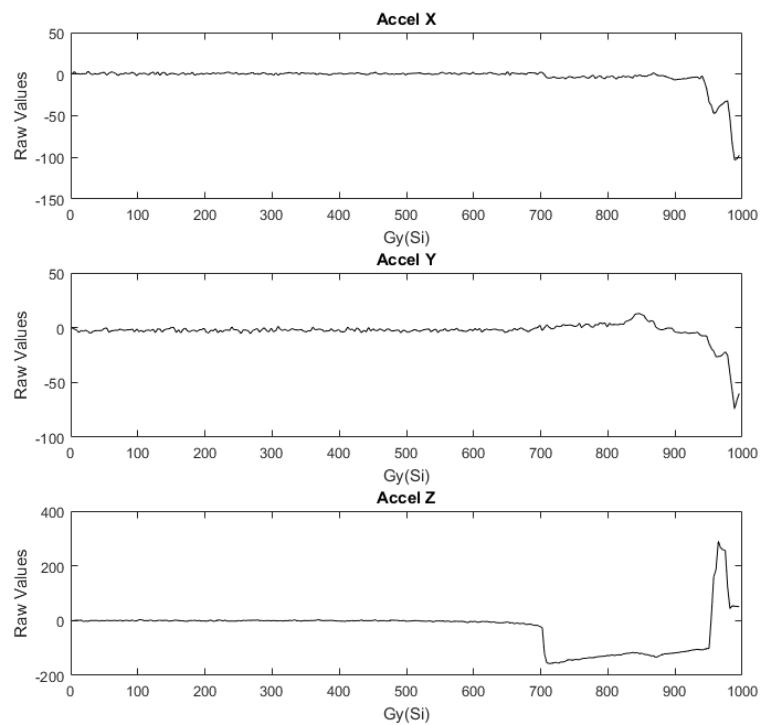


Figure B.42: Further test sample of ADXL335 accelerometer showing degradation with an increasing dose

Appendix C

Supplementary Power Regulation Tests Information

C.1 Schematics

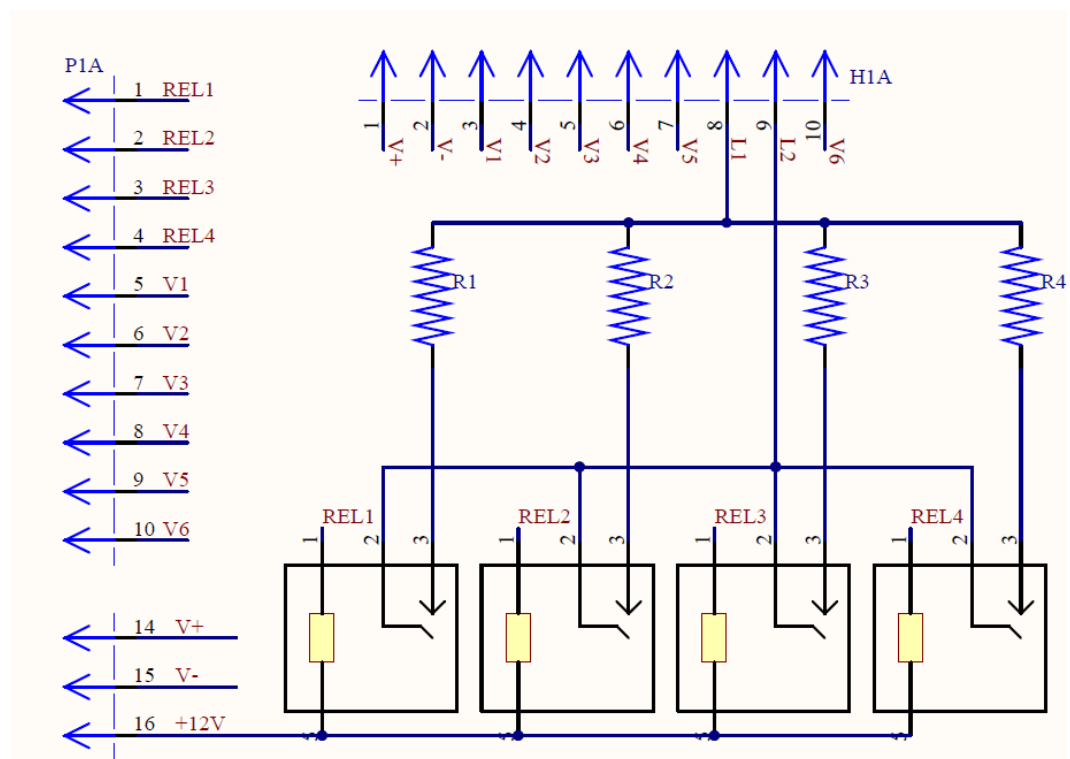


Figure C.1: Schematic of the switching circuit used during irradiation tests

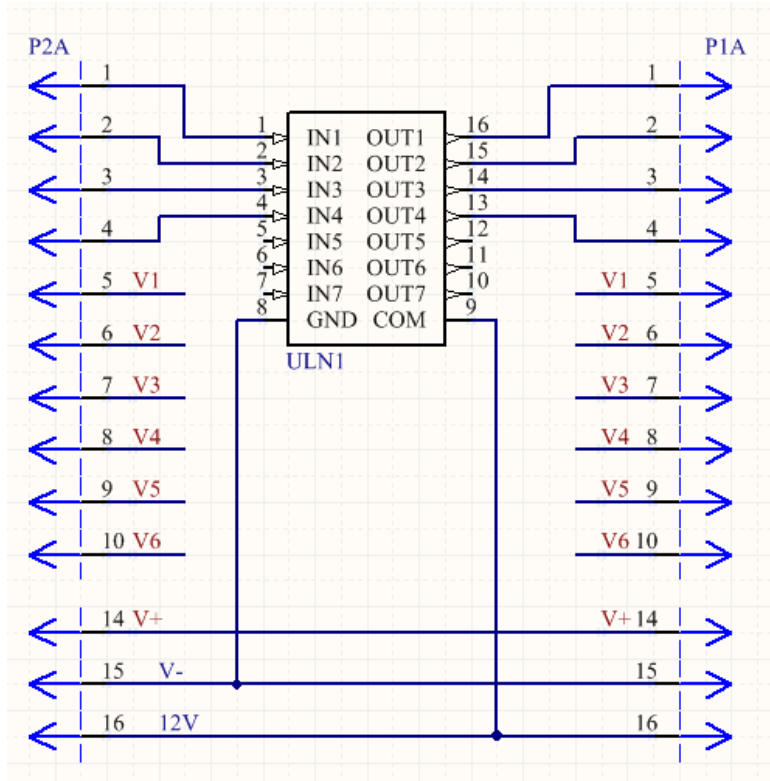


Figure C.2: Schematic of the relay drivers used to control the switching circuit used during irradiation tests

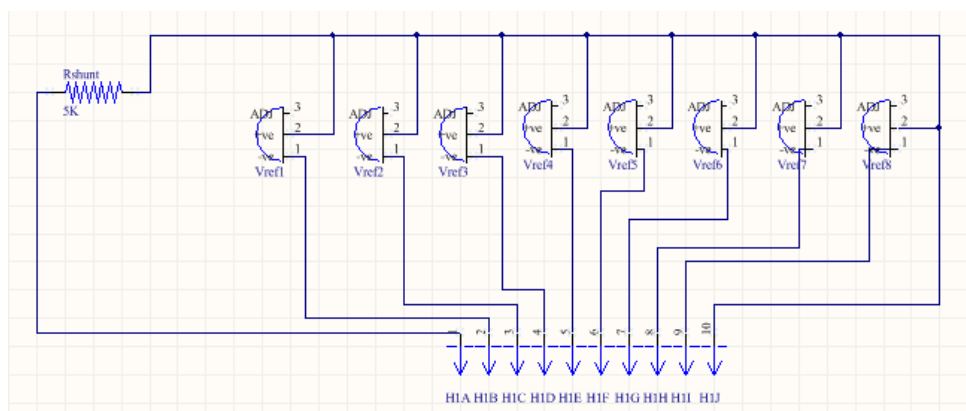


Figure C.3: Schematic of the voltage reference test sample circuit used during irradiation tests

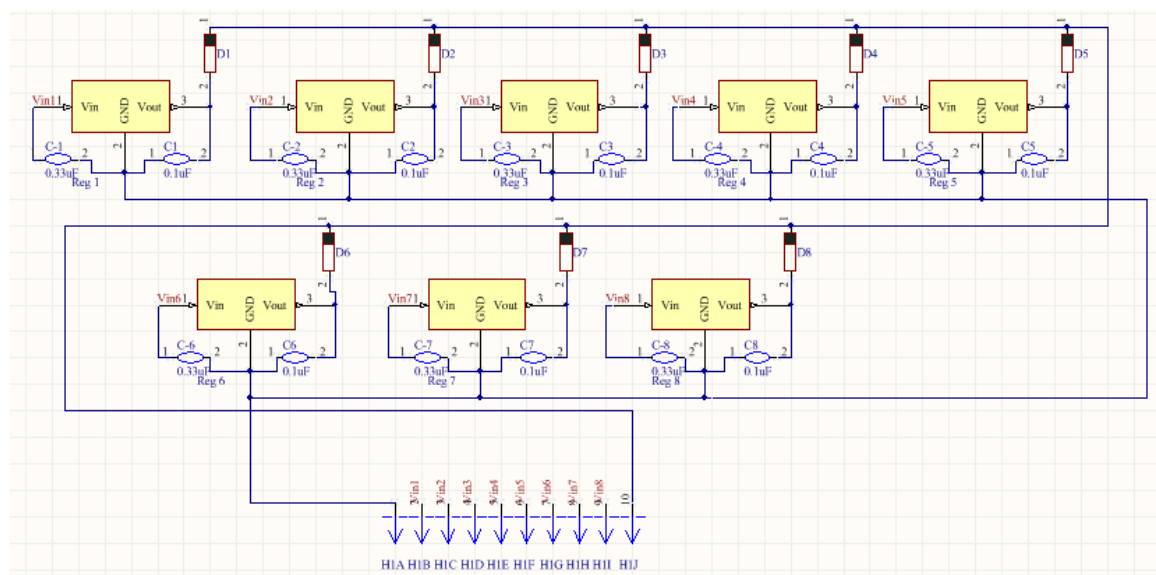


Figure C.4: Schematic of the voltage regulator test sample circuit used during irradiation tests